ELECTROMAGNETIC SURFACE WAVE MEDIATED ABSORPTION AND TRANSMISSION OF RADIATION AT MICROWAVE FREQUENCIES

Submitted by

MATTHEW JOHN LOCKYEAR

To the University of Exeter
as a thesis for the degree of
Doctor of Philosophy

NOVEMBER 2004

I certify that all material in this thesis which is not my own work has been identified and that no material is included for which a degree has previously been conferred upon me.

_____

ABSTRACT

Modes that propagate along the surface of a conductor are often referred to as surface plasmons (SP's) at optical frequencies, and at microwave frequencies simply as surface currents. It is the purpose of this thesis to show that at microwave frequencies, by altering the surface of a metal through the addition of a photonic structure, the properties of these modes may be controlled. In particular, control over the way in which these modes interact with incident radiation opens up the possibility of developing new and exciting photonic devices capable of controlling the resonant absorptive and transmissive nature of microwave structures.

The work presented in this thesis is divided into two main sections. The initial experimental chapters are concerned with the coupling of incident radiation to a SPP mode that propagates along a dual periodic, corrugated aluminium-air interface, resulting in extremely efficient absorption of the incident radiation. Further, the frequency at which the resonant absorption occurs is shown to be remarkably independent of the angle of incidence and, in addition, occurs at a frequency which is predetermined by the physical parameters of the grating, demonstrating the potential of selectively absorbing designer-surfaces.

The subsequent experimental chapters are concerned with the extraordinary transmission of radiation through sub-wavelength apertures, mediated by either a photonic surface, or wave-guide modes within the aperture. This is the first experimental study of the enhanced transmission phenomenon to be conducted in the microwave regime, and together with the finite element method modelling of the system provides remarkable and original insight into the characteristics observed in the transmission spectra through such structures.

This thesis is dedicated to my Father, Victor Norman Lockyear (1926-1993),
who knew me only as an academic under-achiever.
I wish he could have read it.

A college education does not make a bad man virtuous.
It merely puts a polish on his wickedness.

D. Jarvis 2004
(and A. Lincoln, 1850)

TABLE OF CONTENTS

LIST OF FIGURES AND TABLES

Acknowledgements

Here I would like to take the opportunity to thank all the people who have offered me help, advice and support during my postgraduate research in the Thin Film Photonics Group at Exeter. After a year away, working with some of my now most highly regarded friends at British Nuclear Fuels in Cumbria, I returned, specifically to meet Professor Tim Naylor to discuss the possibility of undertaking a PhD in astrophysics. During my visit I was offered several projects by different research supervisors (I don't know what they see in mature students) including research opportunities with my very good friends Ian Summers, Alex Savchenko, Steven Matcher, and Dave 'Bradders' Bradley. However, with multiple projects on offer, there was only ever one option, and that was due to the supervisor who tended it, Professor Roy Sambles. He is the only person in the whole department that makes me feel like an eleven year old schoolboy sat outside the principal's office as soon as he enters the room. Roy is without doubt the most enthusiastic and passionate person about his chosen subject that I have ever met. He has an unquenchable interest in the work that we do, and a drive that borders on hyperactivity, with which he is able to bulldoze students through their PhD research before they know what's hit them. Throughout life, especially if you make friends as easily as I do, you are probably destined to meet only a handful of people who are very, very special. Roy definitely falls into this category, and for that I thank him. It's been a real privilege, and I don't make that remark lightly. He has also kicked my backside on more than one occasion, and there aren't many people who can say that! I wouldn't have had it any other way.

Second only to Roy, the person to which I owe the most thanks for helping me through my postgraduate research is Alistair Hibbins. Alistair has helped me on too many occasions to remember, and proof read every scientific piece of work that I have ever written. He has shown me an unlimited amount of patience, and during my time as a post grad I have witnessed his development into a full blown supervisor in his own right. I have no doubt that in time, he will be as good for his students as Roy was for us. I like to think that we have become very good friends over the last three or so years, and provided each other with lots of laughs, such as spray mounting all of Jimmy Heads stuff to his desk, and winding up Gloria by telling him I had won the

Mullard award and had received a huge PDR payment. Making up spoof email addresses and sending Simon an invitation to the Pop Stars audition from Simon Cowell (which he fell for). Teaching Simion Astillian colourful language without him knowing it, and setting up my computer remotely so it would scream Sharron!! in Ozzy Osborne's voice while she was having a meeting in the office. Thanks Al. In return I would like to confer upon you the honouree title of Ned the Cabin Boy, and grant you life membership to the Smugglers Soc.

I would also like to take this opportunity to thank Chris Lawrence, my Qinetiq supervisor. With a house, a wife, and three kids, my bills are huge. Without the case award the PhD would not have been an option financially. Chris has been the best case supervisor anyone could wish for. He never once pressured me, but instead just let me get on with it under my own initiative. I hope he was pleased with the productivity and results.

Next it is customary to thank the old guard, the people that made up Groups 13 and 20 who, during my postgraduate study, moved on to pastures new. Phil 'Jive Bunny' Worthing, the king of campness. Nobu, who moved back to Japan, but whom I am still in daily contact with, to offer my own brand of advice in wooing the ladies. Needless to say he hasn't had any luck yet. Not even a slap. To Pete 'Hobbit' 'Hairy Jeremy' Hobson, a man undoubtedly on my wavelength and who shares my taste in women (Pete had enough sense to pack a 12 inch bowie knife and a book on home made incendiary devices in his luggage on a post 9/11 conference trip to America). To Hazel Went, who was good company in the early days, and who has fed me jaffa cakes on many occasions. To John Wasey, a frighteningly clever guy. I'm sorry mate, I have to admit that during all our conversations I was just nodding and agreeing politely, because I never understood a word you said. To Fuzi and 'switch on, switch off' Lizhen. We made a fairly odd couple up in 110, but I enjoyed Fuzi's company. He could whistle Chinese Red Army marching songs for two hours straight. If you started humming a few bars of any Beatle's song or such like, he would pick it up subconsciously and flit between the two songs seamlessly. I once had him whistling seven tunes, simultaneously! To Simion Astillian. He put on two stone while lodging with my mum. No wonder he never wanted a cuppa in the morning, she was forcing the finest Brazilian blend down his neck with his breakfast. Lastly to Piers, a Post Doc

with an extremely broad range of knowledge, who took real pleasure in helping others and who could keep explaining the same principle over and over in a myriad of different ways, until you got it. You should never have left mate, everyone misses you.

Now to the current members of Groups 13 and 20 in no particular order. To Sharon 'the little mermaid' Jewell. I'm sorry Sharon, for everything I have ever said or done and for being at the swimming baths with Joseph when you turned up to take part in a water aerobics class. I say allsorts, but never mean, or believe, any of it. To Mike 'Marvel' Jory. Hey Michael, I see Wedgie's acknowledgements imply that you ride a bike with stabilisers and frilly pink handlebar ribbons. I would never stoop so low mate. You hang in there, if you build it they will come. By the way, my 'Table-tops' were infinitely better than yours. To Andy 'pint of Guinness and a packet of crisps' Murray, a fellow member of film club, and responsible for such showings as Convoy, and Battle Royale. Cheers Andy, for being there to bounce ideas off of, and being a really good mate. Give up that sporty stuff, its bad for you. Look at me, a fine physical specimen in perfect health, and I don't go in for any of that rubbish! To Wedgie, a fellow secret snooker player (sssshhh Stevo, it's still a secret), fellow biker, and who was one of the three amigos in the undergraduate days. This man makes the best cakes I have ever tasted in my entire life (and I've tasted a few, let me tell you). He is going to make you a lovely wife one day Lucy. To Ian 'Gloria' '34 tutees and counting' Hooper. You have enough there to start your own pink army Ian. Cheers mate, for being the group's donut police, for stepping into Phil's winkle pickers, and for being the man to see when you have SP problems. Or is that SPP at microwave frequencies? Driving range on Thursday, O.K? To the other members of the microwave group, Jimmy 'The Head' 'Men in Tights' Suckling, who has a women's rod, but is thinking of trading it in for a mans one, Robert Kelly, and Ben. How old are you Robert? Are you sure you're old enough to drive that car? They have had to put up with a lot from me, and deserve a medal. Don't forget, you have to put my name on ~~that paper~~ all papers, preferably first (Roy said). To Pete 'Lucky' Vukusic, a fellow family man, surfer dude (in one of my previous lives) and a real mate. Cheers for sharing all those apple and blackcurrant turnovers with me, I recognise just how special that is. And for sharing <u>your</u> office. I still can't believe how lucky you are. Tokyo, Hawaii, America, the list is endless. And that press officer, knocking on your

door and phoning you up all the time! Hail to the king baby. To Jimmy 'K' Kerslake, a most brilliant guitar player, drummer and bell ringer. Gosh Jim, you are tall. Get writing mate. If I can do it, you can. To Simon Garrett. I've deleted your self proclaimed nickname, because it is simply not a fair description of you. Besides, you don't need a nickname with a middle name like Hornby!! I'm sorry Simon, for any practical jokes I have played on you, including the Simon Cowell incident. Thanks for providing me with a new laugh on a weekly basis, including the infamous 'wall of death'. I still laugh to myself about that one. I think John Crabb needed 6 weeks of counselling because the incident was visually traumatic! I'm glad all that free advice that I have given you on the fairer sex has paid off. Keep that chin up. Before you know it you'll have 200 pages. To John 'The Bear' Birkett. Sorry about that nickname John, it just stuck. And to the two Tims. Tim A is an absolute wizard, and gives the best group meeting presentations ever, whilst Tim T is the new master of the liquid crystal kit, and has had to put up with me stealing his whiz-bang computer while he was on holiday. Sorry Tim. To Gemma and Armando. I am really not that scary when you get to know me, honest. To Pete 'the Belmont Bulldog' 'get your head under that extractor fan' Cann. Thanks Pete, I appreciate all your help, technical expertise, common sense solutions and letting me jump to the head of the queue more often than not. It's a shame United will be first division next year. Still, tickets will be easier to come by. Well, I think that covers the entire group except for Bill Barnes. You have a really great bunch of people there Bill. I would tell you that you should be very proud of them, but I know you already are.

Next I must thank the support staff of the department. In the microwave group, we rely heavily on the absolutely amazing quality of work produced by our own mechanical workshop. Once again, in no particular order, thanks to Kevin 'Snogger' White. I appreciate the shear quality of your work, and the fact that you are a like minded individual. We have had some great cracks in the workshop. Cheers for making me a member of the drinking club, and for putting up with me twiddling all the knobs on the various machines. Throw that file in the bin and buy yourself bike to ride rather than fix. To Dave 'Mr M^{c}Kye' Jarvis. I know why those shoes of yours are so highly polished. Sorry I lost all those grand master keys, a lesser person would have stopped doling them out to me. To PBW, John 'Trigger' Meakin, Russ, Paul, Dave Manning, Adam, and Steve 'Tabby' Tuckett. You run a remarkably tight and

efficient ship there Tuckett. Shame we can't say the same about your swing. To Phil Vossler, who saved my computer from being thrown straight through the first floor window on numerous occasions. To Chris, who helped me sort out the aluminium etching technique, and Texas Tom, who helped sort the LED lights on the Bandit.

Finally I would like to thank my family. My wife Jacqui, children Robbie, Katherine and Joseph, and my dog Teal. Teal was a fine jet black 3 year old working lab and potential field trial champion when I embarked on my academic career, now he is fat, old, and retired, with a white chin, selective hearing and a bladder problem. And they say dogs are like their owners. My family have had to put up with a lot over the past 8 years, especially at exam time and during the writing of this thesis. We have scrimped and scraped through financially for more years than I care to remember, and for that I apologise. I wouldn't have made it through without them. I am most certainly not the man Jacqui married fourteen years ago, and to be perfectly honest, I'm not too sure if she thinks that's a good thing or a bad thing. One thing is for sure though. I'm definitely wider.

Chapter 1
Introduction

The work presented in this thesis is related to two areas of physics which are currently generating great interest within the scientific community, and linked by a common physical phenomenon; electromagnetic surface modes. The initial experimental chapters are concerned with the coupling of incident radiation to a surface mode that propagates along the interface between a metal and a dielectric, resulting in remarkably efficient absorption of the incident radiation. This mode is known as the surface plasmon polariton (SPP) and its excitation was first experimentally observed in the spectra from ruled diffraction gratings by *Wood* in 1902. The subsequent experimental chapters are concerned with the extraordinary transmission of radiation through sub-wavelength apertures, mediated by either a photonic surface, or wave-guide modes within the aperture.

Chapter 2 presents a brief historical overview of the developments in the understanding of the physics describing the SPP. A derivation of the planar-interface dispersion relation of the SPP is presented, and the spatial extent of the fields associated with the mode is examined. This demonstrates that the mode is non-radiative, and consists of longitudinal oscillations of surface charge whose fields are well confined to the interface. Methods for coupling radiation into the mode are described, with particular emphasis on grating-coupling (since this method of coupling incident radiation to the mode is used exclusively throughout this thesis). In addition, the phenomena of SPP-mediated polarisation conversion and grating-induced band gaps are discussed.

Chapter 3 reviews waveguide theory, concentrating on metal clad waveguides that support transverse electric (TE), transverse magnetic (TM) and transverse electromagnetic (TEM) modes. The characteristic properties of each of the three waveguide modes are introduced, before embarking on a geometrically specific discussion. The transverse fields and cut-off wavelength of each mode is derived from Maxwell's equations in the context of three separate geometries; rectangular, circular

and coaxial. Further, detailed field profiles pertaining to each mode are presented, calculated using a finite element method (FEM) modelling code.

In *Chapter 4,* the fundamentals regarding the FEM modelling code (*the theoretical code used exclusively throughout this thesis*) are detailed. The physical principles underpinning the modelling software are described, and both the advantages and limitations of the finite element method discussed. The specific models used to predict the theoretical electromagnetic response of each sample presented in this thesis are detailed, describing sample geometry, and applied boundary conditions.

Chapters 5 and *6* present thorough incident and azimuth angle dependent studies of the specular reflection from zero-ordered dual period crossed gratings, milled into aluminium alloy substrates. In *Chapter 5* it is demonstrated that the efficient absorption of incident radiation may be attained through SPP excitation at frequencies pre-determined by the periodicity of the structure. The study is conducted in the microwave regime, providing an ease of manufacture and level of accuracy which would be difficult to replicate at optical frequencies. The depth and width of the reflectivity minima that appear in the specular reflection from the sample is shown to be dependent predominantly on the optical properties of the lossy dielectric used as an absorptive over-layer, filling the grating grooves. In addition, the frequency of the dominant reflectivity minima is shown to be incident angle independent. Further, the reflectivity minima are shown to be largely independent of azimuth angle, owing to the surface structure being comprised of two identical dual period grating profiles, crossed at 90 degrees with respect to each other in the surface plane of the substrate. In *Chapter 6* the degree of azimuth angle independence is increased by introducing a third identical dual-periodic profile, with the three profiles orientated at 60 degrees with respect to each other in the surface plane of the profile. The resulting zero-ordered, dual period hexagonal tri-grating is shown to exhibit up to seven surface plasmon polariton resonances (SPPR's) in the specular reflectance from the sample, with the majority of these resonances being largely incident and azimuth angle independent, and up to 95% efficient in the absorption of incident radiation.

Chapter 7 presents the first detailed study of the enhanced transmission phenomenon through a circular sub-wavelength aperture to be conducted in the microwave regime.

The sample consists of a circular aperture of diameter $d = \lambda_0/2$, where λ_0 is the wavelength of the incident radiation, which is countersunk from each side. A 17 fold enhancement in the transmission through the structure is exhibited with the addition of a photonic surface, consisting of concentric grooves centred on the aperture, forming a 'bull's eye' structure. The fundamental physics underlying the enhanced transmission phenomenon are discussed, and the contributions to the increased transmission from dynamical diffraction, and SPP enhancement are separated experimentally for the first time.

In *Chapter 8* a transmitting structure formed by a circular hole in a thick aluminium alloy substrate with a solid cylindrical core of the same medium but slightly smaller radius is examined. Resembling a terminated coaxial transmission line, this structure may be considered as a sub-wavelength slit with circular symmetry. As such, waveguide modes are supported within the cavity, negating the requirement of a photonic surface to enhance transmission. Instead it is shown that diffraction occurring at the annulus entrance couples incident radiation to Fabry Perot like waveguide modes within the slit, which are quantised by the geometry of the structure, providing enhanced transmission at multiple values of frequency. Further, the angular distribution of the transmitted signal is investigated, and shown to be remarkably confined at some values of frequency whilst exhibiting dual lobe characteristics at others. The finite element method modelling software allows the quantised waveguide modes within the slit to be examined at peak transmission wavelengths, providing a valuable insight into the characteristics of this efficient transmitting structure, which acts as a dipole antenna at certain frequencies.

Finally, *Chapter 9* contains a summary of the work presented in this thesis, possible ideas for future work, and a list of publications arising from the studies presented here.

Chapter 2
Surface plasmon polaritons.

2.1 Introduction

Surface plasmon polaritons (SPP's) have been extensively studied over the past century, and are accepted as being longitudinal oscillations of surface charge density, which propagate along the interface between a metal and dielectric without radiative loss. The SPP may be coupled to by incident radiation, whereupon the resulting surface wave takes on both transverse and longitudinal characteristics, and is transverse magnetic (TM) or *p*-polarised in nature, since on a planar interface it may only be excited by *p*-polarised incident radiation. This is because there needs to be a component of the incident electric vector normal to the interface to generate the necessary surface polarisation charge. *p*-polarised radiation is defined by having its electric vector in the plane of incidence, whereas transverse electric (TE) or *s*-polarised radiation will not result in the excitation of the SPP at a planar interface, since for this polarisation the electric vector is normal to the plane of incidence. As we will learn in the following sections, the dispersion of the SPP closely follows the light line, before curving away to an asymptotic limit as the surface plasma frequency is approached. In the region of momentum space where the dispersion is close to the light line, the mode is more 'grazing photon like'. In the region that the dispersion curves away from the light line, the mode is more plasmon like. In the microwave regime, this asymptotic limit is never reached, since microwave frequencies are several orders of magnitude less than the surface plasma frequency. Thus the surface mode is always close to the light line, unless perturbed heavily by a band gap in the modes dispersion.

In this chapter, some of the physics and properties of SPP's propagating on planar and corrugated surfaces are described. The dispersion relation for the propagation of the SPP on a planar metal-dielectric interface is derived and the spatial extent of the electric fields associated with the mode is also explored. A historical overview of the understanding of the Wood (radiative SPP) and Rayleigh anomalies (pseudo-critical edge), which were first observed around the turn of the 20^{th} century is presented.

Coupling incident radiation to the SPP is also discussed with emphasis on grating coupling. The phenomenon of SPP mediated polarisation conversion is explored, and the creation of grating induced gaps in the SPP dispersion curve is explained.

Although there exists an extensive amount of literature regarding SPP studies at optical frequencies, at microwave frequencies the SPP is often referred to as a surface wave or surface current. This is understandable since, as shown in section 2.4, the propagation length of the SPP on a planar interface at microwave frequencies is much longer than at optical frequencies, and the fields associated with the SPP may decay hundreds of wavelengths into the dielectric media whilst being nearly totally excluded from the metal. It is an underlying aim throughout this background chapter however, to show that although characteristics of the mode may differ between the two frequency regimes, surface currents may be thought of as SPP's at microwave frequencies.

2.2 Historical Overview

The electromagnetic surface waves discussed throughout this thesis have attracted much scientific interest over the past one hundred years. Wood studied the spectra of ruled metallic gratings illuminated with an incandescent lamp in 1902, and observed anomalies manifested as a series of light and dark bands in the *p*-polarised reflectivity spectra. At the time, the theory of diffraction gratings was unable to explain these observed anomalies, and it was not until Lord Rayleigh published his Dynamical Theory of Gratings in 1907 that these observed bright bands were (in-part) explained. He showed that these were pseudo-critical edges, caused by a diffracted order becoming evanescent and its energy being redistributed among the other propagating orders. His theory also suggested that the dark band anomalies only appear when the incident electric field is polarised perpendicular to the grating grooves, predicting no anomalies for the orthogonal polarisation. Further experiments over the next few decades [*Wood* (1912) and (1935), *Ingersoll* (1920) and *Strong* (1935)] verified these initial results, however Strong demonstrated that the angular position of the reflection minima was dependent upon the metal of which the grating was made, and not solely due to the gratings geometry as was the case for the pseudo-critical edge. It was not until *Fano* (1941) published a seminal paper on the subject that the nature of the dark and light bands was fully explained.

Consider the (in-plane) grating equation verified by Fraunhofer in 1821:

$$\lambda_g (\sin \vartheta_N - \sin \theta) = N\lambda_0 \qquad \textit{Equation 2.2.1}$$

where θ and ϑ_N are the angles of incidence and diffraction of the *N*th order respectively, and λ_g is the grating period. The grating equation (*Equation 2.2.1*) illustrates that the component of the momentum of the incident radiation parallel to the average plane of the grating surface will be changed by integer multiples of $2\pi/\lambda_g$, and a series of diffracted orders will result. Fano proposed that when this component is greater than the momentum of the incident beam ($\sin \vartheta_N > 1$), it becomes evanescent and will be diffracted into a pair of surface waves travelling along the grating surface and exponentially damped in the direction perpendicular to it. These waves are not able to

leave the interface since both the dielectric and the metal repeatedly reflect them, and no part of their energy is dispersed outside the surface region.

As discussed previously, the polarisation charge associated with the surface waves can only be excited at the interface if there is a component of the incident wave polarised with its electric vector perpendicular to the surface. In addition, the electrons will oscillate resonantly only if the tangential momentum of the oscillations approaches a permissible value determined by the real part of the permittivity of the metal (ε_r). It is the negative sign of ε_r that inverts the direction of the normal component of the electric field at the interface and allows the possibility of coupling incident radiation to the charge density oscillation induced on the metallic surface.

Due to further understanding of metals, and the development of the plasma concept for describing free electrons, *Ferrell* (1958) was able to confirm that a beam of electrons incident upon a metal film would emit radiation at the plasma frequency. *Steinmann* (1960) observed this to be the case, whilst *Ritchie* and *Eldridge* (1961) showed that the emitted radiation had characteristic energies of $h\omega_p / 2\pi$ and $h\omega_p / 2\pi\sqrt{2}$, where ω_p is the plasma frequency and $\omega_p / \sqrt{2}$ is the surface plasma frequency for air. This work lead to the superficial waves described by *Fano* becoming known as SPP's.

It was *Fano* (1941) who realised that the superficial waves he proposed that propagate along the boundary between a dielectric and a metal were simply a special case of the surface waves first suggested by *Zenneck* (1909) and *Sommerfeld* (1909). Since these waves propagate along the metal boundary with a momentum greater than that of the incident radiation in the dielectric (air) medium, it is impossible for them to radiate or for radiation to couple to them directly on a planar interface. However *Teng* and *Stern* (1967) used an optical grating that could impart some additional momentum to the SPP, so that it could couple to a radiating electromagnetic field. Their experiment consisted of bombarding the grating with a high-energy electron beam and observing peaks in the out-coupled *p*-polarised radiation. To verify that the SPP was the cause of these peaks, electromagnetic radiation incident at the emission angle and of the same frequency as the peaks should be absorbed as it excites the surface plasmon polariton. This was the case, and as the angle of incidence with respect to the grating normal was varied, minima appeared at the same position as the peaks in the electron-beam experiment.

Using the angular positions of these peaks, the authors were able to determine the wavevector parallel to the surface of the grating of the SPP and hence the dispersion curve could be mapped out. This confirmed the excitation of SPP's unequivocally and presaged their direct optical coupling with the use of a grating, confirming Wood's observations.

Fano's theory was further verified experimentally by *Ritchie et al.* (1968), and *Beaglehole* (1969). They each provided one of the first comprehensive experimental studies of optically excited SPP's on metal gratings. Ritchie *et al.* were able to experimentally derive the dispersion curve of the excited SPP by plotting the positions of the peaks in the p-polarised spectra from their grating. Meanwhile Beaglehole was able to illustrate that coupling to the mode is possible for both *p* and *s*-polarised light if the grating grooves are twisted with respect to the plane of incidence, and provided that there is a component of the electric field along the direction of surface plasmon polariton propagation.

2.3 The surface plasmon polariton dispersion relation

Let us first consider the planar interface between two semi-infinite isotropic media that are characterised by frequency dependent and complex dielectric constants $\varepsilon = \varepsilon_r + \varepsilon_i$, where the subscripts r and i refer to the real and imaginary parts of the dielectric constant respectively. From Maxwell's equations, it can be shown that the normal component of the electric displacement **D** must be continuous across the interface. Further, the relation that links the electric displacement to the electric field **E** states

$$\mathbf{D} = \varepsilon_r \varepsilon_0 \mathbf{E} \qquad \textit{Equation 2.3.1}$$

where ε_r is the relative dielectric constant of the medium in question and ε_0 is the permittivity of free space. It is clear, that if the upper medium is a dielectric with positive ε_r and the lower medium is a metal possessing a negative ε_r, then the normal component of **E** will change direction as the interface is traversed. It is this discontinuity in the normal **E** field that is responsible for setting up the sheet of polarisation charge trapped at the interface. It is clear at this point that if the metal is replaced by a perfectly conducting medium, then the fields are totally excluded from that medium and the surface polarisation charge is not formed, hence the SPP is not supported. Metals at microwave frequencies are indeed approximated to near perfectly conducting, however this is of course an ideal. It will be shown in the next section that the skin depth of metals at microwave frequencies is on the order of a micron, and hence field penetration within the metal is more than adequate to generate the necessary polarisation charge. If the fields then pertain to time-dependent electromagnetic waves, the dispersion relation of the resultant surface charge oscillation may be derived. The following treatment is adapted from *Raether* (1988).

Figure 2.3.1 shows a *p*-polarised electromagnetic wave incident at the interface between two semi-infinite, non-magnetic media, the upper medium being a dielectric with dielectric constant ε_1 and the lower a metal with a dielectric constant ε_2. The waves propagate in the *xy*-plane.

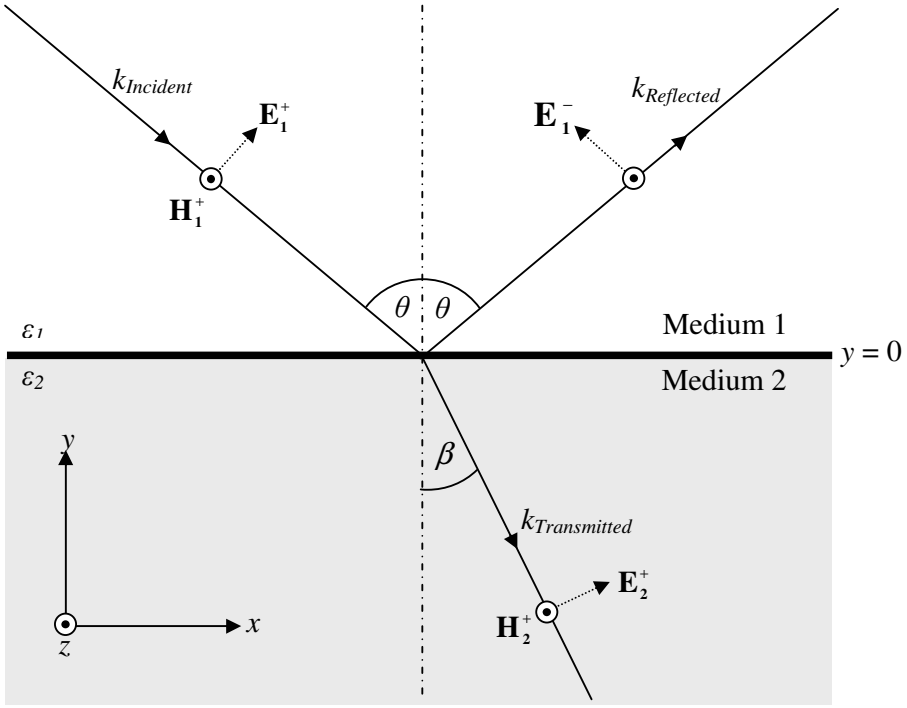

Figure 2.3.1 The incident, transmitted and reflected fields associated with a *p*-polarised electromagnetic wave incident upon a planar interface between a metal and a dielectric. The *z*-axis is out of the page.

For *p*-polarised light, propagating with wave-vector $\mathbf{k} = (k_x, k_y, 0)$ the electric and magnetic fields may be written as:

$$\mathbf{E} = [E_x, E_y, 0]\exp(i(k_x x + k_y y - \omega t)) \qquad \textit{Equation 2.3.2}$$

$$\mathbf{H} = [0, 0, H_z]\exp(i(k_x x + k_y y - \omega t)) \qquad \textit{Equation 2.3.3}$$

By applying Maxwell's equation in the absence of free charge:

$$\nabla \times \mathbf{H} = \varepsilon \frac{\partial \mathbf{E}}{\partial t} \qquad \textit{Equation 2.3.4}$$

we obtain

$$H_z = \frac{\varepsilon \omega E_x}{k_y} = -\frac{\varepsilon \omega E_y}{k_x} \qquad \textit{Equation 2.3.5}$$

and by combining *Equations 2.3.2* and *2.3.3* with *Equation 2.3.5* we obtain the following expressions for the incident, reflected and transmitted fields:

$$\mathbf{E}_1^+ = E_{x1}^+\left[1,-\frac{k_x}{k_{y1}},0\right]\exp\left(i\left(k_x x + k_{y1} y - \omega t\right)\right)$$

$$\mathbf{E}_1^- = E_{x1}^-\left[1,+\frac{k_x}{k_{y1}},0\right]\exp\left(i\left(k_x x - k_{y1} y - \omega t\right)\right)$$

$$\mathbf{E}_2^+ = E_{x2}^+\left[1,-\frac{k_x}{k_{y2}},0\right]\exp\left(i\left(k_x x + k_{y2} y - \omega t\right)\right)$$

$$\mathbf{H}_1^+ = E_{x1}^+\left[0,0,+\frac{\omega\varepsilon_1}{k_{y1}}\right]\exp\left(i\left(k_x x + k_{y1} y - \omega t\right)\right)$$

$$\mathbf{H}_1^- = E_{x1}^-\left[0,0,-\frac{\omega\varepsilon_1}{k_{y1}}\right]\exp\left(i\left(k_x x - k_{y1} y - \omega t\right)\right)$$

$$\mathbf{H}_2^+ = E_{x2}^+\left[0,0,+\frac{\omega\varepsilon_2}{k_{y2}}\right]\exp\left(i\left(k_x x + k_{y2} y - \omega t\right)\right)$$

As the SPP is non-radiative, either the incident or reflected field may be set to zero (arbitrarily the incident field is set to zero). Further, the boundary condition at a metal-dielectric interface is such that the tangential components (x and z) of the electric and magnetic fields must be continuous across it. Hence,

$$E_{x1} = E_{x2} \qquad \textit{Equation 2.3.6}$$

and

$$H_{z1} = H_{z2} \qquad \textit{Equation 2.3.7}$$

Therefore,

$$H_z = -E_{x1}^- \frac{\varepsilon_1 \omega}{k_{y1}} = E_{x2}^+ \frac{\varepsilon_2 \omega}{k_{y2}} \qquad \textit{Equation 2.3.8}$$

By combining *Equations 2.3.6* and *2.3.8* we can then obtain:

$$\frac{\varepsilon_1}{k_{y1}} = -\frac{\varepsilon_2}{k_{y2}} \qquad \textit{Equation 2.3.9}$$

Equations 2.3.6 and *2.3.7* also imply $k_{x1} = k_{x2} = k_x$, which is a statement of the conservation of momentum parallel to the interface. This is to be expected since the interface is translationally invariant. The *y*-component of the wavevector of the reflected and transmitted fields in terms of the total wavevector and the in-plane wavevector of the fields may also be obtained:

$$k_{yj} = \left(\varepsilon_j k_0^2 - k_x^2\right)^{1/2} \qquad \textit{Equation 2.3.10}$$

where the *j* subscript corresponds to the medium in which the field is propagating. By substituting *Equation 2.3.10* into *Equation 2.3.9* the SPP dispersion relation is obtained:

$$k_x = k_0\left(\frac{\varepsilon_1\varepsilon_2}{\varepsilon_1 + \varepsilon_2}\right)^{1/2} = k_{SPP}\,. \qquad \textit{Equation 2.3.11}$$

The above equation for the SPP dispersion relation is mathematically correct for any frequency regime, since the epsilons are complex. However it is common at optical frequencies to use *Equation 2.3.11* and approximate by using the real part of the dielectric constants only. However, as we will discover in the following section, at microwave frequencies the imaginary component of the dielectric constant of the metal is positive, and several orders of magnitude larger than the real component. As such, we will use the complete derivation of the dispersion relation, substituting ε_2 with its complex form $\varepsilon_2 = \varepsilon_{2r} + \varepsilon_{2i}$, to obtain an exact expression for the SPP dispersion that readily imparts information regarding the proximity of the SPP to the light line.

Substituting ε_2 and k_x with their complex form into *Equation 2.3.11* and rearranging we obtain:

$$\frac{k_{xr}^2 - k_{xi}^2 + 2ik_{xr}k_{xi}}{k_0^2} = \frac{\varepsilon_1(\varepsilon_{2r} + i\varepsilon_{2i})}{\varepsilon_1 + \varepsilon_{2r} + i\varepsilon_{2i}} \qquad \textit{Equation 2.3.14}$$

Multiplying by the complex conjugate of the denominator allows the second term of *Equation 2.3.14* to be separated into its real and imaginary components:

$$\frac{k_{xr}^2 - k_{xi}^2 + 2ik_{xr}k_{xi}}{k_0^2} = \frac{\varepsilon_1\varepsilon_{2r}(\varepsilon_1 + \varepsilon_{2r}) + \varepsilon_1\varepsilon_{2i}^2}{(\varepsilon_1 + \varepsilon_{2r})^2 + \varepsilon_{2i}^2} + i\frac{\varepsilon_1^2\varepsilon_{2i}}{(\varepsilon_1 + \varepsilon_{2r})^2 + \varepsilon_{2i}^2} \qquad \textit{Equation 2.3.15}$$

therefore

$$\frac{k_{xr}^2 - k_{xi}^2}{k_o^2} = \frac{\varepsilon_1\varepsilon_{2r}(\varepsilon_1 + \varepsilon_{2r}) + \varepsilon_1\varepsilon_{2i}^2}{(\varepsilon_1 + \varepsilon_{2r})^2 + \varepsilon_{2i}^2} \qquad \textit{Equation 2.3.16}$$

and

$$\frac{2k_{xr}k_{xi}}{k_0^2} = \frac{\varepsilon_1^2\varepsilon_{2i}}{(\varepsilon_1 + \varepsilon_{2r})^2 + \varepsilon_{2i}^2} \qquad \textit{Equation 2.3.17}$$

These two equations can be solved simultaneously giving two quadratics in $\frac{k_{xr}^2}{k_0^2}$ and $\frac{k_{xi}^2}{k_0^2}$ respectively:

$$\frac{k_{xr}^4}{k_o^4} - \frac{k_{xr}^2}{k_0^2}\left(\frac{\varepsilon_1\varepsilon_{2r}(\varepsilon_1 + \varepsilon_{2r}) + \varepsilon_1\varepsilon_{2i}^2}{(\varepsilon_1 + \varepsilon_{2r})^2 + \varepsilon_{2i}^2}\right) - \frac{\varepsilon_1^2\varepsilon_{2i}}{(\varepsilon_1 + \varepsilon_{2r})^2 + \varepsilon_{2i}^2} = 0 \qquad \textit{Equation 2.3.18}$$

$$-\frac{k_{xi}^4}{k_o^4} - \frac{k_{xi}^2}{k_0^2}\left(\frac{\varepsilon_1\varepsilon_{2r}(\varepsilon_1 + \varepsilon_{2r}) + \varepsilon_1\varepsilon_{2i}^2}{(\varepsilon_1 + \varepsilon_{2r})^2 + \varepsilon_{2i}^2}\right) + \frac{\varepsilon_1^2\varepsilon_{2i}}{(\varepsilon_1 + \varepsilon_{2r})^2 + \varepsilon_{2i}^2} = 0 \qquad \textit{Equation 2.3.19}$$

Solving equations *2.3.18, 2.3.19*, and simplifying yields:

$$\frac{k_{xr}}{k_0} = \sqrt{\frac{\varepsilon_1\left(\varepsilon_e^2 + \sqrt{\varepsilon_e^4 + \varepsilon_1^2\varepsilon_{2i}^2}\right)}{2\left(\left(\varepsilon_1 + \varepsilon_{2r}\right)^2 + \varepsilon_{2i}^2\right)}} \qquad \textit{Equation 2.3.20}$$

$$\frac{k_{xi}}{k_0} = \sqrt{\frac{\varepsilon_1\left(\sqrt{\varepsilon_e^4 + \varepsilon_1^2\varepsilon_{2i}^2} - \varepsilon_e^2\right)}{2\left(\left(\varepsilon_1 + \varepsilon_{2r}\right)^2 + \varepsilon_{2i}^2\right)}} \qquad \textit{Equation 2.3.21}$$

where $\varepsilon_e^2 = \varepsilon_{2r}^2 + \varepsilon_{2i}^2 + \varepsilon_1\varepsilon_{2r}$. Hence the real part of k_x (*Equation 2.3.20*) provides us with an exact expression for the real wave-vector of the non-radiative SPP at any frequency, with the SPP position relative to the light-line being given by $1 - \frac{k_{xr}}{k_0}$. *Equation 2.3.21* yields the imaginary part of k_x and describes non-radiative damping of the mode.

2.4. Spatial extent of the Surface-plasmon Fields

The introduction of an imaginary component to the SPP wavevector, k_{xi}, leads to an exponential decay of the mode as it propagates along the interface of the metal and the dielectric. From *Equation 2.3.2* the fields associated with the SPP will fall off as $\exp(k_{xi}x)$ and so the intensity falls off as $\exp(2k_{xi}\ x)$. The propagation length L_x is defined as the distance over which the intensity falls off by $1/e$ of its initial value. Thus:

$$L_x = \frac{1}{2k_{xi}} = \frac{1}{2k_0}\sqrt{\frac{2\left(\left(\varepsilon_1 + \varepsilon_{2r}\right)^2 + \varepsilon_{2i}^2\right)}{\varepsilon_1\left(\sqrt{\varepsilon_e^4 + \varepsilon_1^2\varepsilon_{2i}^2} - \varepsilon_e^2\right)}} \qquad \textit{Equation 2.4.1}$$

Before a numerical value of a typical propagation length of the SPP on a metal-dielectric interface at microwave frequencies may be obtained, the dielectric function of the material constituting the interface must be ascertained. For most loss-free dielectrics, including air, the dispersion of the dielectric constant is negligible due to the lack of electronic resonances. Hence for an air-metal interface, ε_1 may be considered as frequency independent. However, since the dielectric function of a metal describes the response of conduction electrons to an applied EM field, ε_2 is found to vary markedly with frequency. *Figures 2.4.1* (a) and (b) show the real and imaginary dielectric

constant respectively as a function of wavelength for aluminium, using a Drude free-electron model of the form:

$$\varepsilon_r = 1 - \frac{\omega_p^2 \tau^2}{(1+\omega^2\tau^2)} \qquad \textit{Equation 2.4.2}$$

$$\varepsilon_i = \frac{\omega_p^2 \tau}{\omega(1+\omega^2\tau^2)} \qquad \textit{Equation 2.4.3}$$

Here, τ is the mean collision time, and is equivalent to the time constant for the decay of a current with no driving field. ω_p is the plasma frequency, and in the free particle context,

$$\omega_p = \sqrt{\frac{Ne^2}{\varepsilon_0 m}} \qquad \textit{Equation 2.4.4}$$

where N, e^2 and m are the electron density, the square of the electron charge, and electron mass respectively. To generate the plots, $\omega_p = 1.93\times10^{16}\ s^{-1}$, and $\tau = 5.07\times10^{-15}$ s are used, which are empirically derived by fitting to the reflectance data of the material [*Bohrem* and *Huffman*, *Absorption and Scattering of Light by Small Particles*, Wiley, N.Y. (1983)] on the appropriate side of the inter-band transition that occurs in the near infrared, the effects of which have been omitted for clarity.

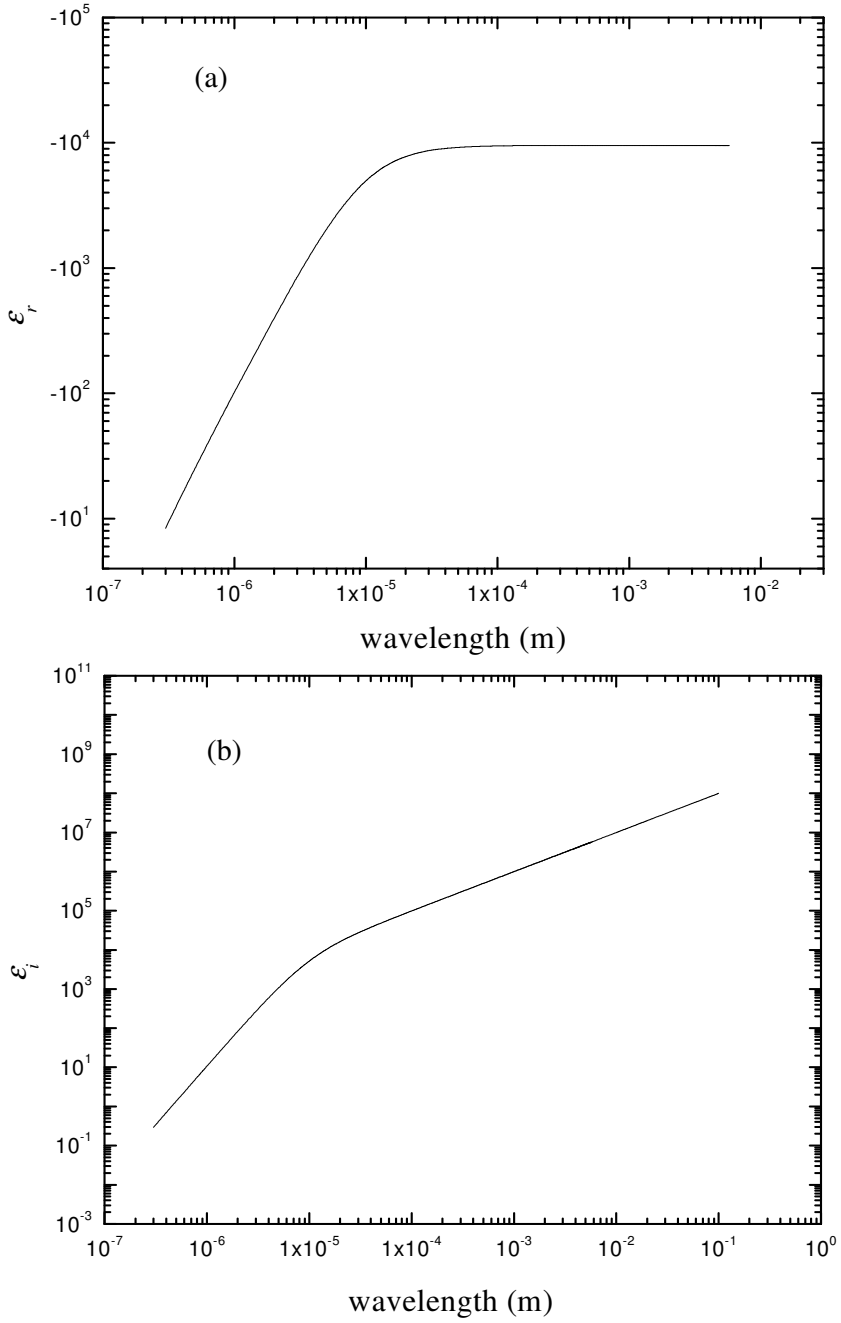

Figure 2.4.1 (a) ε_r as a function of wavelength derived using a Drude free-electron model with $\omega_p = 1.93\times10^{16}\ s^{-1}$, and $\tau = 5.07\times10^{-15}\ s$. (b) ε_i as a function of wavelength using the above parameters.

It is thus possible, using *Equation 2.4.1* and values obtained for the dielectric constant of aluminium derived from the Drude model, to obtain the SPP propagation length at a planar air–aluminium interface for a range of wavelengths, as shown by *Figure 2.4.2*

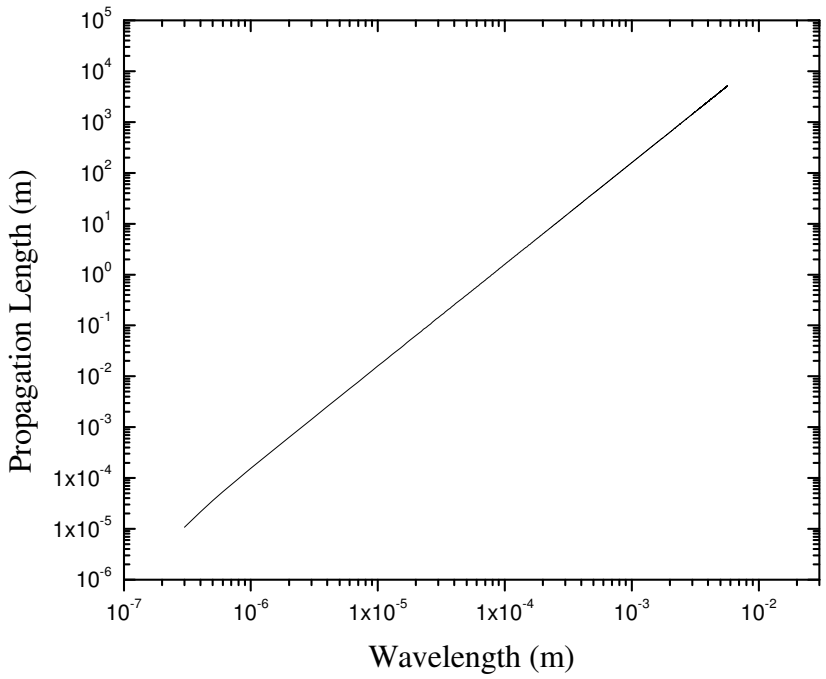

Figure 2.4.2 Propagation length as a function of wavelength for a planar air-aluminium interface.

It is clear that at microwave frequencies, the propagation length of the SPP supported by such an interface is in excess of 1km, and although it is important to recall that this analysis only considers the effect of non-radiative damping, it is easy to see why the SPP is often considered a surface current rather than a surface wave in this regime.

The amplitudes of the fields associated with the SPP decrease exponentially into the surrounding media due to the imaginary nature of the normal wavevector k_y. A useful measure of this characteristic decay is the penetration length, or skin depth L_y, which is defined as the distance normal to the interface over which the field strength falls to 1/e of its value at the interface. In order to obtain an expression for L_y, it is necessary to obtain an expression for the imaginary part of k_y. Using $k_y^2 = k_0^2 \varepsilon_j - k_x^2$,

$$\frac{k_{jy}}{k_0} = \sqrt{\left(\varepsilon_{jr} + \varepsilon_{ji}\right) - \left(\frac{k_x^2}{k_0^2}\right)} \qquad \textit{Equation 2.4.5}$$

where the subscript j denotes the medium in which k_y is being determined ($j = 1(air), 2(metal)$). This expression can then be split into real and imaginary parts which give;

$$\frac{k_{jy}}{k_0} = \sqrt{\left(\varepsilon_{jr} - \frac{\varepsilon_1 \varepsilon_e^2}{(\varepsilon_1 + \varepsilon_{2r})^2 + \varepsilon_{2i}^2}\right) + i\left(\varepsilon_{ji} - \frac{\varepsilon_1^2 \varepsilon_{2i}}{(\varepsilon_1 + \varepsilon_{2r})^2 + \varepsilon_{2i}^2}\right)} \qquad \textit{Equation 2.4.6}$$

and therefore:

$$\frac{k_{jyr}^2 - k_{jyi}^2 + 2ik_{jyr}k_{jyi}}{k_0^2} = \left(\varepsilon_{jr} - \frac{\varepsilon_1 \varepsilon_e^2}{(\varepsilon_1 + \varepsilon_{2r})^2 + \varepsilon_{2i}^2}\right) + i\left(\varepsilon_{ji} - \frac{\varepsilon_1^2 \varepsilon_{2i}}{(\varepsilon_1 + \varepsilon_{2r})^2 + \varepsilon_{2i}^2}\right) \qquad \textit{Equation 2.4.7}$$

This gives two equations, one for the real part, and one for the imaginary part, which may be solved simultaneously as in the case for k_{xi}, yielding:

$$\frac{k_{jyi}}{k_0} = \sqrt{\frac{\varepsilon_{jr} - \frac{\varepsilon_1 \varepsilon_e^2}{(\varepsilon_1 + \varepsilon_{2r})^2 + \varepsilon_{2i}^2} - \sqrt{\left(\varepsilon_{jr} - \frac{\varepsilon_1 \varepsilon_e^2}{(\varepsilon_1 + \varepsilon_{2r})^2 + \varepsilon_{2i}^2}\right)^2 + \left(\varepsilon_{ji} - \frac{\varepsilon_1^2 \varepsilon_{2i}}{(\varepsilon_1 + \varepsilon_{2r})^2 + \varepsilon_{2i}^2}\right)^2}}{-2}}$$

Since $L_{yj} = 1/k_{yj}$, the final expression for penetration depth is obtained:

$$L_{yj} = \frac{1}{k_{jyi}} = \frac{\lambda_0}{2\pi} \sqrt{\frac{-2}{\varepsilon_{jr} - \frac{\varepsilon_1 \varepsilon_e^2}{(\varepsilon_1 + \varepsilon_{2r})^2 + \varepsilon_{2i}^2} - \sqrt{\left(\varepsilon_{jr} - \frac{\varepsilon_1 \varepsilon_e^2}{(\varepsilon_1 + \varepsilon_{2r})^2 + \varepsilon_{2i}^2}\right)^2 + \left(\varepsilon_{ji} - \frac{\varepsilon_1^2 \varepsilon_{2i}}{(\varepsilon_1 + \varepsilon_{2r})^2 + \varepsilon_{2i}^2}\right)^2}}}$$

Figures 2.4.3 (a) and (b) show penetration depth as a function of wavelength for (a) aluminium and (b) air. From this analysis, it is clear that at a planar aluminium-air interface, and a frequency of 30 GHz, aluminium has a penetration depth of 0.7 microns whereas air yields L_y = 18.5 m. However, even though field penetration into the incident dielectric medium is so large at microwave frequencies, the resulting surface wave may

still be considered a SPP, since it remains a bound surface state (although rather loosely bound compared to optical frequencies), with fields decaying exponentially into both media. The localised nature of the SPP field is shown schematically in *Figure 2.4.4.*

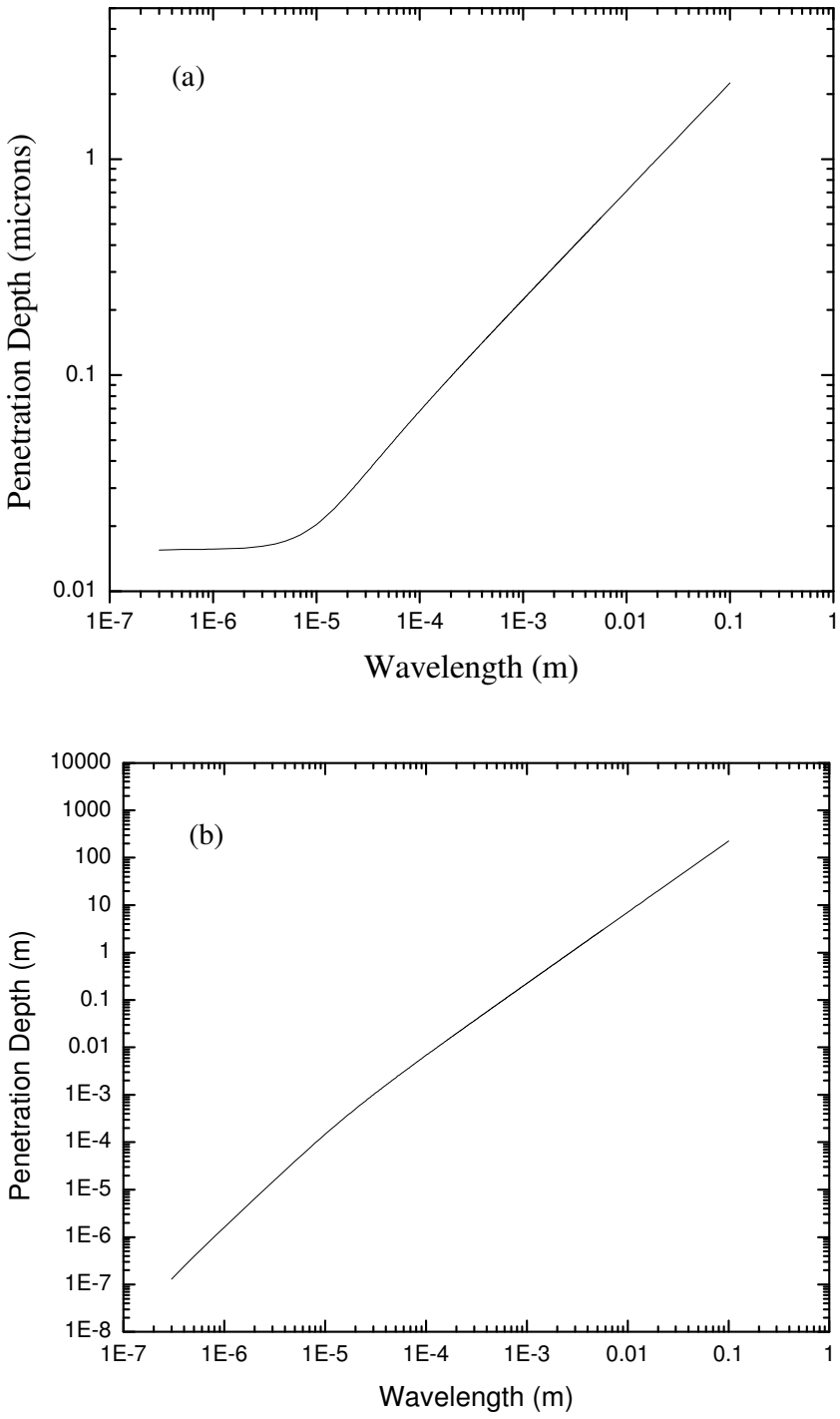

Figure 2.4.3 Penetration depth as a function of wavelength for (a) aluminium and (b) air.

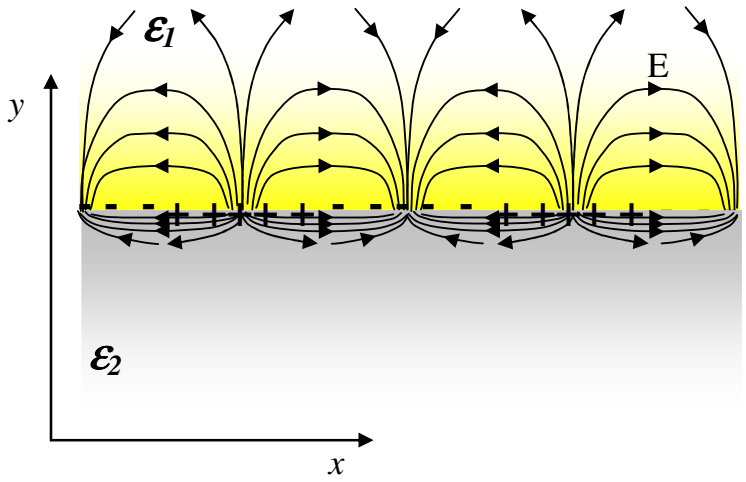

Figure 2.4.4 Schematic representation of the polarisation surface charge density and associated electric field for the SPP mode. The field decays exponentially into each media, penetrating the metal (ε_2) to a lesser extent than the dielectric.

2.5. The SPP dispersion curve

In this section the effect of describing the metal with a frequency dependent dielectric constant is discussed, and the dispersion curve of the SPP explored, describing its asymptotic limits. Initially however, Brewster and Fano modes are discussed, and the SPP is shown to represent a Brewster mode on a metal-dielectric interface.

By combining equations *2.3.10*, and *2.3.11*, the following expressions for k_{yj}^2 may be obtained:

$$k_{y1}^2 = k_x^2 \frac{\varepsilon_1}{\varepsilon_2} \qquad \textit{Equation 2.5.1}$$

$$k_{y2}^2 = k_x^2 \frac{\varepsilon_2}{\varepsilon_1} \qquad \textit{Equation 2.5.2}$$

These equations illustrate that in the frequency regions where ε_1 and ε_2 are both purely real and positive, k_{y1} and k_{y2} are also real. Conversely, when ε_1 and ε_2 have opposite signs, k_{y1} and k_{y2} are imaginary. It is therefore not surprising that different wavevector regions, or frequency regions support different types of interface modes.

The interface modes that occur when ε_1 and ε_2 are purely real and have opposite signs correspond to surface electromagnetic modes that propagate without radiation loss along the interface and whose fields decay exponentially to zero in the *y*-direction. These modes are known as *Fano modes* (section 2.2) and are equivalent to the propagation of the SPP along a planar, non-lossy metal-dielectric interface.

The interface modes that occur when ε_1 and ε_2 are both positive correspond to *Brewster modes*, and since k_{y1} and k_{y2} are both real and have the same signs, the surface mode generated is in fact not bound to the interface. By inspection of *Equation 2.5.1* and *Equation 2.5.2*, and *Figure 2.3.1* we can appreciate that this mode is generated when

$$\tan\theta = \frac{n_2(\omega)}{n_1(\omega)} = \sqrt{\frac{\varepsilon_2(\omega)}{\varepsilon_1(\omega)}} = \frac{1}{\tan\beta} = \tan\theta_B \qquad \textit{Equation 2.5.3}$$

which occurs when

$$\theta + \beta = 90° \qquad \textit{Equation 2.5.4.}$$

Note that, although Brewster modes are not bound to the surface (*i.e.* they do not attenuate with distance from the interface like Fano modes), they do satisfy the criterion for interface modes that there is only one electromagnetic wave in each medium (*i.e.* they involve an incident wave but no reflected wave in one medium, and a refracted wave in the other).

To demonstrate that the expression derived in *Equation 2.3.11* and the Brewster mode dispersion relation are equivalent, the dispersion relation for the Brewster mode is derived separately below.

$$\sin\theta_B = \frac{n_2}{[n_1^2 + n_2^2]^{\frac{1}{2}}} = \left[\frac{\varepsilon_2}{\varepsilon_1 + \varepsilon_2}\right]^{\frac{1}{2}} \qquad \textit{Equation 2.5.5}$$

$$\therefore k_x = n_1 k_0 \sin\theta_B = k_0 \frac{n_1 n_2}{\left(n_1^2 + n_2^2\right)^{\frac{1}{2}}} = \left(\frac{\omega}{c}\right)\left(\frac{\varepsilon_1\varepsilon_2}{\varepsilon_1 + \varepsilon_2}\right)^{\frac{1}{2}} \qquad \textit{Equation 2.5.6}$$

where $k_0 = \omega/c$ is the wavevector of the incident radiation in free space and $n_j = \varepsilon_j^{1/2}$ is the refractive index of the j^{th} medium.

The equivalence of *Equation 2.3.11* and *Equation 2.5.6* demonstrates that the SPP is a manifestation of the Brewster mode for which the media have purely real permittivities of opposite signs (*e.g.* a non-lossy metal-dielectric system). It is clear that Brewster modes have values of k_x that are smaller than the wavevector of the bulk polaritons in either medium. However, the opposite is true for Fano modes, which therefore cannot directly couple to bulk polaritons in the dielectric, *i.e.* the SPP is described as *non-radiative*.

To obtain the frequency dependent SPP dispersion curve for a planar aluminium-air interface, the dielectric constants given in section 2.4 are substituted into the dispersion relation derived in section 2.3. A schematic representation of the resulting dispersion curve is shown in *Figure 2.5.1.*

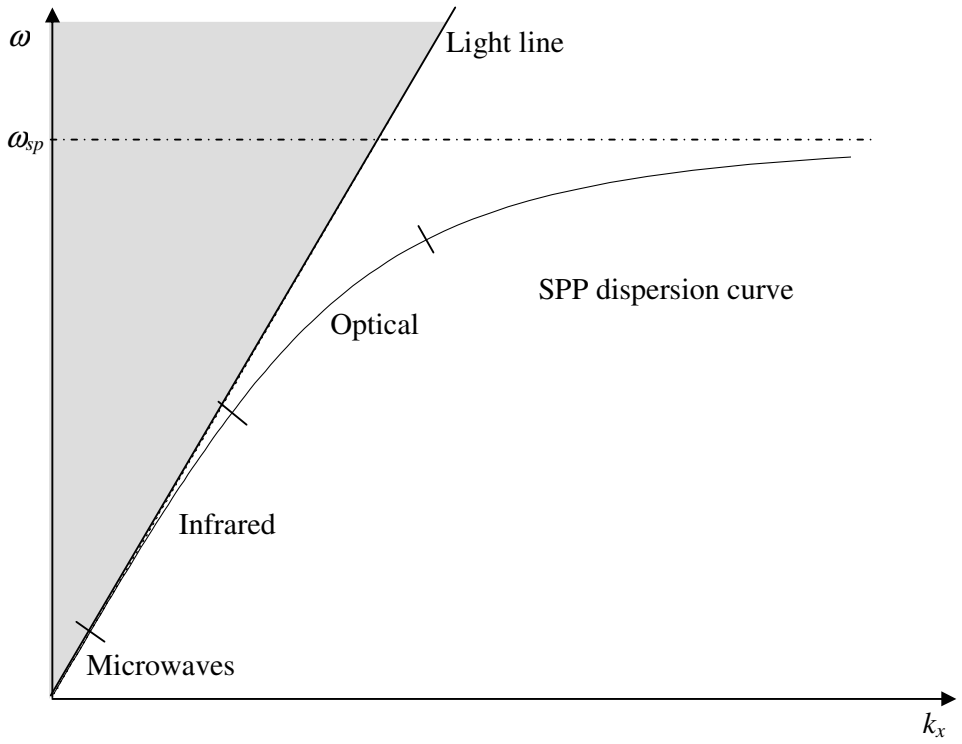

Figure 2.5.1. A schematic representation of the SPP dispersion curve

The SPP dispersion curve is shown, along with the light-line, which corresponds to the maximum in-plane wavevector an incident photon may have for a particular frequency, *i.e.* the wavevector of a grazing photon as a function of ω. The SPP dispersion curve has two asymptotic limits. For high frequencies the SPP dispersion curve becomes asymptotic to the surface plasmon frequency at $\omega_{sp} = \omega_p / (1+\varepsilon_1)^{1/2}$ which is the frequency at which the real part of the dielectric function of the metal is equal, but opposite in sign, to the real part of the dielectric function of the dielectric. This limit arises since at frequencies above ω_{sp} and below ω_p, k_x is purely imaginary, and above ω_p, k_y (given by $k_y^2 = \varepsilon_1 k_0^2 - k_x^2$) is real, indicating that it is no longer a trapped surface wave. In the region of the dispersion curve where it is close to ω_{SP} the SPP is 'plasmon like', both the phase velocity (ω / k) and the group velocity ($\partial\omega / \partial k$) of the mode tend to zero. The second asymptote is the low frequency limit where the SPP dispersion curve approaches the light line. In this regime, (which includes the microwave regime) the metal approximates to a perfect metal more closely. A perfect metal will respond instantaneously to an applied electric field to cancel it, and is also lossless, and is thus

characterised by a dielectric constant which is entirely imaginary and infinite in magnitude. At this limit the SPP dispersion equation reduces to the form $k_x = \sqrt{\varepsilon_1}(\omega/c)$, which is identical to the dispersion relation of a photon propagating parallel to the interface in the dielectric media. Hence the behaviour of the SPP mode in the low frequency limit is described as light like. It is clear from the dispersion curve, that the surface plasmon polariton and surface plasmon are just extremes of the same surface mode.

We have assumed here that the radiation is incident in the *xy*-plane. Since the surface is planar the dispersion curve obtained in section 2.3 is valid for radiation incident in any plane, since the polarisation of the incident radiation is defined relative to the plane of incidence. Therefore, the full dispersion curve, which takes into account the *z*-component of the wavevector of the incident radiation, has a horn shape, formed by rotating the dispersion curve shown in *Figure 2.5.1* around the *y*-axis.

The SPP dispersion curve is always at higher values of in-plane wavevector than that obtainable by incident photons (the grey shaded region of *Figure 2.5.1.* represents the range of frequencies and wavevectors accessible to a photon propagating in the dielectric medium). For this reason the SPP may not be excited on a planar dielectric / metal interface without some coupling mechanism to enable the incident photon to gain enough in-plane wavevector for the wavevector matching condition to be satisfied. At microwave frequencies, because of the close proximity to the light line, only a relatively small amount of 'extra' momentum is required, and may be provided using momentum matching techniques outlined in the following section.

2.6. Grating coupling

In sections 2.1 and 2.5 of this chapter, it was shown that the SPP mode at a planar metal-dielectric interface is non-radiative, that is to say the SPP dispersion curve exists within a region of momentum space beyond the light line, and is inaccessible to an incident photon, as the SPP possesses a tangential wavevector greater than that of a grazing photon of the same frequency propagating in the dielectric. In section 2.5, a schematic representation of the SPP dispersion was shown, and attention was drawn to the close proximity of the SPP mode to the light line at microwave frequencies. The distance between the light line and the SPP dispersion curve on an ω vs. k plot is also a measure of the extra momentum required to allow coupling of an incident photon to the SPP mode, therefore the momentum required to match an incident photon to the SPP mode is small compared to that required in the optical regime. Nevertheless, a means of enhancing the incident photon momentum is required, and this can be achieved through two main methods, both of which involve altering the surface environment. The first, commonly used at optical frequencies, is prism coupling, or attenuated total reflection (ATR) [*Kretchmann* and *Raether*, (1968), *Otto*, (1968)]. The second, which is used exclusively throughout this thesis, is grating coupling.

By introducing a surface roughness, or corrugation to the interface between two media, the translational symmetry of the surface is destroyed, and the tangential momentum of a photon incident upon the surface need no longer be conserved. Any periodicity associated with the surface profile allows light to be scattered by an integer number of grating vectors $\boldsymbol{k_g}$ ($k_g = 2\pi/\lambda_g$, where λ_g is the grating pitch) in the direction normal to that of the grating grooves. This is the origin of the diffracted orders produced by such a surface. When a diffracted order has a wavevector greater than that of the maximum momentum permissible for the incident radiation in medium 1 it will cease to propagate, becoming evanescent. It is the enhanced momentum of these evanescent fields which allows the incident radiation to couple to surface modes which exist beyond the light line leading to the condition for the grating vector lying in the plane of incidence

$$k_{SPP} = k_0 \sin\theta \pm Nk_g \qquad \textit{Equation 2.6.1}$$

where θ is the angle of incidence, $k_0 \sin\theta$ is the in-plane wavevector of the incident radiation, and N is an integer. The mechanism for grating coupling to the SPP is best described by considering the influence of the periodic corrugation on the SPP dispersion curve as illustrated schematically by *Figure 2.6.1.* For this situation, the grating wave vector is in the incident plane.

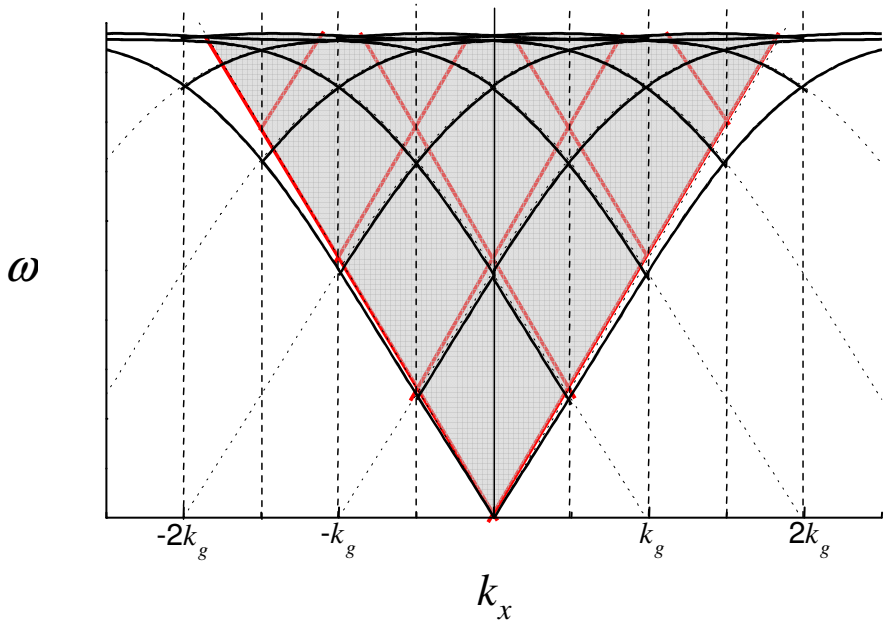

Figure 2.6.1. The dispersion curve for grating-coupled SPP's which has been reflected at the Brillouin zone boundaries. Parts of the scattered dispersion curves that fall between the light lines (shaded) can be radiatively coupled.

The periodicity of the surface corrugation may be represented as a line of points in reciprocal space separated by the grating vector k_g. The SPP dispersion curve as well as the incident radiation cone are both displaced by these points through the addition or subtraction of momentum by integer multiples of k_g. Radiative coupling of incident *p*-polarised radiation to the SPP may now be achieved since the dispersion curve of the diffracted SPP now exists between the light lines. Note here that by corrugating the surface, the dispersion relation for the planar interface may be distorted due to the introduction of effective surface impedance, but in the limit of a small amplitude corrugation, the planar dispersion relation is a good approximation.

The co-ordinate system used throughout this thesis to describe the orientation of the grating is shown in *Figure 2.6.2.* The polar angle θ is defined as the angle of incidence

as measured from normal to the average surface plane of the profile. The azimuth angle ϕ describes the rotation of the plane of incidence from the positive *x*-axis (parallel to the grating vector), and the polarisation of the incident radiation is defined with respect to the plane of incidence (recall that TM (*p*-polarised) radiation has its electric vector in the plane of incidence, TE (*s*-polarised) has its electric vector normal to the plane of incidence).

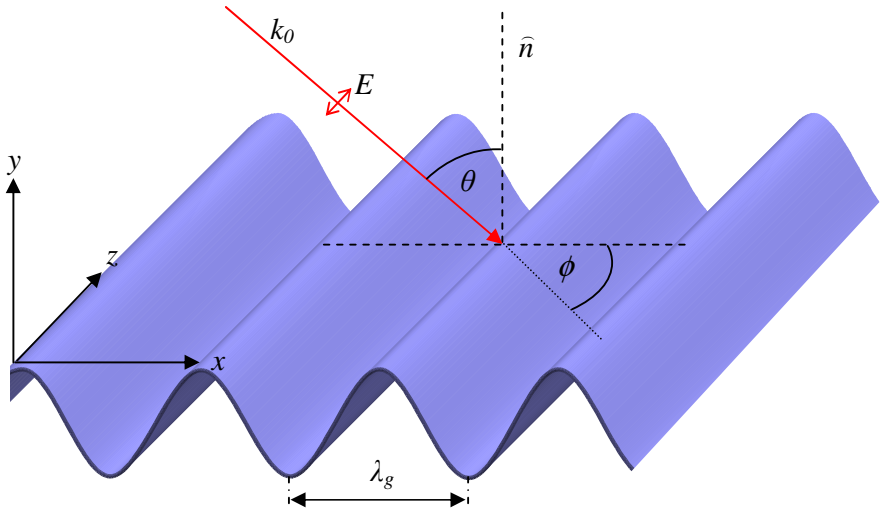

Figure 2.6.2. The coordinate system used throughout this thesis, illustrated using a sinusoidal grating. The direction of the electric field vector is shown for incident TM-radiation.

If the azimuthal angle ϕ is not equal to zero, then $\boldsymbol{k_{spp}}$, $\boldsymbol{k_0}$ and $\boldsymbol{k_g}$ are no longer collinear and the scalar equivalent of *Equation 2.6.1* becomes

$$k_{SPP}^2 = n_1^2 k_0^2 \sin^2\theta + N^2 k_g^2 \pm 2 n_1 N k_g k_0 \sin\theta\cos\phi \qquad \textit{Equation 2.6.2.}$$

Figure 2.6.3 shows a schematic 2-D reciprocal space diagram illustrating the possible solutions of *Equation 2.6.2.*

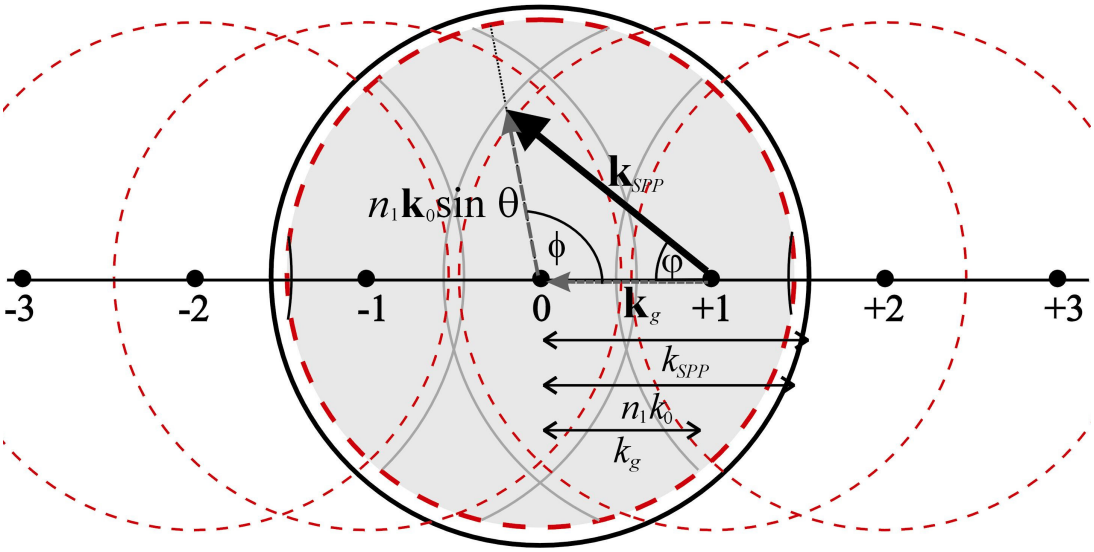

Figure 2.6.3. A 2-D reciprocal space representation of the SPP modes and light circles produced by a grating. The circle with a thick-dashed radius represents the maximum possible momentum in the plane available from a photon propagating above the grating. The circle with the thick solid radius represents the momentum of the zero-order SPP mode; the arcs of the diffracted SPP modes that fall within the shaded are also shown (grey solid arcs). Coupling incident radiation to the SPP is only possible in the shaded area. The arrows indicate the coupling between a photon at angle of incidence θ and azimuth angle ϕ, to a SPP via a grating vector of k_g, that propagates at an angle φ with respect to the grating grooves.

The dashed circle, centred about the origin, represents the maximum wavevector available to the incident photon. Hence coupling is only possible to modes that fall within the shaded area. The outer, solid circle centred on the origin represents the SPP wavevector, which is always larger than the incident wavevector, preventing direct coupling. $k_0 \sin\theta$ is the in-plane wavevector of the incident radiation required for SPP excitation from the k_g scattering process. The grating allows the wavevector of the SPP to be changed by integer multiples of k_g, hence we observe SPP circles about each scattering centre. Portions of adjacent SPP circles now fall within the shaded region, allowing coupling to occur.

Previously, for the planar interface, the polarisation of the incident radiation was defined with respect to the plane of incidence. It was shown that only *p*-polarised incident radiation could excite the SPP, since a component of electric field perpendicular to the interface is required to set up the necessary surface charge. Once the interface is corrugated, the symmetry of the surface is broken. Incident radiation may now have a component of electric vector normal to the interface for both *p* and *s*-polarisations, depending upon the orientation of the grating grooves with respect to the plane of incidence. For an azimuth angle (ϕ) of zero (the classical mount), SPP excitation is still only possible with *p*-polarised radiation, as the electric vector for the *s*-polarised case is tangential to the entire grating surface. However, when $0^\circ < \phi < 90^\circ$ (the conical mount), both *s* and *p*-polarised radiation may result in SPP excitation. For $\phi = 90^\circ$ and for a symmetric grating sample, only *s*-polarised incident radiation results in the excitation of the SPP at normal incidence.

2.7. Coupling strength and reflectivity features

It is now well known that the excitation of a SPP mode propagating on a corrugated interface by incident *p*-polarised radiation will result in the manifestation of surface plasmon polariton resonance (SPPR) features in the specular reflection of the sample, but this is not the only characteristic feature that occurs in the specular reflectance. *Meecham* and *Peters* (1957) studied the reflection of radiation of wavelength λ_0 = 32 mm from a grating and observed a redistribution of energy among the diffracted orders. This occurred at a point at which a diffracted order ceased or began to propagate. This reflectivity feature is of course the Rayleigh anomaly, or pseudo critical edge, as discussed in *section 2.2*. Consider *Figure 2.7.1,* the theoretical reflectivity as a function of incident angle, produced using the s-band modelling code for a sinusoidal air – aluminium interface with parameters λ_0 = 633nm, λ_0/λ_g = 1.583, a/λ_g = 0.038. The frequency dependent dielectric constant of the aluminium in this case is chosen to be $-5.92 + 21.7i$, which is appropriate for an incident wavelength of 633nm [*Palik, Handbook of Optical Constants of Solids, Academic press (1985)*]. The Rayleigh anomaly appears as a cusp in the specular reflection from the grating sample, due to a redistribution of energy into the remaining diffracted orders when one appears, or

ceases to propagate, as shown by *Figure 2.7.1* (a) and marked by the dotted line to the right of the reflection minima. The size of the step in reflectivity is related to the amplitude of the grating, since the efficiency of a diffracted order increases with grating amplitude.

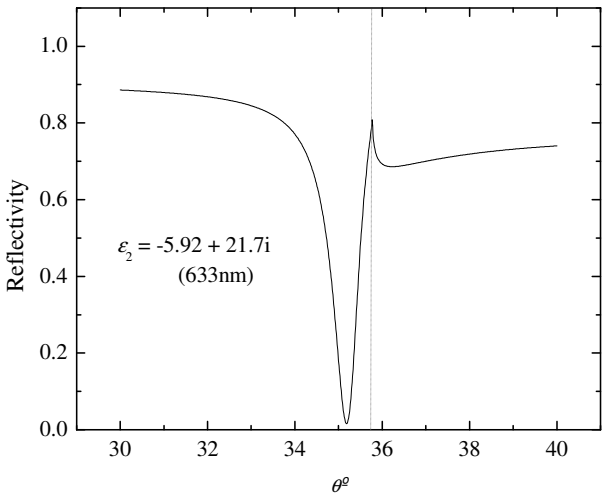

Figure 2.7.1 Theoretical reflectivity as a function of incident angle, calculated using the s-band modelling for a sinusoidal air – aluminium interface with parameters λ_0/λ_g = 1.583 and a/λ_g = 0.038. The frequency dependent dielectric constant of the aluminium in this case is chosen to be $-5.92+21.7i$, which is an appropriate value for an incident wavelength of 633nm.

The second, and most noticeable feature in the reflectivity spectrum displayed in *Figure 2.7.1*, is the SPPR itself, which forms the basis of the angle dependent study in the first two experimental chapters of this thesis. The SPPR appears as a reflectivity minimum due to the combination of the reflected incident radiation, and the re-radiated radiation from the coupled SPP. Incident radiation directed onto the sample will undergo two processes; direct reflection into the specular beam, and scattering by the grating profile into a diffracted order when the coupling condition (*Equation 2.6.1*) is satisfied. The SPP is excited, which then propagates along the surface, and may undergo a second scattering, re-radiating the radiation back into the specular beam. That which is directly reflected undergoes a 180º phase shift, since the electric field is reversed upon reflection from a metal surface. That which excites the SPP, undergoes a 90º phase shift because the 1st evanescent diffracted order is 90º out of phase with respect to the incident

radiation, and then undergoes a further 90º phase shift when exciting the SPP, as the SPP acts as a forced damped oscillator. This process is repeated to couple the radiation back out into the specularly reflected beam, and therefore the re-radiated light undergoes a phase shift of 360º. As the specularly reflected and re-radiated radiation are 180º out of phase with respect to each other, they cancel, producing a reflectivity minimum. It is also important to note here however that the incident radiation may undergo a multiple scattering event to couple into the SPP mode. For the case where the incident radiation undergoes two single k_g scattering events to couple to the SPP, an extra 180º of phase is introduced to the re-radiated radiation, and the SPPR then manifests itself as a reflectivity maximum.

The shape of the SPPR is governed by the strength of the coupling into and out of the SPP, and the absorption of energy into the metal. The re-radiation and absorption of energy are the damping terms, and as with all resonant systems, the width of the resonance is due to the total damping of the oscillator. The re-radiation term increases with grating amplitude since the energy of the SPP may be re-radiated into a propagating diffracted order, the efficiency of which increases as a^2 to first order [*Kitson et al.* (1995)]. Re-radiated energy may also be channelled into the specular reflectivity of the sample, and as we will learn in *section 2.10* of this chapter, may occur as polarisation conversion when the grating grooves are neither parallel nor perpendicular to the plane of incidence. Further, as discussed in *section 2.4*, the propagation length of the SPP on a planar interface is large at microwave frequencies due to the fields being nearly excluded from the metal. However, as the amplitude of the grating profile increases, the propagation of the mode decreases since the probability of scattering increases. Hence the SPP does not sample an infinite number of grooves, but is instead scattered by a range of wavevectors determined by the Fourier transform of such a finite set of corrugations. This will introduce a range of angles over which the SPP may re-radiate into one of the propagating diffracted orders, inferring an angular width to the SPPR.

In the absence of absorption in the dielectric adjacent to the metal, the absorptive part of the damping term is due to Joule heating of the metal, caused by the oscillatory motion of the surface polarisation electrons. Also, the depth of the SPPR is given by the ratio of the radiative damping to the absorptive damping, with maximum depth occurring when

these two terms are equal [*Raether* (1988)]. At microwave frequencies, since the penetration of the field into a nearly perfectly conducting medium with such a large and negative real part of the dielectric function is small ($L_{y2} \approx 0.6$ μm), Joule heating of the substrate is not a significant loss channel. Hence the SPPR appears as a very narrow and shallow feature on shallow gratings. This effect becomes immediately obvious on comparison of *Figure 2.7.1* with *Figure 2.7.2* (a) and (b).

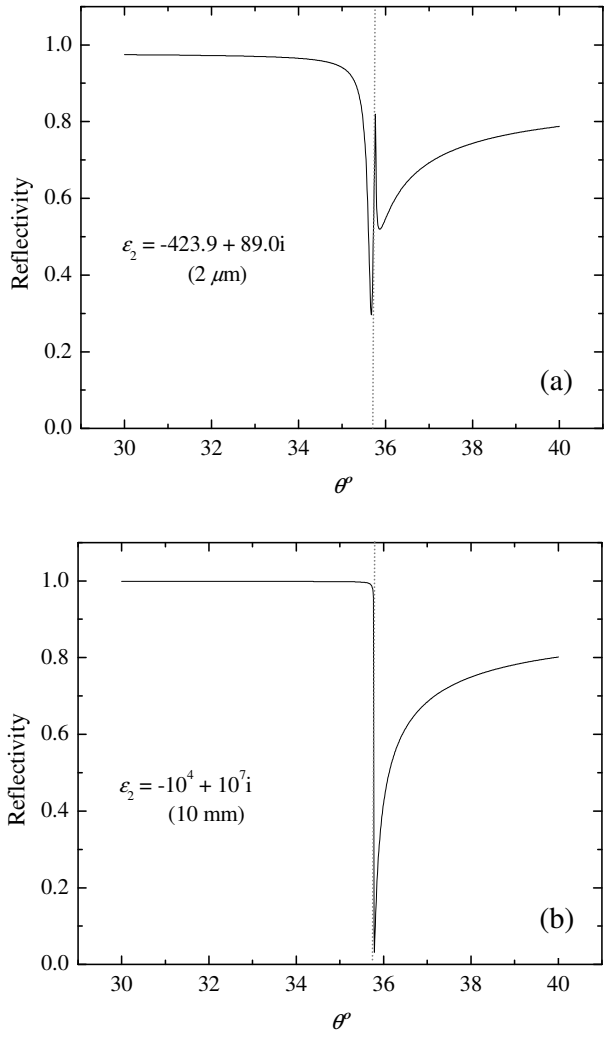

Figure 2.7.2 Theoretical reflectivity as a function of incident angle, calculated using the s-band modelling for a sinusoidal air – aluminium interface with parameters $\lambda_0/\lambda_g = 1.583$ and $a/\lambda_g = 0.038$, as *Figure 2.7.1*. However in this case, the frequency dependent dielectric constant of the aluminium is chosen to be (a) –423.9 + 89.0i, and (b) $-10^4 + 10^7$i, with incident wavelengths of 2μm and 10mm respectively.

Reproduced in the same way, and for exactly the same structure as discussed in *Figure 2.7.1*, these two theoretical reflectance plots show the reflectance near critical edge for an incident wavelength of (a) λ_0 = 2μm and (b) λ_0 = 10mm, with suitable values of ε_{2r} and $\varepsilon_{2i.}$ It is clear that as the substrate becomes effectively more metallic, the SPPR becomes much narrower. Further, the minimum moves in angle toward the pseudo critical edge to such an extent that at microwave frequencies the two features become indistinguishable. This is to be expected since from the dispersion relation (*Equation 2.3.11*), as $(k_{SPP}\text{-}k_0)\rightarrow 0$, $\varepsilon_{2r} \rightarrow \infty$.

Indeed, the SPPR in the zero ordered region of *Figure 2.7.2* (b) (to the left of the grey dotted line) is not visible, instead only the wing of the plasmon may be seen in the diffractive region. This is because if such a structure is zero-ordered, that is to say that the structure supports no real propagating diffracted orders, then there is no radiative (other than p-s conversion) or absorptive loss channel available for the SPP. As a result the SPPR is very narrow, approximating to a delta function. In order to clearly see the SPPR in the reflectance from such a sample, it is necessary to fill the grooves with a slightly lossy dielectric, such as wax. It will be shown later in this thesis, through the variation of the complex dielectric constant of this lossy over-layer, that the dielectric constant of this over-layer may dominate the shape and depth of the SPPR at these frequencies.

2.8. Effective permittivity

Metallic gratings with groove depth much narrower than the wavelength of incident radiation may be considered as high impedance surfaces [*Sievenpiper* (1999) and references therein], with the top surface of the structure being assigned a ‘sheet impedance’, equal to the impedance of the individual grating grooves. Many properties of such high impedance surfaces may be described by the effective medium model, which is derived from the geometry of the system. This is on condition that the incident radiation can not resolve individual features of the structure, but senses only an averaged response, which may be characterised by an *effective* dielectric constant of the plasma form assigned to the substrate. As shown by *Sievenpiper* (1999) and *Pendry* (2004), the effective medium concept may be applied to surface waves. Pendry

proposed that the introduction of a textured surface will result in a bound surface state even on a perfectly conducting medium, with a dispersion relation typical of the SPP.

The idea that the texturing of a metal interface changes the *effective* dielectric constant of the metal, since the metallic medium at the interface (which is perceived as being flat by the incident radiation) is now partly dielectric due to the voids in the metal formed by the grooves, also has implications on the character of the surface mode. As previously discussed, on a planar metal interface at optical frequencies the SPP mode is plasmon like, the associated fields of which are tightly bound to the interface as shown by *Figure 2.8.1* (a). At microwave frequencies however, fields are nearly totally excluded from the metal and extend many wavelengths into the dielectric with the mode being polariton like, as shown by *Figure 2.8.1* (b). The introduction of a corrugation to the interface results in the field within the dielectric reducing in spatial extent, as shown by *Figure 2.8.1* (c). Hence a surface mode supported on a corrugated metal-dielectric interface is more plasmon like than that supported by a planar interface at microwave frequencies.

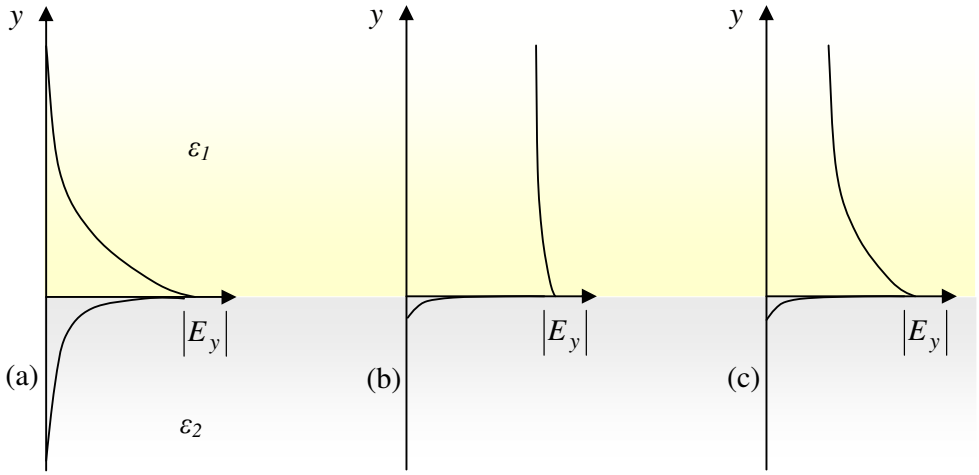

Figure 2.8.1 Schematic representation of the associated tangential electric field in each media for the SPP mode supported (a) at optical frequencies on a planar interface, (b) at microwave frequencies on a planar interface, and (c) at microwave frequencies on a corrugated interface.

2.9 Band gaps in the dispersion of grating coupled SPP's.

In a similar way to the electrons in a crystal, energy gaps open up in the dispersion relation of surface plasmon polaritons propagating along a corrugated metal-dielectric interface. Work by *Yablonovitch* (1987 and 1993) predicted and demonstrated, in the microwave regime, the existence of photonic band gaps in a three-dimensional structure with refractive index modulations that are periodic on the scale of the wavelength of the incident radiation. Such a material is termed a *photonic crystal*. Likewise, the surface of a diffraction grating may also be regarded as a 1-D (single-grating) or 2-D (bi-grating) photonic crystal. Grating induced photonic band gaps were first reported by *Ritchie et al.* in 1968, and later by *Chen et al.* (1983) who recorded their magnitudes.

Consider a SPP propagating perpendicular to the grooves on a metallic grating with pitch $k_g = 2\pi/\lambda_g$ and profile given by

$$A(x) = a_1 \sin(k_g x + \Phi_1) + a_2 \sin(2k_g x + \Phi_2) + \ldots + a_N \sin(Nk_g x + \Phi_N) + \ldots \qquad \textit{Equation 2.9.1}$$

where $a_1, a_2, \ldots a_N$ are the amplitudes of the harmonic components of the corrugation, and $\Phi_1, \Phi_2, \ldots \Phi_N$ are the relative phases. When radiation is incident upon such a distorted grating with a finite first harmonic component, the $2k_g$ wave vector will result in the forward and backward travelling waves [$\exp(\pm ik_g x)$] interfering constructively to set up a standing wave. Using simple symmetry arguments, we expect two different standing wave solutions to arise

$$\Psi_1 = \exp(ik_g x) + \exp(-ik_g x) = 2\cos(k_g x) \qquad \textit{Equation 2.9.2}$$

$$\Psi_2 = \exp(ik_g x) - \exp(-ik_g x) = 2i\sin(k_g x) \qquad \textit{Equation 2.9.3}$$

The nodes for one of these standing waves coincide with the peaks of the grating; the other has its nodes aligning with the troughs. The field distributions and hence the energies of the two waves are different and thus an energy gap occurs at the point of intersection of the –1 and the +1 dispersion curves. By deriving the field distribution

around the interface, it can be shown that the extrema of the normal field component and surface charge distribution for the high energy standing-wave solution occur at the troughs of the grating profile, whereas for the low energy solution, they occur at the peaks [*Barnes et al.* (1996)]. These distributions are illustrated in *Figure 2.9.1*. It is clear that due to the relative distortion of the fields between the two solutions, a different energy will be associated with the two standing waves. The grating perturbs the field distributions associated with the surface charges so that when the charges are located at the troughs of the profile, the field lines are compressed together increasing the stored energy associated with the mode (ω_+). The opposite occurs at the peaks (ω_-).

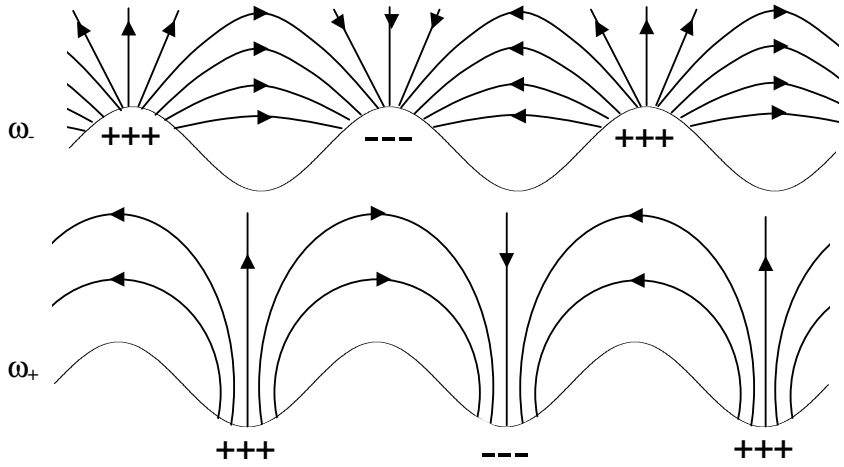

Figure 2.9.1 A schematic representation of the E-field lines and surface charge distribution for the two standing wave solutions at the boundaries of a band gap. The upper sketch represents the lower frequency mode. Note in the lower sketch that the field lines are more distorted, illustrating the greater energy stored in the fields by this mode.

In the absence of a first harmonic in the grating profile, coupling is still possible between the two counter-propagating modes via two consecutive k_g scatters. However, this second-order process is much less probable than a direct $2k_g$ scatter, and hence the size of the induced photonic band gap is comparatively small for small amplitude gratings. *Chen et al.* (1983) studied the gaps that open up at the crossing of the (-1,2), (-2,2), (-1,3), (-2,3) and (-1,4) diffracted dispersion curves requiring scatters of up to $5\,k_g$.

Coupling incident radiation to the surface mode on each side of the band gap will be discussed further in the first experimental chapter of this thesis.

2.10 Polarisation conversion

Linearly polarised radiation incident upon a grating may be converted to an orthogonal polarisation state in one of two ways, the first being via SPP excitation [*Inagaki*, *Goudonnet*, and *Arakawa* (1986), *Bryan-Brown*, *Sambles* and *Hutley* (1990), *Elston*, *Bryan-Brown* and *Sambles* (1991), *Depine* and *Lester* (2001)]. As discussed in section 2.6, when a grating is orientated such that $0^\circ < \phi < 90^\circ$, both *s* and *p*-polarised incident radiation may be utilised for the purpose of SPP excitation. This implies that when radiation is re-radiated back out into the specular or a diffracted beam, both *s* and *p*-polarised radiation may be emitted. If *p*-polarised radiation is incident, and the grating grooves are orientated such that they do not lie within the plane of incidence, both *s* and *p*-polarised radiation may be re-radiated. For shallow mono-gratings it may be shown that the polarisation converted signal varies as $\sin^2(2\phi)$, by considering the electric field components relative to the grating profile [*Bryan-Brown et al.* (1990)]. Maximum polarisation conversion occurs at $\phi = 45^\circ$ since at this orientation coupling strength for *s* and *p*-polarised incident radiation is approximately equal. However, it will be shown later in this thesis that some structures, including bi-gratings, have a maximum in polarisation that occurs at azimuthal angles other than 45º.

The second way in which polarisation conversion occurs is also ϕ dependent, but cyclic with groove depth [*Watts* and *Sambles* (1997)]. Consider normally incident radiation upon a mono-grating at a wavelength for which the grating is non-diffractive. The electric field of the incident radiation may be split into two components, one parallel to the grating grooves (E_z) and one parallel to the grating vector (E_x). Since E_z does not cut the grating grooves, this component of the electric field will be reflected as if it were reflected from a planar surface at the position of the average surface plane of the grating. The E_x component however does cut the grating grooves, and may produce a single, or multiple loops of circulating field within the grating grooves. It is this circulating field which alters the position of the average surface plane of the profile as felt by the incident E_z component. The difference in height of these two '*effective*'

average surface planes for the two components of incident electric field may result in a phase difference between them, rotating the plane of polarisation. The amount of polarisation therefore depends upon groove depth of the grating, with the maximum occurring when the phase difference between E_x and E_z is 180º.

2.11. Summary

In this chapter, we have introduced the SPP as an oscillation of surface polarisation charge density at the interface between a metal and a dielectric. We have shown that on a planar interface, the SPP is non-radiative, but on a corrugated surface may be coupled to by incident radiation, whereupon the coupled SPP acts as a forced damped oscillator. An exact expression for the dispersion of the surface mode has been derived, and the spatial extent of the SPP fields discussed. We have shown that at microwave frequencies the mode is polariton like in character, with exponentially decaying fields which extend many wavelengths into the dielectric, and possess a penetration depth into the metal on the order of microns. SPP propagation on gratings has been examined, including a brief discussion on the formation of band gaps in the modes dispersion. Finally, SPP induced polarisation has been explained.

CHAPTER 3

Waveguide modes

3.1. Introduction

In *Chapters 7* and *8* of this thesis, a detailed angle dependent study of two separate *sub-wavelength* transmitting apertures is presented. The first takes the form of a circular aperture whose diameter is equal to $\lambda_0/2$ where λ_0 is the wavelength of peak resonant transmission. The second structure takes the form of an annulus in a thick aluminium substrate, which may be thought of as a sub-wavelength slit with circular symmetry. Although the underlying physics regarding each structure is discussed in each experimental chapter, it is necessary to provide here a thorough review of waveguide theory. Since the aperture is circular, and the annular arrangement resembles a terminated transmission line, we will restrict our discussion to perfect metal clad waveguides (infinite conductivity is a reasonable approximation at microwave frequencies since the penetration depth is small compared to the wavelength), with emphasis on the cylindrical and coaxial geometries. All hollow conducting tubes discussed are assumed to be uniform and of infinite extent in the direction of propagation with the axis of the guide taken as the z-axis. Further, it will be assumed that the guide is filled with lossless dielectric of permittivity ε and permeability μ. Derivations presented in this chapter have been adapted from *Microwave Engineering*, D. M. Pozar, Wiley, New York (1998).

3.2. Boundary conditions; Fields at a perfectly conducting wall.

Before we can begin our discussion of waveguide theory, we must first consider boundary conditions at the surface of a perfect conducting wall. Since skin depth tends to zero as conductivity (σ) tends to infinity, all fields are excluded from within the conductor. Boundary conditions may be found using Maxwell's equations and Gauss's law, employing a pillbox or rectangle spanning the interface and assuming uniform fields over it. As one side of the rectangle or face of the pillbox is situated within a region where $E=B=0$, the boundary conditions are as follows:

$$\hat{n} \cdot \boldsymbol{D} = \rho_s \qquad \textit{Equation 3.2.1}$$

$$\hat{n} \cdot \boldsymbol{B} = 0 \qquad \textit{Equation 3.2.2}$$

$$\hat{n} \times \boldsymbol{E} = 0 \qquad \textit{Equation 3.2.3}$$

$$\hat{n} \times \boldsymbol{H} = J_s \qquad \textit{Equation 3.2.4}$$

where ρ_s and J_s are the electric surface charge density and current density respectively and $\hat{n}$ is the normal unit vector of the perfectly conducting surface. Such a surface is known as an *electric wall*, since the tangential components of *E* within the dielectric must vanish at the conducting wall, in effect being 'shorted out'.

3.3. General solutions for TE, TM and TEM waves.

In the interior of the waveguide, the solutions of Maxwell's equations may be divided into two groups, or modes. For one set of modes there exists no longitudinal or axial magnetic field component. The magnetic vector is entirely transverse to the direction of wave propagation and therefore these are the transverse magnetic or TM solutions (sometimes referred to as 'electric type' since they do possess an axial component of electric field). The second set of solutions are the transverse electric or TE modes. These modes have no axial component of electric field but possess an axial component of magnetic field. As such they are sometimes referred to as 'magnetic type' solutions. TEM or transverse electromagnetic modes actually belong to the TM set of solutions, since the TEM mode is the fundamental TM solution. It is characterised by possessing no magnetic or electric axial field components and so both the magnetic and electric vectors are entirely transverse.

All hollow waveguides have many properties in common. For this reason we will begin by finding general solutions of magnetic and electric type for a waveguide with arbitrary cross-section, an example of which is shown in *Figure 3.3.1*.

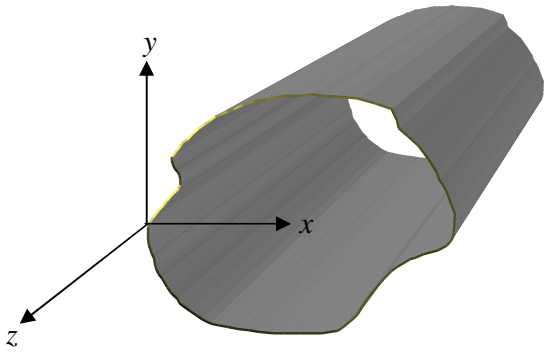

Figure 3.3.1 A Hollow perfectly conducting waveguide of arbitrary cross-section. The waveguide is considered uniform along the z-axis and of infinite extent.

We assume at this point time harmonic fields with a time variation of the form $e^{j\omega t}$. We can then write for the spatial parts:

$$\mathbf{E} = \left[\overline{E}(x,y) + \hat{z}E_z(x,y)\right]e^{-jkz} \qquad \textit{Equation 3.3.1}$$

$$\mathbf{H} = \left[\overline{H}(x,y) + \hat{z}H_z(x,y)\right]e^{-jkz} \qquad \textit{Equation 3.3.2}$$

where $\overline{E}(x,y)$ and $\overline{H}(x,y)$ are the transverse field components, H_z and E_z the axial field components, and $k_z = 2\pi/\lambda_z$ where λ_z is the wavelength of the guided wave. Assuming the waveguide is source free,

$$\nabla\times\mathbf{E}=-j\omega\mu\mathbf{H} \qquad \textit{Equation 3.3.3}$$

$$\nabla\times\mathbf{H}=j\omega\varepsilon\mathbf{E} \qquad \textit{Equation 3.3.4}$$

Since we have an e^{-jkz} axial dependence, the three components of each of the above vector equations may be reduced to:

$$\frac{\partial E_z}{\partial y} + jk_z E_y = -j\omega\mu H_x \qquad \textit{Equation 3.3.5}$$

$$-jk_z E_x - \frac{\partial E_z}{\partial x} = -j\omega\mu H_y \qquad \textit{Equation 3.3.6}$$

$$\frac{\partial E_y}{\partial x} - \frac{\partial E_x}{\partial y} = -j\omega\mu H_z \qquad \textit{Equation 3.3.7}$$

$$\frac{\partial H_z}{\partial y} + jk_z H_y = -j\omega\varepsilon E_x \qquad \textit{Equation 3.3.8}$$

$$-jk_z H_x - \frac{\partial H_z}{\partial x} = j\omega\varepsilon E_y \qquad \textit{Equation 3.3.9}$$

$$\frac{\partial H_y}{\partial x} - \frac{\partial H_x}{\partial y} = -j\omega\varepsilon E_z \qquad \textit{Equation 3.3.10}$$

We can now solve the above equations for the four transverse field components in terms of E_z and H_z to give:

$$H_x = \frac{j}{k_c^2}\left(\omega\varepsilon\frac{\partial E_z}{\partial y} - k_z\frac{\partial H_z}{\partial x}\right) \qquad \textit{Equation 3.3.11}$$

$$H_y = \frac{-j}{k_c^2}\left(\omega\varepsilon\frac{\partial E_z}{\partial x} - k_z\frac{\partial H_z}{\partial y}\right) \qquad \textit{Equation 3.3.12}$$

$$E_x = \frac{-j}{k_c^2}\left(k_z\frac{\partial E_z}{\partial x} + \omega\mu\frac{\partial H_z}{\partial y}\right) \qquad \textit{Equation 3.3.13}$$

$$E_y = \frac{j}{k_c^2}\left(k_z\frac{\partial E_z}{\partial y} + \omega\mu\frac{\partial H_z}{\partial x}\right) \qquad \textit{Equation 3.3.14}$$

where $k_c^2 = \omega^2\varepsilon\mu - k_z^2 = k_0^2 - k_z^2$ is the cut-off wave number. Equations *3.3.11* to *3.3.14* are general results that we will apply to the rectangular, cylindrical and coaxial wave

guide. Before we can do this however, these results must be tailored to the three specific wave types, TE, TM and TEM.

3.3.1 TE waves

As discussed in the previous section, TE waves are characterised by $E_z = 0$ and $H_z \neq 0$. It is then clear that equations *3.3.11* through *3.3.14* reduce to the following:

$$H_x = -\frac{jk_z}{k_c^2}\frac{\partial H_z}{\partial x} \qquad \textit{Equation 3.3.15}$$

$$H_y = -\frac{jk_z}{k_c^2}\frac{\partial H_z}{\partial y} \qquad \textit{Equation 3.3.16}$$

$$E_x = \frac{-j\omega\mu}{k_c^2}\frac{\partial H_z}{\partial y} \qquad \textit{Equation 3.3.17}$$

$$E_y = \frac{j\omega\mu}{k_c^2}\frac{\partial H_z}{\partial x} \qquad \textit{Equation 3.3.18}$$

In the TE case, the propagation constant is a function of both frequency and the geometry of the guide. To apply equations *3.3.15* through *3.3.18* to a specific geometric problem subject to boundary conditions, H_z must be found using the Helmholtz wave equation;

$$\nabla^2 \mathbf{H} + \omega^2\mu\varepsilon\mathbf{H} = 0 \qquad \textit{Equation 3.3.19}$$

which, since $H_z(x,y,z) = H_z(x,y)e^{-jkz}$ reduces to a 2-D wave equation for H_z:

$$\left(\frac{\partial^2}{\partial x^2} + \frac{\partial^2}{\partial y^2} + k_c^2\right)H_z = 0 \qquad \textit{Equation 3.3.20}$$

3.3.2 TM waves

As TM waves are defined by $E_z \neq 0$, $H_z = 0$, equations *3.3.11* through *3.3.14* reduce to:

$$H_x = \frac{j\omega\varepsilon}{k_c^2}\frac{\partial E_z}{\partial y} \qquad \textit{Equation 3.3.21}$$

$$H_y = \frac{-j\omega\varepsilon}{k_c^2}\frac{\partial E_z}{\partial x} \qquad \textit{Equation 3.3.22}$$

$$E_x = \frac{-jk_z}{k_c^2}\frac{\partial E_z}{\partial x} \qquad \textit{Equation 3.3.23}$$

$$E_y = \frac{jk_z}{k_c^2}\frac{\partial E_z}{\partial y} \qquad \textit{Equation 3.3.24}$$

As in the TE case, the wave equation reduces to a 2-D wave equation for E_z:

$$\left(\frac{\partial^2}{\partial x^2} + \frac{\partial^2}{\partial y^2} + k_c^2\right)E_z = 0 \qquad \textit{Equation 3.3.24}$$

3.3.3 TEM waves

TEM waves are characterised by $E_z = H_z = 0$. As a result, it can be seen from equations *3.3.11* through *3.3.14* that the transverse fields are also zero unless $k_c = 0$, providing a singularity in the first term. Therefore TEM modes (where supported) propagate without cut-off. Further, $k_c = 0$ implies that $k_z = k_0$. Thus if the medium within the waveguide is either air or vacuum, the phase velocity of the guided wave is c regardless of the geometry of the guide and whatever the frequency. The wave equation reduces to a 2-D wave equation for E_x;

$$\left(\frac{\partial^2}{\partial x^2} + \frac{\partial^2}{\partial y^2}\right)E_x = 0 \qquad \textit{Equation 3.3.25}$$

and a similar result is obtained for E_y. Therefore;

$$\nabla_t^2 \overline{E}(x, y) = 0 \qquad \textit{Equation 3.3.26}$$

where $\overline{E}(x, y)$ are the transverse electric field components and $\nabla_t^2 = \partial^2/\partial x^2 + \partial^2/\partial y^2$ is the Laplacian operator in the transverse dimensions. Thus the fields of a TEM wave satisfy Laplace's equation. These fields are the same as the static fields that can exist between conductors. As in the electrostatic case, the electric field can be expressed as the gradient of a scalar potential $\Phi(x,y)$;

$$\overline{E}(x, y) = -\nabla_t \Phi(x,y) \qquad \textit{Equation 3.3.27}$$

where $\nabla_t = \hat{x}(\partial/\partial x) + \hat{y}(\partial/\partial y)$ is the transverse gradient operator. Further, applying;

$$\nabla \cdot D = \nabla \cdot \varepsilon \overline{E}(x, y) = 0, \qquad \textit{Equation 3.3.28}$$

shows

$$-\nabla_t^2 \Phi(x,y) = 0 \qquad \textit{Equation 3.3.29}$$

This result shows that $\Phi(x,y)$ also satisfies Laplace's equation as expected from electrostatics. It can be noted here that a closed conductor such as a rectangular or cylindrical waveguide cannot support a TEM mode. This is because the static potential in such a region would be constant, leading to $\overline{E}(x, y) = 0$.

3.4 The rectangular waveguide.

To begin to apply the general results found in the previous sections, we must first consider the geometry of the wave guide so that the 2-D wave equation can be solved. Transverse fields can then be found from E_z and H_z, and boundary conditions can then be applied to the appropriate field components to find the unknown constants, k_c and k_z. Initially, rectangular geometry will be considered as this is somewhat simpler than a waveguide with circular symmetry.

3.4.1 TE modes

The geometry of the rectangular waveguide is shown in *Figure 3.4.1.* Recall that all waveguide geometries considered in this chapter are assumed to be hollow tubes formed from a perfectly conducting media, and either empty, or filled with a lossless dielectric media with parameters ε and μ. By convention, the longest side of the face of the waveguide is parallel to the x-axis, and $a > b$ where a and b are the side lengths. The waveguide is considered uniform in the z-direction and infinite in extent.

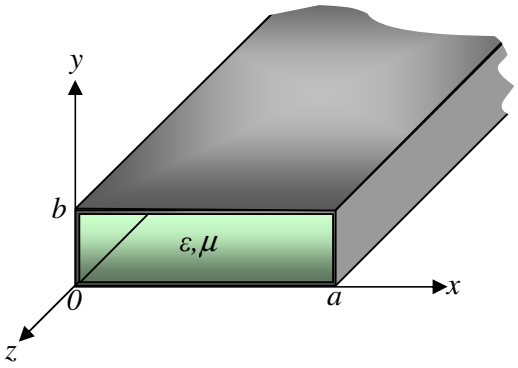

Figure 3.4.1. The geometry and co-ordinate system for the rectangular waveguide.

For the TE modes, with $E_z = 0$, H_z must satisfy the wave equation *3.3.20.* This partial differential equation may be solved through the separation of variables to yield;

$$\frac{1}{X}\frac{d^2X}{dx^2}+\frac{1}{Y}\frac{d^2Y}{dy^2}+k_c^2=0 \qquad \textit{Equation 3.4.1}$$

where $H_z(x,y) = X(x)\ Y(y)$. Then, since each of the terms in the above expression must be equal to a constant, we define separation constants k_x and k_y such that;

$$\frac{d^2X}{dx^2}+k_x^2X=0 \qquad \textit{Equation 3.4.2}$$

$$\frac{d^2Y}{dy^2}+k_y^2Y=0 \qquad \textit{Equation 3.4.3}$$

$$k_x^2+k_y^2=k_c^2 \qquad \textit{Equation 3.4.4}$$

The general solution for H_z can then be written as:

$$H_z(x,y)=\left(A\cos k_x x+B\sin k_x x\right)\left(C\cos k_y y+D\sin k_y y\right) \qquad \textit{Equation 3.4.5}$$

To evaluate the constants *A,B,C* and *D* the boundary conditions on the electric field components tangential to the waveguide walls must be applied, that is:

$E_x(x,y) = 0$ at $y = 0,b$ *Equation 3.4.6*

$E_y(x,y) = 0$ at $x = 0,a$ *Equation 3.4.7*

We can then find expressions for E_x and E_y from H_z using equations *3.3.17* and *3.3.18.*

$$E_x=\frac{-j\omega\mu}{k_c^2}k_y\left(A\cos k_x x+B\sin k_x x\right)\left(-C\sin k_y y+D\cos k_y y\right) \qquad \textit{Equation 3.4.8}$$

$$E_y = \frac{-j\omega\mu}{k_c^2} k_x \left(-A\sin k_x x + B\cos k_x x\right)\left(C\cos k_y y + D\sin k_y y\right) \qquad \textit{Equation 3.4.9}$$

From *3.4.8* and *3.4.6* it is clear that $D = 0$, and $k_y = n\pi/b$ for $n = 1,2,3\ldots$. Similarly, from *3.4.9* and *3.4.7, B* = 0 and $k_x = m\pi/a$ for $m = 1,2,3\ldots$.The final solution for H_z is then:

$$H_z(x,y,z) = A_{mn}\cos\frac{m\pi x}{a}\cos\frac{n\pi y}{b}e^{-jk_z z} \qquad \textit{Equation 3.4.10}$$

where A_{mn} is an arbitrary amplitude constant composed of the constants A and C.

The transverse field components may then be found by substituting the above expression for H_z into equations *3.3.15* through *3.3.18*.

$$E_x = \frac{j\omega\mu n\pi}{k_c^2 b} A_{mn}\cos\frac{m\pi x}{a}\sin\frac{n\pi y}{b}e^{-jk_z z} \qquad \textit{Equation 3.4.11}$$

$$E_y = \frac{-j\omega\mu m\pi}{k_c^2 a} A_{mn}\sin\frac{m\pi x}{a}\cos\frac{n\pi y}{b}e^{-jk_z z} \qquad \textit{Equation 3.4.12}$$

$$H_x = \frac{jk_z m\pi}{k_c^2 a} A_{mn}\sin\frac{m\pi x}{a}\cos\frac{n\pi y}{b}e^{-jk_z z} \qquad \textit{Equation 3.4.13}$$

$$H_y = \frac{jk_z n\pi}{k_c^2 b} A_{mn}\cos\frac{m\pi x}{a}\sin\frac{n\pi y}{b}e^{-jk_z z} \qquad \textit{Equation 3.4.14}$$

And the propagation constant is:

$$k_z = \sqrt{k_0^2 - k_c^2} = \sqrt{k_0^2 - \left(\frac{m\pi}{a}\right)^2 + \left(\frac{n\pi}{b}\right)^2} \qquad \textit{Equation 3.4.15}$$

From *3.4.15* the propagation constant is real when k_0 is greater than the cut-off wavevector, corresponding to a propagating mode. Each TE mode supported by the rectangular waveguide (which corresponds to a combination of *m* and *n,* i.e. *m* and *n*

refer to the periodicity of the field in the direction to which they pertain) has a cut off frequency $f_{c(m,n)}$ given by;

$$f_{c(m,n)} = \frac{1}{2\pi\sqrt{\varepsilon\mu}}\sqrt{k_0^2 - \left(\frac{m\pi}{a}\right)^2 + \left(\frac{n\pi}{b}\right)^2} \qquad \textit{Equation 3.4.16}$$

The mode with the lowest cut-off frequency is termed the dominant mode, and since for this geometry $a > b$ the dominant mode is the $TE_{10.}$ Further, from *3.3.40-43*, if both m and n are zero the transverse field components are also zero and the TE_{00} mode is not supported. *Figure 3.4.2* shows the field profiles corresponding to eigen-solutions of the TE modes supported by an air-filled perfectly conducting metal waveguide, obtained using a finite element method (FEM) modelling code which will be described in detail in *Chapter 4*. In this instance, $b = a/2$. Red corresponds to a field magnitude of 1, blue corresponds to a field magnitude of zero, and each figure shows (i) the *E*-field magnitude calculated over a surface plane parallel to the *xy*-plane of the waveguide, at a phase corresponding to maximum field enhancement, (ii) and (iii) the *E* and *H*-vector magnitudes, again calculated over a surface plane parallel to the *xy*-plane of the waveguide, at a phase corresponding to maximum enhancement. The wave guide is modelled as uniform, and infinite in the *z*-direction, although only a thin cross section is shown here.

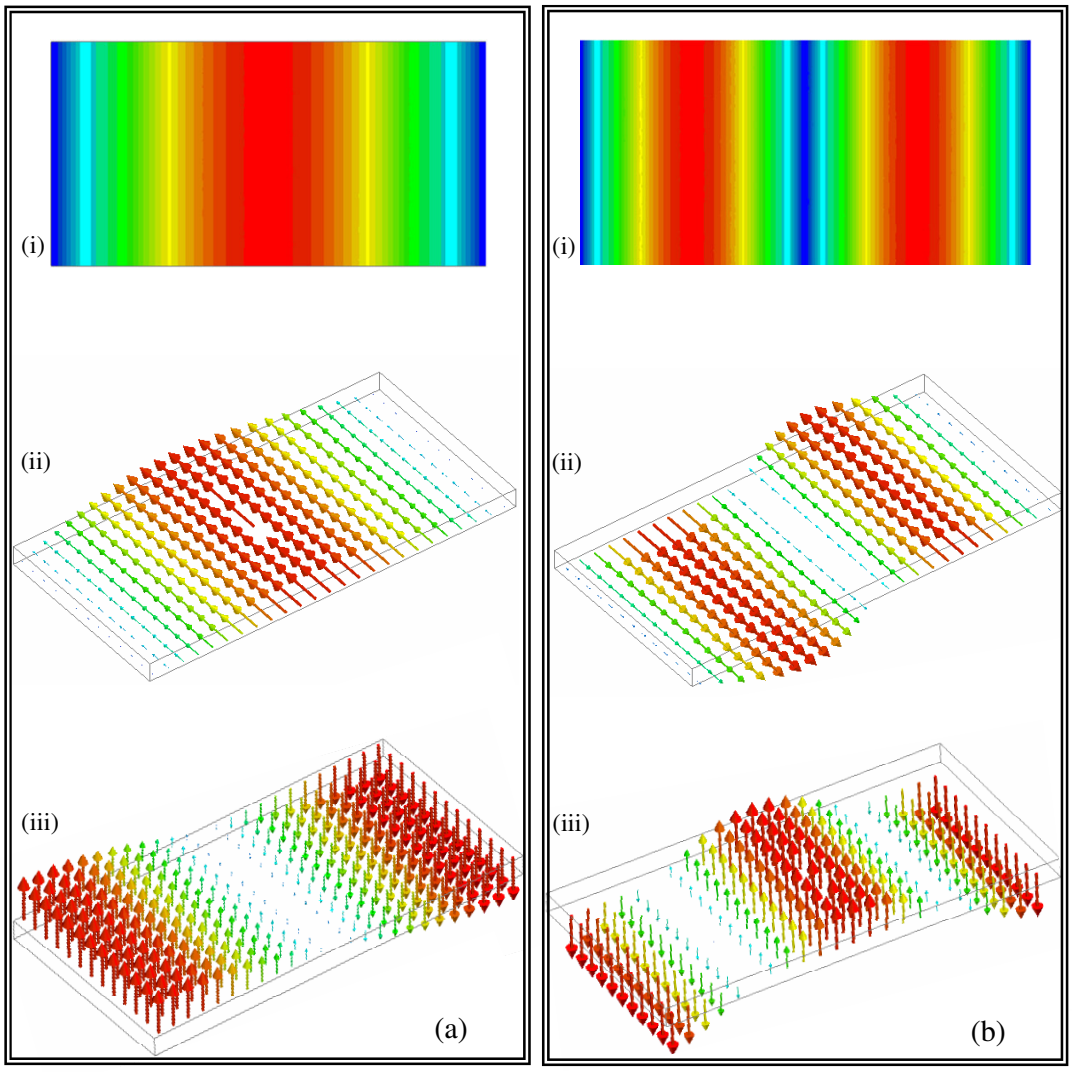

Figure 3.4.2 The field profiles corresponding to the eigen-solutions of (a) the TE_{10} and (b) the TE_{20} modes supported by an air-filled perfectly conducting metal waveguide, obtained using a finite element method (FEM) model. Red corresponds to a field magnitude of 1, blue corresponds to a field magnitude of zero, and each figure shows (i) the *E*-field magnitude calculated over a surface plane parallel to the *xy*-plane of the waveguide, at a phase corresponding to maximum field, (ii) and (iii) the *E* and *H*-vector magnitudes, again at a phase corresponding to maximum field. The wave guide is modelled as uniform, and infinite in the *z*-direction.

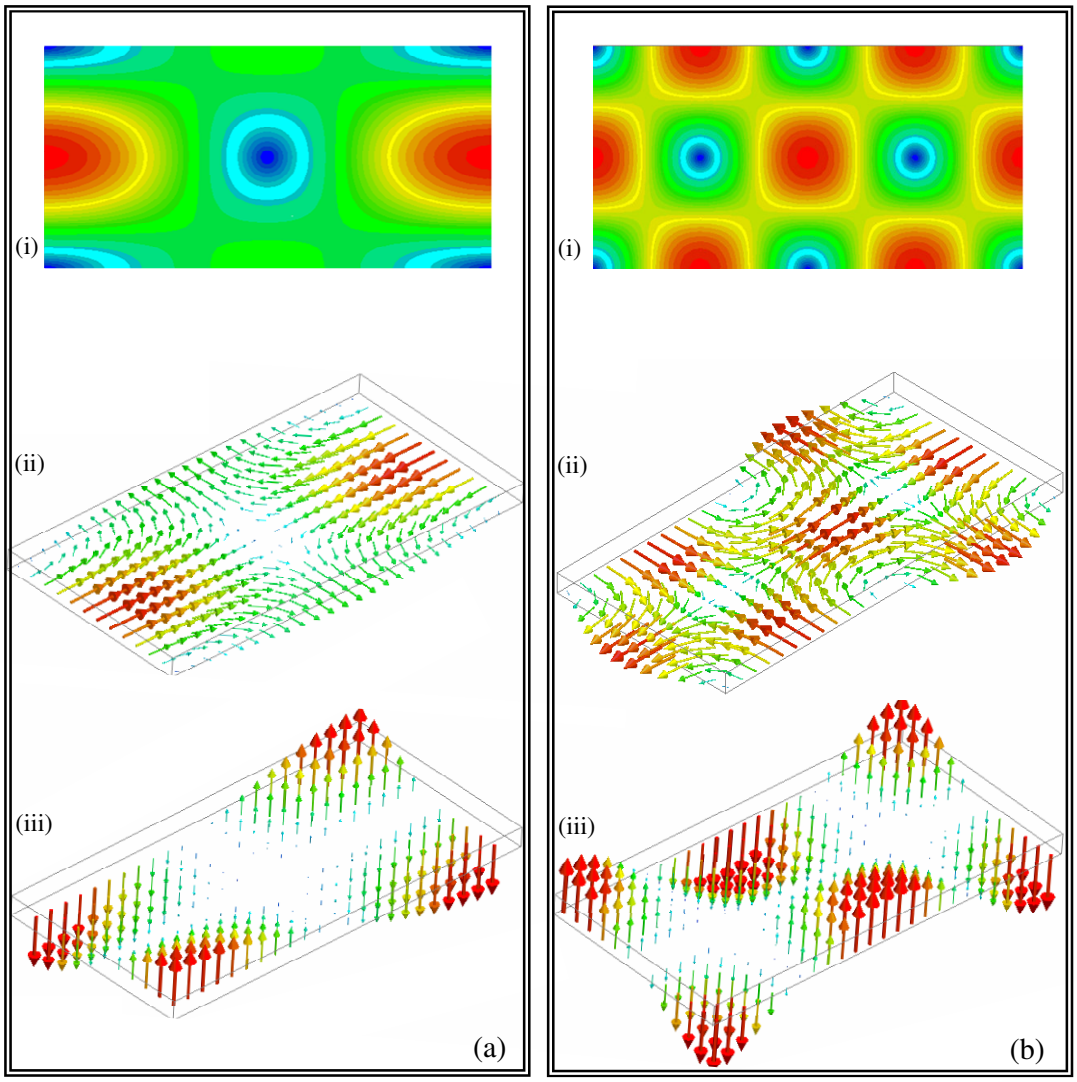

Figure 3.4.3 The field profiles corresponding to the eigen-solutions of (a) the TE_{01} and (b) the TE_{11} modes supported by an air-filled rectangular metal waveguide. Each figure shows (i) the *E*-field magnitude, (ii) and (iii) the *E* and *H*-vector magnitudes, calculated at a phase corresponding to maximum field magnitude.

3.4.2 TM modes

As discussed, the TM modes are characterised by $H_z = 0$, whilst E_z must satisfy the wave equation of *3.3.24* with $E_z(x,y,z) = E_z(x,y)e^{-jkz}$ and $k_c^2 = k_0^2 - k_z^2$. The wave equation may be solved using the separation of variables as in the case for the TE modes, with the general solution given by:

$$E_z(x, y) = \left(A\cos k_x x + B\sin k_x x\right)\left(C\cos k_y y + D\sin k_y y\right) \qquad \textit{Equation 3.4.17}$$

The boundary conditions can then be applied directly to E_z:

$E_z(x,y) = 0$ at $x = 0,a$ *Equation 3.4.18*

$E_z(x,y) = 0$ at $y = 0,b$ *Equation 3.4.19*

Applying *3.4.18* to *3.4.17* we find $A = 0$, and $k_x = m\pi/a$ where $m = 1,2,3..$ Similarly, applying *3.4.19* to *3.4.17* yields $C = 0$ and $k_y = n\pi/b$ for $n = 1,2,3\ldots$ The solution for E_z is then

$$E_z(x, y, z) = B_{mn}\sin\frac{m\pi x}{a}\sin\frac{n\pi y}{b}e^{-jk_z z} \qquad \textit{Equation 3.4.20}$$

where B_{mn} is an arbitrary amplitude constant. The transverse fields can be obtained by combining equation *3.4.20* with equations *3.3.21* through *3.3.24* to yield:

$$E_x = \frac{-jk_z m\pi}{ak_c^2}B_{mn}\cos\frac{m\pi x}{a}\sin\frac{n\pi y}{b}e^{-jk_z z} \qquad \textit{Equation 3.4.21}$$

$$E_y = \frac{-jk_z n\pi}{bk_c^2}B_{mn}\sin\frac{m\pi x}{a}\cos\frac{n\pi y}{b}e^{-jk_z z} \qquad \textit{Equation 3.4.22}$$

$$H_x = \frac{j\omega\varepsilon n\pi}{bk_c^2}B_{mn}\sin\frac{m\pi x}{a}\cos\frac{n\pi y}{b}e^{-jk_z z} \qquad \textit{Equation 3.4.23}$$

$$H_y = \frac{-j\omega\varepsilon m\pi}{ak_c^2} B_{mn} \cos\frac{m\pi x}{a} \sin\frac{n\pi y}{b} e^{-jk_z z} \qquad \textit{Equation 3.4.24}$$

The propagation constant is then given by;

$$k_z = \sqrt{k_0^2 - k_c^2} = \sqrt{k_0^2 - \left(\frac{m\pi}{a}\right)^2 - \left(\frac{n\pi}{b}\right)^2} \qquad \textit{Equation 3.4.25}$$

and is real for propagating modes, imaginary for evanescent modes. The cut-off frequency for TM_{mn} modes is identical to the cut-off frequency for TE_{mn} modes, as is the phase velocity. However, the TM_{00}, TM_{01} and TM_{10} modes are not supported by a rectangular guide since the field expressions for the transverse components of *E* and *H* given by equations *3.4.21* through *3.4.25* are zero if either *m*, or *n* are zero. Hence the lowest order TM mode to propagate is the TM_{11}, with a cut-off frequency given by;

$$f_{c(1,1)} = \frac{1}{2\pi\sqrt{\varepsilon\mu}} \sqrt{k_0^2 - \left(\frac{\pi}{a}\right)^2 + \left(\frac{\pi}{b}\right)^2} \qquad \textit{Equation 3.4.26}$$

which is the same cut-off frequency as the TE_{11} mode. Therefore the first seven modes to propagate in the rectangular waveguide case are (*in order*) the TE_{10}, TE_{20}, TE_{01}, the TE_{11} and TM_{11}, and the TE_{21} and TM_{21}. Field profiles pertaining to the TM_{11}, TM_{21} and TM_{12} are shown in *Figures 3.4.4* and *3.4.5*.

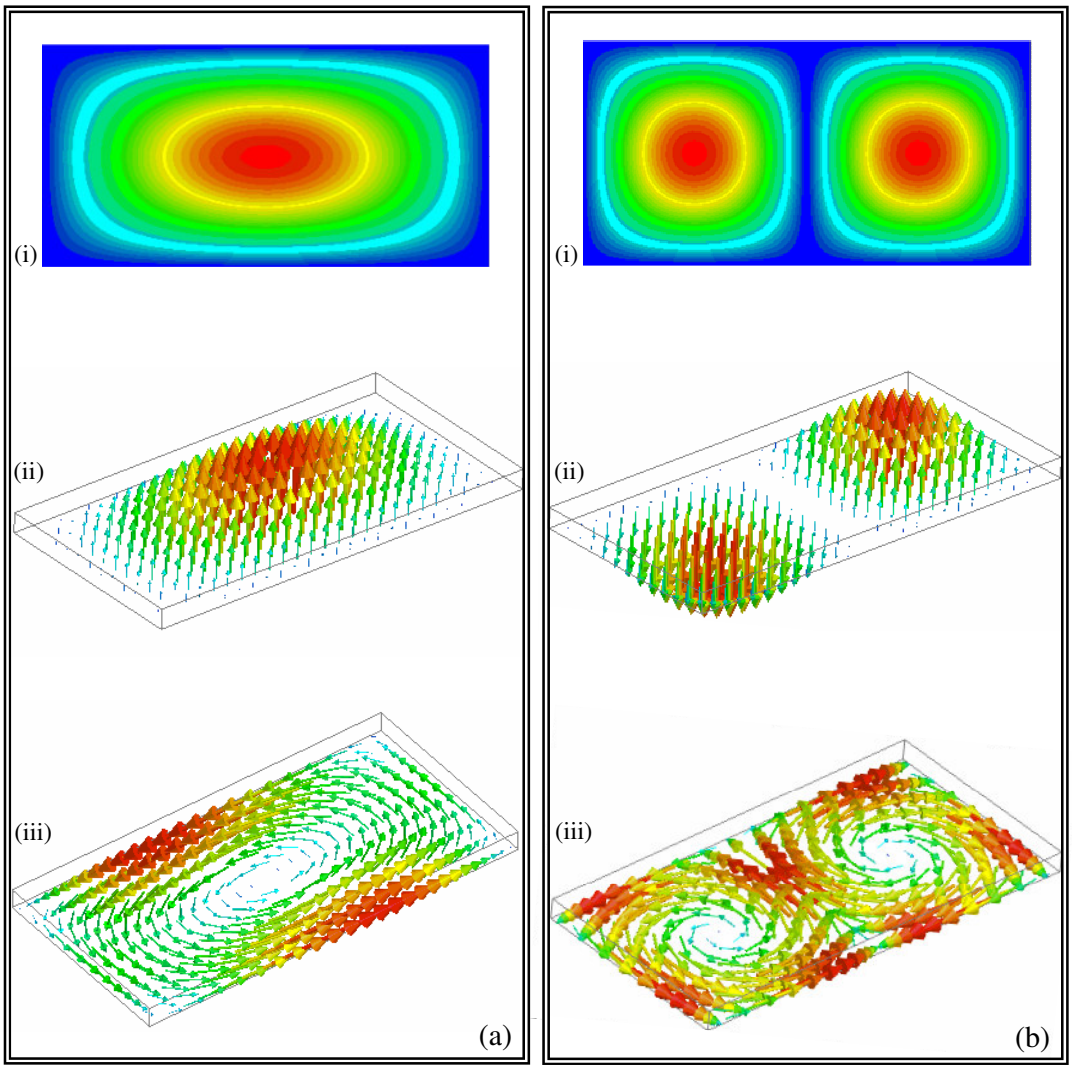

Figure 3.4.4 The field profiles corresponding to (a) the TM_{11} and (b) the TE_{21} waveguide modes supported by an air-filled rectangular metal waveguide. Each figure shows (i) the *E*-field magnitude, (ii) and (iii) the *E* and *H*-vector magnitudes, calculated at a phase corresponding to maximum field.

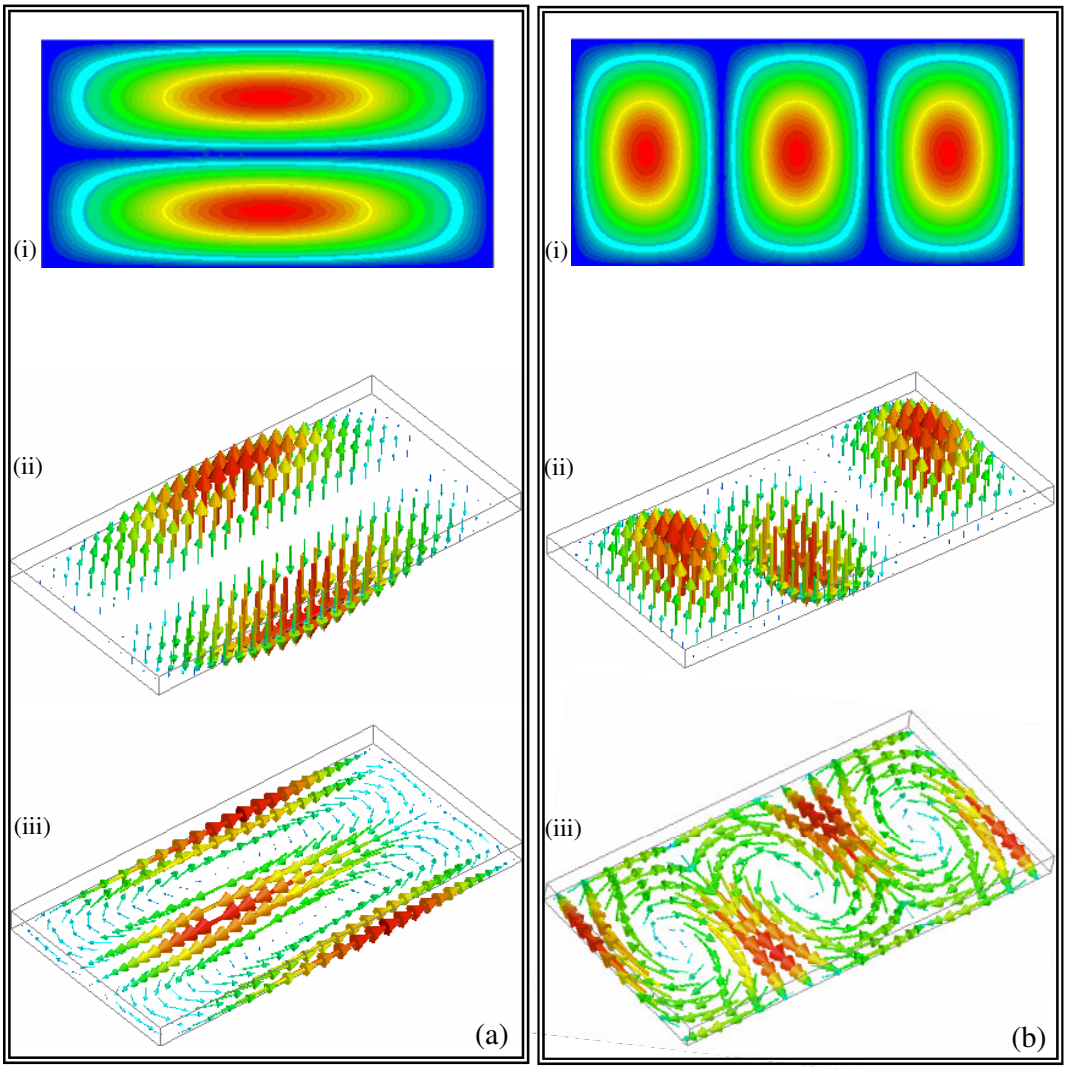

Figure 3.4.5 The field profiles corresponding to (a) the TM_{12} and (b) the TM_{31} modes supported by an air-filled rectangular metal waveguide. Each figure shows (i) the *E*-field magnitude, (ii) and (iii) the *E* and *H*-vector magnitudes, calculated at a phase corresponding to maximum field.

3.5 The circular waveguide

The circular waveguide supports both TE and TM guided modes, the transverse field components and cut-off frequencies of which may be found using a similar treatment as used in the rectangular case. As we will see, the circular guide does not support TEM modes due to the boundary condition that the tangential component of electric field must fall to zero at the waveguide wall. Consider the geometry shown in *Figure 3.5.1*. Since the waveguide geometry is now circularly symmetric, cylindrical co-ordinates will be used.

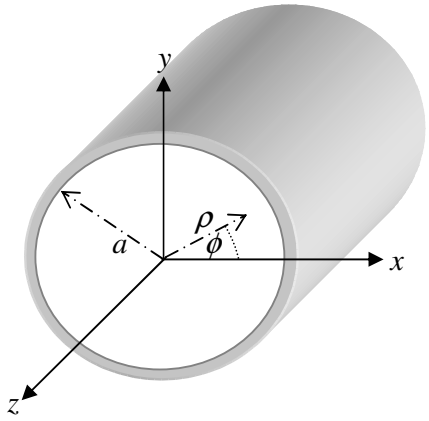

Figure 3.5.1 The geometry and co-ordinate system for the circular waveguide.

As in the rectangular case, the transverse field components of the TE and TM modes may be derived from the longitudinal components E_z and H_z expressed in cylindrical-polar co-ordinates.

$$E_\rho = \frac{-j}{k_c^2}\left(k_z \frac{\partial E_z}{\partial \rho} + \frac{\omega\mu}{\rho}\frac{\partial H_z}{\partial \phi}\right) \qquad \textit{Equation 3.5.1}$$

$$E_\phi = \frac{j}{k_c^2}\left(\frac{k_z}{\rho}\frac{\partial E_z}{\partial \phi} - \omega\mu\frac{\partial H_z}{\partial \rho}\right) \qquad \textit{Equation 3.5.2}$$

$$H_\rho = \frac{j}{k_c^2}\left(\frac{\omega\varepsilon}{\rho}\frac{\partial E_z}{\partial \phi} - k_z\frac{\partial H_z}{\partial \rho}\right) \qquad \textit{Equation 3.5.3}$$

$$H_\phi = \frac{-j}{k_c^2}\left(\omega\varepsilon\frac{\partial E_z}{\partial\rho} - \frac{k_z}{\rho}\frac{\partial H_z}{\partial\phi}\right) \qquad \textit{Equation 3.5.4}$$

3.5.1 TE modes

For TE modes $E_z = 0$ and H_z is a solution of the wave equation which may be expressed in cylindrical polar co-ordinates as;

$$\left(\frac{\partial^2}{\partial\rho^2} + \frac{1}{\rho}\frac{\partial}{\partial\rho} + \frac{1}{\rho^2}\frac{\partial^2}{\partial\phi^2} + k_c^2\right)H_z(\rho,\phi) = 0 \qquad \textit{Equation 3.5.5}$$

where $H_z(\rho,\phi) = H_z(\rho,\phi)e^{-jkz}$. Again, this equation may be solved using the separation of variables. Letting $H_z(\rho,\phi) = R(\rho)P(\phi)$, substituting into *3.5.6* and re-arranging we obtain:

$$\frac{\rho^2}{R}\frac{d^2R}{d\rho^2} + \frac{\rho}{R}\frac{dR}{d\rho} + \rho^2k_c^2 = \frac{-1}{P}\frac{d^2P}{d\phi^2} \qquad \textit{Equation 3.5.6}$$

Since the left hand side of the above equation depends only upon ρ, whilst the right hand side depends only upon ϕ, each side must be equal to a constant, which we will denote k_ϕ^2. Then,

$$\frac{d^2P}{d\phi^2} + k_\phi^2P = 0 \qquad \textit{Equation 3.5.7}$$

$$\rho^2\frac{d^2R}{d\rho^2} + \rho\frac{dR}{d\rho} + \left(\rho^2k_c^2 - k_\phi^2\right) = 0 \qquad \textit{Equation 3.5.8}$$

Note here that k_c has dimensions of $1/e$, however k_ϕ is dimensionless. The general solution to 3.5.7 is

$$P(\phi) = A\sin k_\phi\phi + B\cos k_\phi\phi \qquad \textit{Equation 3.5.9}$$

and since the solution to H_z must be periodic in ϕ, k_ϕ must be an integer n, thus:

$$P(\phi) = A\sin n\phi + B\cos n\phi \qquad \textit{Equation 3.5.10}$$

Substituting n for k_ϕ into equation *3.5.8* shows it to be a Bessel differential equation, with a solution of the form

$$R(\rho) = CJ_n(k_c\rho) + DY_n(k_c\rho) \qquad \textit{Equation 3.5.11}$$

where $J_n(x)$ and $Y_n(x)$ are the Bessel functions of the first and second kinds respectively and C is a constant. Since as $Y_n(k_c\rho)$ becomes infinite as $\rho \to 0$, this term is unacceptable for circular symmetry, and $D = 0$. Then the solution for H_z may be written as;

$$H_z(\rho,\phi) = \left(A\sin n\phi + B\cos n\phi\right)J_n(k_c\rho) \qquad \textit{Equation 3.5.12}$$

By applying the boundary condition that tangential E is zero at the waveguide wall, and since E_z is also zero for TE modes, we may write

$$E_\phi(\rho,\phi) = 0, \qquad \text{at } \rho = a \qquad \textit{Equation 3.5.13}$$

Then from *3.5.2* we find the transverse fields;

$$E_\rho(\rho,\phi,z) = \frac{-j\omega\mu n}{k_c^2\rho}\left(A\cos n\phi + B\sin n\phi\right)J_n(k_c\rho)e^{-jk_z} \qquad \textit{Equation 3.5.14}$$

$$E_\phi(\rho,\phi,z) = \frac{j\omega\mu}{k_c}\left(A\sin n\phi + B\cos n\phi\right)J_n'(k_c\rho)e^{-jk_z} \qquad \textit{Equation 3.5.15}$$

$$H_\rho(\rho,\phi,z) = \frac{-jk_z}{k_c}\left(A\sin n\phi + B\cos n\phi\right)J_n'(k_c\rho)e^{-jk_z} \qquad \textit{Equation 3.5.16}$$

$$H_\phi(\rho,\phi,z) = \frac{-jk_z n}{k_c^2}\left(A\cos n\phi + B\sin n\phi\right)J_n(k_c\rho)e^{-jk_z} \qquad \textit{Equation 3.5.17}$$

where $J_n'(k_c\rho)$ is the first derivative of J_n with respect to its argument. For E_ϕ to vanish at $\rho = a$, this derivative must equal zero. If the roots of this function are defined as p'_{mn} where p'_{mn} is the m^{th} root of $J_n'(k_c\rho)$, then k_c must take the value:

$$k_{c(m,n)} = \frac{p'_{nm}}{a} \qquad \textit{Equation 3.5.18}$$

the cut-off wave number for the TE_{mn} modes. Here, n refers to the number of circumferential nodes of the field and m the number of radial nodes. The propagation constant k_z for the TE_{mn} mode in a circular waveguide is given by

$$k_z = \sqrt{k_0^2 - k_c^2} = \sqrt{k^2 - \left(\frac{p'_{nm}}{a}\right)^2} \qquad \textit{Equation 3.5.19}$$

with a cut-off wavelength of

$$\lambda_{c(n,m)} = \frac{2\pi a}{p'_{nm}} \qquad \textit{Equation 3.5.20}$$

Hence the first mode to propagate (referred to as the dominant circular waveguide mode), is the one with the lowest numerical value of p'_{nm}, which from *Table 3.5.1* is shown to be the TE_{11} mode.

n	p'_{n1}	p'_{n2}	p'_{n3}
0	3.832	7.016	10.174
1	1.841	5.331	8.536
2	3.054	6.706	9.970

Table 3.5.1 Values of p'_{nm} for the TE modes of a circular waveguide

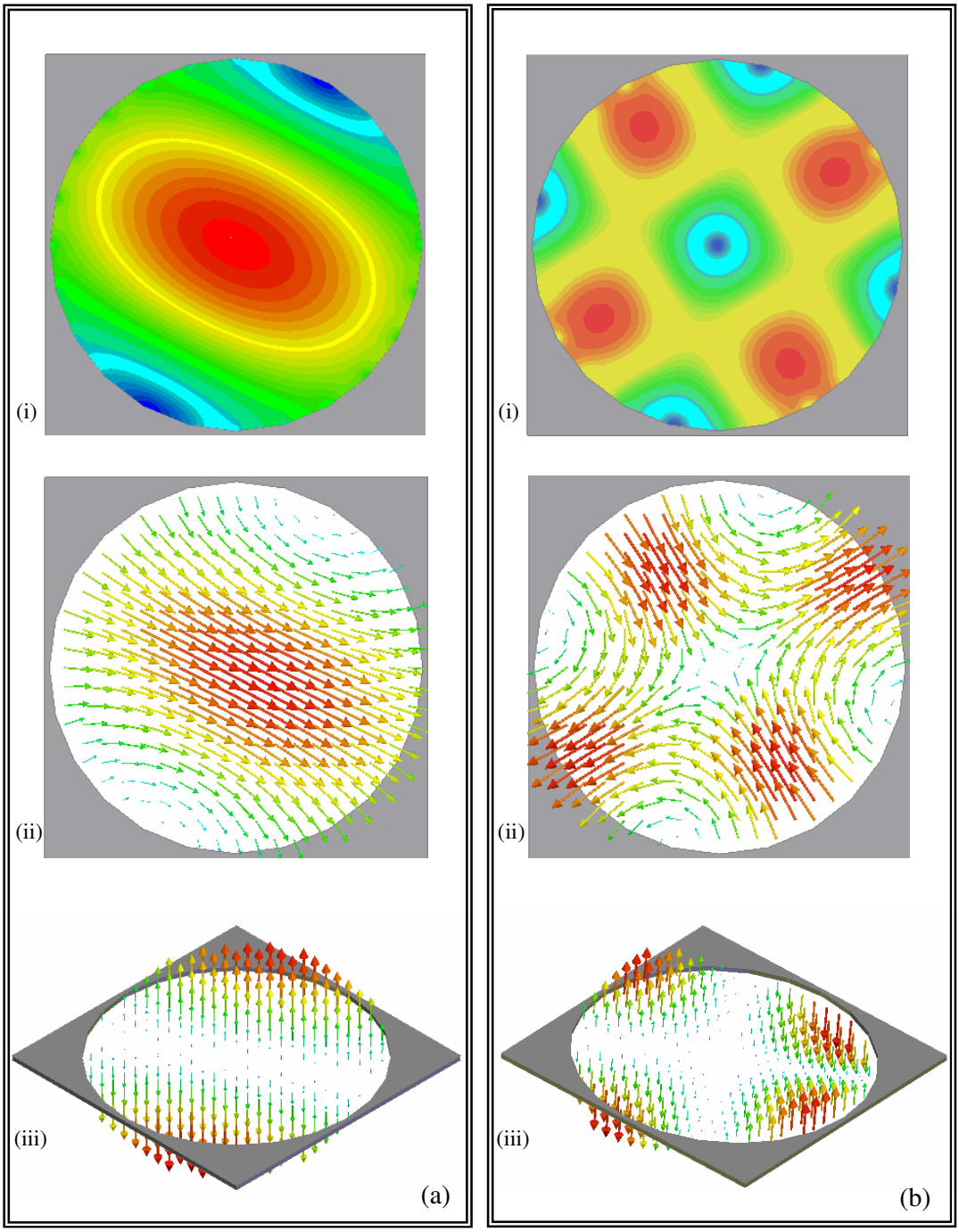

Figure 3.5.2 The modelled field profiles corresponding to (a) the TE_{11} and (b) the TE_{21} modes supported by a cylindrical air-filled perfectly conducting metal waveguide. Each figure shows (i) the *E*-field magnitude calculated over a surface plane parallel to the *xy*-plane of the waveguide, (ii) and (iii) the *E* and *H*-vector magnitudes, calculated at a phase corresponding to maximum field. The wave guide is modelled as uniform, and infinite in the *z*-direction.

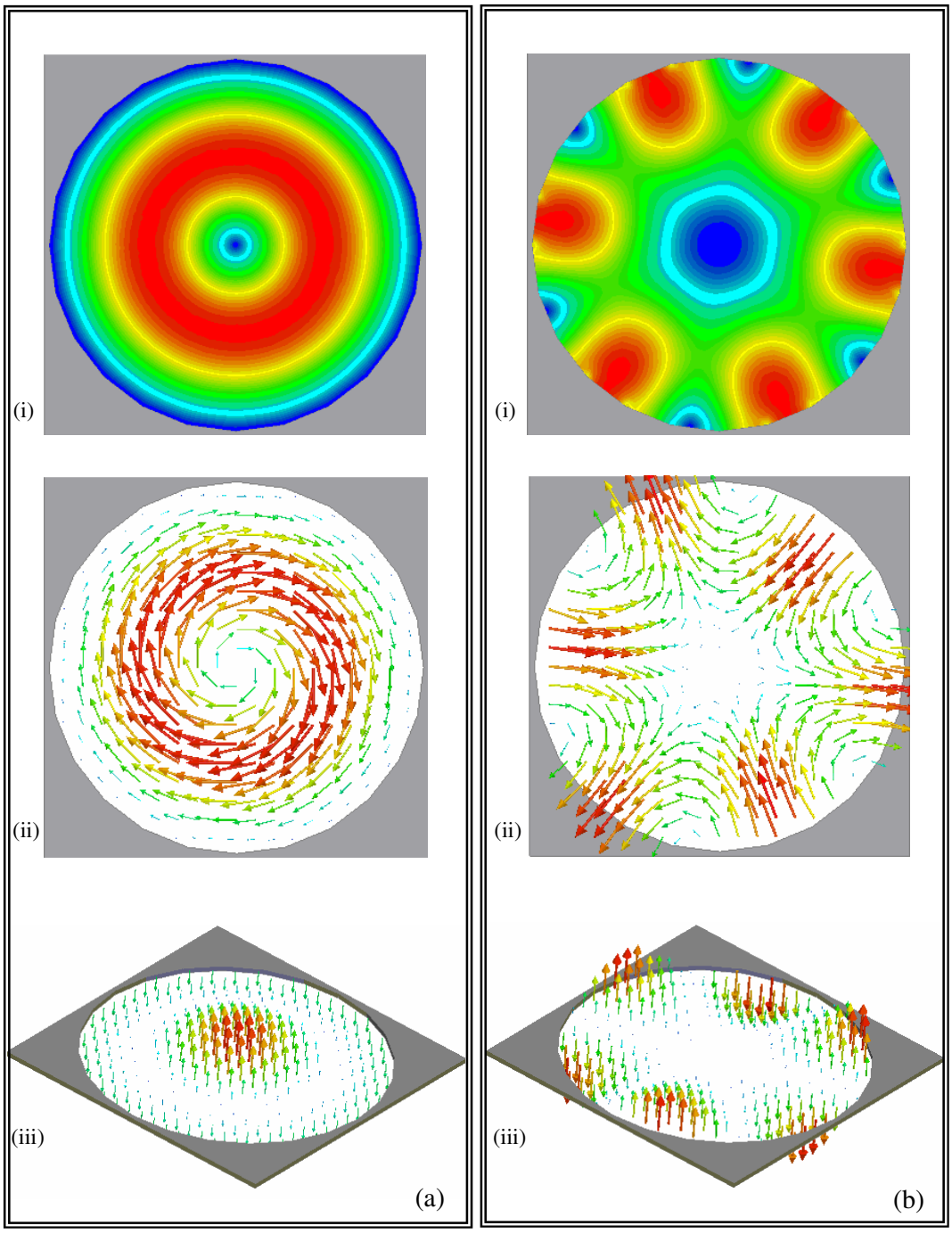

Figure 3.5.3 The modelled field profiles corresponding to (a) the TE_{01} and (b) the TE_{31} modes supported by the cylindrical waveguide. Each figure shows (i) the *E*-field magnitude calculated over a surface plane parallel to the *xy*-plane of the waveguide, (ii) and (iii) the *E* and *H*-vector magnitudes, calculated at a phase corresponding to maximum field.

3.5.2 TM modes

For the TM modes of the circular waveguide, the Helmholtz wave equation of *3.3.19* must be written in cylindrical polar co-ordinate form and solved in terms of E_z where $E_z(\rho,\phi,z) = E_z(\rho,\phi)e^{-jkz}$:

$$\left(\frac{\partial^2}{\partial\rho^2}+\frac{1}{\rho}\frac{\partial}{\partial\rho}+\frac{1}{\rho^2}\frac{\partial^2}{\partial\phi^2}+k_c^2\right)e_z = 0 \qquad \textit{Equation 3.5.21}$$

which has a general solution of the form:

$$e_z(\rho,\phi) = \left(A\sin n\phi + B\cos n\phi\right)J_n(k_c\rho) \qquad \textit{Equation 3.5.22}$$

For the TM solutions, since

$$E_z(\rho,\phi) = 0, \qquad \text{at } \rho = a \qquad \textit{Equation 3.5.23}$$

the boundary conditions may be directly applied to E_z, thus

$$J_n(k_c a) = 0 \qquad \textit{Equation 3.5.24}$$

and

$$k_{c(n,m)} = \frac{p_{nm}}{a} \qquad \textit{Equation 3.5.25}$$

where p_{nm} is the m^{th} root of the Bessel function, that is $J_n(p_{nm}) = 0$. The first few values of p_{nm} are listed in *Table 3.5.2.*

n	p_{n1}	p_{n2}	p_{n3}
0	2.405	5.520	8.654
1	3.832	7.016	10.174
2	5.135	8.417	11.620

Table 3.5.2 Values of p'_{nm} for the TM modes of a circular waveguide

The propagation constant of the TM$_{mn}$ mode is

$$k_z = \sqrt{k_0^2 - k_c^2} = \sqrt{k_0^2 - \left(\frac{p_{mn}}{a}\right)^2} \qquad \textit{Equation 3.5.26}$$

and the cut-off wavelength is

$$\lambda_{c(n,m)} = \frac{2\pi a}{p_{mn}} \qquad \textit{Equation 3.5.27}$$

From *Table 3.5.2* and equation *3.5.27*, the first TM mode to propagate is the TM$_{01}$, with $p_{01} = 2.405$. As with the TE modes, $m \geq 1$, so there is no TE$_{10}$ or TM$_{10}$ supported, but there are TE$_{01}$ and TM$_{01}$ modes.

From *3.5.1* through *4*, the transverse fields of the TM modes may be derived as:

$$E_\rho(\rho,\phi,z) = \frac{-jk_z}{k_c}\left(A\sin n\phi + B\cos n\phi\right)J'_n(k_c\rho)e^{-jk_z} \qquad \textit{Equation 3.5.28}$$

$$E_\phi(\rho,\phi,z) = \frac{-jk_z n}{k_c^2\rho}\left(A\cos n\phi - B\sin n\phi\right)J_n(k_c\rho)e^{-jk_z} \qquad \textit{Equation 3.5.29}$$

$$H_\rho(\rho,\phi,z) = \frac{-j\omega\varepsilon n}{k_c^2\rho}\left(A\cos n\phi - B\sin n\phi\right)J_n(k_c\rho)e^{-jk_z} \qquad \textit{Equation 3.5.30}$$

$$H_{\phi}(\rho,\phi,z)=\frac{-j\omega\varepsilon}{k_c}\left(A\sin n\phi+B\cos n\phi\right)J_n'(k_c\rho)e^{-jk_z z} \qquad \textit{Equation 3.5.29}$$

Once again, the field configurations of the first four TM modes are shown in *Figures 3.5.4* and *3.5.5*, derived from a perfectly conducting circular waveguide using the finite element code.

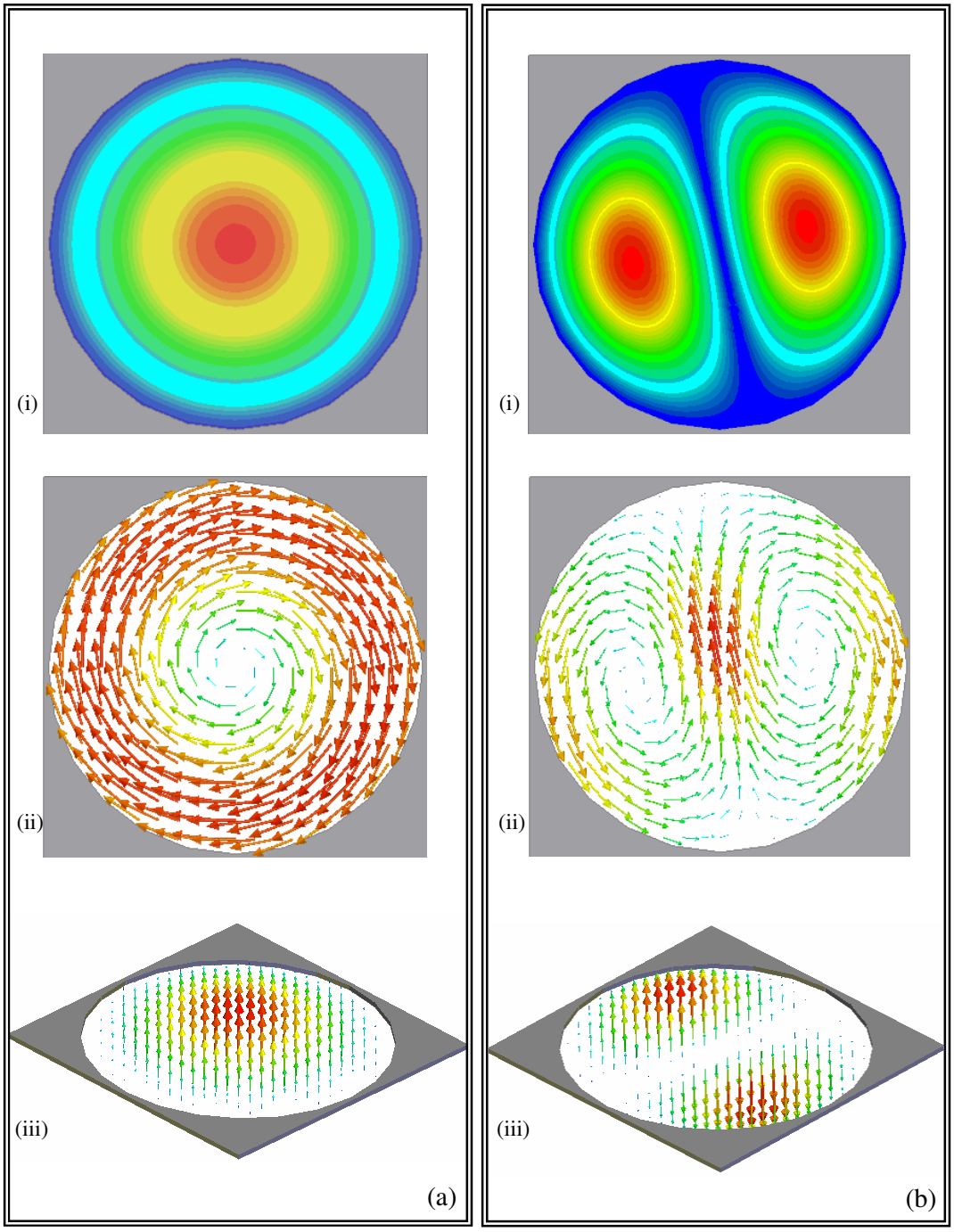

Figure 3.5.4 The modelled field profiles corresponding to (a) the TM_{01} and (b) the TM_{11} modes supported by the cylindrical waveguide. Each figure shows (i) the *E*-field magnitude calculated over a surface plane parallel to the *xy*-plane of the waveguide, (ii) and (iii) the *E* and *H*-vector magnitudes, calculated at a phase corresponding to maximum field.

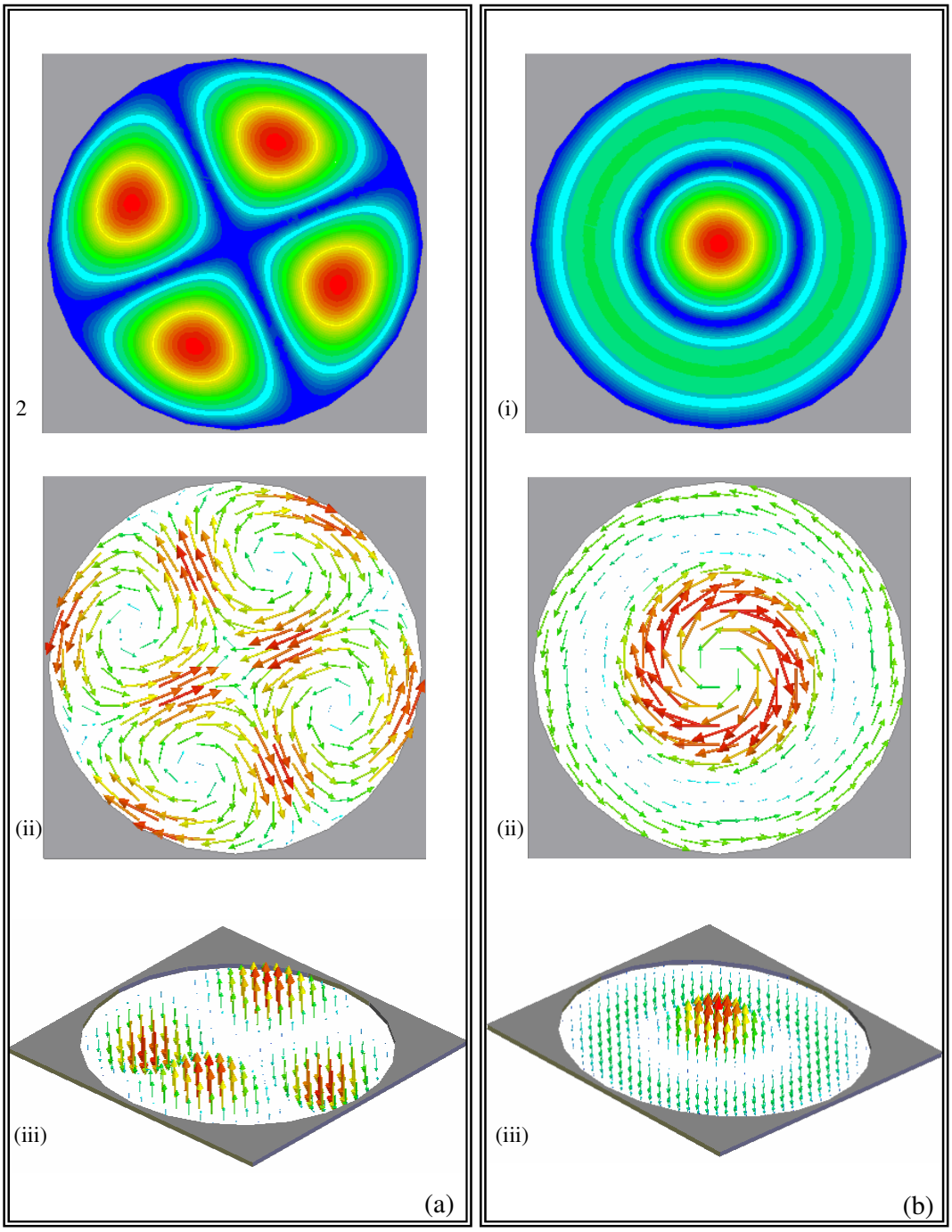

Figure 3.5.5 The modelled field profiles corresponding to (a) the TM_{21} and (b) the TM_{02} modes supported by the cylindrical waveguide. Each figure shows (i) the *E*-field magnitude calculated over a surface plane parallel to the *xy*-plane of the waveguide, (ii) and (iii) the *E* and *H*-vector magnitudes, calculated at a phase corresponding to maximum field.

3.6 The coaxial transmission line

The coaxial waveguide differs from the previous two geometries considered in this chapter as it does not possess a simply connected cross section but rather one that is multiply connected, by virtue of the two separate conducting surfaces as shown in *Figure 3.6.1.* Normally, coaxial waveguides are used to guide only the TEM mode, since the guide distorts complex wave forms. However, in *Chapter 8* we will discuss waveguide mediated transmission via a sample resembling a terminated transmission line, and it is therefore necessary to consider higher order modes in this section.

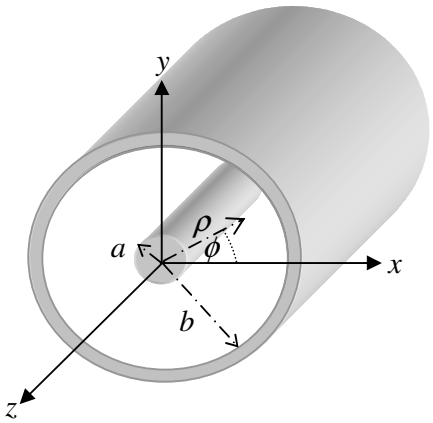

Figure 3.6.1 The geometry and co-ordinate system for the coaxial waveguide.

3.6.1 TEM modes

Consider the geometry shown in *Figure 3.6.1*, with the inner conducting cylinder of radius a set at a potential of V_0 volts, and the outer conductive cylinder of radius b set to zero volts. The potential of the inner conductor with respect to the outer conductor is commonly referred to as the *line voltage*. From our treatment of the general TEM waveguide solution [*section 3.3.3*], we already know that the fields are derivable from a scalar potential function $\Phi(\rho,\phi)$ which is a solution to Laplace's equation. For the transmission line geometry it is once again sensible to use cylindrical polar co-ordinates, and as such Laplace's equation takes the form:

$$\frac{1}{\rho}\frac{\partial}{\partial\rho}\left(\rho\frac{\partial\Phi(\rho,\phi)}{\partial\rho}\right)+\frac{1}{\rho^2}\frac{\partial^2\Phi(\rho,\phi)}{\partial\phi^2}=0 \qquad \textit{Equation 3.6.1}$$

Equation 3.6.1 must be solved for $\Phi(\rho,\phi)$ subject to the boundary condition that at ρ = *a,* $\Phi(\rho,\phi) = V_0$, and at ρ = *b,* $\Phi(\rho,\phi) = 0$. Once again, the method of separation of variables must be employed, letting $\Phi(\rho,\phi)$ be expressed in product form as:

$$\Phi(\rho,\phi) = R(\rho)\, P(\phi) \qquad \textit{Equation 3.6.2}$$

Substituting *3.6.2* into *3.6.1* we obtain

$$\frac{\rho}{R}\frac{\partial}{\partial\rho}\left(\rho\frac{dR}{d\rho}\right)+\frac{1}{\rho^2}\frac{d^2P}{d\phi^2}=0 \qquad \textit{Equation 3.6.3}$$

Since each term in the above equation must be equal to a constant,

$$\frac{\rho}{R}\frac{\partial}{\partial\rho}\left(\rho\frac{dR}{d\rho}\right)=-k_\rho^2 \qquad \textit{Equation 3.6.4}$$

$$\frac{1}{\rho^2}\frac{d^2P}{d\phi^2}=-k_\phi^2 \qquad \textit{Equation 3.6.5}$$

where $k_\rho^2 + k_\phi^2 = 0$.

The general solution to *3.6.5* is given by

$$P(\phi) = A\cos k_\phi\phi + B\sin k_\phi\phi \qquad \textit{Equation 3.6.6}$$

and since ϕ must be cyclic, k_ϕ = *n* must be an integer. Further, since the boundary conditions do not change withϕ, neither should $\Phi(\rho,\phi)$, thus *n* = 0. As $k_\rho^2 + k_\phi^2 = 0$, this implies k_ρ is also zero and equation *3.6.4* reduces to

$$\frac{\partial}{\partial\rho}\left(\rho\frac{dR}{d\rho}\right)=0 \qquad \textit{Equation 3.6.7}$$

the solution to which is given by:

$$R(\rho) = C \ln \rho + D = \Phi(\rho, \phi) \qquad \textit{Equation 3.6.8}$$

Applying the boundary conditions that at $\rho = a$, $\Phi(\rho,\phi) = V_0$, and at $\rho = b$, $\Phi(\rho,\phi) = 0$, to the above equations gives two expressions for the constants C and D

$$\Phi(\rho, \phi) = V_0 = C \ln a + D \qquad \textit{Equation 3.6.9}$$

$$\Phi(\rho, \phi) = 0 = C \ln b + D \qquad \textit{Equation 3.6.10}$$

which may be solved simultaneously to yield the final expression for $\Phi(\rho,\phi)$:

$$\Phi(\rho, \phi) = \frac{V_0 \ln b/\rho}{\ln b/a} \qquad \textit{Equation 3.6.11}$$

Since $\nabla_t \Phi(\rho,\phi) = E(\rho,\phi)$, where $E(\rho,\phi,z) = E(\rho,\phi)\, e^{-jk_z}$, the electric field of the propagating TEM mode may be expressed generally as

$$E(\rho, \phi) = \frac{V_0 \hat{\rho}}{\rho \ln b/a} \qquad \textit{Equation 3.6.12}$$

The wave impedance of a TEM mode (Z_{TEM}) (not to be confused with the characteristic impedance of a transmission line Z_0) is given by the ratio of the transverse electric and magnetic fields. Since there are two locally orthogonal pairs of transverse field components,

$$Z_{TEM} = \frac{E_\rho}{H_\phi} = \frac{\omega\mu}{k_z} \qquad \textit{Equation 3.6.12}$$

and

$$Z_{TEM} = \frac{-E_\phi}{H_\rho} = \frac{\omega\mu}{k_z} \qquad \textit{Equation 3.6.13}$$

Combining these two equations yield a general result for the transverse magnetic fields:

$$H(\rho,\phi) = \frac{k_z}{\omega\mu}\hat{z}\times e(\rho,\phi) \qquad \textit{Equation 3.6.14}$$

3.6.2 Higher order transmission line modes.

In addition to the fundamental TEM mode that propagates without cut-off, the coaxial line also supports higher order TE and TM modes. The TE_{11} is the next dominant mode and it will be shown later in this section that the TE_{11} and fundamental TM mode are separated by such a large increment in frequency, we need only be concerned with the TE mode solutions in this thesis.

For TE modes, $E_z = 0$ and H_z satisfies the wave equation

$$\left(\frac{\partial^2}{\partial\rho^2} + \frac{1}{\rho}\frac{\partial}{\partial\rho} + \frac{1}{\rho^2}\frac{\partial^2}{\partial\phi^2} + k_c^2\right)H_z(\rho,\phi) = 0 \qquad \textit{Equation 3.6.15}$$

where $H_z(\rho,\phi,z) = H_z(\rho,\phi)\,e^{-jk_z z}$ and $k_c^2 = k_0^2 - k_z^2$. The general solution to this equation as derived in section 3.5 is given by

$$h_z(\rho,\phi) = \left(A\sin n\phi + B\cos n\phi\right)\left(CJ_n(k_c\rho) + DY_n(k_c\rho)\right) \qquad \textit{Equation 3.6.16}$$

except that in the case of the coaxial geometry, $a \le \rho \le b$, so we can not justify discarding the Y_n term. The boundary conditions are such that $E_\phi = 0$ for $\rho = a,\ b$. Using equation *3.5.2* to find E_ϕ from the above equation yields:

$$E_\phi = \frac{j\omega\mu}{k_c}(A\sin n\phi + B\cos n\phi)(CJ_n'(k_c\rho) + DY_n'(k_c\rho))e^{-jk_z z} \qquad \textit{Equation 3.6.17}$$

Applying the boundary condition gives two equations:

$$CJ_n'(k_c a) + DY_n'(k_c a) = 0 \qquad \textit{Equation 3.6.18}$$

$$CJ_n'(k_c b) + DY_n'(k_c b) = 0 \qquad \textit{Equation 3.6.19}$$

and since this is a homogeneous set of equations, the only solutions other than $C = D = 0$ occurs when the determinant is zero. Thus

$$J_n'(k_c a) + Y_n'(k_c b) = J_n'(k_c b) + Y_n'(k_c a) \qquad \textit{Equation 3.6.20}$$

This is an eigen-value equation for the cut-off wave vector, with the values of k_c that satisfy *3.6.20* defining the TE_{nm} modes, and it must be solved numerically. A good approximation to the cut-off wavelength (λ_c) for the TE_{11} mode in this geometry is simply the average circumference $\lambda_c = 2\pi(a+b)/2$. This simple approximation is valid even as *a* tends to zero, and the coaxial pair approximates to a cylindrical wave guide. Recall here that the expression for λ_c of the dominant TE_{11} mode in a cylindrical wave guide (*derived from the first derivitive of the Bessel function of the first kind*) yields $\lambda_c = 2\pi b/1.841$. Solutions for the TM modes may be found in a similar manner, since equation *3.6.20* is the same for both TE and TM modes, except for the derivatives. *Figure 3.6.2* (a) and (b) show the first two modes supported by the coaxial geometry in order of cut-off frequency, the TE_{11} and TE_{21} modes. Fields are produced using the eigen-mode solution of the finite element code which will be discussed in the next chapter, and show the electric field strength at a phase corresponding to maximum field (red corresponds to a field magnitude of 1, blue to a field magnitude of 0). Also shown is the corresponding magnetic and electric field vector magnitudes. All field profiles are calculated over a plane parallel to the *xy*-plane, and the geometry is considered as infinite and uniform in the *z*-direction (although only a thin slice is shown here). Since the finite element code (when run as an eigen-problem) locks on to the cut-off frequency of a mode for a particular geometry, it is not possible to show the TEM mode in the same format. Further, *Figure 3.6.3* (a) and (b) show the field profiles corresponding to the first two TM modes. Note here the periodicity in ρ. Since the magnetic vector needs to change direction over a relatively small distance equal to the separation between the two conductive cylinders, the first propagating TM mode has a much higher cut-off frequency than the dominant TE mode (this modelling has shown that for coaxial geometry with a = 0.5mm, b = 1mm, the cut-off frequency for the TE_{11} is 64 GHz whereas the cut-off frequency for the TM_{01} is 299 GHz). This argument is also true for the TE_{nm} where $m > 1$.

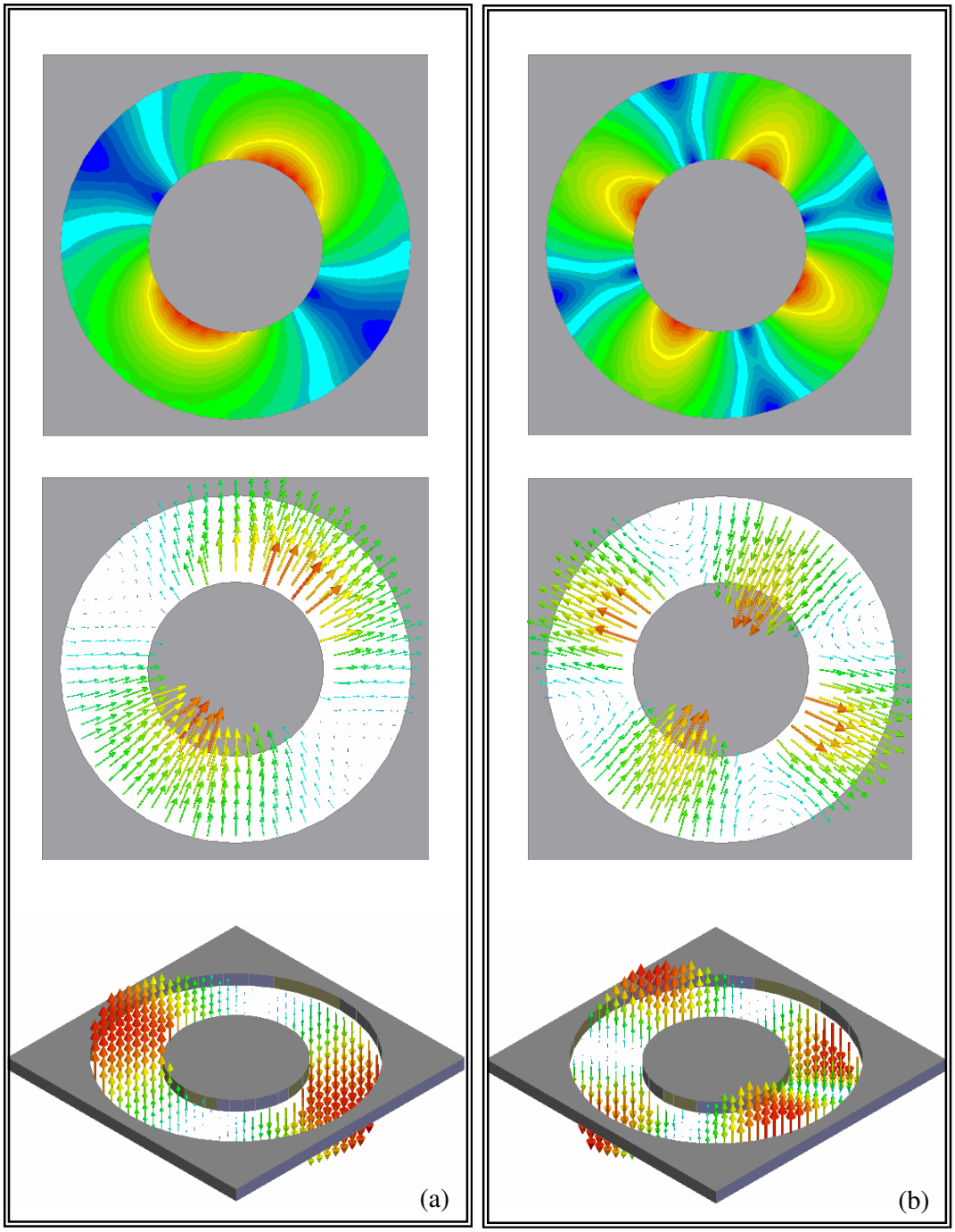

Figure 3.6.2 The modelled field profiles corresponding to (a) the TE_{11} and (b) the TE_{21} modes supported by a coaxial waveguide. Each figure shows (i) the *E*-field magnitude calculated over a surface plane parallel to the *xy*-plane of the waveguide, (ii) and (iii) the *E* and *H*-vector magnitudes.

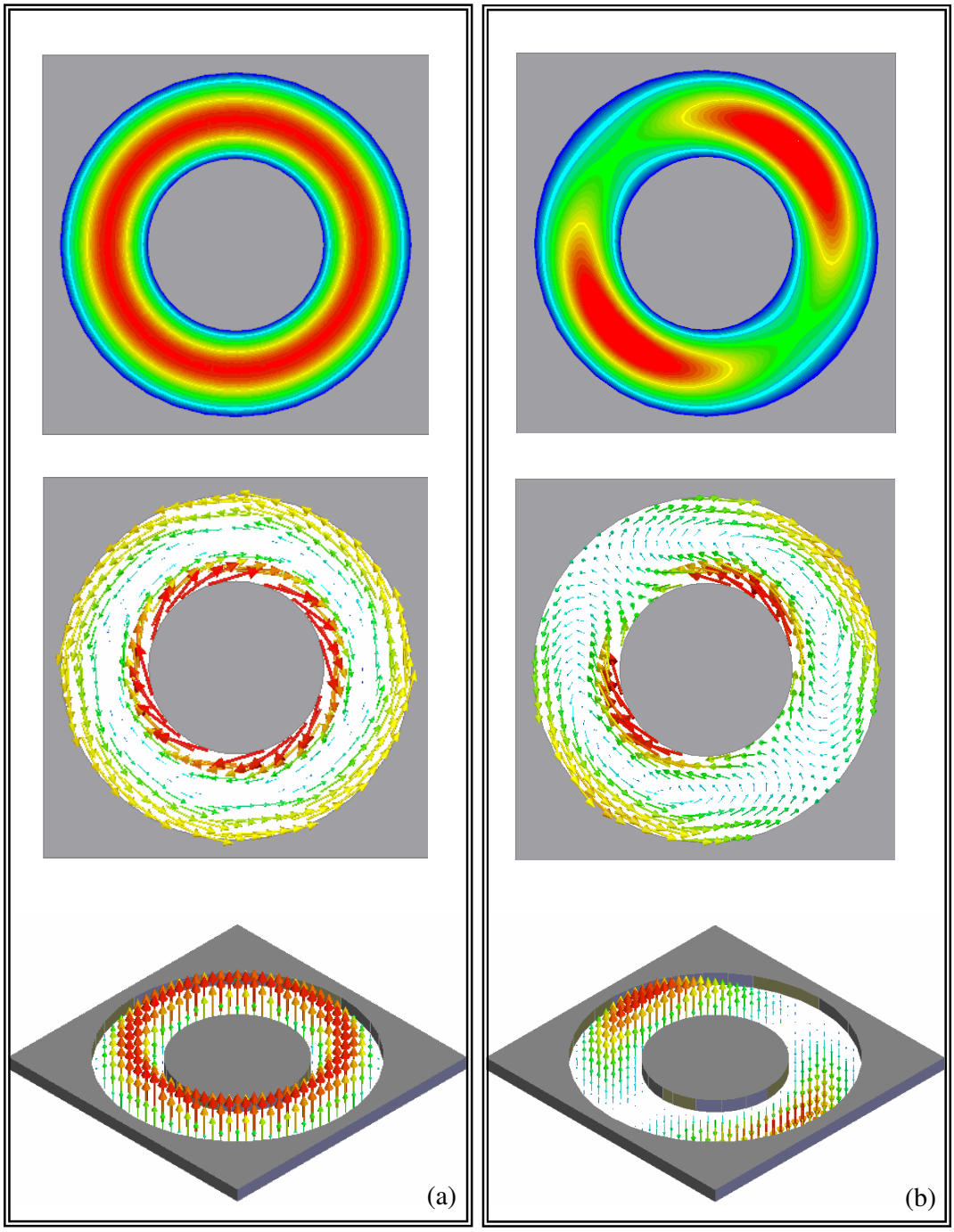

Figure 3.6.3 The modelled field profiles corresponding to (a) the TM_{01} and (b) the TM_{11} modes supported by a cylindrical air-filled perfectly conducting metal waveguide. Each figure shows (i) the *E*-field magnitude, (ii) and (iii) the *E* and *H*-vector magnitudes, calculated at a phase corresponding to maximum field. The wave guide is modelled as uniform, and infinite in the *z*-direction.

3.7 Summary

In this chapter we have outlined the boundary conditions for a smooth, perfectly conducting wall so that we can approximate to perfectly conducting metal clad waveguides (a valid approximation at microwave frequencies). The general solutions for the three types of wave considered in this chapter were then derived. The specific geometries pertaining to the rectangular, cylindrical and coaxial waveguide were then discussed, deriving the transverse field components from the axial field components, and an expression for the cut-off frequency of the modes for each geometric case.

Chapter 4
Modelling

4.1 Introduction

Throughout the experimental chapters of this thesis, Ansoft's High Frequency Structure Simulator (HFSS) version 8.5 is used exclusively to predict the theoretical electromagnetic response of the various structures studied. This EM field simulator utilises the finite element method (FEM), and was predominantly designed to model complex industrial systems such as waveguide connectors and waveguide unions, PCB modelling, and other three dimensional structures where radiation may be 'injected' into the system using a port, or alternatively the eigen-modes of the system may be calculated. However, the microwave section of the Thin Films Photonic Group at Exeter have worked closely with Ansoft's developers to utilise the flexibility of this finite element code and apply it to incident wave problems with complex surface structures such as those presented in this thesis. We are one of the few groups worldwide who employs HFSS in this manner.

It is the purpose of this chapter to provide a brief overview of Ansoft's HFSS. Initially, a brief description of the finite element method is presented, highlighting that increasing the resolution of the mesh constructed to provide a full wave solution to a particular problem decreases the processing speed, and increases computational memory requirements. The various processes that must be undertaken in order to construct a full wave EM model are then described. Within this section the integral CAD package and the use of symmetry to reduce the computational size of the model is discussed, as is the method by which HFSS calculates the response of frequency dependent materials. The surface approximation used to negate the need to solve Maxwell's equations inside a metallic object is outlined, and both eigen-mode and incident wave solutions are described, with emphasis on the incident wave solution. The various terminating and electromagnetic symmetry boundaries are then detailed, before attention is focused on the finite element mesh, which divides up the entire problem space into a large number of tetrahedra, within which Maxwell's equations are solved numerically. The post

processing package is then outlined, as a prelude to a detailed description of each individual model used to predict the theoretical electromagnetic response of the samples presented in *Chapters 5* through *8*.

4.2 The finite element method.

HFSS employ's the finite element method, dividing the geometric model into a high number of smaller sub regions (*elements*), collectively known as the mesh, representing the field in each element with a local function. For HFSS, elements take the form of tetrahedra, within which the value of a vector field quantity such as the *E* or *H*-field is stored. The components of a field tangential to the edges of an element are explicitly stored at the vertices, whilst tangential field components at the face of an element are explicitly stored at the edges. The field within the element may then be calculated from these nodal values. The system transforms Maxwell's equations into matrix equations and solves numerically. Since the accuracy of the field solution is dependent upon the resolution of the mesh, each element must occupy a region of space that is small enough for the field to be adequately interpolated from the nodal values. However, generating the field solution involves inverting a matrix with as many elements as there are tetrahedra nodes, requiring a significant amount of processing power, time, and computational memory. It is therefore important to generate a mesh which is fine enough to provide an accurate field solution but not too large that it is impossible to solve. HFSS addresses this issue by using an adaptive pass process [*section 4.3.4*] to refine the mesh in regions of high field gradient, and geometric symmetry boundaries [*section 4.3.3*] to reduce the initial size of the problem.

4.3 HFSS overview

4.3.1 Representing the experimental sample.

HFSS uses an integral three dimensional CAD package which enables the user to recreate the experimental sample to scale. Simplistic 1-D, 2-D, and 3-D objects may be drawn using the appropriate drawing commands, whilst more complex 3-D objects may

be constructed by the manipulation of a 2-D object along a plane, or by sweeping about an axis or along a vector path. Further, a high level of complexity may be introduced to the model through the addition or subtraction of two or more objects to 'build up' a larger structure. The modeller automatically records the sequence of drawing commands as a macro which may be accessed at any time, allowing the properties of individual objects such as size, position and shape to be altered. Once recorded by the drawing macro, each parameter may be assigned as a variable simply by replacing a numerical parameter stored in the drawing macro with a variable name. Each variable may then be assigned a value, or made a dependent of other parameters or user defined expressions, allowing the geometry of the model to be altered automatically whilst the simulation is in progress.

4.3.2 Assigning materials.

Once constructed, the geometric model may be assigned material properties using the material manager. HFSS possesses a materials database containing a range of materials, to which new materials may be added. In addition to ordinary dielectrics and metals, materials within HFSS may be defined as perfectly conducting, anisotropic or ferrite, and characterised by the following properties:

- Relative permeability ($\mu_r + \mu_i$)
- Relative permittivity ($\varepsilon_r + \varepsilon_i$)
- Bulk conductivity ($(j\omega\varepsilon + \sigma)E$)
- Electric loss tangent ($\varepsilon_i / \varepsilon_r$)
- Magnetic loss tangent (μ_i / μ_r)

Numerical values for the above quantities may be used directly; however HFSS also allows each property to be defined as a user specified function. In addition, if the material property is frequency dependent, a small number of values over the desired frequency range may be defined, from which HFSS automatically interpolates values corresponding to the specific value of each solution frequency throughout the solving process using either a linear or polynomial fitting procedure.

For a perfectly conducting medium HFSS solves at the surface only, since fields are excluded from within the medium. For real metals with finite conductivity, HFSS assigns a finite conductivity boundary for which the following condition holds:

$$E_t = Z_s(\hat{n} \times H_t) \qquad \textit{Equation 4.3.1}$$

E_t and H_t are the components of the fields tangential to the surface, and Z_s is the surface impedance, which for a good conductor is given by;

$$Z_s = \frac{E_t}{H_t} = (1+j)\left(\frac{\omega\mu}{2\sigma}\right)^{1/2} \qquad \textit{Equation 4.3.2}$$

where σ is the conductivity, μ the permeability, and ω is the solution frequency, or frequency of the incident wave. The fact that the *E*-field has a tangential component at the surface of an imperfect conductor simulates a lossy surface. It is important to re-emphasise here that HFSS does not solve fields within such a material but instead approximates the behaviour of the fields at the surface of the object using the above condition, an approximation which is only valid if the thickness of the material is much larger than the skin depth in the specified frequency range.

4.3.3 Assigning boundary conditions and defining sources.

The 3-D boundary manager not only allows the terminating boundaries of the model to be defined, but in addition allows the user to specify the properties of the incident wave when solving a driven solution. A driven solution in HFSS is a model for which radiation is incident upon the sample, either simulated in the incident medium, or injected through a port, such as a waveguide. When simulated in the incident medium, incident radiation may take the form of a plane, Gaussian, or spherical wave. Throughout the experimental chapters of this thesis, incident plane wave radiation is used, for which the incident angle and electric vector orientation must be specified using either Cartesian or spherical polar co-ordinates.

Outermost faces of the model must be assigned as a boundary, and there are several different types one can choose depending on the type of problem being solved. For example, perfect E boundaries represent the surface of perfect conductors and as such, the final solution must satisfy the condition that tangential E falls to zero at the boundary. Perfect/natural H boundaries force the tangential component of H to be identical on each side of the boundary. For internal surfaces this results in a natural boundary through which the field propagates. Impedance boundaries are used to model resistive surfaces for which both the reactance and resistance must be stipulated, whilst radiation boundaries are used to represent open problems that allow waves to radiate infinitely far into space, by first absorbing scattered radiation and then ballooning it outward.

As the level of computational power required to solve a particular geometric problem is directly related to the size of the problem space, it is important to make good use of symmetry. The boundary editor allows the user to insert electromagnetic symmetry planes, thereby modelling only part of a problem, shortening the solution time and reducing the volume of the model. For example, if modelling the electromagnetic response of a rectangular waveguide, appropriate use of symmetry planes enables the user to reproduce a full electromagnetic solution when modelling only half, or one quarter of the symmetric system. Consider the rectangular waveguide shown in *Figure 4.3.1*, at a frequency corresponding to the propagation of the TE_{10} mode, with the red arrows representing the electric vector orientation.

The rectangular waveguide has two electromagnetic symmetry planes. One vertically and one horizontally through the centre of the guide. The vertical one is a perfect H-symmetry plane since the E-field is entirely tangential whilst the H-field has a normal component to the plane. The horizontal one is a perfect-E symmetry plane since the H-field is entirely tangential to the plane. It is important to note here however that these are boundary conditions, which are referred to as symmetry planes because they may be inserted at a plane of electromagnetic symmetry, not because they either mirror or translate the adjacent field. For certain solutions of a particular structure the orientation of the E or H-vector may change. In this case, a previously designated perfect E symmetry plane may need to be reassigned as a perfect H symmetry plane.

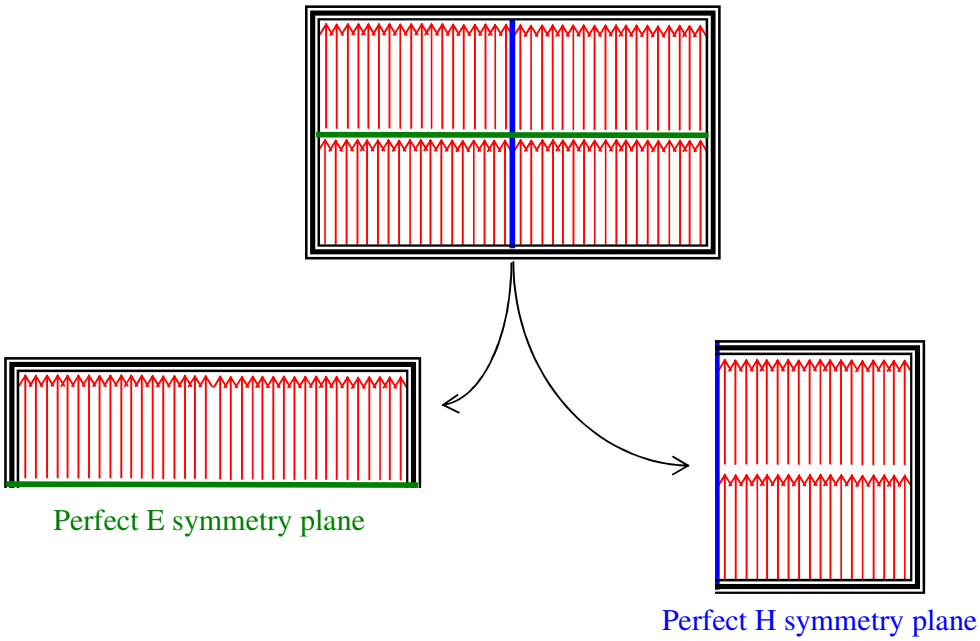

Figure 4.3.1 A cross section of a rectangular waveguide supporting a TE_{01} mode, illustrating the planes of electromagnetic symmetry.

Further, master-slave boundaries, are designed to allow infinite periodic structures or arrays to be represented as a unit cell, as shown in *Figure 4.3.2.* The field on one outer boundary (the slave) is forced to match that on an opposite boundary (the master) with a specified phase relationship between the two boundaries. Unlike perfect E or H symmetry planes, the electric or magnetic vector does not need to be either entirely tangential or normal to the symmetry plane, but the fields must have the same magnitude and direction (or opposite direction).

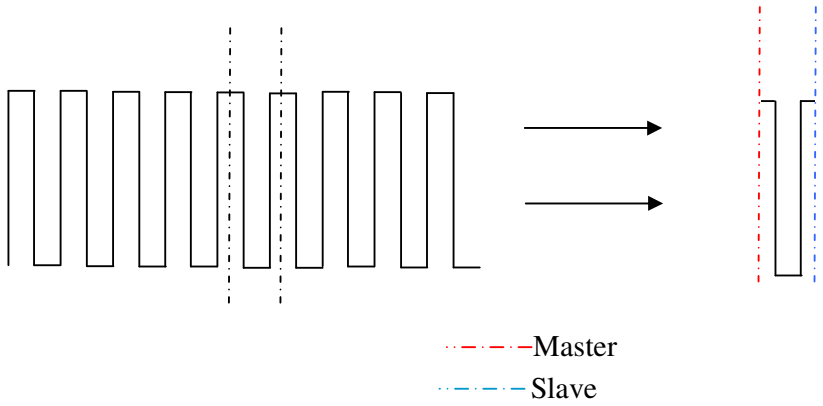

Figure 4.3.2. Master-slave boundaries are designed to allow infinite periodic structures or arrays to be represented as a unit cell, by forcing the fields at the slave boundary to be identical to that at the master.

4.3.4 Mesh construction.

Once boundaries and materials have been specified for a particular model, the initial solution may be obtained using a crude mesh. This initial mesh, which generally contains approximately 6000 tetrahedra, forms the basis of subsequent and more refined meshes, with the final solution containing between 20,000 and 100,000 elements. The initial mesh is based upon the incident wavelength and once constructed, may be refined in a number of ways. Using the adaptive pass process, the fields that exist within or around the structure at the solution frequency are calculated using the initial mesh. HFSS then uses that finite element solution to estimate the regions of problem space that contain large errors (usually corresponding to regions containing large field gradients). A second mesh is then generated, with the number of tetrahedra increased in those regions. This iterative process continues, until the code converges on a stable solution, and can be repeated for each solution frequency.

If required, the final mesh may be further refined using the manual mesh option. Individual objects that constitute the model may be selected, and the mesh refined either at the surface, or within the volume of the object, by specifying either the maximum number of elements, or by specifying the maximum size of individual elements. In addition, tetrahedra may be refined in this way within any user defined volume that exists within the problem space. The manual mesh option is useful when geometric surfaces or volumes within the model are much smaller than the incident wavelength, to ensure an adequate element density. The manual mesh process may also be used to *over*-mesh a model, which can be particularly useful when performing a frequency sweep solution. Over a given frequency range, the electromagnetic field solution will change. Regions of high field may reduce, and low field regions may increase. A mesh with a high density of tetrahedra throughout the whole region of problem space is more likely to cope with the variation in the field profile over the given frequency range than a solution tailored to a specific frequency. This over-meshing process allows a stable solution to be obtained for different values of frequency using the same mesh. Solving in this way saves a considerable amount of computational time since only one mesh construction process at a single frequency (usually a combination of adaptive and manual refinement at the resonant frequency of the structure where field magnitude is high) is required.

4.3.5 Types of solution

HFSS allows a model to be solved in two ways. In this thesis, we are primarily concerned with the driven solution, since all experimental samples are illuminated with planar incident radiation at some incident angle and azimuthal orientation. The driven solution recreates an incident wave within the dielectric medium surrounding the sample being modelled, and this is why models presented in this thesis contain a region designated as the incident medium (air), to allow the formulation of the incident wave. This incident wave is not restricted to be planar. Indeed, incident Gaussian or spherical wave fronts may also be modelled.

In addition to the driven solution, an eigen-solution may be obtained. Eigen-solutions calculate the eigen-modes or resonances of a structure from the geometry, materials and boundaries of the system. The quality factor *Q* (a measure of the energy losses within a system (*in eigen-solution mode, the Q factor is a calculation of the energy loss due to lossy materials only*)) may also be calculated. Eigen-solutions do not rely upon an incident wave driving the system, and this is particularly advantageous for models such as the infinite wave-guide presented in *chapter 3*, where the issue of resonant excitation of a particular mode configuration by incident radiation is of no interest.

The construction of an eigen-solution model is somewhat simpler than that for a driven solution since there is no incident wave to consider. Instead, only the basic geometry of the structure is needed, and since symmetry boundaries work in the same way for both driven and eigen solutions, the user may take advantage of any electromagnetic planes of symmetry to reduce the size of the model further. It is important to note here however that radiation boundaries may not be assigned, and frequency sweeps are not available. Instead, the user must specify the frequency at which HFSS should begin looking for eigen-modes of the system, and how many eigen-mode solutions are required (up to a maximum of 20).

Once the model is constructed, and boundaries are assigned, the mesh may be constructed either by adaptive passes, manual meshing, or a combination of both. While adaptive meshing, the convergence data is viewed in the form of the maximum delta frequency as a function of the number of tetrahedra constituting the mesh. The

maximum delta frequency is essentially the largest percentage difference in the resonant frequency of the modes from one adaptive pass to the next, giving a measure of accuracy and stability of an adaptive pass solution. Once solved, the resonant frequencies of the eigen-modes and corresponding Q factors may be viewed, and the field profile corresponding to individual eigen-modes evaluated using the field processor.

4.3.6 Post processing.

Once solved at a particular frequency, the field solution may be examined using the post processor. Plots of the electric field or electric vector magnitudes, and derived quantities such as the current density or Poynting vector may be obtained over any face of the geometric model. In addition, two dimensional planes (*cut-planes*) may be defined by the user, allowing evaluation of the incident, total, and scattered field solutions over its surface. Incident fields show the incident wave as it would exist in the volume of modelled space, in the absence of the geometric sample. Total fields show the physically measurable field that exists in the presence of the sample, when illuminated by a non-zero incident field. Scattered fields show the differential field, formed by subtracting the incident from the total fields. In a reflection model, the scattered field solution corresponds to the reflected fields. However, for a transmission model where two regions of space are separated by an opaque substrate but connected by an aperture, scattered fields correspond to the reflected radiation in the upper half space only (the incident half space), with the total field solution corresponding to the transmitted fields in the transmitted half space.

Transmission and reflection may be evaluated using the field calculator directly, by integrating the normal component of the Poynting vector over a cut-plane, or user defined surface. For transmission, the evaluation surface must be situated in the transmitted half-space. Total fields are then selected and the normal component of the Poynting vector integrated over the surface. This calculation is then repeated for the incident field solution. The total field solution is then divided through by the incident field solution providing normalised transmission. A similar process is used to evaluate the specular reflection from a sample. These calculations are recorded in the form of a

macro, automating the reflection and transmission calculations for use when scanning frequency. Once the post processing macros for the field quantities required are written, HFSS may be automated using the optimetrics interface. Optimetrics is a user interface that sits in front of HFSS, and in conjunction with the Ansoft macro language, allows variables such as frequency, model geometry, and material properties, or any other quantity designated by the user as a variable within HFSS to be altered. Hence field quantities may be evaluated as a function of the selected variable, which is especially useful when optimising a structure, or evaluating reflectivity and transmission as a function of frequency.

4.4 Thesis specific modelling

4.4.1 The dual period bi-grating

Chapter 5 presents a full angle dependent reflectivity study of a dual period grating, the dual periodicity arising from the fact that there are two deep grooves (2.2 mm) and one shallow (1.9 mm) groove per repeat period, cut into a thick aluminium substrate, giving a pitch of λ_g = 7.2 mm. All grooves are equally spaced (1.6 mm) and possess a uniform width (0.8mm). A second dual periodic profile, which is identical to the first, is also milled into the surface of the substrate but rotated through an angle of 90º with respect to the original. This structure is considered as infinite in the surface plane; hence the theoretical model used to predict the electromagnetic response of the structure comprises of a unit cell, of dimensions 7.2 × 7.2 mm.

To reproduce the unit cell, a rectangular aluminium substrate (*assigned a conductivity of* 3.8×10^7 *siemens/meter*) of dimensions 7.2 × 7.2 × 3.22 mm was constructed. From this, three boxes equal to the dimensions and spacing of the two deep and one shallower groove per repeat period were subtracted. This process was repeated in the orientation at 90º to the original grooves to form the bi-grating unit cell as shown in *Figure 4.4.1.*

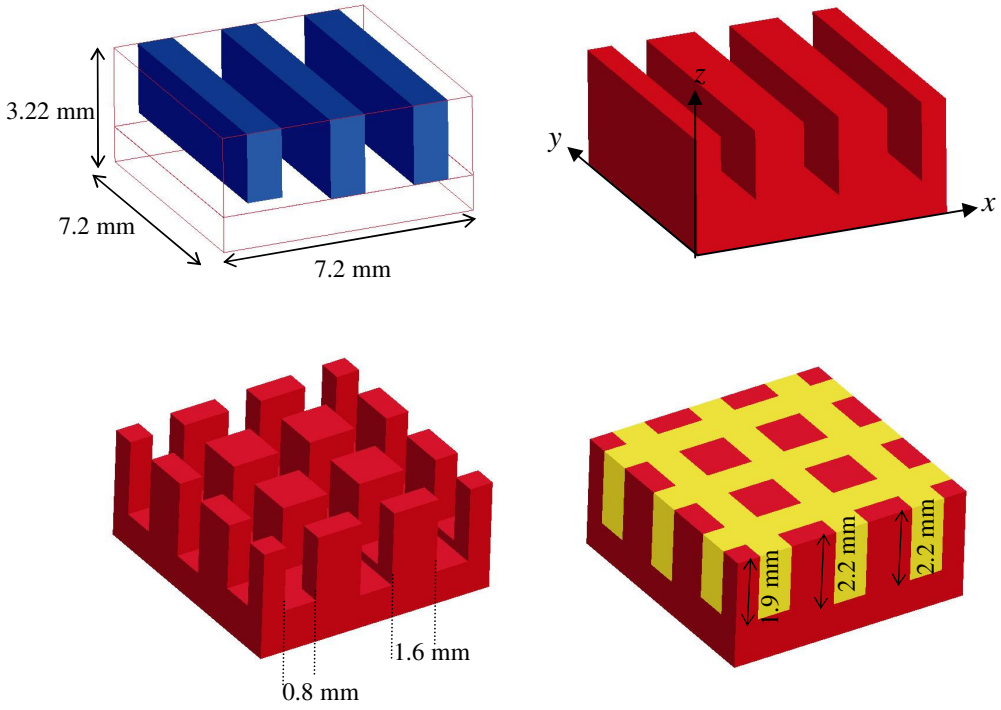

Figure 4.4.1. The unit cell of the bi-grating with grooves cut from several solid rectangles. The material indicated in red is the aluminium substrate. The wax is modelled as a separate object (shown in yellow) forming a negative image of the substrate. Each separate object within the 3-D modeller may then be assigned its own material parameters.

Since experimentally, the grating grooves were filled with a slightly lossy dielectric (wax) a 7.2 × 7.2 × 2.2 mm box was created and aligned with the top surface of the substrate, from which a duplicate of the substrate was subtracted. This formed a further 6 boxes which could be designated as wax filler ($\varepsilon_{d(final)} = 2.16 + 0.02i$). Since the structure is illuminated with an incident plane wave, a separation is required between the source and the illuminated structure in which the incident plane wave may be simulated. It is recommended that this separation should be greater than 1.5 wavelengths, to reduce any reflection from the outer boundaries. An air box of height 20 mm was therefore added. To prevent reflection of the scattered radiation from the upper surface of the air box, a perfectly matched layer (PML) was added to act as an absorber. PML's are a more efficient boundary between the model and free space, especially when illuminating the structure at non-normal angles of incidence. Using a radiation boundary in close proximity to a reflecting structure can result in reflections of the

scattered field from the radiation boundary, acting as a secondary source. PML's are fictitious, complex anisotropic media specifically designed for reflection-free termination of a model, produced by creating a volume which is usually situated with its base coinciding with the outside face of the terminating boundary and designated as a PML using the materials editor. It is important to note here however that the electromagnetic field entering the PML volume decays exponentially in the z-direction only. As a result the PML is less effective as an absorber for models with non-normal angles of incidence, and therefore it is necessary to increase the height of the PML for such models, providing a greater distance over which the scattered fields may decay.

To reproduce the unit cell in symmetry, the four outer faces of the unit cell are assigned as master-slave boundaries, with the top PML surface assigned a natural H boundary, as shown in *Figure 4.4.2*.(a). An initial wavelength dependent mesh was created by solving the project before a further 16 adaptive passes were added, increasing the number of tetrahedra by a maximum of 25% per pass, producing a final mesh in excess of 20,000 elements. Note from *Figure 4.4.2* (b) that the element density is greater in the region of the substrate, since it is in the grating grooves that the region of maximum field intensity occurs.

Once created, several parameters including the depth and width of each individual groove within the model were assigned as variables. This would allow variation of those parameters using optimetrics, for optimisation purposes and to allow the theoretical electromagnetic response of the structure to be 'fitted' to the experimental data through adjustment within experimental error bounds. As discussed in *Chapter 2*, and *Chapter 5*, the complex permittivity of the absorbing wax over-layer is an important parameter, through which the position in frequency, and the depth and width of the SPPR, may be adjusted. The real part of the permittivity of the wax was therefore allocated as a variable, with the imaginary part allocated as a variable indirectly, through the description of the electric loss tangent as a function of ε_i.

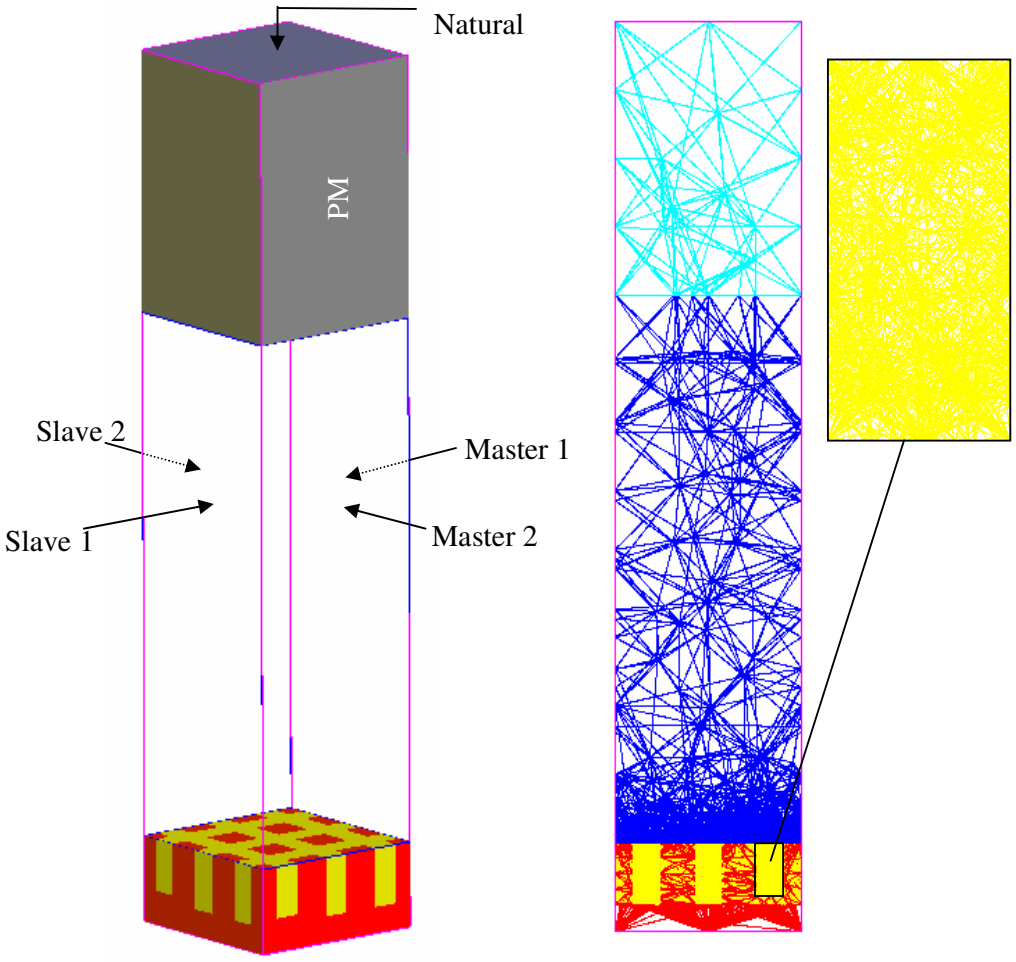

Figure 4.4.2. (a) The unit cell, air-box and PML. The four outer faces of the model are assigned as master-slave boundaries, with the top PML surface assigned a natural H boundary. (b) The finite element mesh formed through the adaptive pass process, clearly illustrating the increased mesh density in the vicinity of the grating grooves where field magnitudes are greatest.

4.4.2 The dual period 60º crossed grating

In *Chapter 6*, a full angle-dependent reflectivity study of a dual period hexagonal grating is presented. The sample consists of three dual periodic profiles identical to those constituting the bi-grating and discussed in the previous section, orientated at 60º with respect to each other in the plane parallel to the average surface plane of the grating. Once again there are two deep (2.2 mm) and one shallow (1.9 mm) grooves per repeat period, cut into a thick aluminium substrate, with a pitch λ_g = 7.2 mm. All grooves are equally spaced (1.6 mm) and possess a uniform width (0.8mm). Thus the unit cell for this structure is a lozenge with side lengths equal to $\lambda_g / \cos\alpha$, as shown in *Figure 4.4.3*.

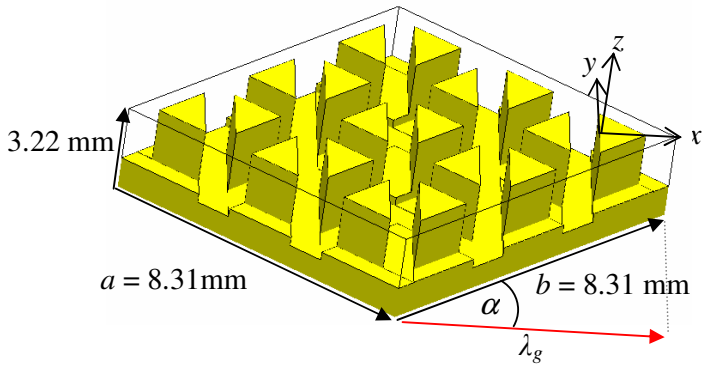

Figure 4.4.3 The 60º crossed grating unit cell.

For the initial model, the hexagonal structure was created using a similar process to the bi-grating in the previous section, with rectangular volumes created to represent the grating grooves subtracted from the solid substrate. To construct the rhombic shaped substrate, the poly-line tool must be employed. This command creates a 2-D closed surface described by the Cartesian co-ordinates of each vertex. Once created, the 2-D surface could then be swept through a vector in the direction of the surface normal, creating a three dimensional object. Subsequent objects requiring this geometry, such as the air-box and PML could then be derived from the substrate. However, initial modelling of the hexagonal symmetry proved problematic. The hexagonal grating model is to be considered as infinite in extent in the surface plane, and therefore master-slave boundaries must be employed to reproduce the unit cell. As previously discussed,

these boundaries force the fields at the two surfaces over which they are applied to be identical. To accomplish this, the master and slave boundaries must be identical, as must the mesh at each pair of boundaries. Since these boundaries are derived from the initial rhomboid drawn to construct the unit cell, they are described in terms of the substrates vertices, in Cartesian co-ordinates. The projection of the primitive lattice vectors *a* and *b* (*Figure 4.4.3*) onto the *x* and *y*-axis were first calculated and specified manually as *x*-*y* co-ordinates to a maximum permissible input of eleven decimal places. However, it was found that HFSS calculates to thirteen decimal places. As a result, the approximation made for the position of the vertices of the model in 3-dimensional space implied that the master-slave boundaries differed, and the model could not be solved. To rectify this, the drawing packages co-ordinate axis must be rotated such that the *x* or *y*-axis is parallel to the lattice vector before inputting the co-ordinates of the vertex, or each point must be described as a variable, so that the co-ordinate values can be specified in trigonometric form.

The final unit cell construction consisted of a rhombic substrate of thickness 3.22 mm, modelled as aluminium using a conductivity $\sigma = 3.8\times10^7$ siemens/meter, and a wax filler (ε_d*= 2.16 + 0.02i prior to optimisation of the model*). An air box of vertical height 20 mm was placed over the surface of the structure, upon which a PML of thickness 10 mm was situated, allowing the reflectivity from the sample to be calculated at non-normal angles of incidence without the possibility of reflections of the scattered field from the upper terminating boundary. The parallel outer boundaries of the model were assigned master-slave boundaries.

The mesh used to solve the fields pertaining to the hexagonal structure was produced using an initial wavelength based refinement. A subsequent eleven adaptive refinements increasing the number of tetrahedra within the mesh by a maximum of 20% per pass, provided a mesh of approximately 20,000 tetrahedra. Unlike the bi-grating structure, the removal of the three sets of grating grooves results in the formation of triangular ‘pillars’, the corners of which support high concentrations of charge, providing small regions of space within the dielectric filler with comparatively high electric field magnitudes. It was therefore necessary to manually insert a further 10,000 tetrahedra, refined over the surface of the structure. The resulting manual mesh was then used as a platform for a further three adaptive passes for each value of frequency at which the

reflectivity was calculated. Hence the mesh providing the final solution for the hexagonal grating was in excess of 48,000 tetrahedra.

4.4.3 The sub-wavelength aperture

Chapter 7 presents an investigation of enhanced transmission obtained via a sub-wavelength circular aperture, in conjunction with a photonic surface. Unlike the previous structures, this is a singular structure rather than an infinite array, consisting of 4 concentric rectangular profile grooves of depth l = 0.55 mm and width w = 1.50 mm, cut into 1.50 mm thick flat aluminium alloy sheet. The grooves surround a central countersunk circular aperture (d = 2.50 mm) with the radii of the grooves providing a periodicity of 5.00 mm, measured from the centre of the aperture to the centre of each groove. The theoretical model used to design and optimise this structure and then predict the electromagnetic response initially consisted of seven concentric grooves, but due to computational limitations, this number was reduced to four.

The sample was constructed using a poly line which was swept through 90º about the z-axis, as shown by *Figure 4.4.4.* This allowed each vertex of the profile (red crosses) to be assigned a y-z co-ordinate which could then be assigned as a variable. Constructing the model in this way allowed fully automated control over the depth, width and position of individual grooves relative to the aperture centre for optimisation purposes, and also allowed grooves to be removed.

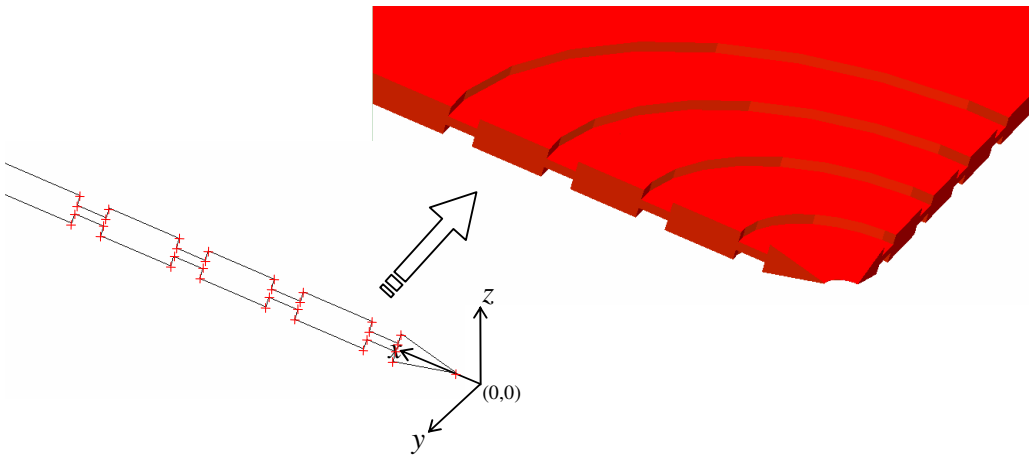

Figure 4.4.4. The poly line used to create the aperture profile, showing the co-ordinate points (red crosses) which are assigned as variable parameters with respect to the origin. The profile is swept through 90º about the vertical axis, forming a quadrant of the experimental sample.

The experimental wavelength range was chosen to be $4 < \lambda_0 < 6$ mm, and hence to allow sufficient space for the simulation of the incident plane wave, the sample was enveloped by a 17 × 22.5 × 28 mm air box. Since the aperture model was solved for normal incidence only, a PML was not required. Impedance boundaries were assigned to the outer surfaces of the model in the transmitted half space and radiation boundaries to the outer surface in the incident half space, as recommended by Ansoft's developers for transmission models. The *x*-*z* and *y*-*z* symmetry planes were assigned perfect H symmetry and perfect E symmetry boundaries respectively.

For optimisation, an input plane parallel to the *x*-*y* plane of dimensions 22.5×22.5 mm was used as an evaluation surface over which the power flow for the incident field solution was integrated. A second evaluation surface in the form of a hemisphere was situated in the transmitted half-space as shown by *Figure 4.4.5*, to calculate the transmitted radiation. This allowed total transmission to be evaluated since in the absence of grooves on the exit side of the sample, the aperture is highly diffractive. In addition, a horizontal line of points was inserted in the *xz*-plane, situated in the vicinity of the aperture entrance at a height of $z = 0.5$ mm (where $z = 0$ is situated at the top face of the sample). This allowed optimisation of the field magnitude in this region.

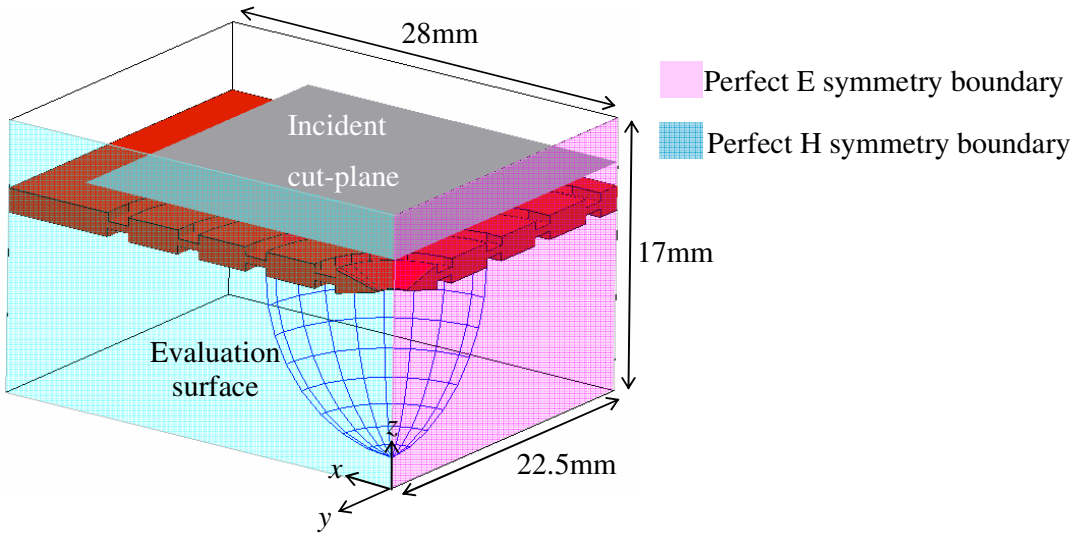

Figure 4.4.5. The geometry of the finite element aperture model showing electromagnetic symmetry boundaries and incident electric vector orientation. Unmarked outer faces are assigned as impedance boundaries in the transmitted half space, and as radiation boundaries in the incident half space. Also shown are the evaluation planes used to calculate the transmittance of the structure.

As for all theoretical models in this chapter, the initial mesh was constructed from a wavelength based refinement, and then refined further using the adaptive pass process, increasing the number of tetrahedra by up to 20% per pass. Once convergence had been achieved, the manual mesh maker was used to increase the mesh density at the surface of the substrate by specifying the minimum side length of tetrahedra. This mesh was then saved and used as a base for a further three adaptive passes for each value of frequency at which the model was solved. The final mesh used to evaluate transmission spectrum through the sample contained in excess of 80,000 tetrahedra.

4.4.4 The sub-wavelength annulus

In *Chapter 8* a study of the transmission obtained through a sub-wavelength cylindrical cavity drilled into an aluminium alloy substrate is presented. A solid cylindrical core of the same metal but slightly smaller radius is inserted into the hole forming a coaxial-like structure with a uniform gap width. Thus the annulus arrangement may be considered as a narrow air-filled slit possessing circular symmetry. Rather than relying upon surface modes supported by a surrounding photonic surface as is the case for the circular aperture, transmission by the annular structure is mediated by waveguide modes in the cavity, with incident radiation coupled to the various modes via diffraction at the annulus entrance. Therefore the surface plane dimensions of the finite model constructed to predict the electromagnetic response of this sample was greatly reduced in comparison to that used for the circular aperture. Hence for convenience, half the structure was modelled rather than a quadrant (which the cylindrical symmetry of the sample would allow), as the configuration of the modes within the cavity would be more readily observable.

The model consisted of a 30 mm thick aluminium volume ($\sigma = 3.8\times10^7$ siemens/meter) bounded by outer dimensions of 20×20 mm. The annulus is formed by subtracting a cylinder of radius 1.50 mm from the substrate to form the outer coaxial cylinder, and then inserting a centralised aluminium inner core of radius 1.25 mm and length 30.00 mm. The cavity bounded by the two concentric cylinders remains air filled. In order to reduce the size of the problem space and increase the resolution of the final mesh, a perfect H symmetry boundary was introduced which bisected the model along the plane of polarisation, as shown by *Figure 4.4.6.* The aluminium annular arrangement was enveloped by an air-box of dimensions 10 × 20 × 65 mm forming the outer boundaries of the model. Since transmittance is evaluated over a plane in the lower half of the model, and the annular arrangement forms a very small linking channel between the incident and transmitted half-space, it was found that secondary reflection of the scattered fields in the incident half of the model had negligible effect. Hence PML's were omitted.

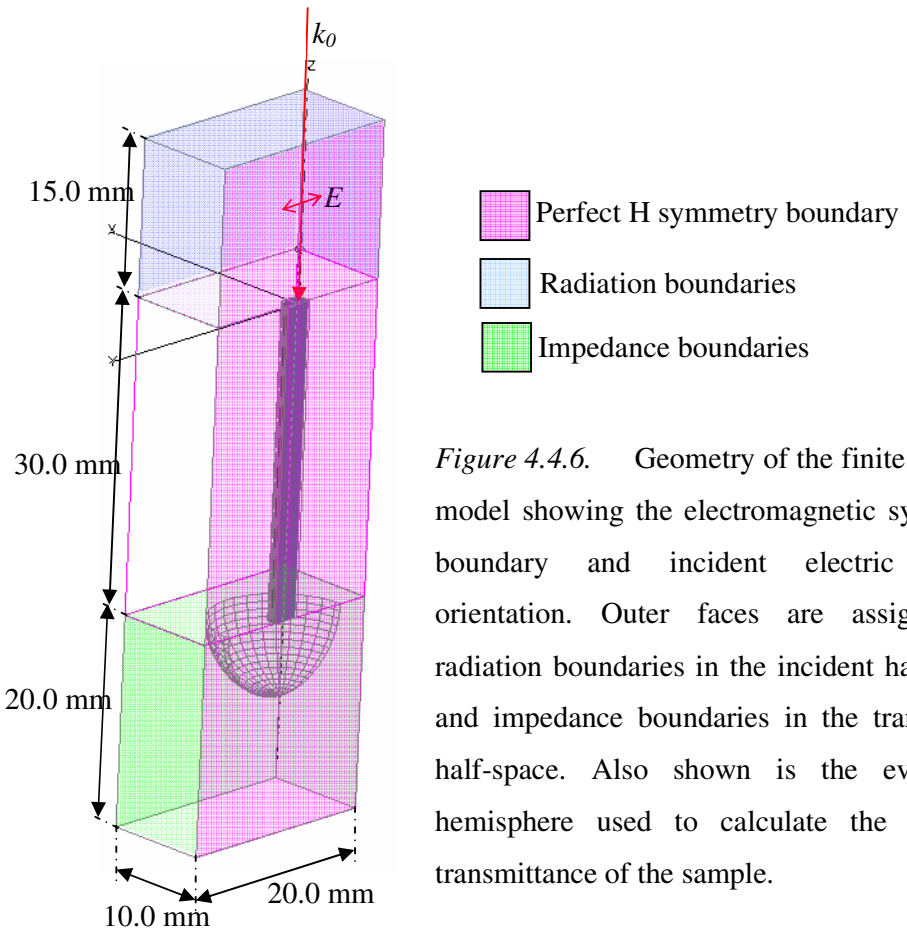

Figure 4.4.6. Geometry of the finite element model showing the electromagnetic symmetry boundary and incident electric vector orientation. Outer faces are assigned as radiation boundaries in the incident half-space and impedance boundaries in the transmitted half-space. Also shown is the evaluation hemisphere used to calculate the far-field transmittance of the sample.

Outer boundaries of the model were assigned as radiation boundaries in the incident half space and impedance (resistance = 377 ohms/square) in the transmitted half-space. A hemispherical evaluation surface was included over which the far field radiation pattern could be calculated.

An initial wavelength based mesh was created and a further 10 adaptive passes of 25% produced a mesh in excess of 22,000 tetrahedra. The mesh was then further refined using the manual mesh maker. An additional 10,000 tetrahedra were added by refining the maximum size of the tetrahedra over the surface of the inner coaxial core, increasing the density of the mesh within the sub-wavelength cavity. The mesh was then further refined by reducing the size of tetrahedra in the transmitted half space. The final manual mesh held in the region of 55,000 tetrahedra, and could be refined further through the adaptive pass process if required.

4.5. Summary

In this chapter an overview of Ansoft's High Frequency Structure Simulator (HFSS) has been presented. The finite element method has been introduced, and the method by which HFSS calculates the response of frequency dependent materials described. The surface approximation used to negate the need to solve Maxwell's equations inside a metallic object has been outlined, and particulars regarding incident wave and eigen-mode solutions investigated. The electromagnetic boundaries used to reduce the size of the problem space have been introduced, and the post processing package detailed. The chapter was concluded with a detailed description of each individual model used to predict the theoretical electromagnetic response of the samples in *Chapters 5* through *8.*

Chapter 5

Low angular-dispersion microwave absorption of a dual-pitch non diffracting metal bi-grating.

5.1 Introduction

In *Chapter 2*, work concerned with the use of corrugated structures to couple incident radiation to resonant SPP's was discussed, and the curved dispersion bands associated with the SPP examined. Deeply corrugated surfaces also warrant discussion, as such structures support highly localised modes which possess zero group velocity over a wide range of wave-vectors, owing to large band gaps in the dispersion of the SPP. Their resonant frequency therefore varies little with incident angle θ, and this characteristic is very useful when employing such profiles as narrow band frequency selective absorbers. However, within the incident light cone, the SPP resonances supported by such profiles tend to be broad and shallow (short ranged) because they are so strongly radiative [*Tan et al*. (1998)]. Recently, theoretical work conducted by *Tan et al.* (2000) showed that it was possible to couple to non radiative regions of these flat bands by multiplying an original large amplitude profile with a slightly shallower oscillation of longer pitch, a result that was advantageous for several reasons. Firstly, the dual period profile allows coupling to the lowest, flat-in-energy branch of the SPP dispersion which normally exists beyond the light line, and thus strong resonant absorption can be achieved. Secondly, the resonant wavelength is determined by the short period oscillation only, whereas the strength of coupling is determined purely by the secondary oscillation of longer pitch. Therefore by choosing suitable parameters, complete control over resonant wavelength, shape and depth of resonance, and dispersive characteristics as a function of incident angle can be achieved. These results have been experimentally observed by *Hibbins* (2002) using a dual pitch square wave metallic grating in the microwave regime. As the first experimental chapter in this thesis, a bi-grating is studied as an extension to the work described above. Formed from two orthogonal dual period square wave profiles, the structure supports modes which

are remarkably non-dispersive as a function of θ and exhibit strong resonant absorption at frequencies pre-determined by the parameters of the fundamental profile. In addition, the rotational symmetry introduced by the second orthogonal profile provides azimuth angle and polarization independence, and also leads to further non-dispersive modes arising from (1,1) scattering.

5.2 Background

The first theoretical investigation of the SPP band structure of a sinusoidal, dual period zero-order grating was conducted by *Tan et al.* (2000). Previous studies had shown [*Andrewartha et al.* (1979), *Laks et al.* (1981), *Tan et al.* (1998), *Sobnack et al.* (1998) and *Garcia-Vidal* (1996)] that extremely flat SPP dispersion bands could be supported by deep, short-pitched sinusoidal metal gratings with each band corresponding to a standing wave SPP mode localised within the grating grooves. However, for the purely sinusoidal profile, no band folding may occur. Hence the SPP modes supported by such structures are naturally radiative branches, and as such tend to give very broad shallow resonances in the reflectivity spectrum. Instead, Tan considered a double period sinusoidal grating described by the two term Fourier series;

$$A(x) = a_1 \sin(k_g x) + a_3 \sin(3k_g x + \alpha_3) \qquad (5.2.1)$$

where k_g is the grating wave-vector, and α the associated phase shift. The fundamental component of this sinusoidal structure has an amplitude a_1 and period λ_g whereas the harmonic possesses an amplitude of a_3 $(>>a_1)$ and period of $\lambda_g/3$. It was shown that the short period harmonic opens a large band gap in the dispersion of the mode, and results in a flattening of the lowest energy branch. In addition, when the amplitude of the fundamental takes a small but non zero value, the extra in-plane momentum provided allows coupling to the long range SPP modes created by the short period component without significant perturbation of the dispersion.

This idea of convolving an original periodicity with a longer oscillation of smaller amplitude to fold the original dispersion back into the light cone was furthered

experimentally by *Hibbins et al.* (2002). Rather than conducting the experiment in the optical regime where wavelength to pitch ratios makes manufacture of the structure problematic, they constructed a lamellar metal grating with a square wave profile for use at microwave frequencies. This study showed efficient coupling to two modes whose resonant wavelengths were determined by the short period component of the dual pitched system. One of the two modes was also shown to be non-dispersive as a function of θ, but both modes showed a cos^2 dependence as a function of azimuth angle (ϕ) and therefore was not fully independent of the incident orientation.

5.2.1 The single period mono-grating

The grating under study in this chapter is formed from two identical but orthogonal zero-order dual period mono-gratings superimposed on each other, thus forming a bi-grating. For simplicity, let us first consider the electromagnetic response from the short pitched harmonic of the grating in a single orientation only (the single period mono-grating).

As previously discussed in detail in *Chapter 2*, for an ideal metal in the microwave region, the dispersion curve for SPP propagation on a flat surface closely follows the light line. With the addition of a small amplitude corrugation, k_{spp} will only be perturbed by the surface modulation at momentum values close to $k_g/2$, where $k_g = 2\pi/\lambda_g$. At this point an energy gap opens up in the dispersion curves, with the high and low energy solutions corresponding to different field configurations [*Barnes et al*. (1996)]. When the depth of the corrugation is increased, these band gaps widen, with the low energy solution reducing in energy until a very flat band is formed. It has been shown in the optical regime by *Sobnack et al*. (1998), that for very deep zero order gratings, the SPP dispersion may become so severely perturbed from the shallow grating case that resonant absorption of light may occur within the zero order region of the spectrum. A family of such modes have been shown to exist, termed self coupled SPP's (SCSPP's) [*Wirgin et al.* (1984)] for reasons which will be discussed later in this chapter.

The short period harmonic of our dual period grating (grooves of all the same depth) has a periodicity of 2.4mm and groove width of 0.8mm, and is formed from a square wave

profile. Thus the periodicity possesses an aspect ratio of 2:1 and a grating pitch of $\lambda_g/3$. To create a square wave profile with pitch $\lambda_g/3$ and an aspect ratio of 2:1 the non-zero harmonics required are the N = 3,6,12,15…. terms whose amplitude decreases as N increases. However, if we only consider the first three Fourier coefficients of this profile then ($a_1 = a_2 = 0$) and the structure is simply a deep sinusoid similar to that of *Tan's*. The a_3 term is associated with the $3k_g$ grating vector which will set up counter propagating SPP modes at the Brillouin zone boundary occurring at $3k_g/2$. As for all standing wave solutions, the group velocity and therefore the gradient of the dispersion of the SPP mode must be zero at the Brillouin zone boundary where a large band gap is established (modelling has shown that the next lowest (radiative) branch of the dispersion occurs well outside the experimental frequency range). *Figure 5.2.1* represents the dispersion bands associated with a constant depth profile. The lowest energy branch of the band gap is highlighted as a bold red line and the Brillouin zone boundaries are denoted by dashed lines.

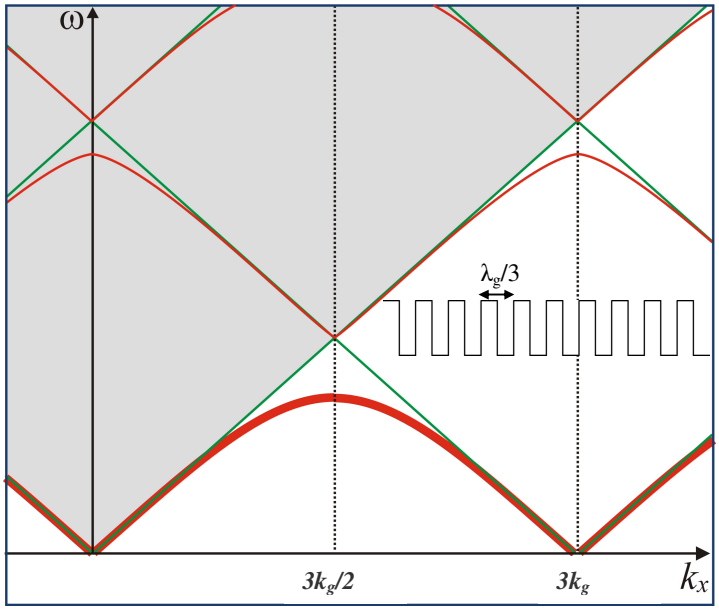

Figure 5.2.1 Schematic representation of the dispersion of the SPP supported by the original profile (all the grooves of the same depth). The lowest energy mode is represented by the bold red line. The shaded area border by the light line represents the region of momentum space within which an incident photon may couple to a mode.

It is important to note that for this simplified analysis, no part of the lowest energy dispersion band exits within the incident light lines, and it is therefore non-radiative. Realistically, the infinite set of Fourier coefficients associated with the square wave profile result in weak folding of the dispersion from a corresponding infinite set of points in momentum space, back into the zero order radiative region. This weak folding manifests itself as a broad, shallow resonance in the reflectivity spectrum as shown by *Figure 5.2.2*.

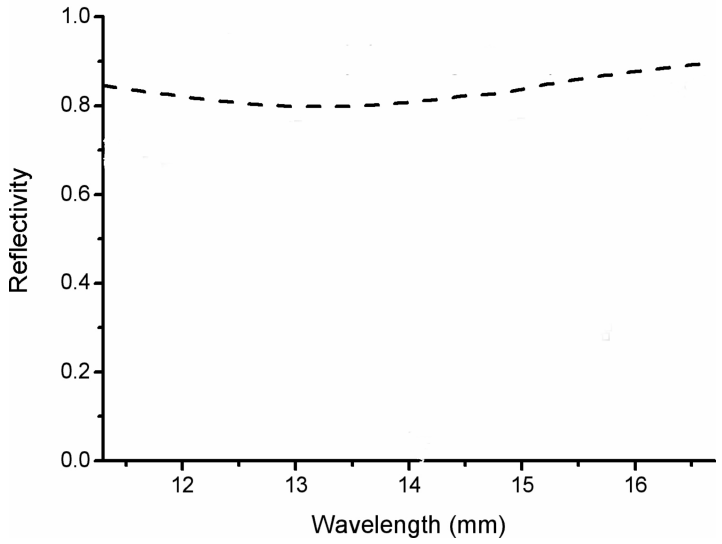

Figure 5.2.2. Modelled response of the single period short pitched square wave profile with a groove depth-separation aspect ratio of 2:1. Folding of the lowest energy branch occurs due to the higher harmonics of the square wave profile, but as the scattering events are numerous but low in probability, the mode appears as a broad weak dip in reflectivity.

5.2.2 The dual period mono-grating

Shallowing every third groove of the profile introduces a fundamental grating wave vector of $k_g = 2\pi/7.2\,\mathrm{mm}^{-1}$. Fourier analysis of the resulting dual pitch profile (*Figure 5.2.3* (black bars)) gives a more complicated series than that obtained from the short pitch harmonic, and although the additional terms are small in amplitude compared to the dominant N = 3,6,12,15 terms, the electromagnetic response of the structure is significantly altered.

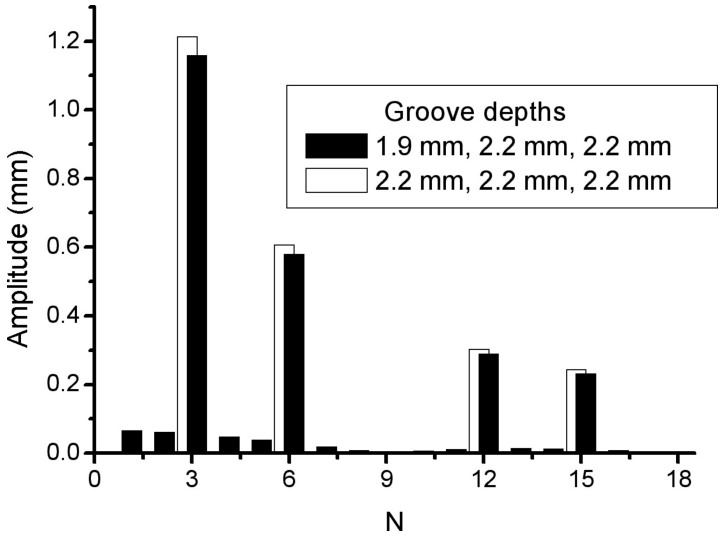

Figure.5.2.3 The first 18 amplitudes of the Fourier series that represents the profile studied in this chapter compared with the series for a profile with the same pitch, but for uniform groove depths.

Additional scattering introduced by the long period convolution results in a folding back of the dispersion such that well defined sections of the short pitch grating dispersion curve now exist within the light cone, as shown by *Figure 5.2.4*. A simple way of thinking about the folding process is that the weak long period component provides extra in-plane momentum to the incident photons, allowing direct coupling to the high momentum long range SPP modes created by the short pitch grating. Thus the originally non-radiative modes now become excitable by incident radiation. Further, because the amplitude of the long period component is small, the band folding occurs without

perturbation of the original dispersion. Hence the formally non-radiative modes remain sharp, leading to potentially strong resonant absorption.

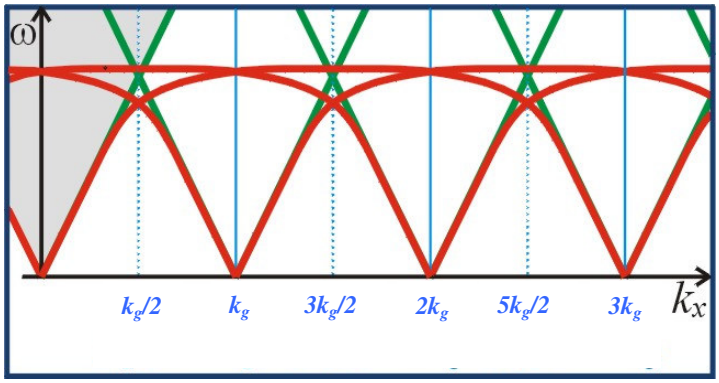

Figure 5.2.4 Schematic representation of the dispersion of the lowest-energy branch of the SPP supported by the dual period profile. The shaded area border by the light line represents the region of momentum space within which an incident photon may couple to a mode.

From *Figure 5.2.4* it is clear that two resonant bands are expected to be formed in the radiative region (grey shaded) by the folding of the lowest energy branch. One originates from k_g scattering which is a more dispersive branch, and a non-dispersive mode originating from $2k_g$ scattering which is reinforced by higher successive integer scattering. This result was observed experimentally by *Hibbins et al.* (2002), however although the upper mode was shown to be non-dispersive as a function of θ, it showed a cos^2 dependence as a function of ϕ. Thus the frequency selective resonant absorption of the dual period mono-grating was observed to be not truly independent of incident angle.

5.2.3 The dual period zero ordered bi-grating

In addition to the obvious polarisation independent properties of bi gratings, the extra dimensionality introduced by the second orthogonal corrugation gives rise to the possibility of coupling to a new set of modes which are not supported by the mono-grating structure. As discussed [*Chapter 2, section 2.6*] a surface with a grating wave vector in only a single direction may be represented by a one dimensional line of lattice points in reciprocal space, separated by a single grating vector k_g. Each lattice point represents a scattering centre, and forms an origin about which a light circle of radius k_0 and plasmon circle of radius k_{spp} ($>k_0$) is situated. In the case of a 90º bi grating, the reciprocal space map takes the form of a two dimensional array of lattice points as shown by *Figure 5.2.5.*

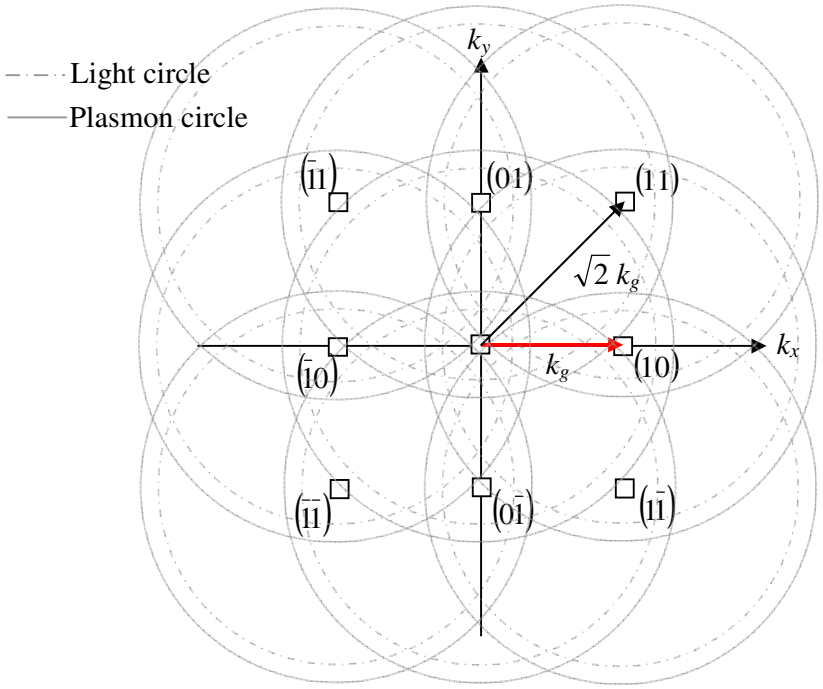

Figure 5.2.5 The reciprocal lattice of the 90º bi-grating. Lattice points are displaced by a single grating vector from the origin at 90º to one another, with the introduction of the second orthogonal grating giving rise to the set of {1,1} lattice points, lying at $(2)^{1/2}k_g$ from the origin.

It is clear that the set of {1,0} lattice points for such a grating are displaced by a single grating vector from the origin at 90º to one another, but the introduction of the second orthogonal grating also gives rise to the set of {1,1} lattice points, lying at $(2)^{1/2}k_g$ from the origin (the vector sum of two orthogonal grating vectors). As the light circle centred on the origin represents the total area of momentum space accessible to a high momentum (grazing) photon, all segments of the circles that fall within it represent real features that are accessible to incident radiation. Thus on a 90º crossed grating the possibility of coupling to a new set of modes associated with {1,1} scatter arises. It is important to note here however that *Figure 5.2.5* illustrates a much simplified representation of the plasmon circles associated with the bi-grating under study in this chapter. Due to the opening of the large band gap in the SPP dispersion due to the $3k_g$ component of the dual period profile, and subsequent flattening of the lowest energy branch, in reality the plasmon circles are heavily perturbed and no longer closely follow the light circles.

5.3 Experimental

5.3.1 The sample

The sample was milled onto an aluminium alloy plate of dimensions 10 × 500 × 500mm, making the sample area much larger than the incident beam (approximately 300 × 300mm) hence reducing any undesirable artefacts in the reflectivity response of the grating arising from the discontinuity in boundary conditions at the grating edge. To remove swarf arising from the milling process, and to limit any difference in average groove depth between the two orthogonal gratings (which manifested itself as a small shift in resonant frequency between ϕ = 0º and 90º) each groove was finished by hand using a small section of a hacksaw blade. Each grating period is formed from three equally spaced (1.6mm) grooves of the same widths (0.8mm), but with one groove shallower than the other two (1.9 and 2.2 mm respectively), as shown in *Figure 5.3.1.* (a) and (b).

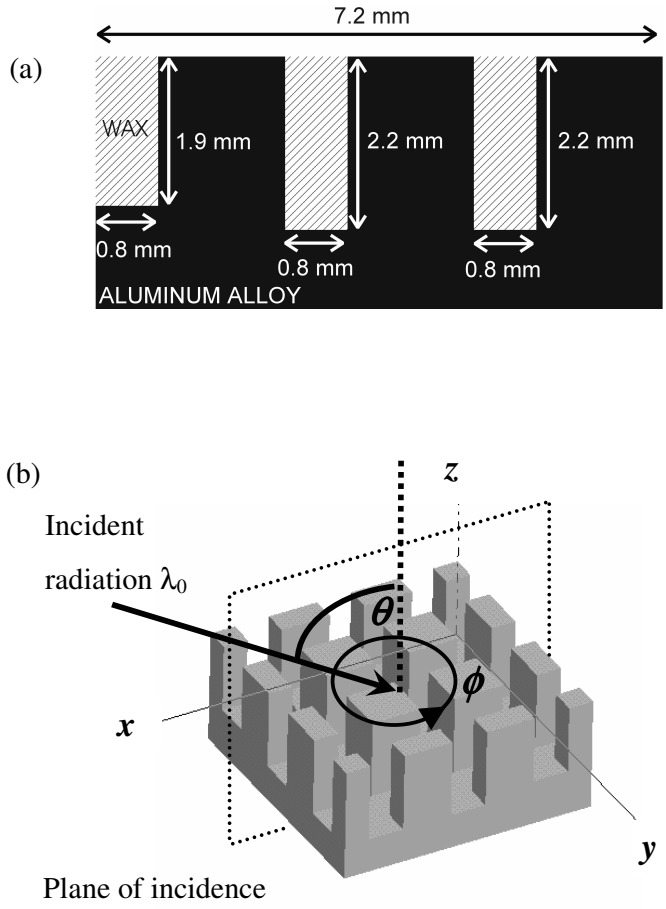

Figure 5.3.1 (a) Schematic of one repeating unit of the profile studied in this work and (b) the unit cell and co-ordinate system illustrating the polar angle θ, azimuth angle ϕ and the plane of incidence with respect to the direction of the grating grooves. The dashed line represents the normal to the surface plane and ϕ = 0º is defined as the angle of rotation at which one of the grating directions lies in the plane of incidence (classical mount).

5.3.2 Reflectivity measurements

In order to conduct reflectivity experiments on the samples described in this thesis, a collimated incident beam with near parallel wave fronts is required. The experimental arrangement shown in *Figure 5.3.2* is similar to that of the Czerny-Turner spectrometer [*James et al.* (1969)] and has been developed in order to reduce beam spread, associated effects of spherical wave fronts, and cross talk. By placing the transmitting horn at the focus of a 2 m focal length mirror (with a diameter greater than that of the beam incident upon it), the beam is well collimated.

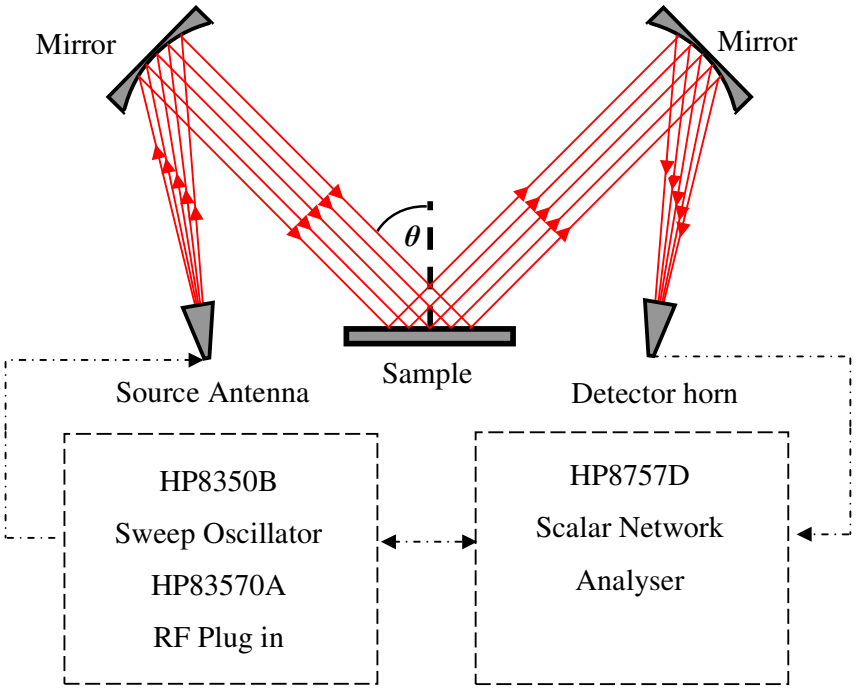

Figure 5.3.2 Schematic diagram illustrating the apparatus used to measure the wavelength-dependent response from a sample at fixed polar angles of incidence (θ).

An identical mirror is positioned to collect the specularly reflected beam from the grating and focus it into the detector. In addition an absorbing aperture is used to reduce the footprint of the beam. Clearly, in order to avoid the introduction of

aberrations in to the reflected beam, these mirrors should be parabolic, but these are difficult to manufacture. However, spherical mirrors can be manufactured relatively easily, and provide a good approximation to a parabolic mirror for beams of diameter much less than the mirror's radius of curvature.

The arrangement shown in *Figure 5.3.2* was used to record the specular reflectivity from the bi-grating as a function of wavelength at set values of polar angle of incidence whilst varying the azimuth angle (ϕ). These angles are set to a precision of ±1°. The apparatus is arranged in a vertical plane, built on concrete benches, where the sample is placed on the rotating table underneath the two mirrors (*Figure 5.3.3*).

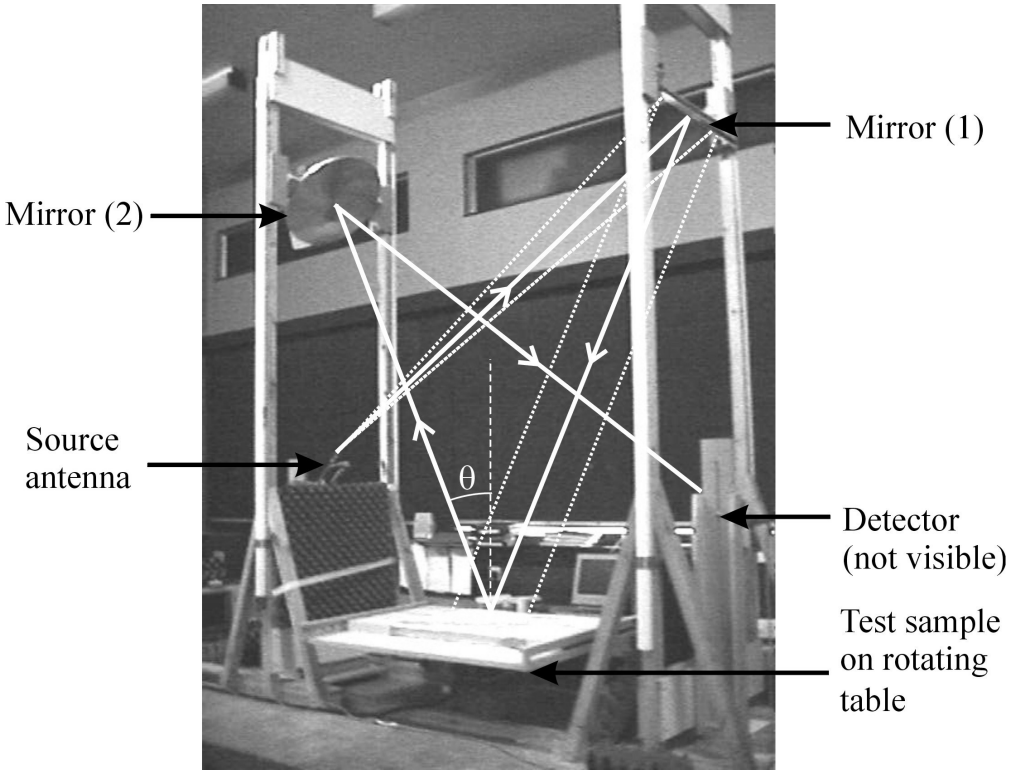

Figure 5.3.3 Photograph of experimental apparatus used to measure the specular reflectivity from reflectivity samples studied in this thesis.

The mirrors are bolted on to structures that are able to slide on rails along the concrete bench and, in order to avoid the undesirable effects of diffraction and scattering, they have been manufactured from wood. The mirrors may be rotated to change the angle of

incidence (θ), and their height may be changed in order to maintain a source-mirror(1), and mirror(2)-detector distance of 2 m. In addition, the source antenna and detector may also be moved along the bench, rotated, and raised or lowered in height.

A Hewlett Packard HP8350B sweep oscillator is used in conjunction with a HP83570A RF plug-in to generate radiation of wavelength $11.3 < \lambda_0 < 16.7$ mm. A Narda 8401 standard gain horn connected to the plug-in via a flexible waveguide directs the emitted radiation onto the sample via the collimating spherical mirror. The source signal is split before emission by a directional coupler into a source and reference signal which is fed into a HP8757D scalar network analyser allowing normalisation of the detected signal. Radiation incident upon the sample is reflected and directed to a matched standard gain horn and crystal detector which is connected to the scalar network analyser, which in turn is connected to a PC using a HP interface bus. The PC records data sets and controls the turntable, allowing the ϕ dependant response of the sample to be recorded.

For the experimental arrangement described above, the source antenna and detector may be set to pass either *p*- (transverse magnetic, TM), or *s*- (transverse electric, TE) polarisations, defined with respect to the plane of incidence. This enables the measurement of R_{pp}, and R_{ss}, and polarisation conversion R_{sp}, and R_{ps} reflectivities where the subscripts refer to the incident and detected polarisations in that order. To account for any fluctuations in the power of the source, the output from the signal detector is divided by that of the reference, and the resulting wavelength and azimuthal angle-dependent data were normalised by comparison with the reflected intensity from a flat metal plate to give absolute reflectivity.

Variation of the magnitude of the incident wave vector in the plane of the grating may generally be achieved by scanning either wavelength (λ_0), or angle of incidence (θ or ϕ). The technique described above keeps the polar angle of incidence constant, in contrast to the conventional method of polar angle scans that are often used for experiments at visible and infra-red wavelengths, and therefore avoids the difficulty of scanning the detector and focusing mirror.

Resonant modes may be observed as minima in the angle-dependant reflectivity with the resonance width being dependent upon the loss channels available [*Pockrand (1976), Raether (1988)].* The grating under study in this chapter is zero order (the periodicity of the grating is sub wavelength) and therefore does not support propagating diffracted orders over the selected frequency range. As a result, no reflectivity losses will occur in the zero order beam due to re-radiation into a diffracted order. Energy dissipation via Joule heating of the substrate is also low since metals behave as near perfect conductors at microwave frequencies. Also, any re-radiation of energy from the mode back into the specular beam when the grating grooves are neither perpendicular nor parallel to the plane of incidence will be rotated in polarisation with respect to the incident beam and detectable as polarisation conversion [*Bryan-Brown et al. (1990)*]. Hence to readily observe the resonant modes in reflectivity when presented in the classical mount, the grating grooves are filled with petroleum wax, which is slightly absorbing at these frequencies.

5.4 Modelling

As discussed in the modelling chapter, when representing mono-gratings using Ansoft's High Frequency Structure Simulator (HFSS) it is possible to reduce the size of the problem space and hence make the model less memory intensive. This is achieved by constructing an accurate geometric model which is essentially a 2-dimensional representation of the profile, with a small but finite width in the direction of the grating grooves. Electromagnetic symmetry boundaries may then be applied to simulate infinite dimensions in the surface plane. For the bi-grating however, it is necessary to use a 3-dimensional construct in order to accurately represent the electromagnetic response of the structure. It was nevertheless possible to reduce the size of the problem space by considering only the unit cell of the bi-grating and inserting master-slave boundaries along planes of electromagnetic symmetry. Thus a 7.2 × 7.2mm unit cell may give the response of a structure which is infinite in the surface plane and hence better represent the experimental set up (that of the sample area being larger than the footprint of the incident beam). The unit cell therefore consisted of three evenly spaced grooves with

one slightly shallower than the other two cut from a solid base in both orthogonal directions (*Figure 5.4.1*).

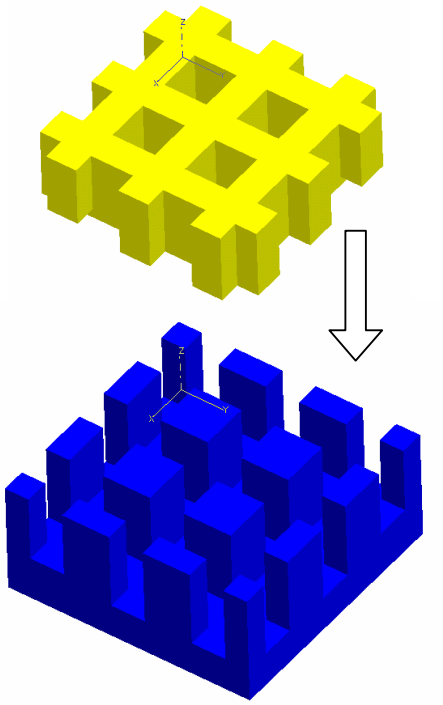

Figure 5.4.1 The unit cell of the bi-grating with grooves cut from a solid rectangle. The material indicated in blue is the aluminium substrate. The wax is modelled as a separate object (shown in yellow) forming a negative image of the substrate. Each separate object within the 3d modeller may then be assigned its own material parameters.

To enable a good fit to the data it was necessary to build into the model any variation in average groove depth that exists between the two orthogonal gratings in the experimental sample. The average values of deep and shallow groove depths in each direction were found (using a sensor attached to the milling machine and a digital read out accurate to 0.0025mm) to be (a) deep = 2.246mm, shallow = 1.940mm and (b) deep = 2.244mm, shallow = 1.941mm. Although the magnitude of the depth variations between the two grating directions are at most 0.002mm, the effect on the electromagnetic response of the structure due to the perturbing of the original dispersion is shown by the theoretical reflectivity comparison in *Figure 5.4.2*.

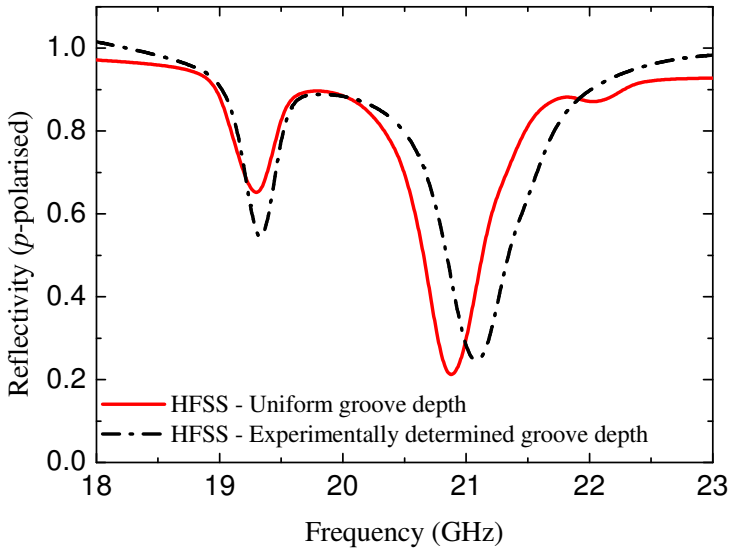

Figure 5.4.2 p-polarised frequency-dependent reflectivity of the bi-grating for $\theta = 30°$ $\phi = 0°$ obtained using HFSS. The solid red line represents the reflectivity spectrum from a sample possessing identical grating profiles in the two orthogonal directions (a) and (b). The dashed line represents the reflectivity from a substrate with experimentally determined groove depths as follows: (a) deep = 2.246mm, shallow = 1.940mm and (b) deep = 2.244mm, shallow = 1.941mm.

Once the substrate is surrounded by an air box to distance any upper boundary from metallic radiating objects, a PML was added to avoid any secondary sources arising from scattered radiation. Final fitting of the theory to the data was achieved by using the optical properties of the wax absorber as fitting parameters. By setting ε_r and the electric loss tangent ($\varepsilon_i/\varepsilon_r$) as functions, it was possible to vary the relative complex permittivity of the wax. The variation of ε_i alters the depth of the reflectivity spectrum as discussed in *Chapter 2* and shown by *Figure 5.3.3*(a), due to alteration of the balance between radiative and non-radiative losses. Further, making the wax more absorbing increases the resonant width of the mode. Increasing ε_r and thus increasing the refractive index of the wax results in a reduction of the resonant frequency of the SPP as shown in *Figure 5.4.3* (b) due to the increase in optical path length and hence effective depth of the grating grooves.

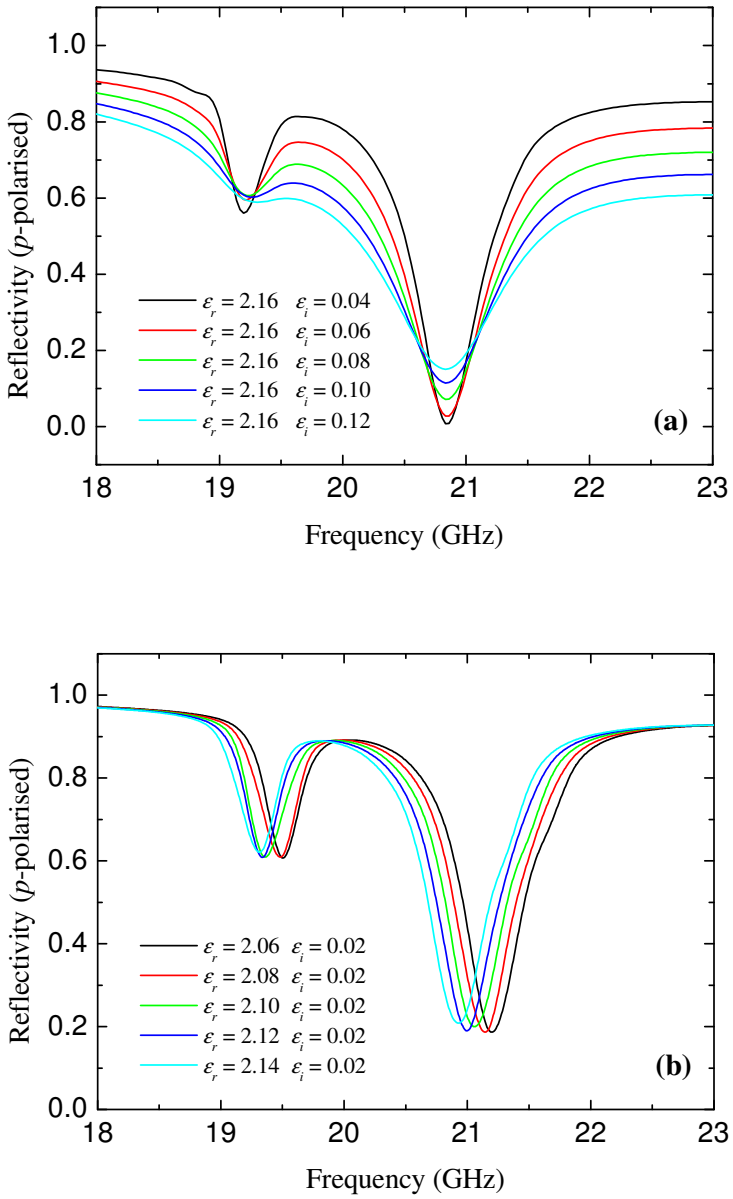

Figure 5.4.3 Modelled reflectivity spectrum of the dual period bi–grating as a function of the (a) imaginary part and (b) real part of the complex permittivity of the wax absorber. The variation of ε_i alters the depth and width of the reflectivity spectrum due to alteration of the balance between radiative and non-radiative losses. Increasing the refractive index by increasing ε_r shifts the resonant frequency of the SPP modes downward due to the increase in the effective depth of the grating grooves, allowing the properties of the wax absorber to be used as fitting parameters.

5.5 Results and Discussion

Figure 5.5.1 shows the p-polarised frequency-dependent reflectivity data obtained for (a) θ = 20.3º and (b) θ = 52º. Source and detector horns are set to pass *p*-polarised radiation The modelled response of the structure is shown for comparison. Also shown is the s-polarised reflectivity data obtained at the said angles of incidence (*Figure 5.5.2* (a) & (b)) with the grating presented in the classical mount, clearly demonstrating the polarisation independent absorption of the bi-grating.

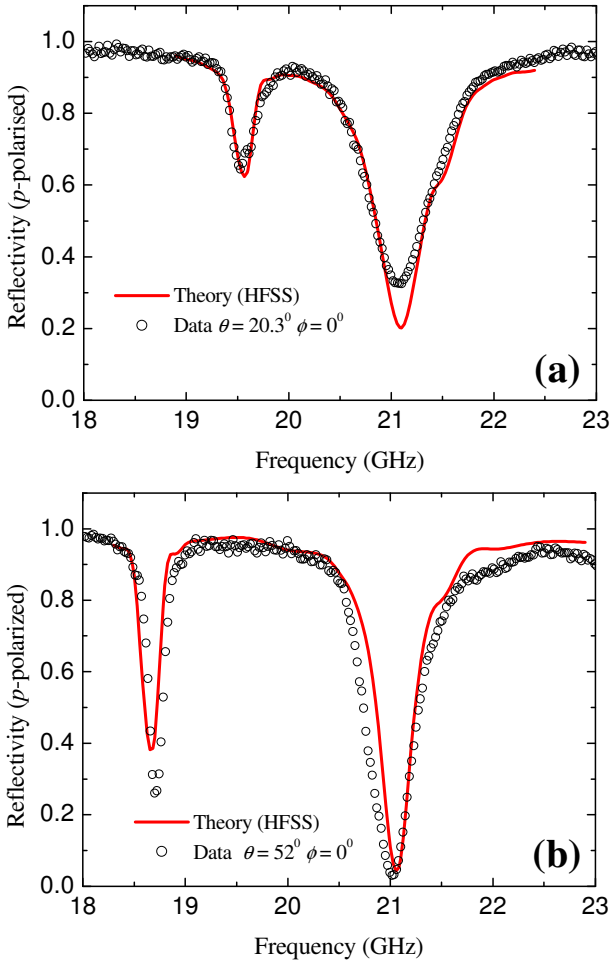

Figure 5.5.1 p-polarised frequency-dependent reflectivity data obtained for (a) θ = 20.3º and (b) θ = 52º. The theoretical response of the structure is obtained using the Ansoft HFSS finite element code. The grating is presented in the classical mount.

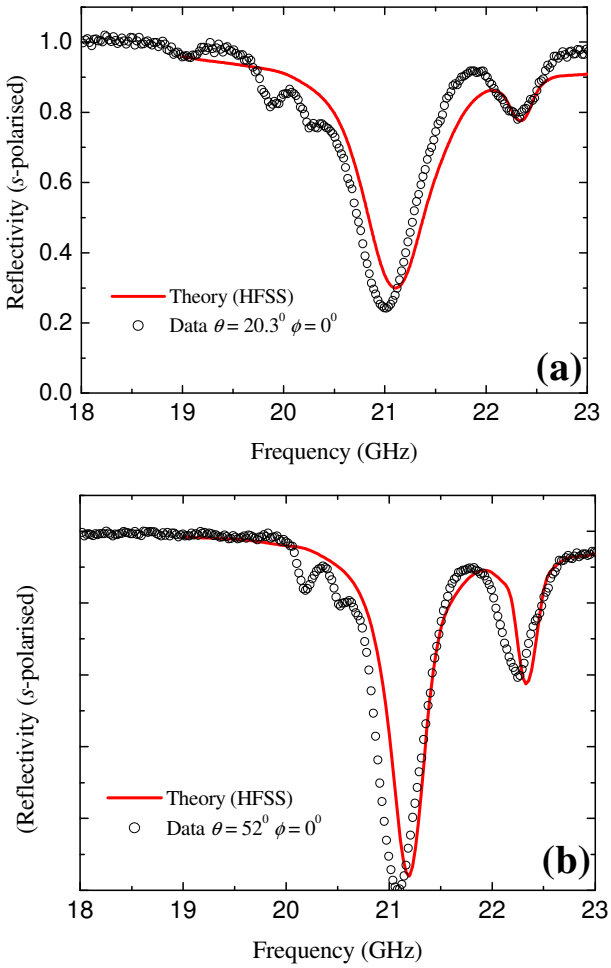

Figure 5.5.2 *s*-polarised frequency-dependent reflectivity data obtained for (a) $\theta = 20.3°$ and (b) $\theta = 52°$. The grating is presented in the classical mount.

Good agreement is obtained between the theoretical model and the data even though the model assumes a perfect plane wave (the experimental incident angle spread is approximately 1°) and treats the sample as infinite in the surface plane. The grating in this instance is presented in the classical mount so by symmetry no p to s conversion may occur, due to the scattering vector of the grating lying in the plane of incidence

[*Elston* et al. (1991)]. For the higher frequency mode, up to 95% of the incident power is absorbed by the wax, with the resonance half width being 0.56 GHz, whilst the lower frequency mode is less well coupled. This difference in coupling is attributed to the probability of excitation of the respective modes. As discussed previously in this chapter, an infinite Fourier series (*equation 5.3.2*) may be used to describe the grating, where the amplitude coefficients (a_N) determine the probability of each of the Nk_g diffraction events, and hence control the coupling strength to each of the modes. However, for a dual pitch square wave profile with a repeat period of 3 grooves, the dominant terms are multiples of the N = 3 term. Thus the $3k_g$ scattering process has a Fourier amplitude coefficient which is much greater than that of the k_g component introduced by the long period shallower grating. Hence the probability of coupling to the higher frequency mode associated with a single $3k_g$ scattering event is greater than the probability of coupling to the lower frequency mode, which requires a multi scattering event. Further, from comparison of *Figure 5.5.1* (a) and (b) it is also evident that an increase in θ of approximately 32º results in a decrease in resonant frequency of the lowest energy mode from 19.5 GHz to 18.7GHz, whilst the higher energy mode remains fixed in frequency. This demonstrates the expected dispersive nature of the two modes, as discussed in *section 5.2.2*.

Figure 5.5.3 (a) and (b) shows the time-averaged magnitude of the total electric field obtained from HFSS at the resonant frequencies of 18.7 and 21 GHz respectively at θ = 52º, plotted over a plane containing the incident wave vector and bisecting the deep grating grooves. It is clear that the electric field magnitude has a minimum situated at the bottom of each groove rising to a maximum at the top of the groove. As the effective depth of the grating grooves is approximately $\lambda_{res}/4$ this is consistent with cavity resonances [*Popov et al.* (1994), *Fournier et al.*(1999), *Garcia-Vidal et al.* (1999)]whose location of field maxima and minima are determined by boundary conditions at the bottom of the groove (fields inside the metal are zero).

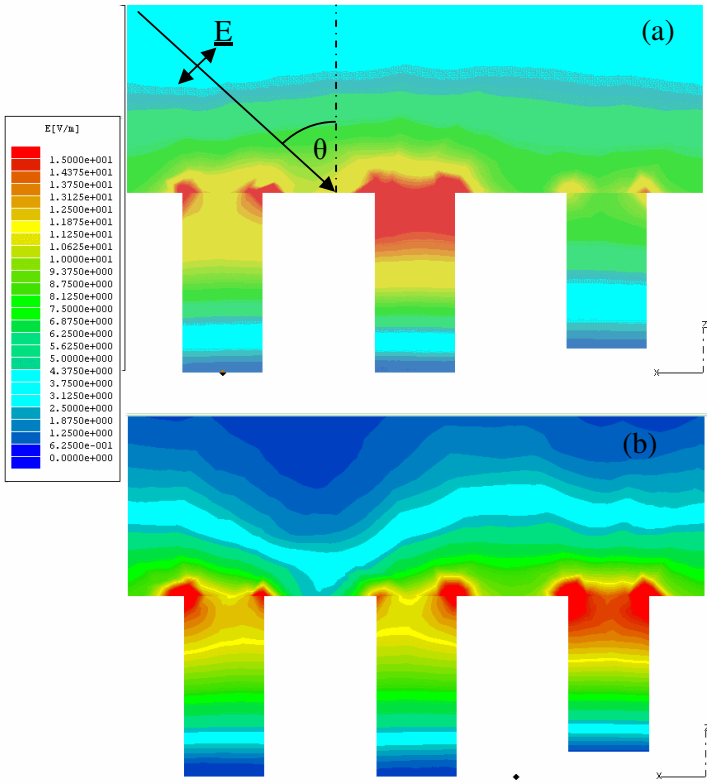

Figure 5.5.3 Modelled time averaged magnitude of electric field at the resonant frequencies (a) 18.7 and (b) 21 GHz obtained at $\theta = 52^o$ plotted over a plane bisecting the deep grating grooves and containing the incident electric vector.

These modes however are not just simple cavity resonances which would exist in a single groove of said dimensions. Instead, these cavity modes could equally be described as self coupled SPP modes (SCSPP's), coupling to which is dependent upon the band folding effects of the long period component of the grating. They are highly localised, possessing a zero group velocity over a wide range of incident wave vectors and although very different from, they are none the less an evolution of the familiar propagating SPP's supported by shallow gratings. The self coupled SPP's are formed when SPP fields on the vertical walls of deep grooves couple together across the cavity, pulling the regions of high field enhancement within the groove cavity [*Hooper et al.*(2002)].

In *Figure 5.5.4* the frequency dependant polarisation conversion data is presented, obtained with (a) the source and detector set to pass *p* and *s*-polarised radiation respectively and (b) the source set to *s*-polarised and detector set to *p*-polarised radiation. Reflectivity for three azimuth angles are shown for each angle of incidence and clearly shows $\phi = 0$ and 90º to be equivalent.

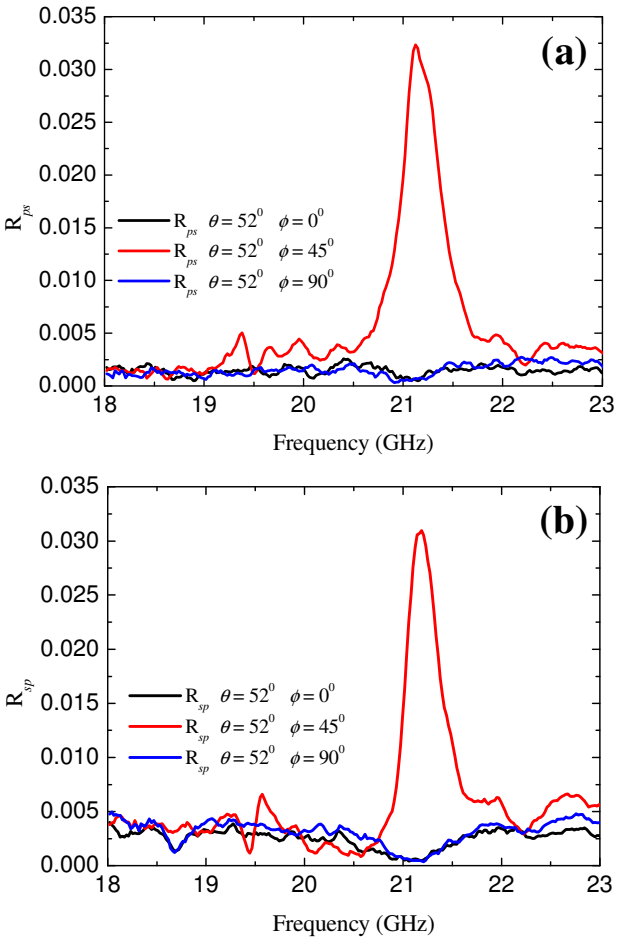

Figure 5.5.4 (a) *p-s* and (b) *s-p* frequency-dependent polarisation conversion data obtained for $\theta = 52º$ $\phi = 0$, 45 and 90º.

As expected, polarisation conversion is maximum when the bi-grating is orientated at an azimuth angle of 45º due to its $sin^2(2\phi)$ dependence upon the degree to which symmetry is broken. However the maximum intensity level of polarisation conversion is 3% which is negligible compared to the resonant absorption of 95% at the same frequency. As no

reflectivity losses occur in the zero order beam due to re-radiation into a diffracted order (the sample is zero order), and energy dissipation via Joule heating of the substrate is not an available loss channel, the width of the resonant features in the specula reflectivity is attributed primarily to absorption by the wax filler.

The dispersion plot shown in *Figure 5.5.5* is constructed by evaluating the resonant frequency of each mode for a fixed value of ϕ (classical mount) for various values of θ between 12º<θ<78º. Corresponding in-plane momentum is then calculated and plotted against frequency. The data shows good agreement with theory until higher angles of incidence are reached, when the theoretical curve of the lower mode decreases more rapidly than the experimental data. Although the θ dependence of the modes is clearly shown, the dispersion plot shows no coupling strength information other than the fact that the lower mode may not be coupled to at angles of incidence close to normal.

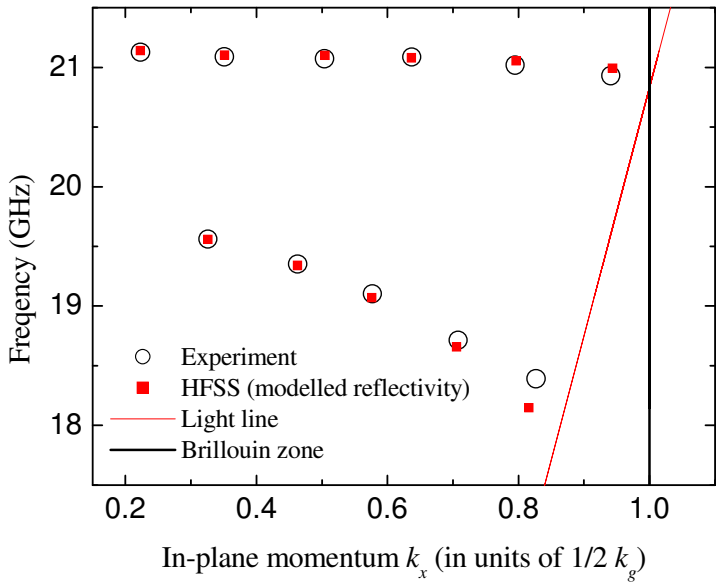

Figure 5.5.5 The theoretical and experimental dispersion curves of the modes supported by the structure when presented in the classical mount. Incident radiation is p-polarised. The vertical line represents the Brillouin zone boundary, and the light line is also shown (red).

The 21GHz mode is shown to be remarkably non-dispersive, whilst the frequency of the lower mode reduces as k_x increases, being less localised in nature, which is consistent with the folding back of the lowest energy dispersion branch into the radiative region. From the comparison of this result with *Figure 5.3.4* it is clear that the non-dispersive mode comprises of the infinite set of flat banded modes arising from the $2k_g$, $3k_g$, $4k_g$..... scattering whereas the lower mode curves downward towards its point of origin, k_g. As the dispersion diagram provides no coupling strength information it is important to note here that no experimental or theoretical resonant frequencies were obtained for the lowest energy mode at angles of incidence below 13º when the sample is presented in the classical mount. This is because as θ reduces, the lower mode broadens and coupling strength reduces such that the resonant frequency of the mode becomes difficult to determine. Further, as the experimental arrangement is limited in the range of incident angles at which reflectivity data may be obtained, it is difficult to obtain data below θ = 11º. It is still apparent however, that the dispersion of the lower mode will not rise and converge to the same frequency as the non dispersive mode at normal incidence, as in our simplified analysis, due to a band gap opening up at the crossing point of the two modes. Further, as discussed in *Chapter 2*, it is the relative phases of the Fourier coefficients of the grating profile that is responsible for the band gap at this point (a_2) that causes the observed reduction in coupling strength to the lower mode as we approach normal incidence [*Webber and Mills* (1985), *Nash et al.* (1995), *Barnes et al.* (1996)].

Figures 5.5.6 and *5.5.7* show (a) p-polarised and (b) s-polarised experimental reflectivity data as a function of both frequency and azimuth at fixed polar angles of 20.3 and 52º respectively. The non-dispersive mode and dispersive lower frequency mode are clearly symmetric in character about ϕ = 45º. All three modes are visible as dark bands (dark regions corrispond to absorption) and clearly shows the coupling charicteristics of each mode as a function of θ for both polarisations.

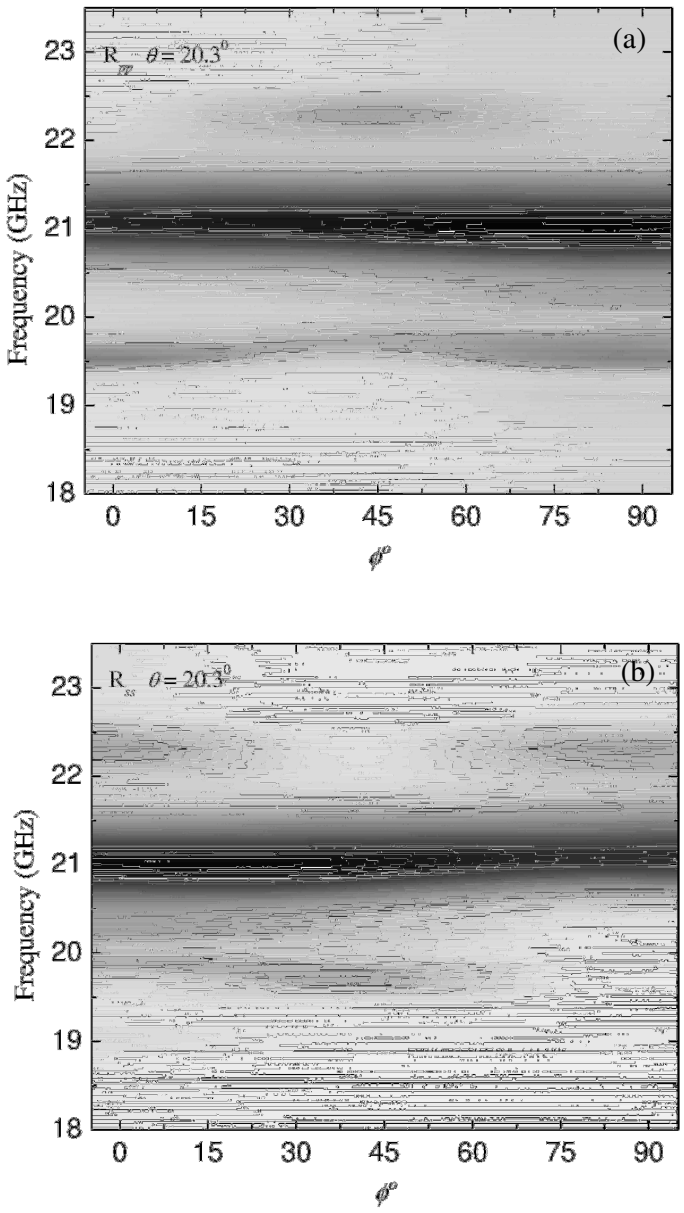

Figure 5.5.6 (a) p-polarised and (b) s-polarised reflectivity data (experimental) as a function of both frequency and azimuth angle at a fixed polar angle of 20.3º. Light regions correspond to strong reflection whilst dark regions correspond to absorption.

Note here the two faint bands forming between the curved lower and non-dispersive 21GHz mode, responsible for the fluctuations in the reflectivity spectrum presented in *Figure 4.5.1* (a) and (b), and *Figure 4.5.2* (a) and (b) which are mode-like rather than an interference phenomenon, and possibly arise from small imperfections in symmetry of the sample.

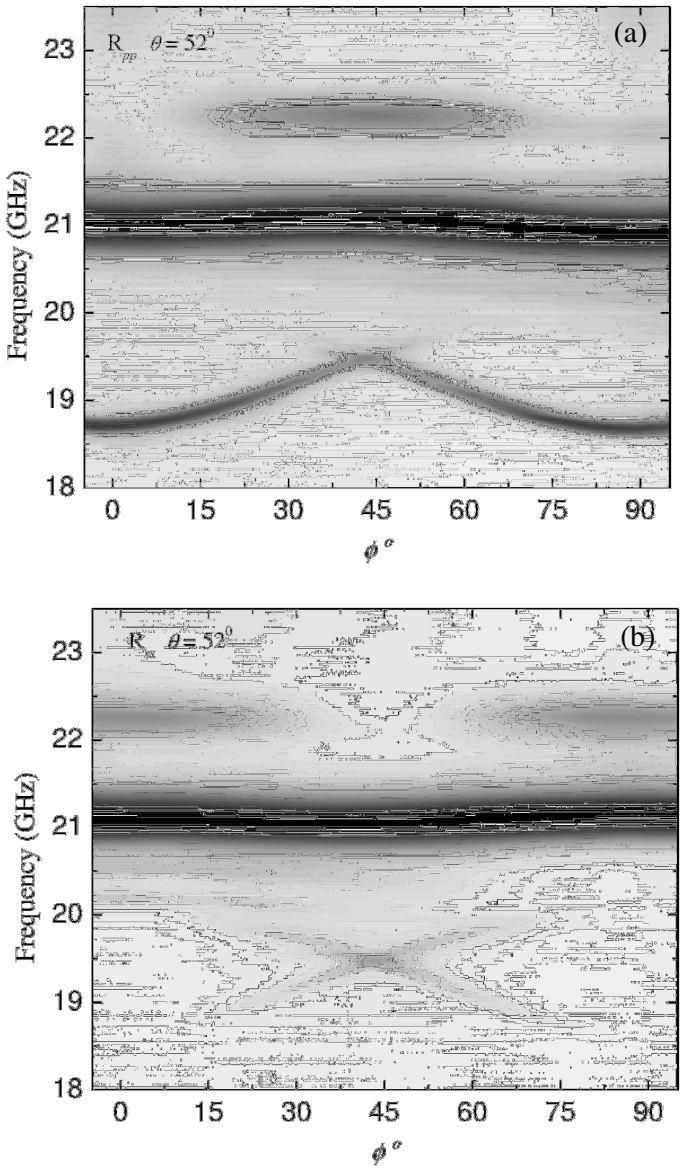

Figure 5.5.7 (a) *p*-polarised and (b) *s*-polarised reflectivity data (experimental) as a function of both frequency and azimuth angle at a fixed polar angle of 52º.

It is apparent that unlike the mono-grating results of *Hibbins et al.* (2002), which showed the modes supported by the dual period mono-grating to be non dispersive with θ only, the frequency and depth of the localised mode is now almost entirely independent of both θ and ϕ. This effect is due to the extra dimensionality that the bi-grating possesses over the mono-grating. For the conical mount mono-grating ($\phi \neq 0$) k_g, k_0 and k_{SPP} are not collinear and the wave vector of the mode is given by:

$$k_{SPP}^2 = \varepsilon_d k_0^2 \sin^2\theta + N^2 k_g^2 \pm 2 n_d N k_g k_0 \sin\theta \cos\phi \qquad (5.6.1)$$

As ϕ increases, the projection of the incident wave vector in the direction of the grating wave vector decreases, and hence the frequency of the lower mode increases to satisfy the momentum conservation criteria. However the four fold symmetry of the bi-grating results in the frequency of the lower mode becoming degenerate at the symmetry angle ϕ = 45º. Beyond 45º, coupling to the mode associated with the second orthogonal grating strengthens and further rotation of the sample results in a reduction of ϕ as measured with respect to the second grating wave vector, and a consequent reduction in frequency. Coupling at ϕ = 90º is therefore entirely associated with the second orthogonal corrugation.

From comparison of *Figure 5.5.7* (a) and (b), the non dispersive but less well coupled 22.25 GHz mode has its strongest coupling at 45º for p-polarised incident radiation and at 0º for the s-polarised case, thus it is opposite in coupling characteristics to the (1,0) mode. This mode is not supported by the dual period mono grating (as shown in previous work conducted by *Hibbins* (2002)), and therefore must be associated with (1,1) scattering. Coupling to the lower more dispersive mode is a maximum for p-polarised radiation at 0º and reduces as ϕ is increased up to 45º. For s-polarised radiation the maximum coupling strength to the lower mode is centred at ϕ = 45º. However, coupling to the non-dispersive deep mode is possible for both p and s polarizations at all ϕ. To help understand the different coupling characteristics of the two (1,0) modes, as a function of both θ and ϕ, it is useful to explore the nature of the electromagnetic fields at each of the resonant frequencies using the finite element model.

Figure 5.5.8 (a) and (b) show the relative field magnitudes at the resonant frequency of the 21 and 19 GHz modes respectively, evaluated over a plane that cuts through the grating cavities at 1/3 the depth of the deep grooves. Grooves *1* and *C* are the slightly shallower grooves. Radiation is incident in the *x*-*z* plane at an angle of 52º to the normal and is p-polarised. In both cases the regions of high field occur within the cavities running parallel to the *y* direction.

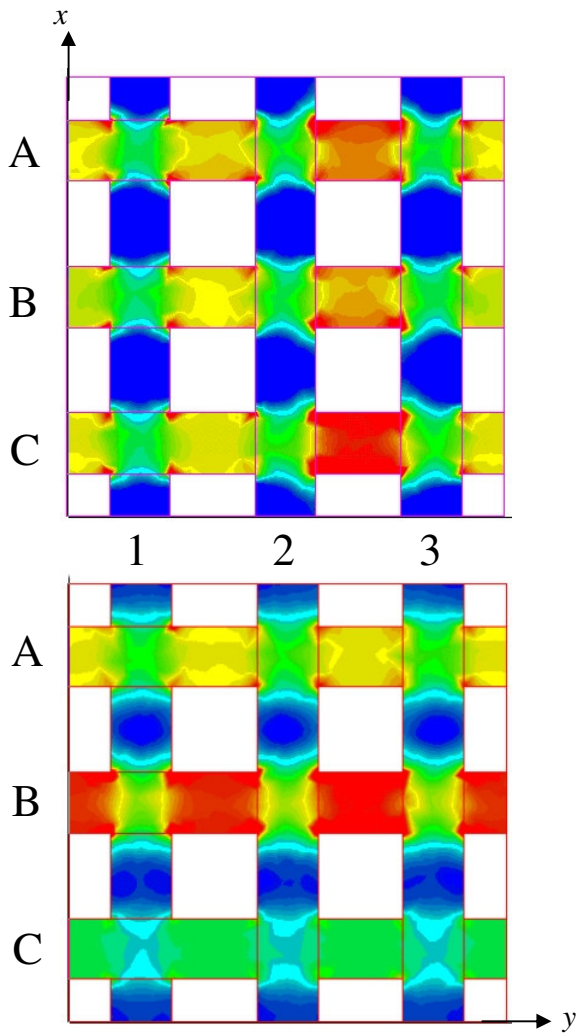

Figure 5.5.8 (a) and (b) The relative field magnitudes at the resonant frequency of the 21 and 19 GHz modes respectively, evaluated over a plane that cuts through the grating cavities at one third the depth of the deep grooves. Field magnitude ranges from dark blue = 1 to red = 15, relative to an input field of 1, averaged over 360º of phase. Grooves *1* and *C*

correspond to the shallower grooves with the remainder being the deep grooves. Radiation is incident in the *x-z* plane at an angle of 52º to the normal and p-polarised.

Evaluation of the electric vector for the 21GHz mode over 180 degrees of phase φ (*Figure 5.5.9*) shows the oscillating nature of the fields pertaining to grooves *A* and *B* to be anti-symmetric whilst the field in groove *C* leads that of *B* by 90º. The field magnitude shows that the high field is confined to a region of the shallow groove (*C*) bounded by two deep grooves. As a result, coupling to the non-dispersive mode is dependent predominantly on field oscillation in the shallow grooves only. Thus this non-dispersive mode may be excited by either p or s-polarised radiation for values of θ up to and including normal incidence due to the symmetric nature of the charge density oscillation.

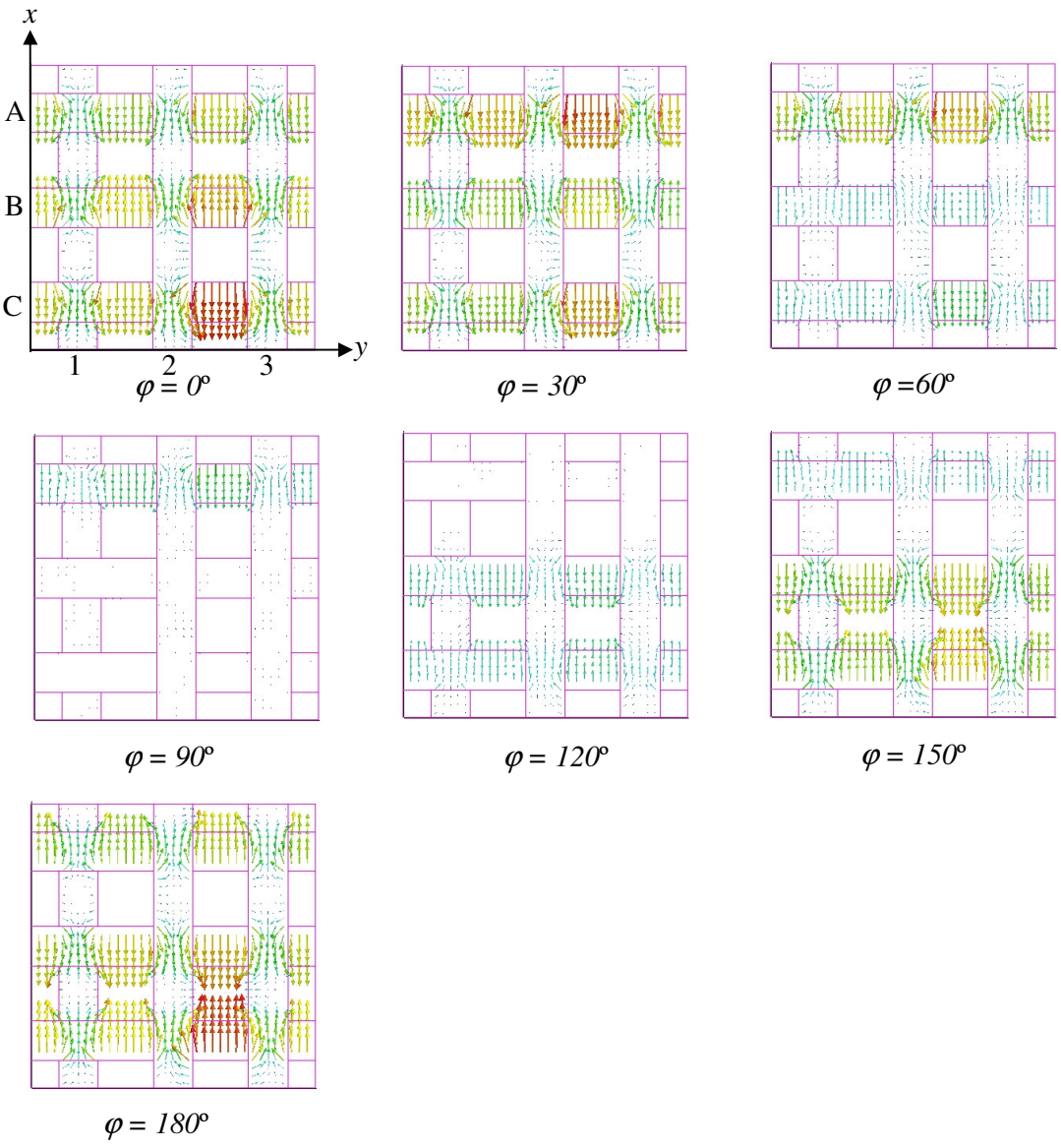

Figure 5.5.9 The modelled electric vector (arrows) of the scattered field at the resonant frequency of the 21GHz mode, evaluated over a plane that cuts through the grating cavities at one third the depth of the deep grooves.

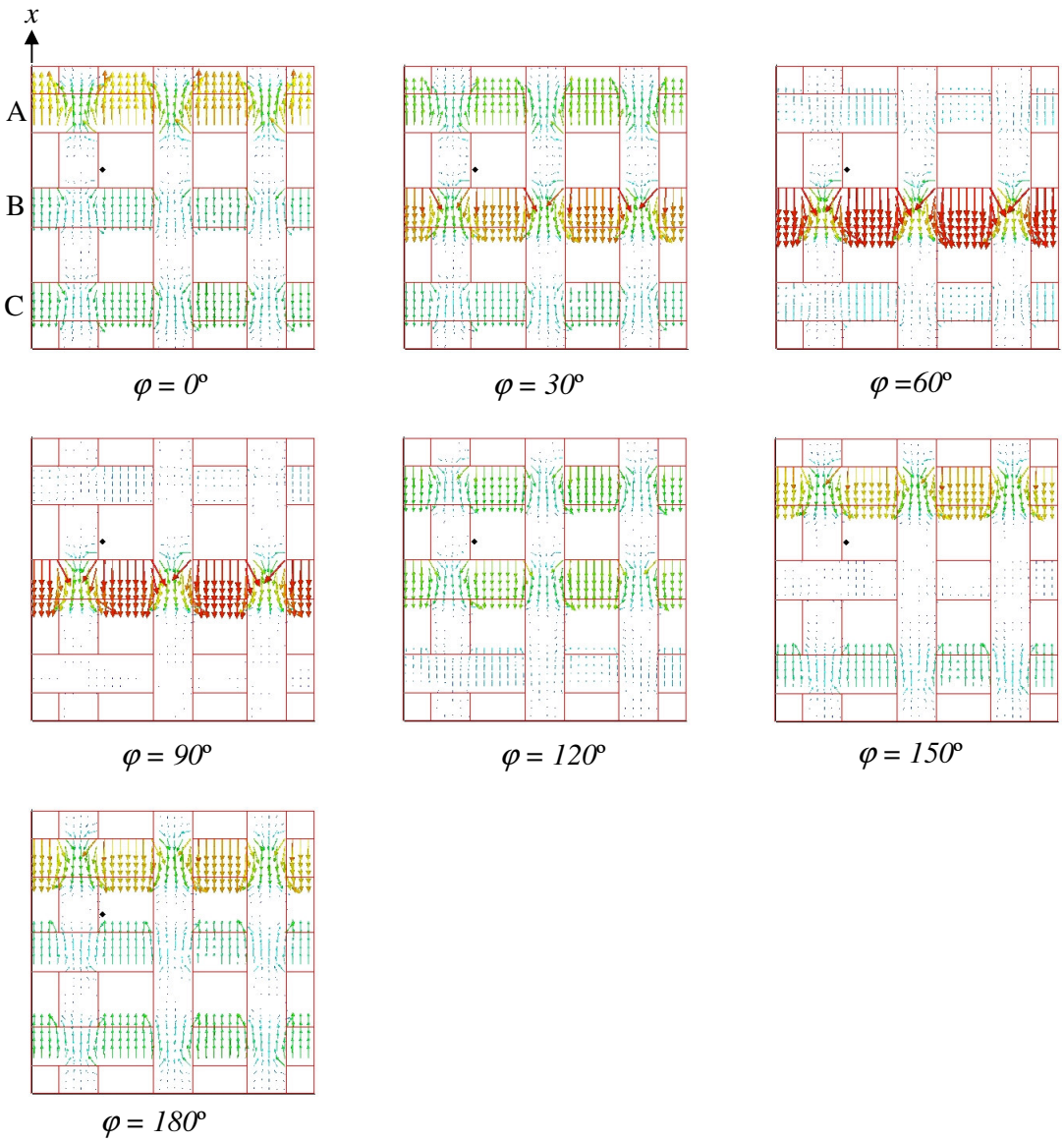

Figure 5.5.10 The modelled electric vector (arrows) of the scattered field at the resonant frequency of the 19 GHz mode, evaluated over a plane that cuts through the grating cavities at one third the depth of the deep grooves.

The fields of the more dispersive 19 GHz mode are seen from *Figure 5.5.8* (b) to be associated with the two deeper grooves (*A* and *B*). Field magnitudes in these two regions are comparable, and from *Figure 5.5.10* the charge density oscillation is close to being in anti phase. For the p-polarised case at finite θ the incident plane wave is able to excite an anti-phase oscillation at $\phi = 0^{\circ}$ due to the phase reversal of the incident electric vector providing a component of electric field in the $+x$ and $-x$ directions in the vicinity of adjacent grooves simultaneously. However, in the s-polarised case the phase reversal of the incident electric vector occurs in the y direction, perpendicular to the direction of mode propagation and thus at $\phi = 0^{\circ}$ it may not excite this mode.

5.6 Summary

In this chapter a thorough reflectivity study of a dual pitch non-diffracting metal bi-grating in the microwave regime has been presented. The dual periodicity and four fold symmetry of the bi-grating results in a structure which not only supports a remarkably non-dispersive SPP mode that is largely independent of θ, but unlike previous dual period gratings is independent of both azimuth angle and polarization of the incident beam. This mode is shown to be an extremely efficient absorber of incident radiation at frequencies which may be tuned by the physical parameters of the grating, clearly demonstrating the potential of selectively absorbing designer-surfaces. Coupling to a further flat-banded mode associated with (1,1) scattering is also noted. Experimental data shows excellent agreement with model predictions, allowing modelled field profiles to be evaluated. Coupling characteristics of the modes are explained as are the fundamental origins of each mode.

Chapter 6

Low angular-dispersion microwave absorption of a metal dual-pitch non-diffracting hexagonal grating.

6.1 Introduction

In *Chapter 5* an angle dependent reflectivity study of a dual period non-diffracting bi-grating is presented, the dual periodicity and four fold symmetry of which supports a SPP mode that is largely independent of θ, but unlike previous dual period gratings, is independent of both azimuth angle and polarisation of the incident beam. This mode is shown to be an extremely efficient absorber of incident radiation at frequencies which may be tuned by the physical parameters of the grating, clearly demonstrating the potential of selectively absorbing designer-surfaces. The obvious progression to this work is to introduce a higher order of rotational symmetry. It will be shown in this chapter that the hexagonal dual period structure, formed from three identical dual period profiles orientated such that each grating vector is parallel to the surface plane of the sample at 60º with respect to each other, introduces 30º rotational symmetry, thereby increasing the degree of azimuth angle independence of the lowest frequency SPPR. In addition, the hexagonal symmetry provides the possibility of coupling to several new modes due to the increase in scattering centres which exist in the conical mount. Seven readily observable modes are supported by the hexagonal structure (as opposed to three supported by the 45º bi-grating), five of which are largely non-dispersive, and independent of ϕ.

6.2 Experimental.

The sample studied in this chapter is a dual period zero-ordered 60º tri-grating. This combination of hexagonal and dual period symmetry gives rise to several possible symmetry configurations. One comprises of a shallower groove from each of the three grating directions crossing at a single point in each unit cell. A second consists of three pairs of shallower grooves crossing at the corners of a triangle, as illustrated by *Figure 6.2.1* (a) and (b).

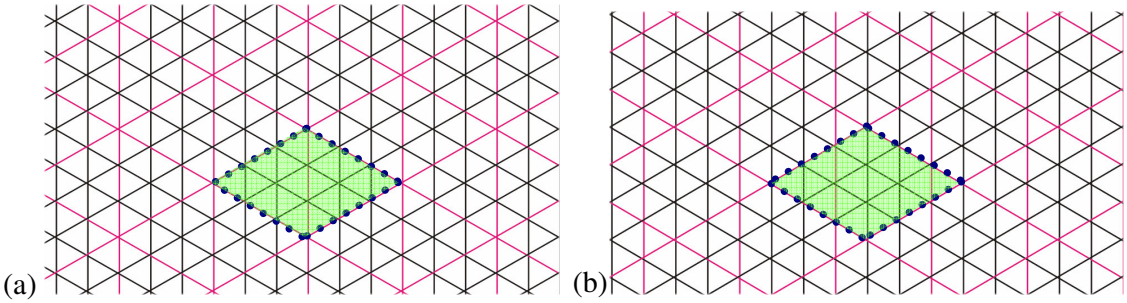

Figure 6.2.1 A schematic representation of just two of the possible symmetry configurations for the dual period hexagonal tri-grating. Deep grooves correspond to black lines and the red lines represent the slightly shallower groove. The unit cell is also highlighted in each case.

Both configurations were extensively modelled using the finite element code, and it is the first symmetry configuration that is presented in this chapter, with the grating profile of two deep (2.19 mm) and one slightly shallower (1.89 mm) evenly spaced 0.8 mm wide grooves per repeat period of λ_g = 7.2 mm, milled in three orientations at 60º with respect to each other into the surface of a circular aluminium alloy plate of radius 410 mm and thickness 20 mm, as shown by *Figure 6.2.2*(a). Due to the position in frequency of the SPPR being highly sensitive to variations in groove depth between each grating profile, as noted for the bi-grating in *Chapter 5*, average groove dimensions were measured using a milling machine in combination with a digital readout and electronic sensor, for use when modelling the theoretical response of the

structure. The angle of incidence θ and azimuth angle ϕ are shown in *Figure 6.2.2* (b) together with the reciprocal lattice vectors for this structure. For simplicity we define ϕ =0º when one of the grating wave vectors lies in the plane of incidence.

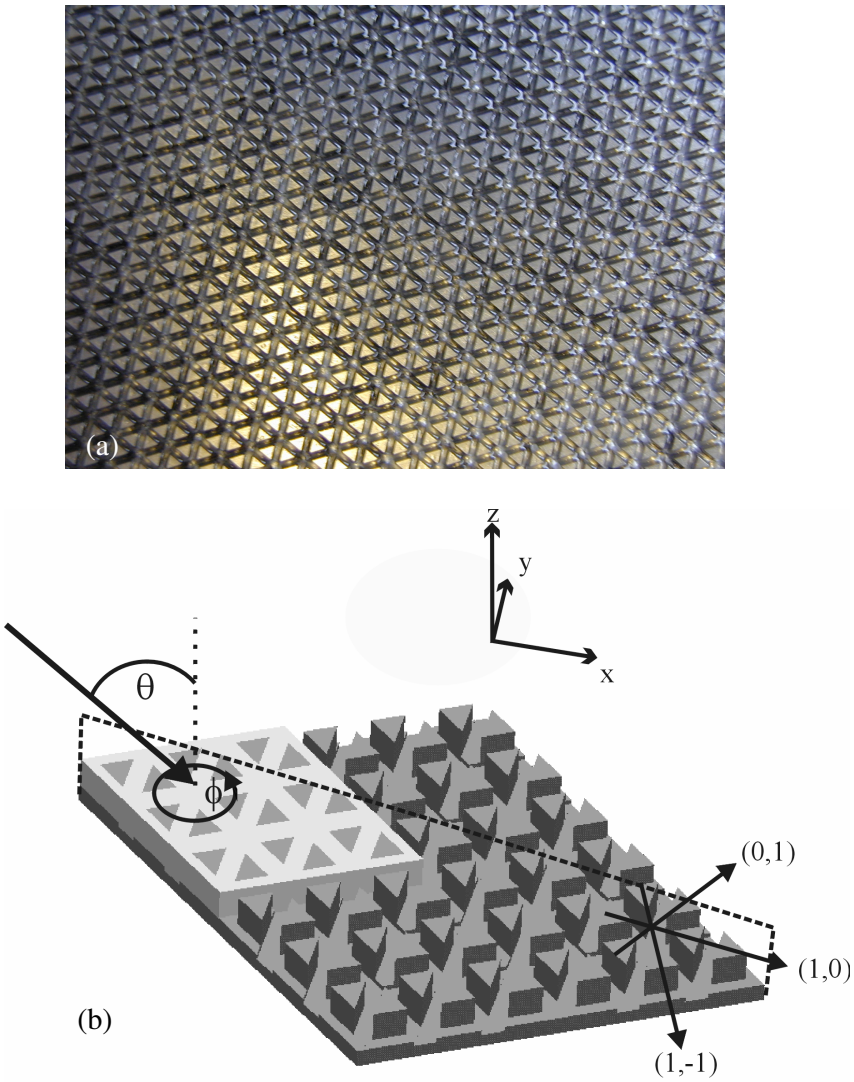

Figure 6.2.2 (a) The hexagonal tri-grating consisting of a grating profile with two deep and one slightly shallower evenly spaced grooves per repeat period of λ_g = 7.2 mm, milled in three orientations at 60º with respect to each other into the surface of an aluminium alloy substrate. (b) The angle of incidence θ and azimuth angle ϕ, together with the reciprocal lattice vectors for the hexagonal dual-period structure.

As in the case of the 45º bi-grating, the hexagonal dual period tri-grating is zero-ordered over the selected frequency regime ($18 < f_0 < 26$ GHz). Hence no reflectivity losses will occur in the zero order beam due to re-radiation into a diffracted order. Since energy dissipation via Joule heating of the substrate is also not an available loss channel [*Chapter 5 section 3.2*], to readily observe the SPPR in the specular reflectivity from the sample the grooves are once again filled with a petroleum wax ($\varepsilon = 2.16 + 0.02i$) which is slightly lossy at these frequencies.

A collimated beam of microwave radiation is directed onto the sample, which is mounted upon a rotating turntable, providing data for $0º \leq \phi \leq 360º$ at fixed values of θ. These angles are set to a precision of ±1°. The signal is normalised to the reflectivity of a flat plate of the same material and surface plane dimensions as the substrate. A spherical mirror is positioned to collect the specularly reflected beam from the grating and focus it into the detector. To reduce the footprint of the beam to a well collimated central part, a circular aperture of diameter 295 mm bounded by highly efficient microwave absorbing material was placed over the source mirror. In addition, at high angles of incidence an adjustable aperture was used, positioned between the source mirror and the sample. This restricted the incident beam to the area of the sample only, reducing interference in the specular reflectance.

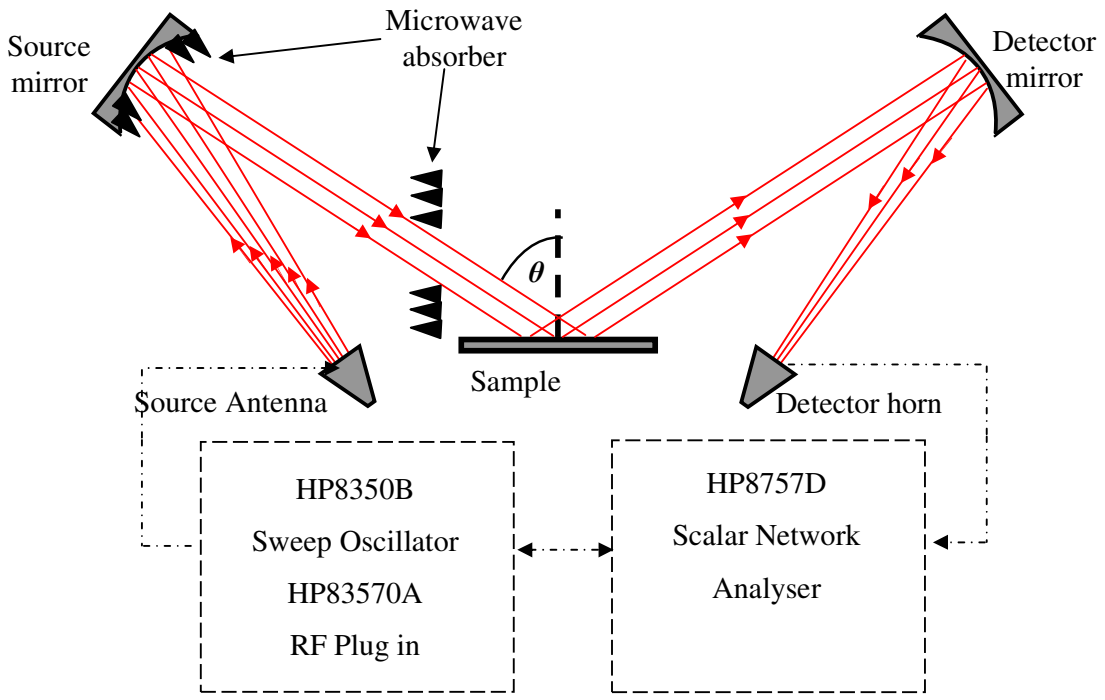

Figure 6.2.3 Schematic diagram illustrating the apparatus used to measure the wavelength-dependent response from a sample at fixed polar angles of incidence (θ).

The Hewlett Packard HP8350B sweep oscillator was used in conjunction with a HP83570A RF plug-in to generate radiation of wavelength $11.3 < \lambda_0 < 16.7$ mm. A Narda 8401 standard gain horn connected to the plug-in via a flexible waveguide directs the emitted radiation onto the sample via the collimating mirror. The source signal is split before emission by a directional coupler into a source and reference signal which is fed into a HP8757D scalar network analyser allowing normalisation of the detected signal. Radiation incident upon the sample is reflected and directed to a matched standard gain horn and crystal detector which is connected to the scalar network analyser, which in turn is connected to a PC using a HP interface bus. The PC records data sets and controls the turntable, allowing the ϕ-dependent response of the sample to be recorded. The source antenna and detector may be set to pass either *p*-, or *s*-polarisations, defined with respect to the plane of incidence. This enables the measurement of R_{pp}, and R_{ss}, and polarisation conversion R_{sp}, and R_{ps} reflectivities.

6.3 Modelling.

The unit cell for this structure comprises of a lozenge with side lengths equal to $\lambda_g / \cos\alpha$, as shown in *Figure 6.3.1,* with 3 shallow grooves converging on a point at each corner.

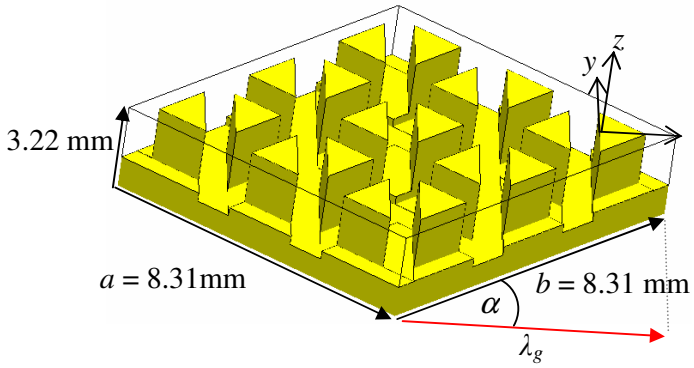

Figure 6.3.1 The 60º crossed grating unit cell.

The substrate (of thickness 3.22 mm) is modelled as aluminium. As discussed in *Chapter 4 section 3.3*, at the surface of metallic objects HFSS assigns a finite conductivity boundary, approximating the behaviour of the fields at the surface of the object using a surface impedance treatment. This surface impedance approximation is based upon the conductivity of the material, in this instance $\sigma = 3.8\times10^7$ siemens/meter. The grooves of the substrate were filled with a volume simulating the wax filler, described by a complex relative permittivity of $\varepsilon_d = 2.16 + 0.02i$. An air box of vertical height 20 mm was placed over the surface of the structure upon which a PML of thickness 10 mm was situated, allowing the reflectivity from the sample to be calculated at non-normal angles of incidence whilst reducing the possibility of reflections of the scattered field from the upper terminating boundary. The parallel outer boundaries of the model were assigned master-slave boundaries.

The mesh used to solve the fields pertaining to the hexagonal structure was produced using an initial wavelength based refinement. A subsequent eleven adaptive refinements increased the number of tetrahedra within the mesh by a maximum of 20% per pass, providing a mesh of approximately 20,000 tetrahedra. Unlike the bi-grating structure,

the removal of the three sets of grating grooves results in the formation of triangular 'pillars', the corners of which support high concentrations of charge, providing small regions of space within the dielectric filler with comparatively high electric field magnitudes. It was therefore necessary to insert a further 10,000 tetrahedra via the manual mesh process, refining over the surface of the structure. The resulting manual mesh was then used as a platform for a further three adaptive passes for each value of frequency at which the reflectivity was calculated. Hence the mesh providing the final solution for the hexagonal grating was in excess of 48,000 tetrahedra.

6.4 Results and discussion

Figure.6.4.1 shows the p-polarised frequency-dependent reflectivity data for (a) θ = 38º ϕ = 0º, and (b) θ = 51º ϕ = 0º together with the modelled response of the structure obtained from the finite element code. Also shown (*Figure.6.4.2* (a) and (b)) is the s-polarised frequency-dependent reflectivity data for the same angles of incidence.

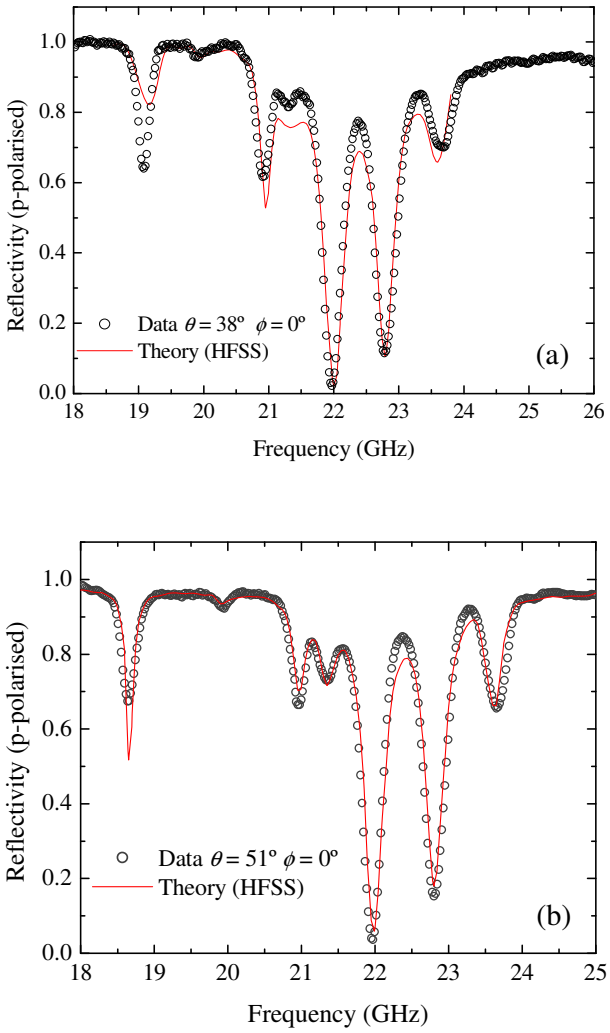

Figure 6.4.1 p-polarised reflectivity data obtained for (a) θ = 38º, ϕ = 0º, and (b) θ = 51º, ϕ = 0º. Seven resonances are clearly visible in the specular reflectance from the hexagonal structure. The modelled response of the structure is obtained using a finite element code.

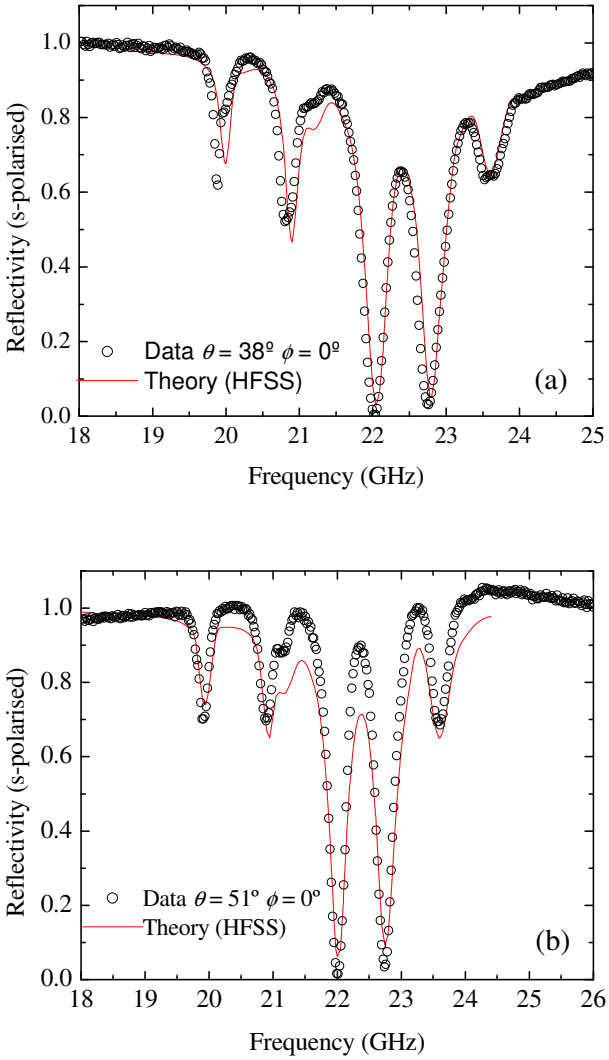

Figure 6.4.2 s-polarised reflectivity data obtained for (a) $\theta = 38°$, $\phi = 0°$, and (b) $\theta = 51°$, $\phi = 0°$.

Good agreement is obtained between the model and data even though the experimental incident angle spread is approximately 1º. For the p-polarised data, a total of seven resonances are visible over the selected frequency range, whilst six resonances are visible in the s-polarised reflectivity data. At the frequency of the two main resonances, as little as 3% of the incident radiation is re-radiated into the specular reflectance. The frequency-dependent polarisation conversion data is presented in *Figure 6.4.3,* for $\theta =$ 51º, obtained with the source and detector set to pass *s* and *p*-polarised radiation data respectively.

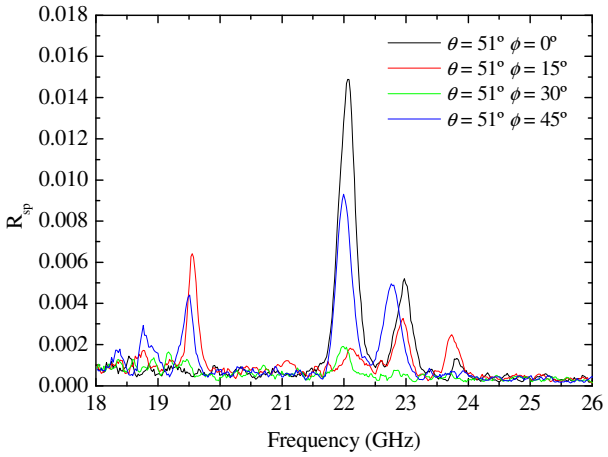

Figure 6.4.3 *s-p* frequency-dependent polarisation conversion data obtained for $\theta = 51°$ $\phi = 0$, 15, 30 and 45°.

Polarisation conversion is shown to be maximum at ϕ = 0° (ϕ = 0° and ϕ = 60° are equivalent for this structure). At the resonant frequency of the first deep mode, polarisation conversion accounts for less than 2% of the signal deficit noted in the specular reflectance. As discussed in *Chapter 5*, the structure is zero-ordered and thus polarisation conversion is the only radiative loss channel available to the SPP. Further, since Joule heating of the metal substrate is negligible at microwave frequencies, the width and depth of the observed resonances may be attributed entirely to the absorbance of the wax filler.

From *Figures 6.4.1* (a) and (b) it is clear that the hexagonal structure supports considerably more modes than the bi-grating discussed in *Chapter 5*, due to the hexagonal symmetry. In order to identify the dispersion of each mode, resonant frequencies at ϕ = 0° over the range 12°<θ<75° are plotted in *Figure 6.4.4* against the associated in-plane momentum $k_x = (2\pi f/c)\sin\theta$ where f is the resonant frequency and c is the speed of light. This plot clearly shows the remarkably non-dispersive nature of the six higher frequency resonances as a function of θ, whilst the lowest frequency mode remains less localised in nature and more dispersive, curving downwards toward k_g at zero frequency. Reflectivities associated with the resonances at 22 and 22.8 GHz are always less than 10 and 22% respectively for θ<60°.

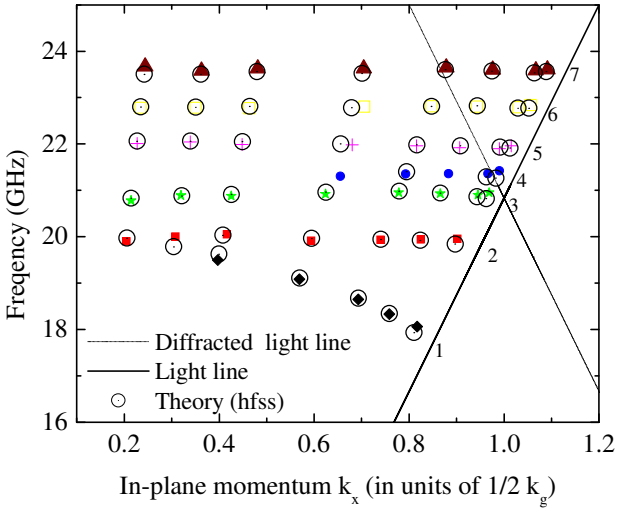

Figure 6.4.4 The experimental and theoretical dispersion curves of modes 1 through 7 (1 being the lowest energy mode and 7 being the highest) at $\phi = 0°$. The position in frequency of each mode in the range $12° < \theta < 75°$ is plotted against the associated in-plane momentum $k_x = (2\pi f/c)\sin\theta$ where f is the resonant frequency and c is the speed of light. Also shown is the light line and the (1,0) diffracted light line.

Figure 6.4.5 shows (a) p-polarised and (b) s-polarised reflectivity data at θ = 38º, demonstrating the polarisation independent properties of the hexagonal grating. Dark regions correspond to strong absorption whilst light regions represent reflection. Modes at 21, 22, 22.8 and 23.7 GHz, are visible, strikingly flat in frequency over the entire range of azimuth angle.

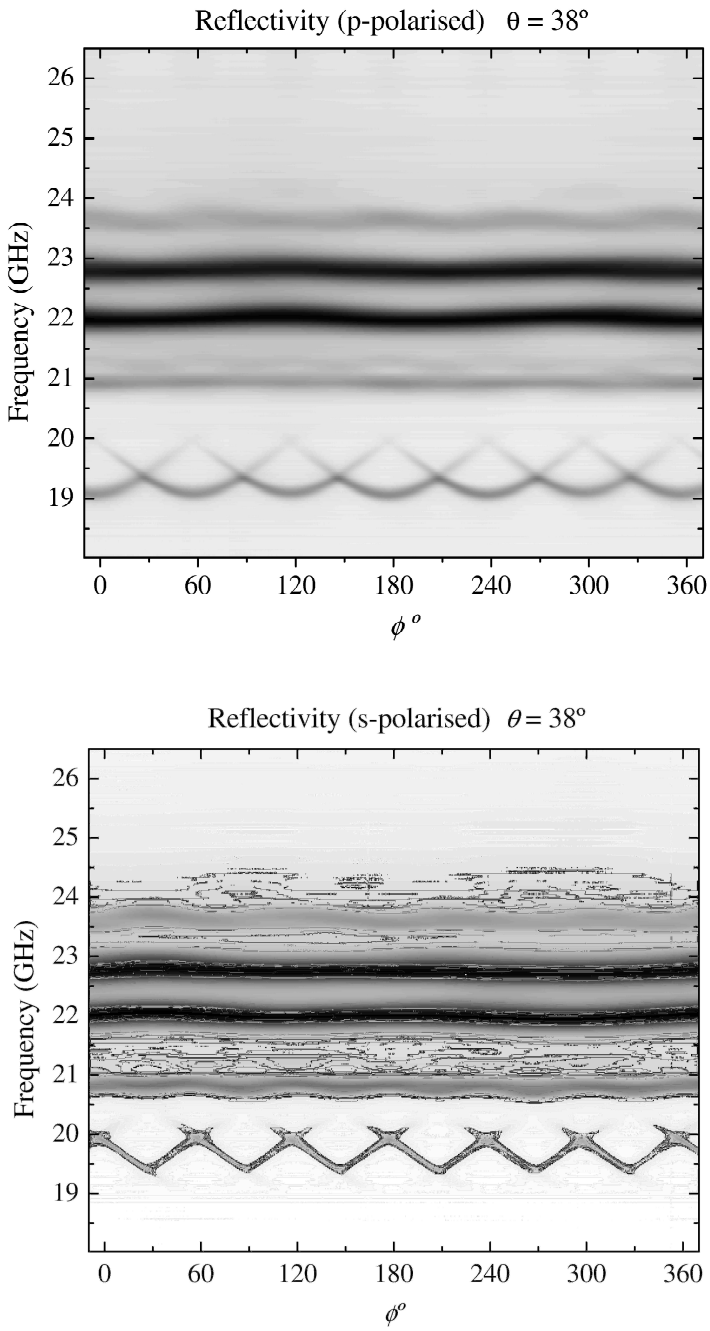

Figure 6.4.5 (a) p-polarised and (b) s-polarised reflectivity data as a function of both frequency and azimuth angle at a fixed polar angle of 38º. Light regions correspond to strong reflection whilst dark regions correspond to absorption.

It is also clear from the ϕ dependent reflectivity data that the two lowest modes exhibit 6 fold symmetry imposed by the hexagonal structure. These two modes intersect at ϕ = 30º identifying them as (1,0) and (0,1) modes respectively, since at ϕ = 30º the (1,0) and (0,1) directions are degenerate (*Figure 6.4.6*).

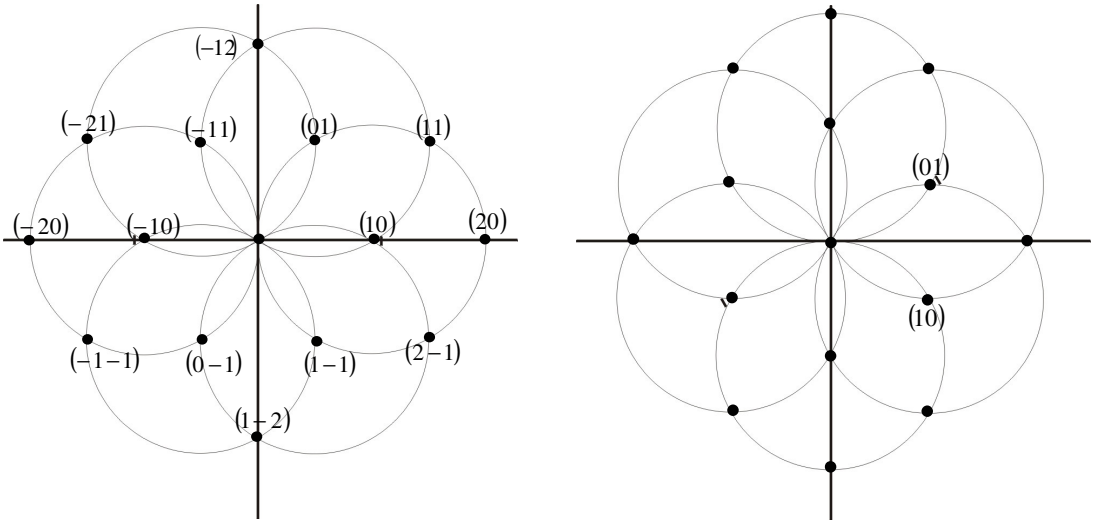

Figure 6.4.6. Schematic representing the reciprocal lattice and light circles for hexagonal symmetry. Upon a 30º rotation, it is clear that the (10) and (01) modes are mirrored by k_x.

To confirm the origins of the lowest two modes it is useful to evaluate the fields at the resonant frequency of each mode using the finite element code. *Figure 6.4.7* shows the relative time averaged magnetic field magnitude calculated over a plane parallel to the surface plane of the grating, at z = -1.1mm (where z = 0 is defined as the uppermost surface of the metallic structure in the xy-plane). Radiation is incident in the x-z plane at an angle of 50.7º to the normal and is p-polarised.

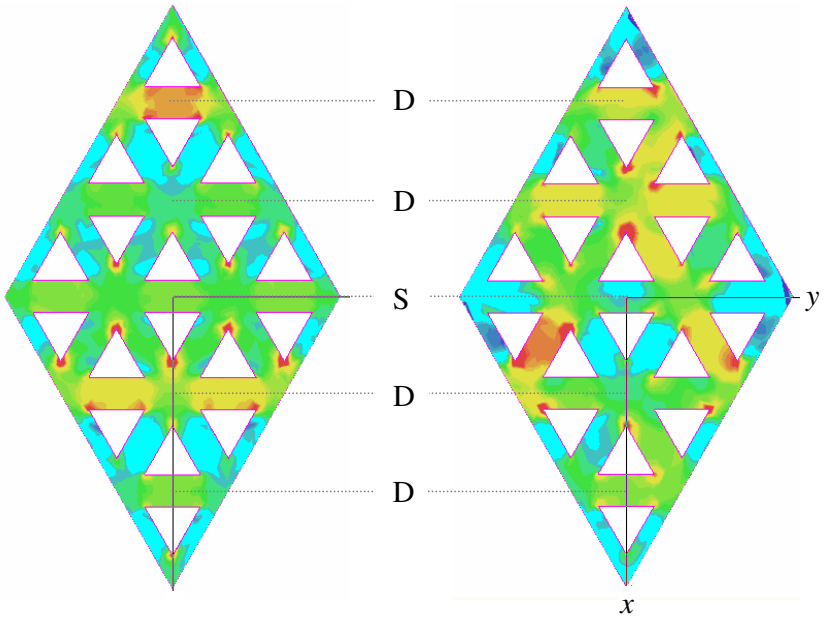

Figure 6.4.7 Relative magnetic field magnitudes at the resonant frequencies of modes 1 and 2 respectively, modelled over a plane parallel to the surface of the unit cell and cutting through the grating cavities at half the depth of the deep grooves. Deep grooves are labelled D, shallow grooves are labelled S.

Regions of high field at the resonant frequency of mode 1 are shown to be confined predominantly to the second deep groove, and displays a periodicity of twice the grating pitch in the (10) direction only. At the resonant frequency of mode 2, this periodicity is repeated in the (01) direction, with regions of high field once again confined to the second deep groove, however some degree of excitation in the remaining two grating directions is evident. On inspection *Figure 6.4.6* (a) once more it is clear that the (01) and (1-1) modes are degenerate at $\phi = 0^{\circ}$, hence mode 2 comprises of the superposition of two modes arising from (10) and (1-1) scatter.

It is important to note here that the SPP modes in reciprocal space pertaining to the dual period 60º tri-grating may not be represented by circles slightly larger in radius than the light circles of *Figure 6.4.6,* since the SPP modes are heavily perturbed by the amplitude of the grating profile. The perturbation of the SPP mode as a function of groove depth is modelled and shown (for simplicity) for a single dual period grating profile in *Figure 6.4.8*.

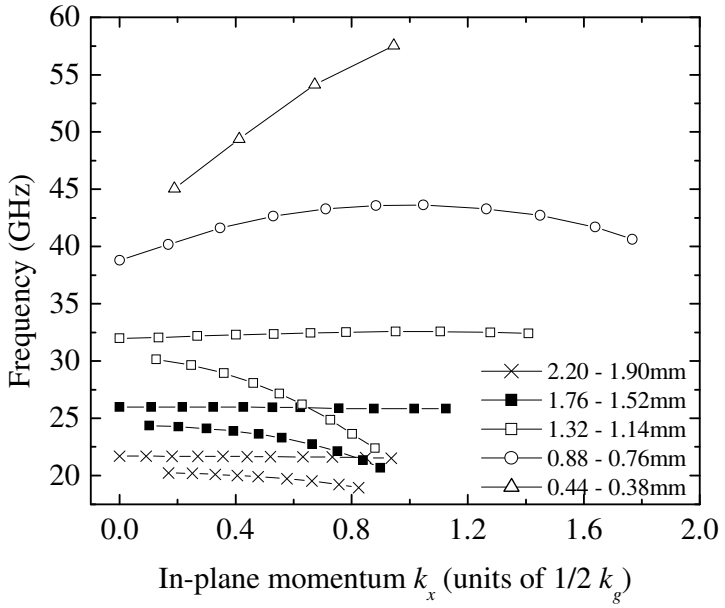

Figure 6.4.8 The dispersion of the SPP modes supported by a single dual-period grating profile (identical to those constituting the 60º tri-grating studied in this chapter) as a function of groove depth.

As the grating amplitude increases, the group velocity of each mode reduces, and both modes reduce in frequency. It is also apparent that although compressed, the higher frequency mode is not so heavily perturbed by the grating amplitude that it passes through the lower frequency mode. Since this is true for a single dual period profile, the same argument holds for the hexagonal structure, and therefore it would seem reasonable to assume that the modes energetically line up in the same order as the diffracted light lines (which to first order are equivalent to the unperturbed SPP case at

microwave frequencies). This is a valid assumption even for the dual-period profile, since as shown in *Chapter 5*, it is only the long period component of the profile that is responsible for the folding of the modes back into the radiative region of momentum space. Consider *Figure 6.4.8*, which shows the diffracted light lines pertaining to the hexagonal structure as a function of frequency, and in-plane momentum. Recall from *Chapter 3* that light circles in 3-dimensions form cones, and thus *Figure 6.4.9* represents the diffracted light-lines of *Figure 6.4.6* (a) but plotted over the *xz*-plane passing through points (10) and (20).

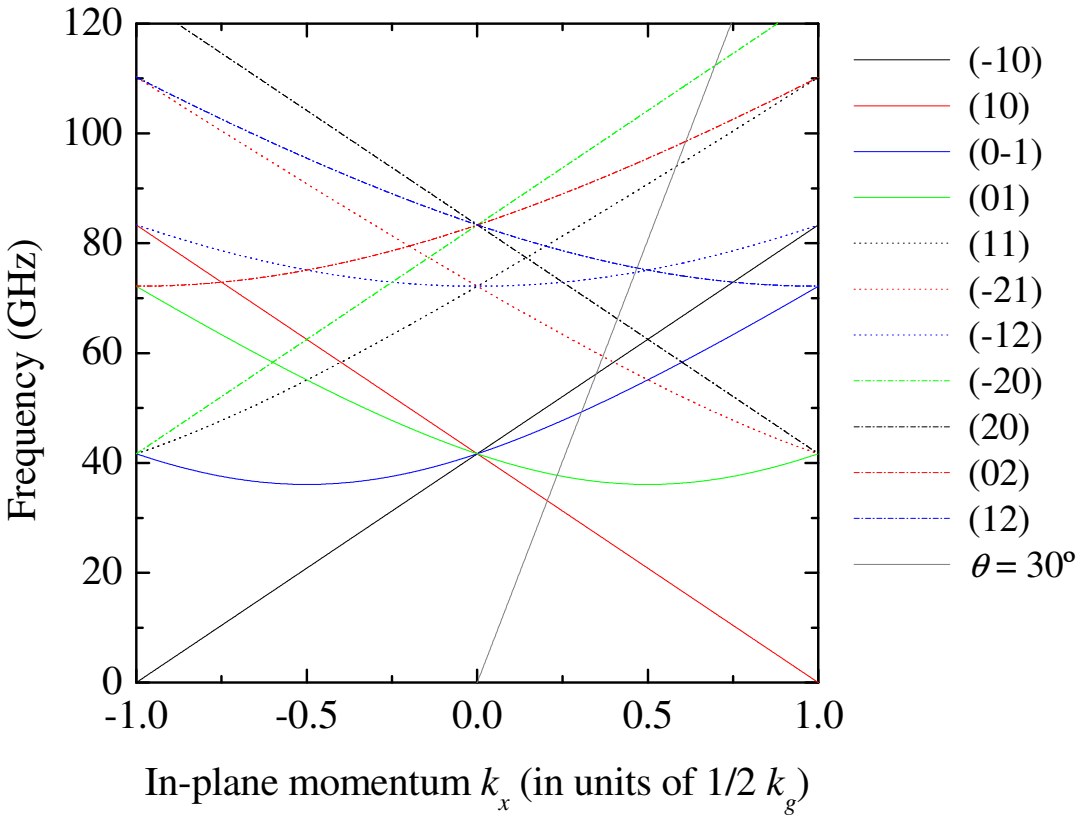

Figure 6.4.9. The diffracted light lines pertaining to the hexagonal dual-periodic structure. $\theta = 38°$ is highlighted by the single grey solid line.

Firstly it is clear that at $\theta = 0$ all light lines intersect at one of three points over the selected frequency range, and hence at normal incidence only three of the hexagonal modes should be visible. This is confirmed by the finite element code in *Figure 6.4.10,* which shows modelled reflectivity from the sample when illuminated by p-polarised normally incident plane wave radiation at $\phi = 0°$. At $\theta = 38°$, highlighted in *Figure 6.4.9* by the grey solid line, 11 light lines are intersected and labelled over the frequency range shown.

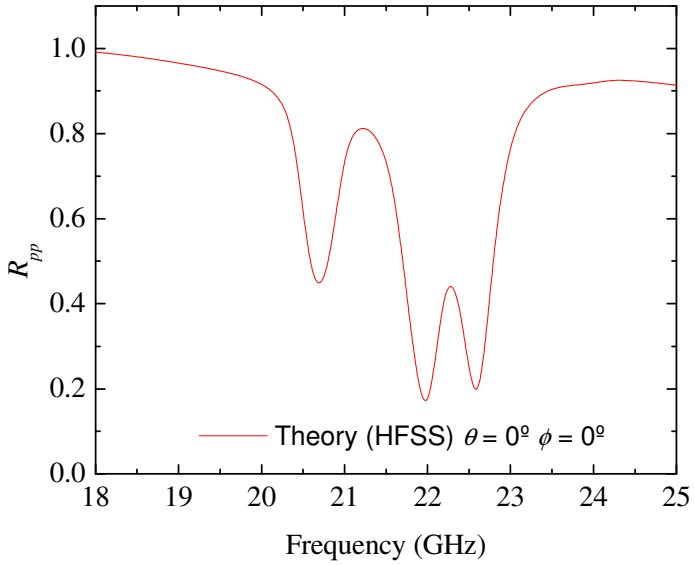

Figure 6.4.10 The theoretical reflectivity of the hexagonal structure when illuminated by p-polarised normally incident plane wave radiation at $\phi = 0°$, obtained using the finite element code.

Once the order from which the SPP modes should arise in frequency for a given value of θ has been inferred by the light line diagram it is simply a question of associating each mode in *Figure 6.4.5* (a) with a diffracted light line. However, due to the perturbation of the modes by the amplitude of the grating, it is impossible to ascertain with the given resolution how many modes exist, since some modes may be squashed

down and superimposed upon one another at single values of frequency. Further, the perturbation gives rise to the possibility of band gaps opening up in the dispersions of the modes.

Instead it is easier to consider the hexagonal grating as three single dual-period profiles with associated grating vectors in the (10), (01) and (1-1) directions. Each of the three profiles supports a 1st order mode, originating from (10), (01) and (1-1) scatter. These modes are generally more dispersive, and they correspond to modes 1 and 2, of *Figure 6.4.5* (a) at $\theta = 0^{\circ}$ (recall from *Figure 6.4.6* that at $\phi = 0^{\circ}$ the (01) and (1-1) points are degenerate, and at $\phi = 30^{\circ}$, the (01) and (10) are degenerate). Modes 5 and 6 are then the modes arising from second order scattering in the three grating directions. These modes are generally much stronger and non-dispersive. Thus mode 5 is a (20) mode, and mode 6 is a (2-2), (02) mixed mode. In a similar manner Modes 3 and 7 correspond to the flat banded modes resulting from (11) and (22) scatter respectively.

6.5 Summary

In this chapter a thorough angle dependent reflectivity study of a dual period, zero-order hexagonal tri-grating has been presented. This work forms an extension to the bi-grating work presented in *Chapter 5*. Although it is difficult to improve upon the remarkable degree of azimuth angle independence displayed by modes supported by the bi-grating structure through the introduction of a higher degree of rotational symmetry, the hexagonal structure gives rise to an increase in the modes supported. It has been shown that a total of seven modes are present in the specular reflection from the sample over the selected frequency range. At least five of these modes are shown to be remarkably non-dispersive as a function of both θ and ϕ. Further, two of the modes are shown to be extremely efficient absorbers of incident radiation at frequencies which may be tuned by the physical parameters of the grating. Experimental data shows good agreement with model predictions, allowing modelled field profiles to be evaluated.

Chapter 7

Surface-topography induced enhanced transmission and directivity of microwave radiation through a sub-wavelength circular metal aperture.

7.1 Introduction

The previous two experimental chapters of this thesis have been primarily concerned with the use of structures that support surface waves, leading to strong resonant absorption of incident radiation at frequencies determined by the surface profile. In this chapter however, attention is turned to the role of the surface structure in the enhancement of transmission through circular apertures whose diameter (d)$\leq\lambda_0/2$. Such apertures are normally assumed to possess poor transmissive properties [*Bethe* (1944)]. Any enhancement of this transmission will have wide ranging device applications, for example near field scanning microscopy where the resolution is largely dependant upon the diameter of the aperture. A historical review of the transmission enhancement phenomenon is presented, followed by the first experimental study at microwave frequencies of a single sub-wavelength circular aperture ($d\sim\lambda_0/2$) surrounded by a surface structure comprising of four concentric grooves on either the illuminated or exit side of the sample or both. Undertaking the experiment at microwave wavelengths allows for a precision of manufacture and optimisation that would be difficult to replicate at optical frequencies, and demonstrates that transmission enhancement may be achieved on near perfect metals where absorption is considered negligible. Further, the use of HFSS to model the theoretical electromagnetic response of the sample allows the fields associated with transmission enhancement to be examined, and hence better understand the role of the surface profile in the enhancement mechanism.

7.2 Background.

From standard aperture theory [*Bethe* (1944)] it is accepted that circular apertures with diameter (d) smaller than the wavelength (λ_0) of incident radiation may be considered to possess poor transmissive properties. Unlike slits of similar dimensions, circular apertures of $d<1.841\lambda_0/\pi$ in an opaque metal layer are unable to support propagating TEM modes [*Chapter 3, section 3.3.3*]. As a result, energy may only be transferred by an evanescent tunnelling process leading to very weak transmission (which is expected to scale as $(d/\lambda_0)^4$ [*Bethe* (1944)]). Further, for $\lambda_0>>d$ the resultant Airy disk pattern of irradiance in the far field is very broad in angle with the aperture resembling a secondary point source. However, the work of *Ebbesen et al.* (1998) in the optical regime generated great interest by showing that it is in fact possible to obtain transmission of light through sub wavelength hole-arrays in thin metal films several orders of magnitude greater than that predicted by standard aperture theory. Although studies of microwave transmission through arrays of circular holes had been conducted as early as 1972 [*N.A. McDonald* (1972) and references therein] it was *Ebbesen's* work that specifically highlighted the enhanced transmission phenomenon through *sub-wavelength* apertures. Their work initiated a number of theoretical and experimental studies at optical frequencies seeking to explain the underlying physics.

The enhanced transmission phenomenon has historically been attributed to the excitation of electromagnetic (EM) surface modes which are often referred to as surface plasmons (SP's) at optical frequencies [*Sambles* (1998), *Ghaemi* (1998) and *Popov* (2000)]. These authors assume that the evanescent fields associated with the SP enhance the evanescent field within the hole. Others suggest that the transmission enhancement may be entirely explained using a multiple diffraction argument [*Treacy* (2002)]. Further, it has been proposed that in the case of an array of sub-wavelength *slits*, the SP may actually play a negative role in transmission enhancement [*Cao* (2002)] due to absorption effects on resonance. Indeed, the arguments regarding the involvement of SP's in the enhancement mechanism intrinsically contain a multiple diffraction argument, as the process of both coupling into and re-radiating from a SP requires multiple diffraction events. Also it is important to note that the physics pertaining to

slits is fundamentally different to that pertaining to circular apertures, as slits may support a propagating TEM mode whereas sub-wavelength circular apertures do not [*R.E. Collin* (1991)].

By obtaining data as a function of incident frequency and in-plane wave vector, *Ghaemi et al.* (1998) strengthened the SP enhancement argument by demonstrating SP dispersion characteristics in the enhanced transmission spectrum through an array of sub-wavelength circular holes. Later, *Grupp et al*. (2000) were able to show that the magnitude of transmission enhancement was dependant only on the metallic properties of the two in-plane surfaces within a skin depth of the surface and was insensitive to the material of the core and walls of the aperture. Good metals showed a marked increase in transmission over poor metals; hence they concluded that the clear dependence of transmission efficiency on the optical properties of the metal-dielectric interface indicated the involvement of SP's. More recently, *Thio et al.* (2001) and *Lezec et al.* (2002) used the SP argument to explain enhanced transmission through a single circular sub-wavelength aperture, surrounded by a bull's eye structure. They attributed the enhancement in transmission to SP's supported on the illuminated surface of the aperture arrangement since the peak transmission wavelength coincides with the periodicity of the surface profile, however the theoretical model presented dealt only with a linear aperture (slit) in a semi-infinite perfectly conducting media. In addition there was strong angular confinement of the transmitted signal (approximately ± 3º) through the circular aperture which was attributed to re-radiation of light back into free space by a SP supported on the corrugated exit side of the sample. *Martin-Moreno et al.* (2001) later presented a theoretical explanation for this beaming effect in terms of surface resonances using a one-dimensional model. Again using a one-dimensional model, *Garcia-Vidal et al.* (2003) identified three main mechanisms that can enhance optical transmission: groove-cavity mode excitation, in-phase re-illumination and waveguide mode resonances within the aperture. However as previously discussed, for sub-wavelength holes (rather than one-dimensional slits), this last mechanism cannot operate. Recently, *Barnes et al.* (2004) not only showed SP polarisation characteristics in the transmittance through a sub-wavelength hole-array, but also showed SP dispersion characteristics in the absorbance, transmittance and reflectance data. They

concluded that although diffraction is central to the transmission phenomenon, the effect is dramatically enhanced when coupling conditions allow SP excitation on one or both of the in-plane surfaces.

Unlike the majority of previous studies into the enhanced transmission phenomenon (of which only a small number have been commented upon here) the experimental investigation presented in the following sections is conducted at microwave frequencies. In this regime, the skin depth of the metal (on the order of microns) is small in comparison to the incident wavelength, and as such the substrates are often wrongly considered as near perfect conductors. Corrugation of the substrate introduces a surface impedance and hence effective dielectric function (*Pendry et al.* 2004) thereby permitting resonant excitation of bound surface modes. However the coupling of incident radiation to such modes is inefficient due to minimal absorption compared to the degree of re-radiation from the mode. Therefore at these microwave frequencies, it is suggested that the role played by the SPP in the transmission enhancement mechanism may be small, and yet it will be demonstrated that with the addition of suitable surface topography, a 17 fold enhancement in transmission is still attained over that observed through a 'bare' aperture.

7.3 Aperture and photonic surface - optimisation and design.

Finite element method (FEM) software [HFSS, Ansoft Corporation, Pittsburgh, U.S.A] is used to predict the EM response of the aperture geometry leading to the optimum aperture design in a 1.5 mm thick substrate with a central cylindrical hole, and is fully described in *Chapter 4*. To reduce the mesh size and computational time, the model is simplified by making an impedance approximation on the surface of the aluminium substrate using a conductivity of $3.8\times10^{7}\,\mathrm{S}\cdot\mathrm{m}^{-1}$. Further, perfect E and H-symmetry boundaries inserted along the lines of electromagnetic symmetry (as shown in *Figure 7.3.1*) reduce the size of the problem space by a factor of four.

The resonant transmission wavelength was chosen such that the peak transmission efficiency would occur in the middle of a single experimental frequency range of $50<f_0<75$ GHz. This corresponds to a wavelength of λ_0 = 5 mm. To allow for a sufficiently deep surface corrugation on both the illuminated and exit side of the sample, the substrate thickness and therefore the cylindrical height (h) of the aperture was required to be at least 1.5 mm. Initial computational modelling demonstrated that the attenuation of the transmitted signal through the 2.50 mm diameter aperture was too high for sufficient signal detection. Hence the area immediately surrounding the hole was countersunk equally from each side, effectively reducing h to zero.

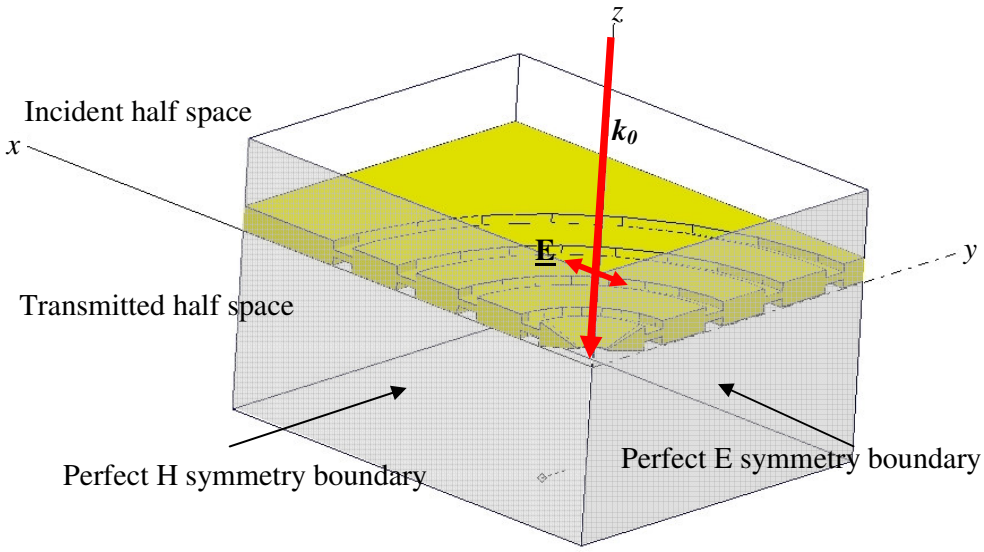

Figure 7.3.1 Geometry of the finite element model showing the electromagnetic symmetry boundaries and incident electric vector orientation. Unmarked outer faces are assigned as impedance boundaries in the transmitted half space, and as radiation boundaries in the incident half space.

Figure 7.3.2 shows field enhancement in the region of the aperture for f_0 = 60GHz as a function of groove position (measured from the centre of the aperture to the centre of

the groove) for a single circular groove of depth l = 0.45 mm and width w = 1.50 mm centred about the aperture.

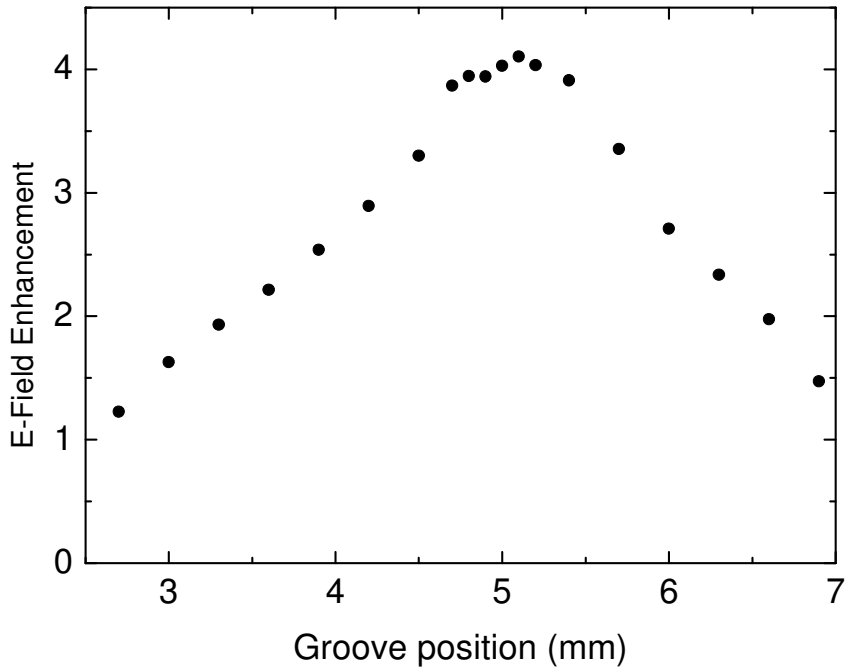

Figure 7.3.2 Computed time averaged maximum electric field enhancement as a function of groove position measured from the centre of the aperture to the centre of the groove for a single groove of depth l = 0.45 mm and width w = 1.50 mm at a fixed frequency of 60GHz.

The optimum field enhancement is found to coincide with a groove spacing of 5mm. In the same way, each groove was added and individually positioned, giving maximum field enhancement when all grooves were regularly spaced with a pitch λ_g = 5mm. The variation of field enhancement as a function of groove depth and width was then also explored. Initially, l was fixed at 0.4 mm as a starting point whilst w was varied for each groove simultaneously between 0.2 and 4 mm. *Figure 7.3.3* shows the magnitude of the time averaged electric field on the illuminated side of the construct as a function of (a) groove depth and (b) groove width.

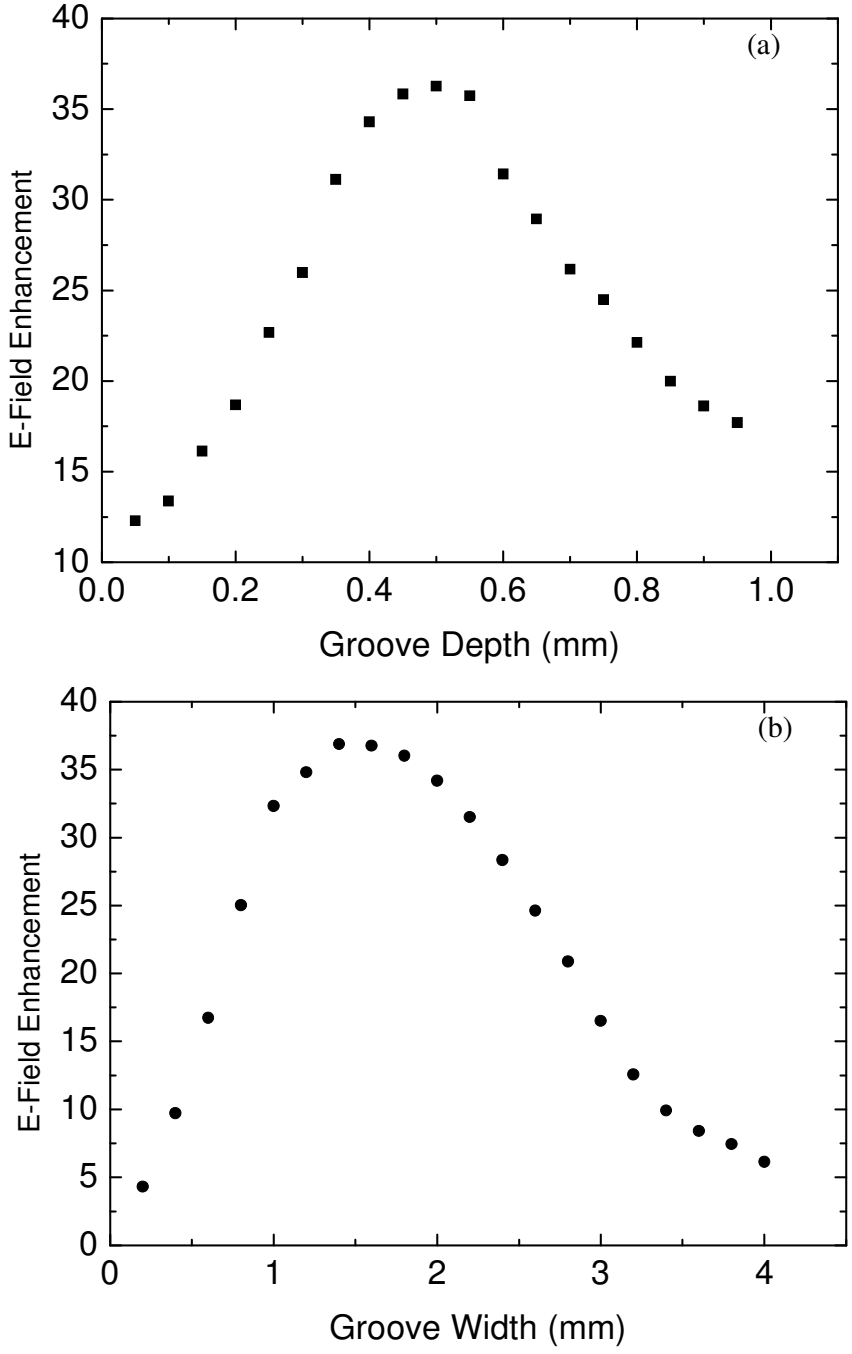

Figure 7.3.3 Time averaged maximum electric field enhancement as a function of (a) groove depth with 7 grooves each spaced by 5 mm with width w = 1.50 mm, and (b) groove width with 7 grooves each spaced by 5 mm with depth 0.50 mm, at a fixed frequency of 60GHz.

Simultaneous variation of the dimensions of all grooves on the illuminated side of the sample clearly shows peak field enhancement to occur when w = 1.50mm and l = 0.50mm. After the optimum groove dimensions and spacing were obtained it was possible to evaluate how the field magnitude in the region of the aperture varied with the number of grooves positioned in the illuminated in-plane surface. *Figure 7.3.4* shows that field magnitude increases steadily as the number of concentric grooves increases. It appears that the field enhancement would continue to increase with the addition of yet more grooves but a computational limit is reached with seven grooves. Subsequent studies and analysis is however constrained to a sample with four concentric rings in order to improve convergence and reduce computation time. This is sufficient to establish all principles.

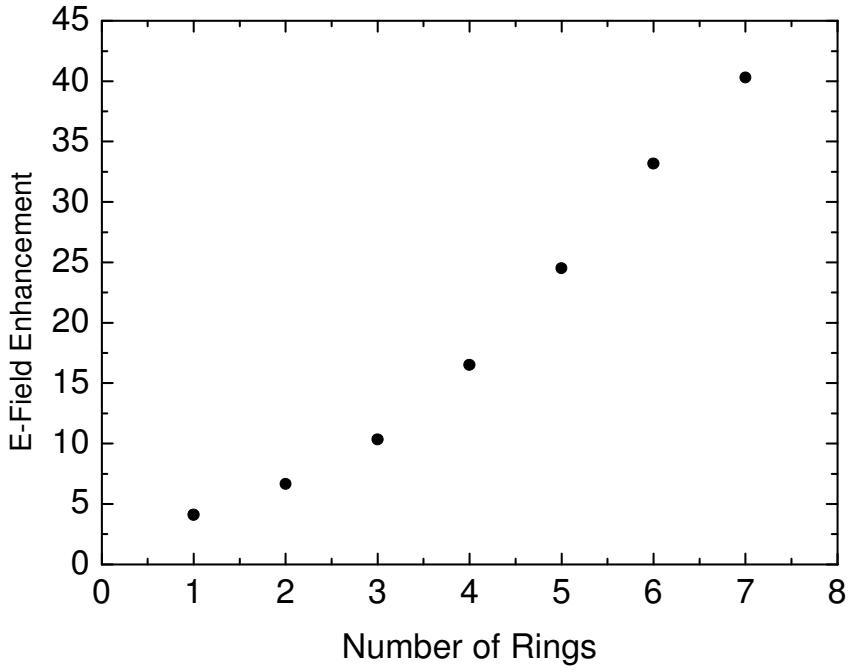

Figure 7.3.4 Time averaged maximum electric field enhancement as a function of the number of concentric rings centred about the aperture at a fixed frequency of 60GHz.

Once optimisation of the surface profile had been achieved with respect to field enhancement, the model could be finalised to run in transmission. It was found that the radiation boundaries situated on the outer faces of the air box in the incident half space required a minimum spacing from the closest radiating surface (the uppermost corner of the outer concentric ring) to avoid contributions to transmission through the sample by reflection. It was this minimum spacing limitation that set the final outer dimensions of the model and therefore the experimental input field plane to be 45×45mm. To ensure that the model accurately represented the experiment it was therefore necessary to limit the experimental size of the input plane wave using a microwave absorbing aperture between the sample and the source of the same dimensions. To obtain a suitable density of tetrahedra in the regions of high field when the computational model was run in transmission, the mesh was constructed from an initial incident wavelength based refinement and then refined further using the adaptive pass process, increasing the number of tetrahedra by up to 20% per pass. Once convergence had been achieved, the manual mesh maker was used to increase the mesh density at the surface of the substrate by specifying the minimum side length of tetrahedra. This mesh was then saved and used as a base for a further three adaptive passes for each value of frequency at which the model was solved. The final mesh used to evaluate transmission spectrum through the sample contained in excess of 80,000 tetrahedra.

7.4 Experimental sample and geometry.

Using optimisation data obtained from the previous section, a total of three samples were cut into 1.50 mm thick flat aluminium alloy sheet (*Figure 7.4.1*). Sample A consisted of a single countersunk circular aperture (d = 2.50 mm) with no patterning. Sample B consisted of an identical aperture surrounded on one face only by four concentric rectangular-profile grooves. This allowed investigation of the influence of surface topography on either the exit (B_1) or illuminated side (B_2) of the structure. The radii of the grooves provided a periodicity of 5.00 mm, measured from the centre of the aperture to the centre of each groove. The machined grooves have a measured depth of l = 0.55 mm and width w = 1.50 mm. Sample C was formed by reproducing the structure in B on both sides of the sample. Radiation of frequency $50 \le f_0 \le 75\,\mathrm{GHz}$ is

normally incident upon the sample (θ = 0º), and polarised such that the electric field vector is in the x-direction. As *Figure 7.4.1* shows, z = 0 is defined as being situated at the uppermost part of the surface on the illuminated side of the sample.

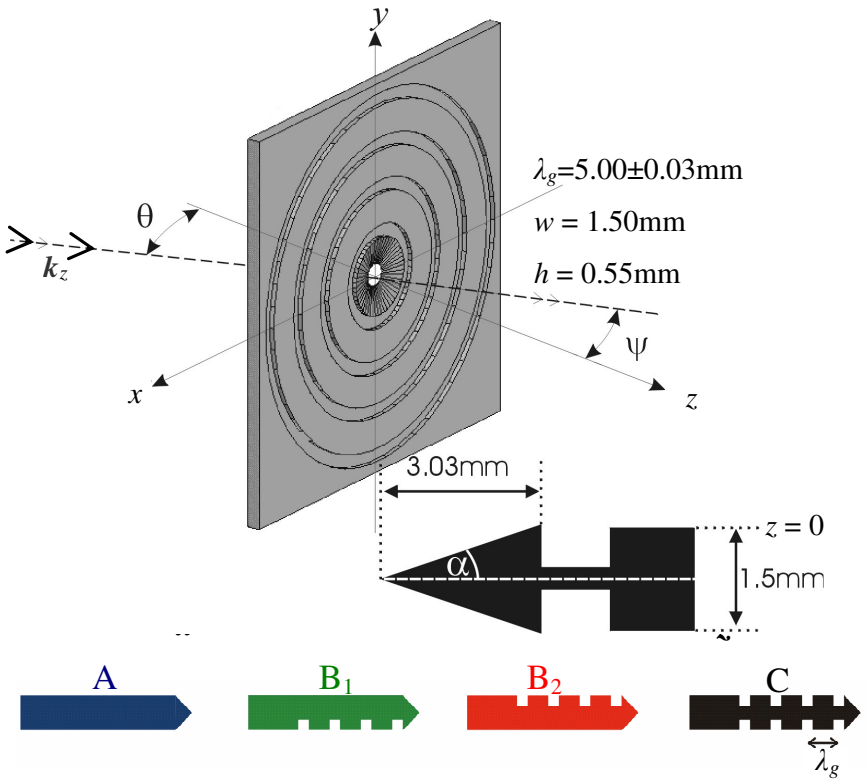

Figure 7.4.1 Sample geometry showing incident angle θ, transmission angle ψ and the countersink angle α of 13.9º. Also shown are the schematic representations of each of the three aperture arrangements with sample B shown in both orientations.

Originally, seven ring samples were cut into 1.50 mm thick aluminium discs of radius 40 mm with the countersunk aperture positioned centrally relative to the disc as shown in *Figure 7.4.2 inset*. However, the transmission data obtained from these samples contained a strong oscillation in transmission intensity as a function of transmitted angle ψ (*Figure 7.4.2*).

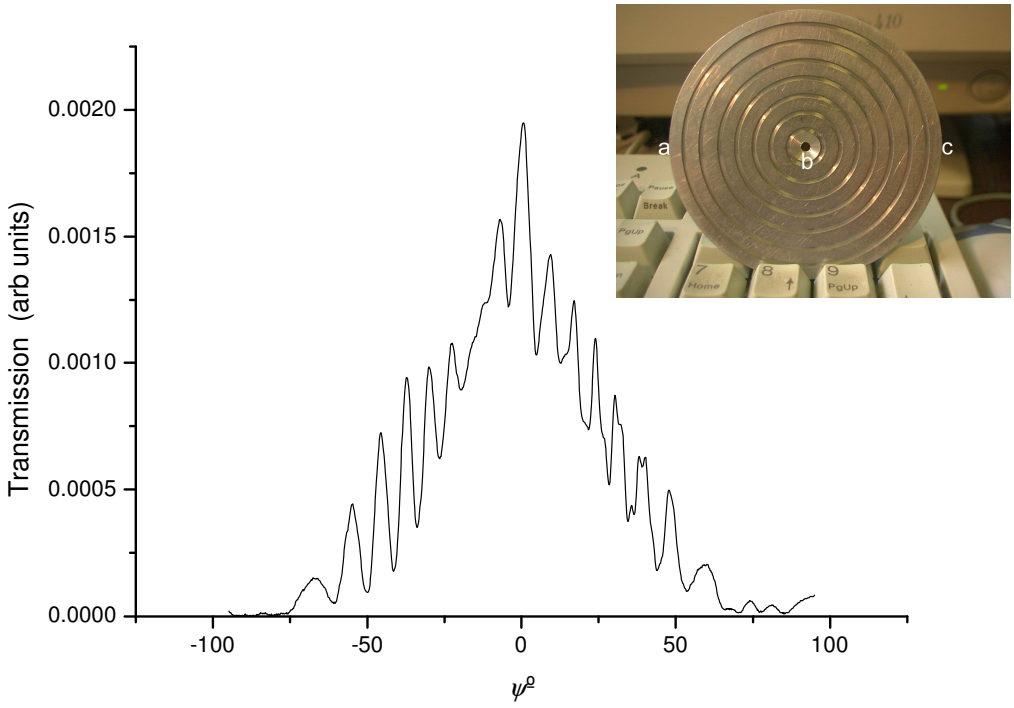

Figure 7.4.2 Transmission intensity as a function of ψ for the single sided aperture arrangement with concentric rings on the illuminated in-plane surface only. A pronounced interference oscillation with peak separation of 7º overlies the transmission maximum, corresponding to the three source interference separation between points *a*, *b* and *c* of the circular sample (*inset*).

Separation of the interference peaks was found to be consistent with three source interference from each edge of the sample and the aperture itself. To overcome the interference, the final experimental samples were milled into 300 × 300 × 1.5 mm

aluminium alloy sheet, the edges of which were covered with microwave absorbing material.

A schematic of the experimental arrangement used to obtain the transmission spectra as a function of transmission angle is shown in *Figure 7.4.3*. Incident radiation of wavelength $4 < \lambda_0 < 6$ mm produced by a HP 8350B sweep oscillator and HP 83550A RF plug in used in conjunction with an Agilent 83557A wave source module was directed onto the sample using a U752C directional coupler and a 24240-25 standard gain horn.

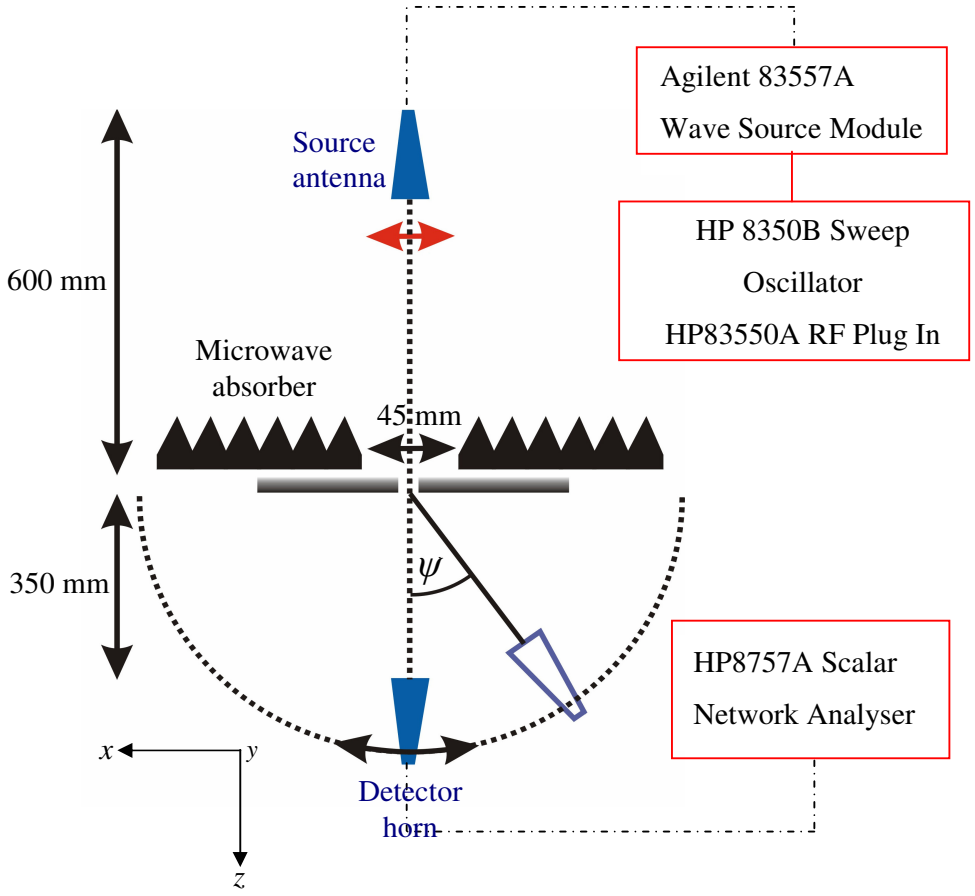

Figure 7.4.3 Plan view of the experimental set up. The detector horn is mounted on an arm extending from a computer controlled turntable (*not shown*) allowing the transmitted signal to be detected over the range $-70 < \psi < 70°$.

The source horn was positioned a perpendicular distance of 600 mm from the sample and orientated such that the incident electric vector is parallel to the x-direction. The sample was mounted in a wooden holder and positioned over the centre of rotation of a computer controlled turntable. A 45×45 mm aperture formed from microwave absorbing material was positioned between the source antenna and sample to restrict the beam to a well collimated central part. A matched standard gain horn and HP U85026A detector was mounted on an arm extending from the computer controlled turntable and positioned a perpendicular distance of 350 mm from the exit side of the sample. The detector was connected to a HP8757A scalar network analyser which was in turn connected to the same PC as the turntable. This arrangement allowed the angular distribution of the transmitted signal in the plane of polarisation to be measured as a function of frequency and transmission angle ψ for fixed values of the incident angle θ.

7.5 Results and Discussion.

Figure 7.5.1 shows the experimental transmission data obtained from sample B_2 (surface profile on the illuminated in-plane surface only) normalised to the transmission through an identical countersunk aperture with no surface topography (sample A). Also shown is the modelled EM response of the sample (solid line) obtained from the finite element code, which shows very good agreement. Plane wave radiation is normally incident upon the sample and the detector is positioned normal to the surface on the exit side ($\theta = 0^o$, $\psi = 0^o$).

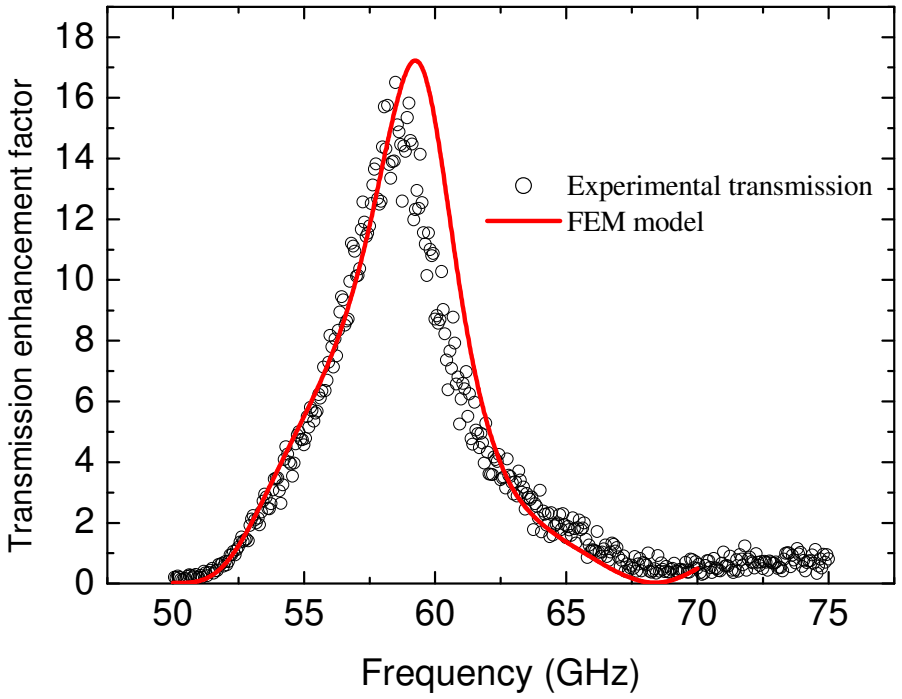

Figure 7.5.1. Transmission enhancement of the experimental double sided sample (C) normalised to the transmission of an identical aperture with no patterning. Also shown is the modelled transmission spectrum predicted by the FEM model, using the measured dimensions of the experimental sample.

It is clear that the presence of the surface corrugation on the illuminated face of the sample results in a 17-fold enhancement in transmission over that observed experimentally via the bare countersunk aperture. Note also that the maximum enhanced transmission occurs at $\lambda_0 \sim \lambda_g$, a condition compatible with any SPP-enhancement argument for normal incidence, since at microwave frequencies, $k_0 \sim k_{SPP}$ [*H. Raether* (1998), *D. Sievenpiper* (1999), *Hibbins et al.* (1999)].

In order to understand the transmission enhancement mechanism, it is useful to evaluate the modelled EM fields close to the sample in the incident half space, at the frequency of resonance. *Figure 7.5.2* shows (a) the instantaneous H field magnitude, and (b) the instantaneous E field strength in the incident half space only. Fields are plotted in the *xz*-plane through the centre of the aperture at a temporal phase (separated by a quarter of a cycle) corresponding to maximum field enhancement.

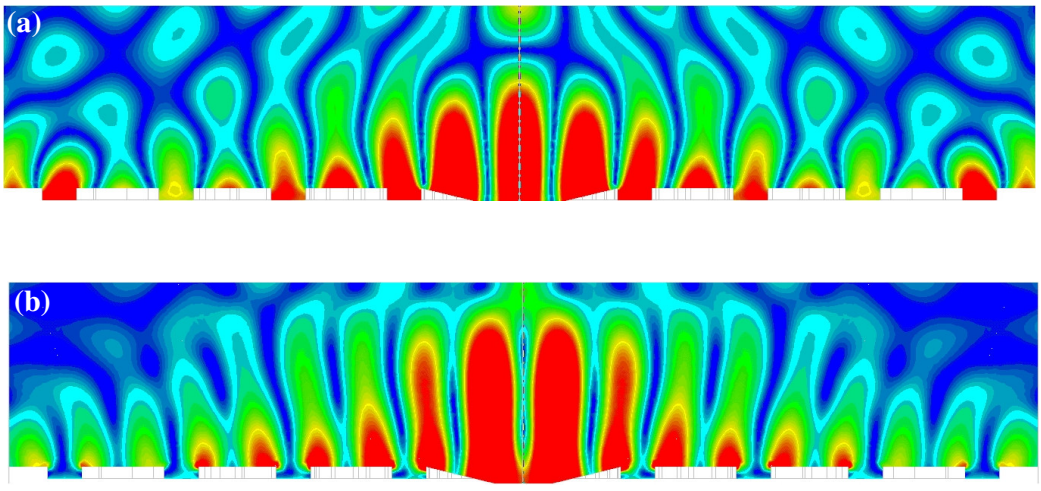

Figure 7.5.2 The modelled instantaneous magnetic field strength (a) and electric field strength (b) at a phase corresponding to maximum enhancement of each field. The surface of the structure has concentric ring patterning on both sides, although only the incident half space is shown here, with radiation normally incident from above.

It is evident that the scattering of incident radiation by the concentric grooves of the sample results in the setting up of a surface wave on the incident in-plane surface, redistributing the EM fields such that regions of high energy density are located in the vicinity of the aperture (*Figure* 7.5.2 *a* and *b*). The E field is shown to possess maxima located at the sharp corners of each concentric groove, with maximum enhancement (25 fold) occurring at the sharp ring formed by the countersinking of the aperture entrance. The H-field however has maxima located centrally on each peak and trough of the profile, as one might expect for a standing wave. Note also that the magnitude of both the E- and H-fields in the *xz*-plane decay as a function of distance away from the aperture. By plotting the relative instantaneous magnitudes of the fields on a line in this plane at a height of z = 0.5 mm (*Figure 7.5.3*), it is possible to show that not only are the anti-nodes in the E- and H-fields separated by 90º of temporal phase, but they are also separated spatially by approximately 90º. Thus the surface wave in this region has standing wave character, with wavelength equal to the grating pitch, formed by the superposition of two counter propagating surface waves.

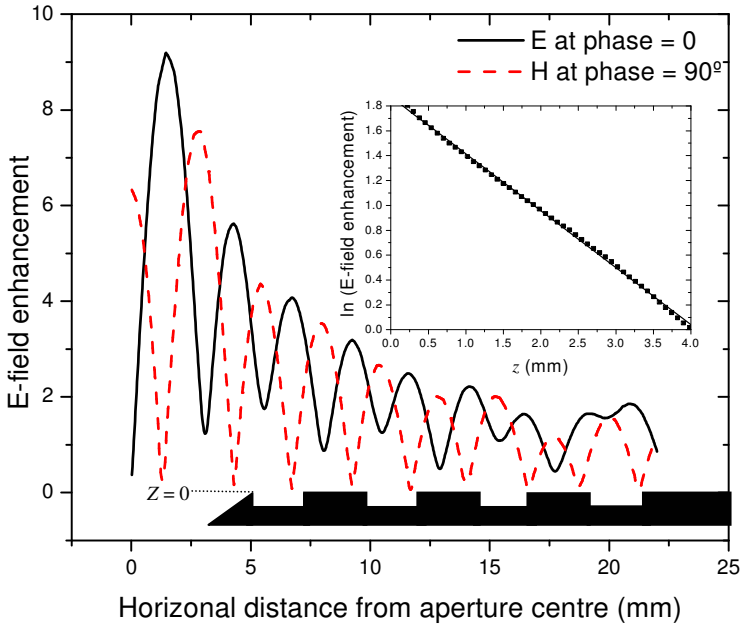

Figure 7.5.3 Relative instantaneous field magnitudes of the E (black solid line) and H (red dashed line) fields plotted over a horizontal line in the *xz*-plane. The evaluation line is situated at a height of z = 0.5 mm where z = 0

is situated at the top face of the sample and fields are obtained at a phase corresponding to maximum enhancement. Inset: The exponential decay of the fields of the pseudo-standing wave. The time averaged E-field magnitude has been plotted as a function of perpendicular distance z from the xy-plane, at a distance of 6 mm from the centre of the aperture in the x direction.

This said, it is not a *true* standing wave. The energy density is clearly not uniform, and in the region immediately surrounding the aperture entrance, the spatial separation of the E- and H-fields reduce slightly. This effect is due to the profile of the countersinking, and distortion of the fields due to the concentration of charge situated on the sharp ring at the aperture entrance, and the circular symmetry of the sample. This results in a small but finite net power flow over the in-plane surface toward the aperture and an increase in the energy density, which must exist for strong transmission to occur.

Figure 7.5.3 (*inset*) shows the time averaged E-field magnitude as a function of perpendicular distance z from the illuminated surface, at a distance of 6 mm from the aperture in the x-direction. It is clear that the E-field reduces exponentially away from the interface into the incident medium (air) suggesting that the pseudo-standing wave is associated with a bound surface mode. It is important to note here however that the surface wave supported by the structure is not a radial wave but instead exists, as one would expect from a diffraction process, with its maximum electric field magnitude on the surface of the sample occurring on a plane through the aperture centre. This dimensionality is evident in *Figure 7.5.4* in which the time averaged E-field magnitude is evaluated over an xy- plane at $z = 0$.

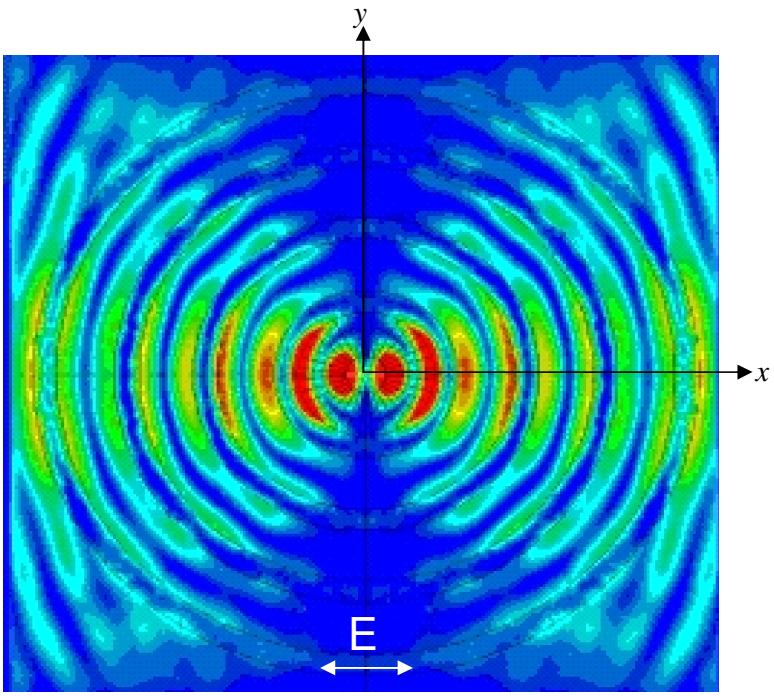

Figure 7.5.4 Modelled time-averaged E-field magnitude evaluated over the *xy*-plane at $z = 0$. Incident radiation is polarised such that the electric vector lies in the direction of the *x*-axis.

Taking the Huygens-Fresnel view of wave propagation, when plane wave radiation is incident on a continuous surface, each point on that surface acts as an identical coherent secondary source of wavelets that mutually interfere to form the reflected wave or waves. When the incident surface possesses a periodicity, the reflected wave fronts are perturbed by a set of spatial modes possessing Fourier components that are matched to that of the structure. Close to the resonant frequency with normally incident plane wave radiation, the structure supports only the specularly reflected beam. If we consider the periodicity in the *x*-direction and approximate the structure as an infinite plane grating, then the ±1 diffracted orders become evanescent at 60 GHz. Hence on the *xz*-plane through the centre of the aperture, the incident radiation will sample the profile of the structure with maximum effect, leading to strongly resonant evanescent diffracted

orders which propagate along the surface undergoing successive k_g scattering and setting up the standing wave. Following the concentric grooves around to the *y*-axis, the component of the electric vector that is co-linear with the radial wave vector reduces until the E-vector is entirely orthogonal to the radial wave vector, and tangential to the surface profile at every point. Through the centre of the aperture in this (*yz*) plane, the surface corrugation results in a variation in the local H-field due to the exclusion of the fields from the metal. Hence diffraction in this plane is extremely weak.

As it is the redistribution of the energy density by the standing wave set up on the illuminated in-plane surface of the sample as a result of diffraction that increases the evanescent fields within the hole, transmission must be proportional to field intensity. It is therefore important to ascertain whether the evanescent fields forming the pseudo-standing wave are further enhanced by the resonant excitation of a SPP. The modelling of the double sided aperture is therefore reproduced with the aluminium alloy substrate being replaced first by a natural E boundary, and then a natural H boundary, simulating the response of identical double sided aperture arrangements formed from a perfect conductor and perfect insulator respectively [*Chapter 5, section 3.3*]. This allowed comparison of each with the modelled response of the structure formed from aluminium alloy (*Figure 7.5.5*).

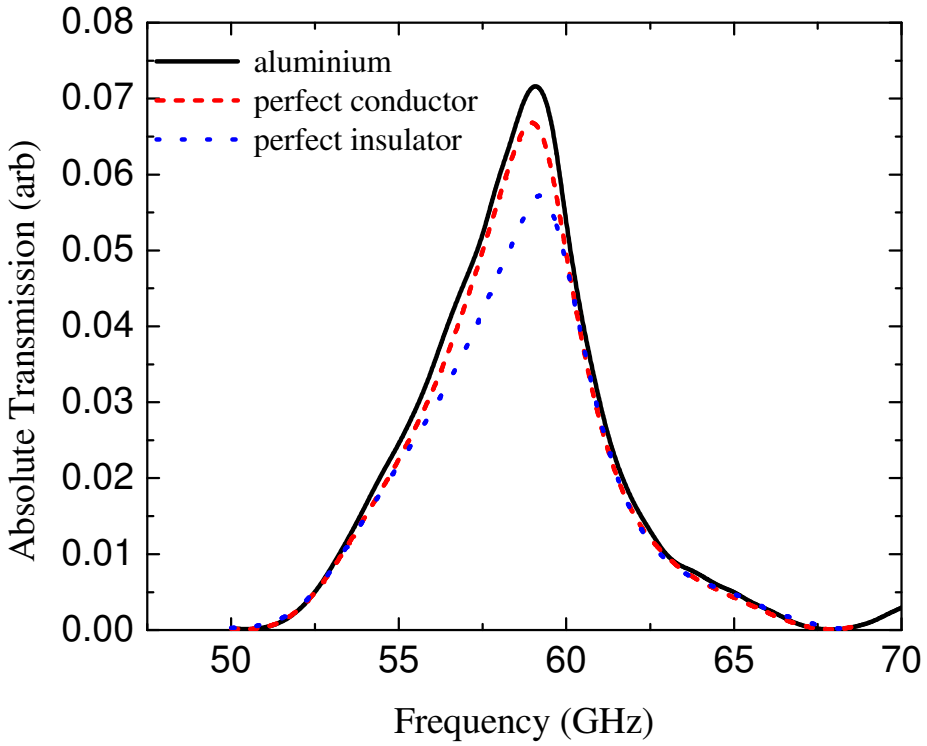

Figure 7.5.5 Modelled response of the double sided aperture describing the structure using the surface impedance approximation for aluminium (black solid line), and then as a perfect conductor (red dashed line) and perfect insulator (blue dotted line).

From *Figure 7.5.5* it is clear that peak transmission occurs at a wavelength approximately equal to the grating pitch for all three substrates. In the case of the perfect insulator, the excitation of a SPP is prohibited due to the absence of free charge density at the air-insulator interface. However, as previously described, diffraction may still occur. Thus the increase in transmission is entirely due to the establishment of a pseudo-standing wave via near field diffraction, the fields of which are in no way enhanced by SPP excitation. For the perfectly conducting substrate however, we note a 16% increase in transmission over that observed for the perfectly insulating sample.

This is attributed to the introduction of surface charge and increased electric field intensity resulting from the change in boundary conditions. Due to the exclusion of the fields from the metal, it is generally assumed that a perfectly conducting structure will not support SP modes. Indeed, for a flat, perfectly conducting surface, bound surface waves do not exist. However, the presence of a corrugation at such an interface introduces effective surface impedance, which results in a bound surface state. This bound surface state is a SP, possessing a dispersion of the plasmon form, but which is characterised by an *effective* dielectric function (*Pendry et al.* 2004)).

The transmission for the aluminium alloy substrate shows a further 8% increase. As discussed in *Chapter 2*, in the microwave regime the skin depth of metals is on the order of a micron, and hence absorption of energy via Joule heating of the metal is low, but non zero. Coupling strength to the SPP was also discussed, and shown to be governed by the balance of radiative and non-radiative loss channels available, with optimum coupling occurring when the two terms are equal [*H. Raether* (1988)]. For the perfect conductor, absorption is zero, and hence any perturbation from this ideal system will improve coupling to the plasmon mode. As a result the fields of the pseudo-standing wave on the aluminium substrate are enhanced, thereby enhancing the fields within the aperture and increasing transmission. So to summarise, modelling would suggest that at these frequencies the primary mechanism for the enhancement in transmission observed for the samples studied in this chapter is diffraction. A pseudo-standing wave is formed, resulting in a redistribution of energy density such that regions of high energy density are located in the vicinity of the aperture. As the substrate is metallic, SPP enhancement of the evanescent fields may occur, but accounts for less than a quarter of the overall enhancement in transmission.

In order to investigate the angular distribution of the transmitted signals, the detector is mounted on a computer controlled turntable sweeping in the *xz*-plane. This allows the transmission spectra to be recorded as a function of frequency and transmission angle, ψ. *Figure 7.5.6* shows the un-normalised ψ-dependent transmission response on resonance of samples A, B_1, B_2 and C at the resonant frequency. As expected, sample

B_2 (grooves on illuminated face only) shows a substantial increase in transmission over that recorded for the aperture with no corrugation (A).

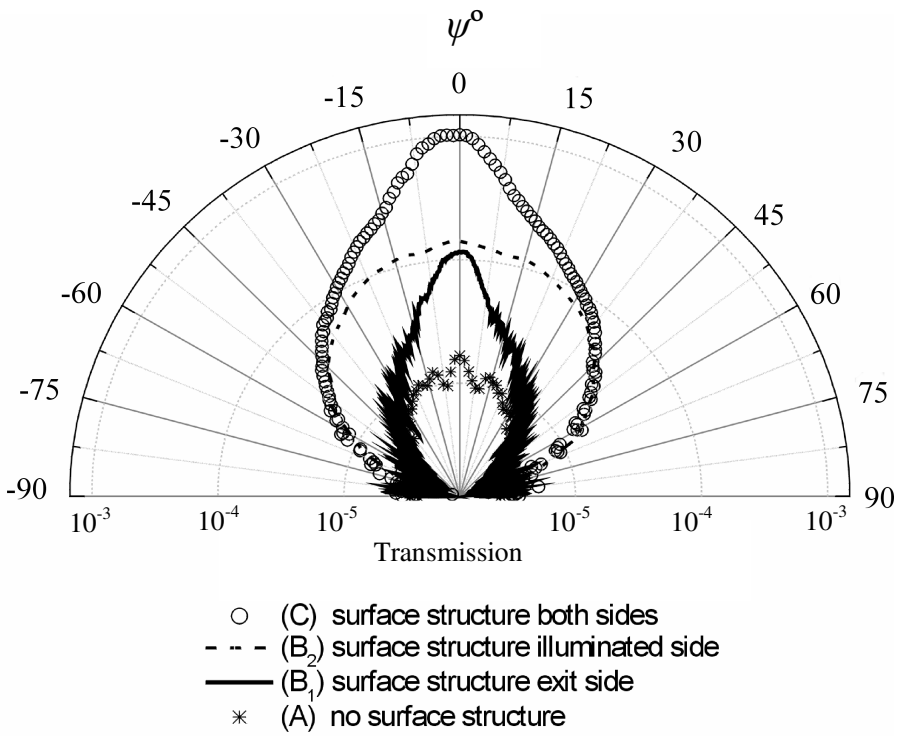

Figure 7.5.6 Experimental angle-dependent transmission spectra at the resonant frequency of each sample. (Note logarithmic scale)

It is important to note here that although the results displayed in *Figure 7.5.6* suggest that the sample B_1 transmits more than sample A, FEM modelling of the absolute transmission normalized to the area of the hole shows that in fact they are equally efficient ($T_A = 2.22$, $T_{B1} = 2.21$). However the corrugation on the exit face of the substrate clearly results in strong angular confinement of the transmitted signal in the forward direction. The apparent increase in transmission efficiency (*Figure 7.5.6*) is because the detector horn used experimentally is limited by its design to detect only radiation which enters close to normal to its front face. Further, diffraction of the beam occurs not only in the *xz*-plane, but in all directions over a wide range of angles as one would expect for a circular hole (*Figure 7.5.7*).

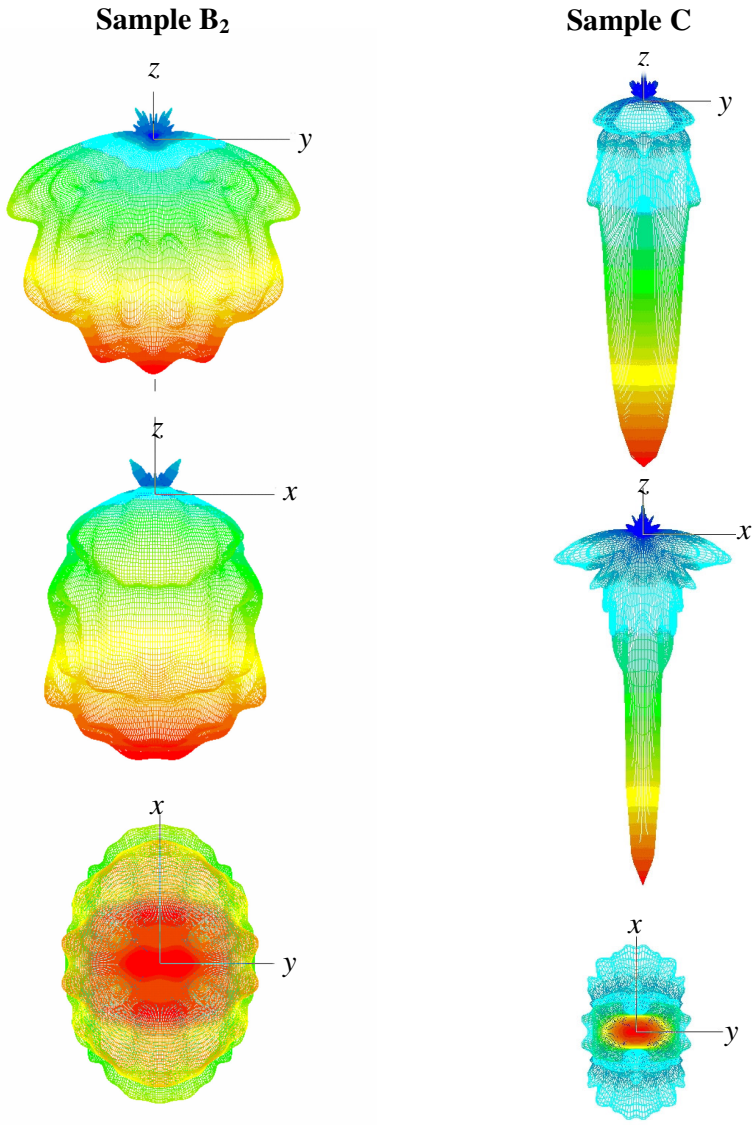

Figure 7.5.7 The modelled total radiated electric field calculated in the far field. These plots show the three dimensional angular distribution of the transmitted signal for samples B_2 (enhancement only) and C (enhancement and focusing) respectively.

The slight forwardness of the angular distribution is due to the ratio of hole diameter to incident wavelength ($d \sim \lambda_0/2$), as angular-invariant diffraction would only occur for $d << \lambda_0$ (Huygens-Fresnel principle). Comparison of the angular distribution of the transmitted signal from sample B_2 with that of sample C (*Figure 7.5.7*) illustrates the

remarkable angular confinement that may be achieved with the addition of grooves on the exit face of the substrate. While the former exhibits a transmission peak at resonance, possessing a width of 74º in the *xz*-plane, that of sample C exhibits a width of only 18º. Thus it is clear that while the concentric ring surface structure on the illuminated surface enhances the transmission efficiency of the aperture, that on the exit side of the sample results in strong angular-confinement of the transmitted beam only. *Figure 7.5.8* shows the un-normalised angle dependent transmission spectrum of the double-sided structure (sample C) on resonance at $\theta = 0$, 10, 20 and 30º.

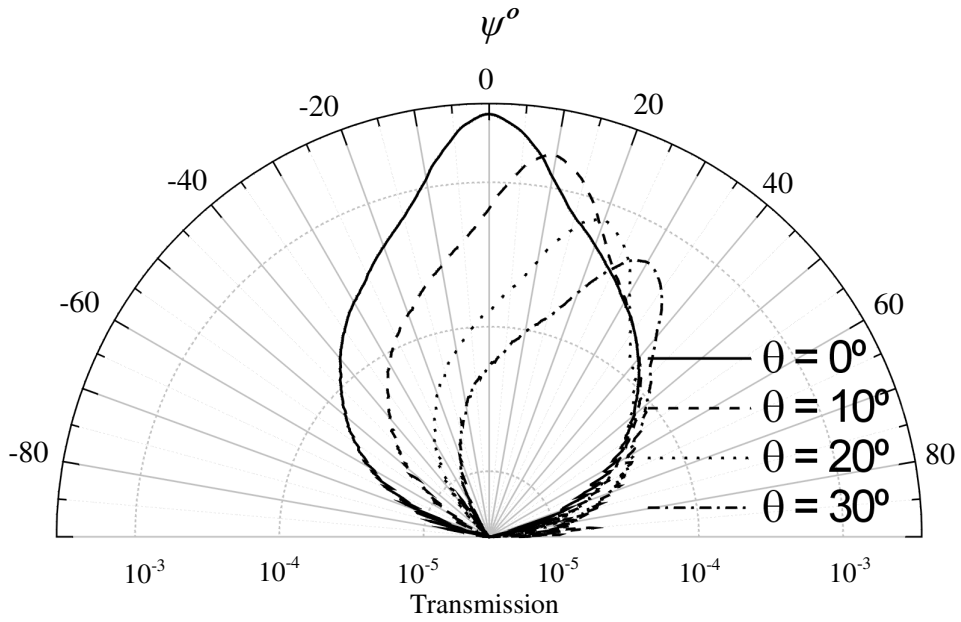

Figure 7.5.8 Experimental angle dependent transmissivity of the structure having concentric rings on both surfaces, at the resonant frequency of the sample for incident angles of 0, 10, 20 and 30º. (Note for non-normal incidence the exit face of the plate is rotated by the incidence angle relative to the direction of the incident beam which defines 0º in this figure.)

Clearly the concentric ring structure on the exit side of the sample not only confines the transmitted signal to a remarkably tight angular distribution but also forces the signal to exit the aperture normal to the surface plane largely irrespective of angle of incidence. Once again, it is useful to evaluate the modelled field profiles obtained from the finite element code in order to understand the remarkable properties of the samples under

study. *Figure 7.5.9* shows (a) the time averaged magnetic field (H) magnitude, and (b) the instantaneous electric field (E) strength plotted through the centre of the aperture over the *xz*-plane with the latter at a phase corresponding to maximum enhancement, clearly showing the enhancement of the E-and H-fields respectively, up to 16 mm from the substrate in the lower half space. As before, radiation is normally incident from above.

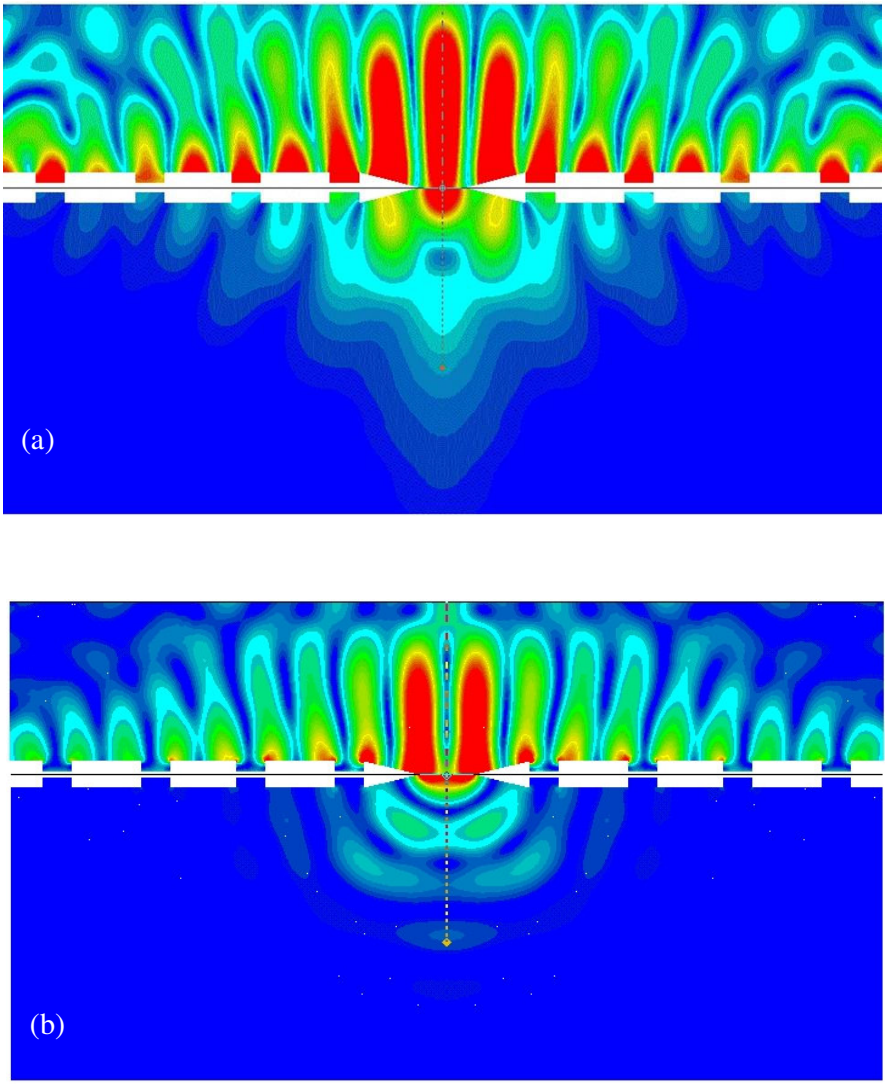

Figure 7.5.9 (a) the time averaged magnetic field (H) magnitude, and (b) the instantaneous electric field (E) strength plotted through the centre of the aperture over the *xz*-plane with the E-field at a phase corresponding to maximum enhancement.

It is clear that the maxima in field magnitude on the exit face of the sample occur with the same regular spacing and position relative to the surface corrugation as those in the upper half space, although reduced in magnitude. Thus the standing wave is reproduced on the exit face of the sample and thus there exist a number of regions of locally high field enhancement which re-radiate power. It is these secondary sources in combination with the primary source (the aperture) that results in the multiple source interference responsible for the strong angular confinement and directivity of the transmitted signal. As the position and relative magnitude of these sources are constant with respect to each other as a function of incident angle, the transmitted signal is emitted normal to the surface of the sample.

7.6 Summary.

In this chapter, a thorough experimental investigation into the extraordinary enhanced transmission and focusing of radiation through a novel sub-wavelength aperture and photonic surface arrangement has been presented. This is the first experimental study of the enhanced transmission phenomenon to be conducted in the microwave regime, and in addition, the finite element modelling of the system has provided remarkable and original insight into the transmission enhancement mechanism. A 17-fold enhancement of transmission has been shown, together with an angular confinement of the transmitted signal comparable with that observed by Lezec *et al*. (2002) in the optical regime. The primary transmission enhancement mechanism has been shown to be a pseudo-standing wave formed from near field diffraction on the illuminated side of the sample. Its presence results in a strong redistribution of energy density such that regions of high density are located in the vicinity of the aperture. However, it is often wrongly assumed that metal substrates at microwave frequencies cannot support SPPs, and we illustrate that the contribution to the enhanced transmission from SPP-coupling is also significant. The angular confinement of the transmitted signal is shown to be a result of identical patterning on the exit side, supporting a standing wave which radiates from the surface as a set of coherent sources. It is the two dimensional pattern of secondary

sources that results in a complex multiple source interference pattern which gives rise to strong angular confinement of the transmitted beam, and maintains its independence to the angle of the incident beam.

Chapter 8

Enhanced transmission and directivity of microwave radiation through a single sub-wavelength annular aperture in a metal substrate.

8.1 Introduction

The work of *Ebbesen et al*. [Nature, 391, 667 (1998)] has recently stimulated great interest in the enhanced transmission of radiation via sub-wavelength circular apertures. However, since apertures of diameter $d<<\lambda_0$ in an opaque metal substrate support no propagating modes, any transmission that does occur (enhanced or otherwise) is reliant upon a weak evanescent tunnelling process. It is the purpose of this chapter to characterise the properties of a transmitting structure based upon an annulus formed from a cylindrical cavity in a thick metal substrate with an inner cylindrical core of smaller radius. Unlike circular apertures, this annulus structure supports a Fabry-Perot like transverse electromagnetic (TEM) mode that propagates along its length without cut-off, leading to transmission efficiencies significantly greater that obtained via sub-wavelength cylindrical holes. Undertaking the experiment at microwave wavelengths allows for a precision of manufacture and optimisation of the structure that would be difficult to replicate at optical frequencies, and demonstrates that transmission enhancement may be achieved with near-perfect metals. Further, the use of a finite element method computational model to study the electromagnetic response of the sample allows for the fields associated with transmission enhancement to be examined, thereby obtaining a better understanding of resonant modes supported by the coaxial structure.

8.2 Background.

The work of *Ebbesen et al.* (1998) has generated renewed interest into the transmissive properties of both sub-wavelength apertures and slits, and a large number of experimental and theoretical studies by many different authors have followed [*Astilean et al.* (2000), *Takakura* (2001), *Hibbins et al.* (2001) and (2002), *Lezec et al.* (2002), *Collin et al.* (2002), *Martin-Moreno et al.* (2003) and references therein]. It is well known that circular sub-wavelength apertures of diameter d and cylindrical height h in an opaque metal substrate do not support TEM modes [*J. A. Stratton*, *Electromagnetic Theory*, (1941)]. Further, no propagating modes are supported within the cylindrical cavity when $d < \lambda_0(x'_{mn})/\pi$ (where x'_{mn} represents the *nth* zero of the derivative of the Bessel function J_m of the first kind of order m, which for the dominant TE_{11} mode takes its minimum value of 1.841 [*Chapter 3, section 3.5.1*]). Hence the transmission mechanism for such a structure is purely reliant upon an evanescent tunnelling process, which may be coupled into by diffraction occurring at the slit entrance [*Treacy* (2002)]. It is also suggested that this coupling efficiency may be further increased by SP excitation, and as such (for a circular aperture) strongly enhanced transmission requires a periodicity on the illuminated face of the sample. This periodicity may arise from either an array of holes with a periodic separation [*Ebbesen et al.* (1998), *Ghami et al*. (1998)], or in the case of a single aperture, a surrounding surface corrugation [*Lezec et al.* (2002), *Lockyear et al.* (2002) and (2004)]. It is important to realise here however, that the resonant transmission process for a slit fundamentally differs from that pertaining to a circular aperture. This is because for radiation polarised with its electric vector perpendicular to the slit axis, a TEM mode is supported that may propagate without cut off [*Popov et al.* (2000)], resembling the mode of a parallel-plate capacitor. Resonances are established due to the partial reflection of a propagating guided wave at each end of the slit resulting in a standing wave mode, which can be considered as either a coupled SPP [*Sobnack et al*. (1998), *Went et al*. (2000)] or more appropriately as a Fabry-Perot-like resonance. Transmission efficiencies are therefore significantly enhanced compared to those obtained through a simply-connected cross section [*Badia et al*. (2003)]. Assuming there are no edge effects [*Sobnack et al.* (1998), *Takakura* (2001)], for a single cavity formed by bringing together two identical metal slabs of

uniform thickness L to a separation distance w, peaks in the transmission spectra will be observed according to the Fabry-Perot condition;

$$f_N = \frac{Nc}{2nL} \qquad \textit{Equation (8.2.1)}$$

where f_N is the resonant frequency of the N^{th} order Fabry Perot mode, c is the speed of light, N is an integer mode number, and n is the refractive index of the dielectric filling the cavity.

The structure forming the basis of this study consists of a cylindrical cavity drilled into an aluminium alloy substrate. A solid cylindrical core of the same metal but slightly smaller radius is inserted into the hole forming a coaxial like structure with a uniform gap width. Thus the annulus arrangement may be considered as a narrow air-filled slit possessing circular symmetry. Fabry-Perot-like modes with resonant frequencies inversely proportional to cavity length L may therefore be supported. Further, the arrangement is able to support modes which are additionally quantised by the circumference of the annulus. Consider the experimental arrangement shown in *Figure* 8.2.1. Radiation of wave vector k_0 is normally incident upon the sample, with its electric vector polarised in the x-direction. Within the coaxial cavity, the total wave vector k_T is given by;

$$k_T^2 = k_\phi^2 + k_L^2 \qquad \textit{Equation (8.2.2)}$$

where $k_\phi = 2\pi/\lambda_\phi$ is the wave vector associated with the circumference of the annulus and $k_L = 2\pi/\lambda_L$ is the Fabry-Perot-type resonance set up between the two open ends. Assuming the total wave-vector within the metal cavity is the same as that in free space, because the metal is a near perfect conductor, then $k_T = k_0$. Thus;

$$k_0^2 = \left(\frac{2\pi}{\lambda_\phi}\right)^2 + \left(\frac{2\pi}{\lambda_L}\right)^2 . \qquad \textit{Equation (8.2.3)}$$

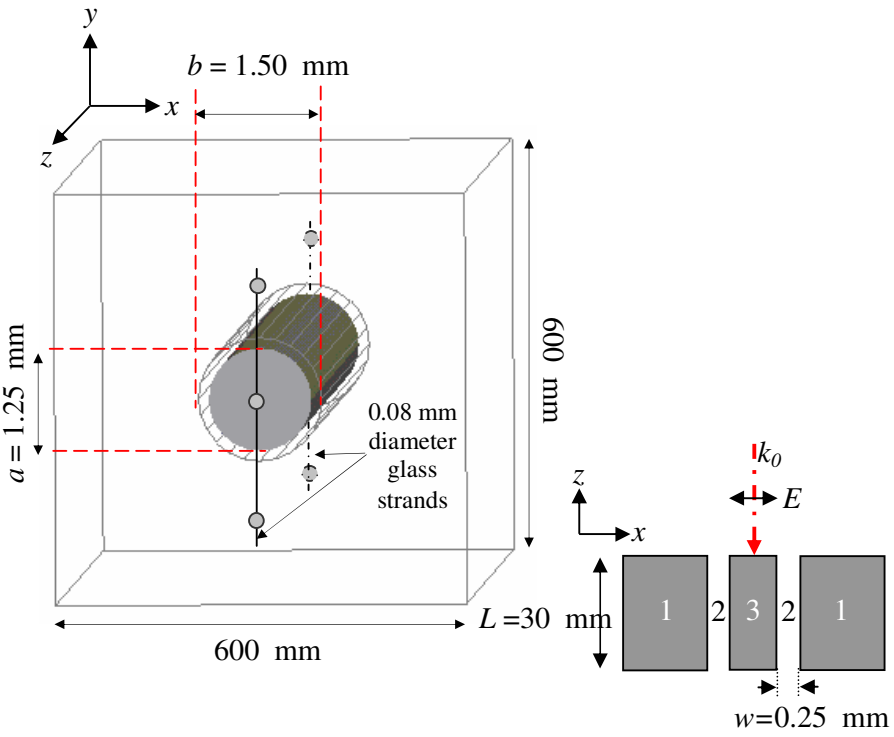

Figure 8.2.1. A cylindrical cavity of outer radius b = 1.50 mm drilled into an aluminium alloy substrate of dimensions 600×600×30 mm. A solid cylindrical core of the same material but slightly smaller radius (a = 1.25 mm) is inserted into the hole forming a coaxial like arrangement of length L = 30 mm with uniform gap width w = 0.25 mm. The inner core is held in position using two 0.08 mm diameter strands of glass fibre. *Inset*; Region 1 is defined as the continuous aluminium alloy substrate of thickness L = 30.0 mm. Region 3 is the inner aluminium alloy coaxial cylinder, whilst region 2 remains air-filled.

For resonance,

$$\lambda_L = \frac{2L}{N}, \qquad \textit{Equation (8.2.4)}$$

and using the average radius of the aperture, $(a+b)/2$

$$\lambda_\phi = \frac{\pi(a+b)}{P} \qquad \textit{Equation (8.2.5)}$$

where P is the integer mode number around the circumference of the annulus, a is the radius of the inner core, b is the outer radius and N is the mode number associated with the cylindrical length of the cavity. Hence peaks corresponding to resonant modes of the structure will occur in the transmission spectrum according to the condition:

$$f_{(P,N)} = \sqrt{\left(\frac{2P}{a+b}\right)^2 + \left(\frac{N\pi}{L}\right)^2} \times \frac{c}{2\pi} \qquad \textit{Equation (8.2.6)}$$

It is important to note here that this analysis does not take into account the radial nature of the E field within the space bounded by the two concentric cylinders, but rather assumes a uniform field as in the case of a two-dimensional slit. This proves to be a good approximation when a is comparable in magnitude to b. A more rigorous treatment of this geometry [*Chapter 3, section 3.6*] would require a Bessel function of the first kind to fully describe the field of a circularly cylindrical wave function. Nevertheless equation *8.2.6* outlines the possibility of coupling into modes quantised by both the circumference and length of the annulus. It will be shown in this chapter that it is indeed possible to couple incident radiation to families of P modes each containing multiple values of N. Further, the transmitted radiation will be shown to possess a P dependent angular distribution. Finite element modelling allows identification of each peak in the transmission spectrum through the investigation of the electromagnetic field profiles at the corresponding resonant frequency.

8.3 Sample fabrication and experimental set up.

In order to determine the initial dimensions of our annulus sample, the eigen-modes of the system were calculated using equation *8.2.6*. *Figure* 8.3.1 shows (a) the resonant frequency as a function of N for b = 1.00, 1.50, 2.00, and 4.00 mm with L = 30.00 mm and w = 0.25 mm, and (b) the resonant frequency as a function of N for b = 1.50 mm and w = 0.25 mm for six values of L from 25.00 to 30.00 mm in increments of 1.00 mm. The resonant frequencies are plotted for two values of circumferential quantum number (P = 0 and 1). It is clear from this analysis that decreasing the outer radius while holding w constant separates in frequency the P-sets of N-modes. Further, the separation of the N modes within the P = 1 sub-set reduces with decreasing frequency. From this analysis, an initial outer radius of 1.50 mm was chosen in order to obtain a transmission spectrum with well separated resonances, and to avoid overlap of the P = 0 and P = 1 modes whilst allowing for a significant number of N modes within the experimental frequency range $\left(30 \le f_0 \le 75GHz\right)$.

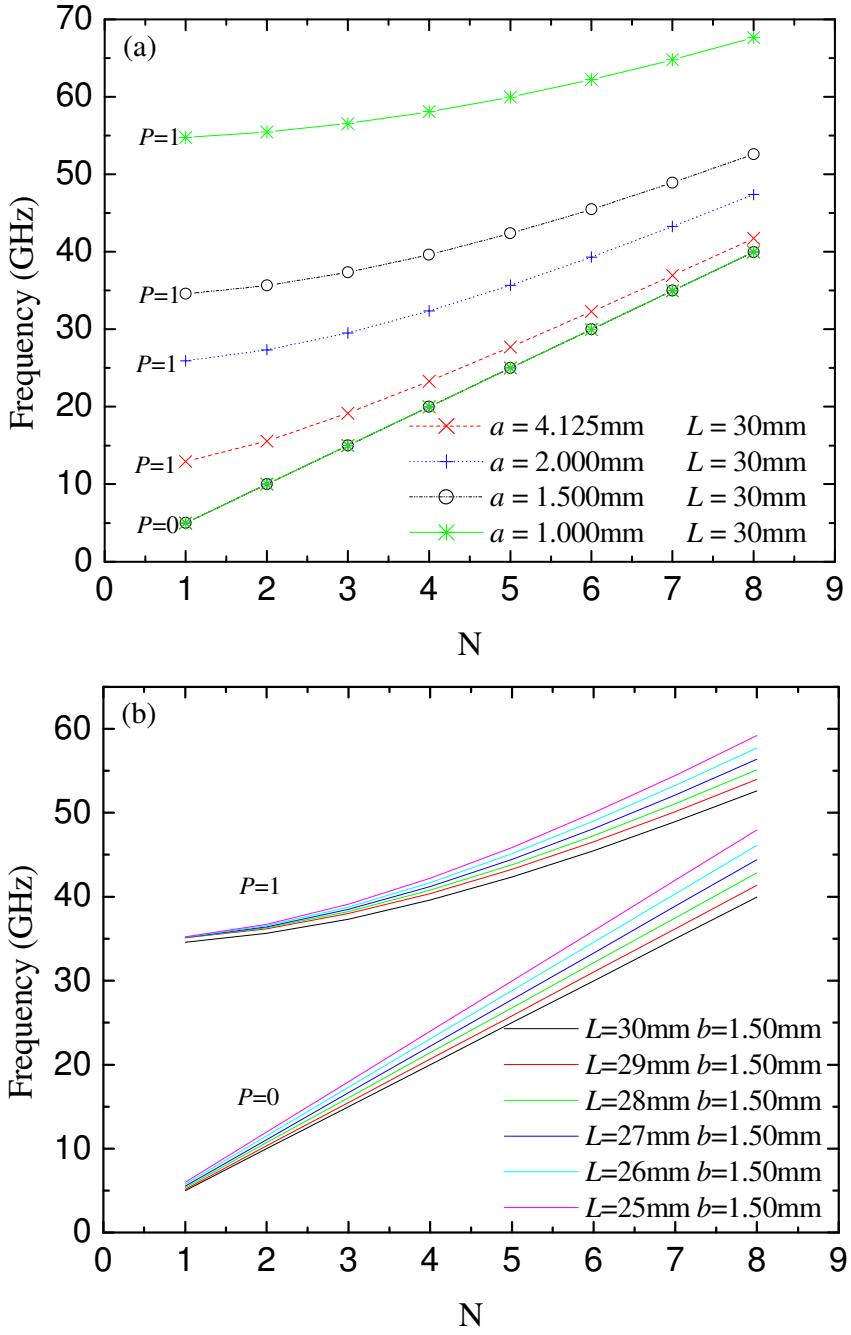

Figure 8.3.1 The eigen-modes of the coaxial system as a function of frequency, calculated for two values of the circumferential quantum number ($P = 0$ and $P = 1$). (a) The frequency dependence of the resonant modes for four values of the outer radius b, with $w = 0.25$ mm and $L = 30$ mm. (b) the frequency dependence of the modes for six values of L, with $w = 0.25$ mm and $b = 1.50$ mm.

The experimental annulus arrangement consists of a cylindrical cavity of radius b = 1.50 mm drilled into an aluminium alloy substrate of dimensions 600×600×30 mm, thus forming an air-filled cylindrical cavity of length L = 30.00 mm. A solid cylindrical core of the same material but slightly smaller radius (a = 1.25 mm) is inserted into the hole to form a coaxial like arrangement with a uniform gap width of 0.25 mm. The substrate dimensions were chosen to be large in comparison with the mean diameter of the annulus and the incident wavelength to avoid multiple source interference in the transmitted signal, arising between the annulus and the outer edges of the sample. The inner core was held in situ by attaching a 0.08 mm diameter glass strand across the substrate and inner core on both the incident and exit in-plane surfaces of the sample, as shown in *Figure* 8.2.1. Each fibre was orientated at 90º to the direction of the incident electric vector to minimise electromagnetic disturbance, and the source horn-antenna was positioned a fixed distance of 0.20m from the sample to provide approximately plane wave incident radiation. A 20×20 mm aperture formed from microwave absorbing material was positioned between the source horn and sample to restrict the incident beam to a well collimated central part, and to eliminate stray signals. In order to produce the range of incident wavelengths used in this study, ($4 < \lambda_0 < 10$ mm) a HP8350B sweep oscillator was used in conjunction with several different RF plug-in units, and mm-wave source modules when required, together with their matched horn-antennae, detectors and waveguides. A full list of equipment used is given in *Table* 8.3.1 for convenience. The source signal for each range is split before emission by a directional coupler into a source and reference signal, the latter being fed directly into the HP8757D scalar network analyser via a directional coupler and coaxial cable, allowing normalisation of the detected signal.

Table 1								
Source						Detector		
f GHz	RF Plug-in	Millimetre Wave Source Module	Directional Coupler	Standard Gain Horn	Connection Type	Crystal Detector	Detector Adaptor	Standard Gain Horn
12-18.5	HP83550A	N/A	HPP752C	V639	Coaxial	HPP424A	HPP281C	V639
18-26.5	HP83570A	N/A	HPK752C	V638	Flexible Waveguide	HPK422C	N/A	V638
26-40	HP83572A	N/A	HPR752C	V637	Flexible Waveguide	HPR422A	HP11664C	V637
40-60	HP83550A	Agilent 83556A	HPU752C	FM242402-5	Coaxial	HPU85026A	N/A	FM242402-5
60-75	HP83550A	Agilent 83557A	Agilent 83557-60001	FM25240-30	Coaxial	Agilent 8525C	Agilent 85025C-K57	FM25240-30

Table 8.3.1 Source and detection equipment used to provide the experimental frequency range of $30 < f_0 < 75$ GHz.

The sample was placed on a platform (which could be manually rotated) and positioned directly above a computer controlled turntable. The detector horn was mounted upon an arm extending from the turntable, and positioned a distance 0.150m from the sample. Whilst the source remained fixed, the sample could be rotated to one of eight discrete values of θ. For each incident angle, the detector scanned the transmission angle ψ within the range $-70^\circ<\psi<70^\circ$ with a resolution of 0.2º. We define $\psi = 0^\circ$ as normal to the surface plane of the sample as shown by *Figure* 8.3.2. Configuring the experimental set up in this way allowed the angular distribution of the transmitted signal in the plane of polarisation to be recorded as a function of frequency, for values of θ in the range $0 < \theta < 70^\circ$, in increments of 10º.

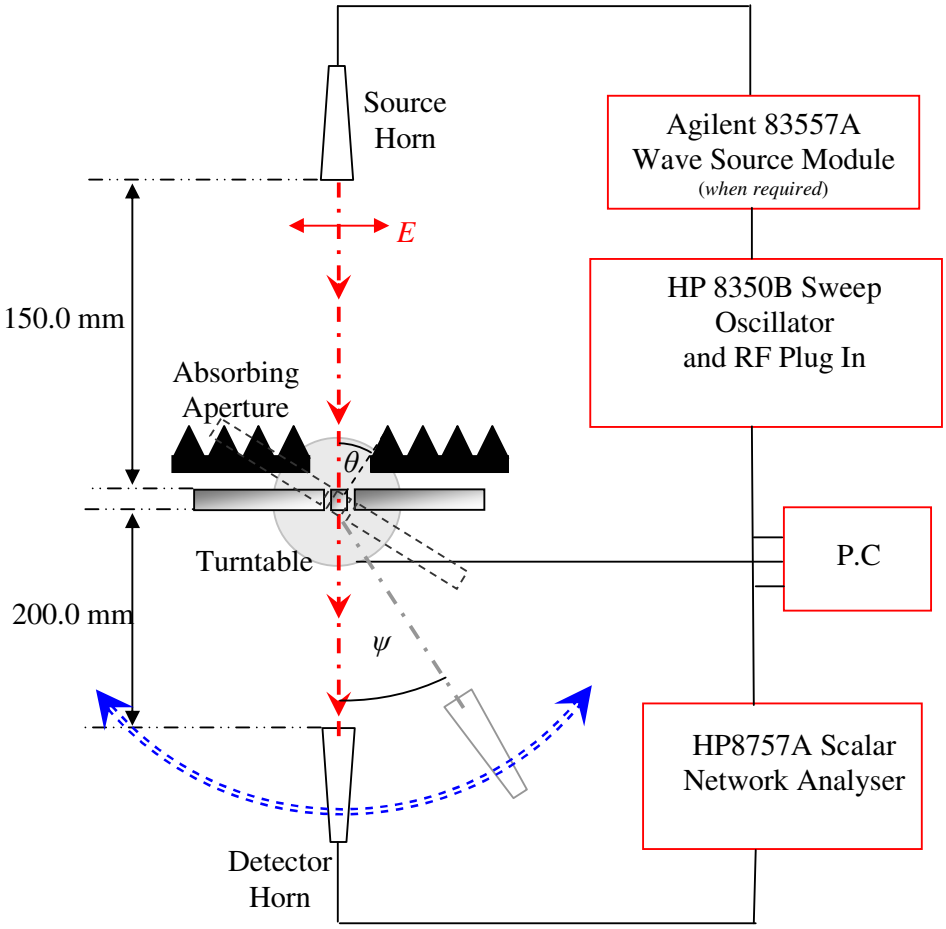

Figure 8.3.2. The experimental arrangement consists of matched standard-gain source and detector horns, connected to a sweep oscillator and scalar network analyser respectively. The source horn remains in a fixed position, whilst the detector is scanned through the transmission angle ψ. Six discrete values of θ are evaluated by manually rotating the sample.

8.4 Modelling.

The finite element model (FEM) used to predict the EM response of the sample consisted of a 30 mm thick aluminium substrate bounded by outer dimensions of 20×20 mm as shown by *Figure* 8.4.1.

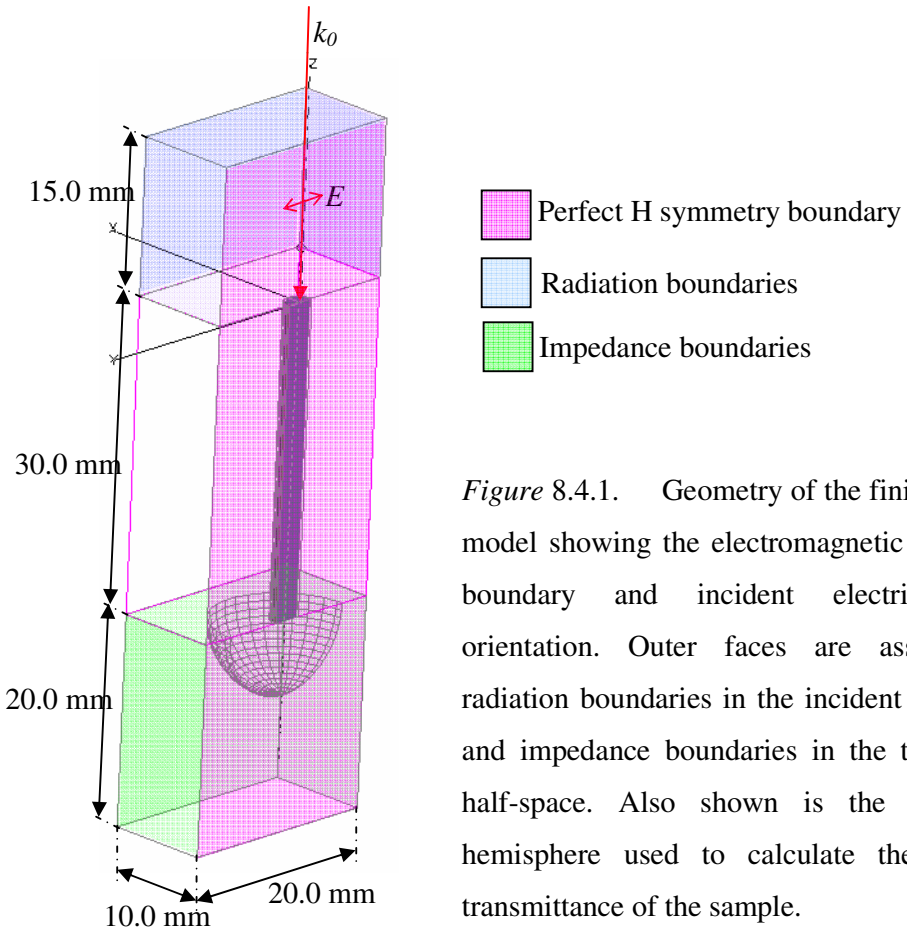

Figure 8.4.1. Geometry of the finite element model showing the electromagnetic symmetry boundary and incident electric vector orientation. Outer faces are assigned as radiation boundaries in the incident half-space and impedance boundaries in the transmitted half-space. Also shown is the evaluation hemisphere used to calculate the far-field transmittance of the sample.

The annulus is formed by subtracting a cylinder of radius 1.50 mm from the substrate to form the outer coaxial cylinder, and then inserting a centralised solid inner core of radius 1.25 mm and length 30.00 mm. The cavity bounded by the two concentric cylinders remains air filled. In order to reduce the size of the problem space and increase the resolution of the final mesh, an electromagnetic symmetry boundary was introduced which bisected the model along the plane of polarisation. Transmission through the aperture is calculated by evaluating the ratio of the Poynting vector for the incident and total field solutions over an evaluation plane situated in the transmitted half

space, parallel to the sample surface in the *xy*-plane. Evaluation over a single plane is possible due to the fact that the FEM injects a plane incident wave everywhere, rather than restricting the incident wave to the incident half space. A hemispherical calculation surface surrounding the exit aperture is also included in the model, allowing far field calculations of the angular distribution of the transmitted signal.

8.5 Results and Discussion.

Figure 8.5.1 shows the frequency dependent transmission spectrum obtained when illuminating the annulus arrangement with plane wave radiation at normal incidence. The detector is positioned at an angle $\psi = 0^{\circ}$, detecting that which exits normal to the plane of the sample. A total of 11 modes, labelled A through K, are clearly visible over the selected frequency range.

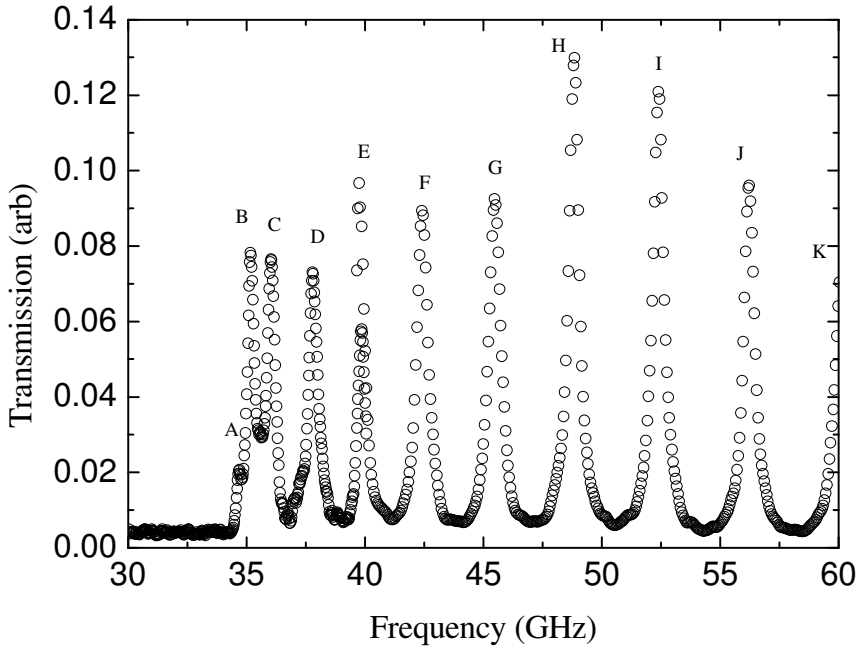

Figure 8.5.1. Transmission spectrum obtained over the range $30 < f_o < 60$ GHz. Plane wave radiation is normally incident on the sample and the detector is positioned normal to the exit face ($\theta = 0$ $\psi = 0^{\circ}$). Eleven resonant modes are clearly visible over the selected frequency range.

The slightly irregular variation of the relative intensities of the modes is thought to be associated with the difference in detection efficiency between the detector horns used for the 26.5 – 40 GHz, and 40 – 60 GHz ranges. In addition, since the horns only collect the transmitted signal over a finite area, any change in the angular distribution of the transmitted beam between the modes will also play a role. Finally, susceptibility to absorption in the system will vary from mode to mode depending on their field profiles (the coaxial structure will support TEM, TE, and TM waveguide modes, as well as hybrid TE-TM modes [*R. E. Collin*, *Field Theory of Guided Waves* (1991)]). These two roles will be discussed in due course. The limitations in detector efficiency also restrict the ability to record absolute transmission via the coaxial arrangement. Since the transmitted signal is diffracted 3-dimensionally over the transmitted half-space, and the detector only detects that which enters normal to the horn aperture, we are restricted to observe the transmission over a two dimensional plane (the *xz*-plane passing through the centre of the annular aperture parallel to the plane of polarisation). To record absolute transmission, one would require a 100% efficient microwave lens to accept the diverging signal transmitted via the annulus and focus it at the detector. Hence transmission is shown in arbitrary units throughout this chapter.

Our earlier simple analysis of the frequency of the modes of the system (*Equation 8.2.6*) predicts that the square of the resonant frequency is linearly related to N^2. The graph shown in *Figure* 8.5.2 clearly demonstrates that this approximation is valid, producing a straight line using the experimental data for $\theta = 0^\circ$ and $\psi = 0^\circ$ for $1 \leq N \leq 13$, and $P = 1$. Also shown are the prediction of the resonant frequencies from the FEM model which agree exceptionally well with the experimental data. However, note that for the shorter wavelengths, the predictions from equation *8.2.6* deviate from both the experimental results and also those from the FEM model (*e.g.* for $N = 10$, equation 8.2.6 predicts the mode to be 0.7 GHz higher than that observed experimentally).

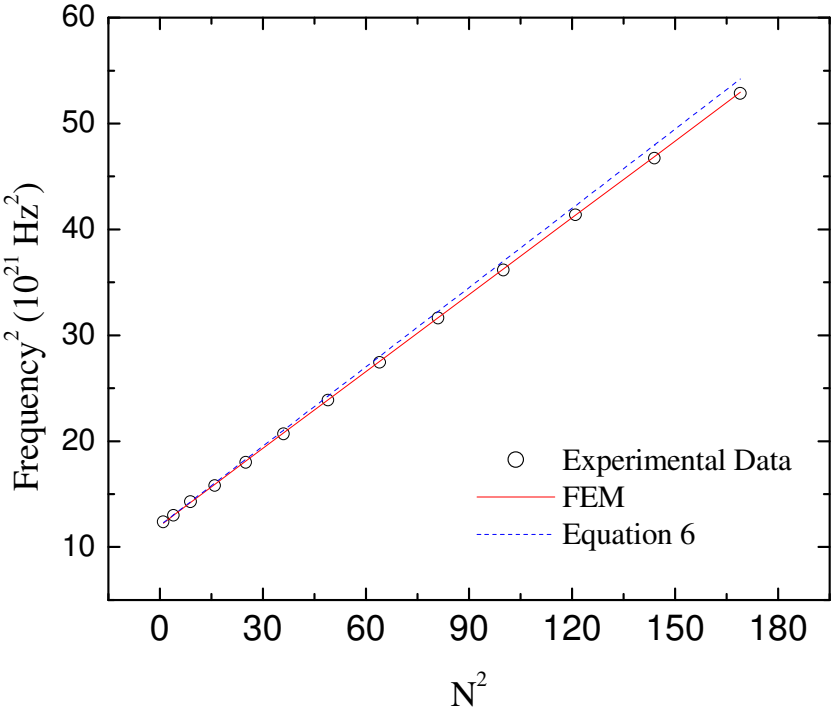

Figure 8.5.2. Resonant frequency squared as a function of N^2 for the experimental transmission data obtained at $\theta = 0^\circ$ $\psi = 0^\circ$, compared to the theoretical electromagnetic response of the sample calculated using the finite element code. Also shown are the predictions of equation *6*, generated using consecutive values of N between 1 and 13, and a circumferential quantum number of 1.

This discrepancy in frequency for the higher energy modes might suggest beam spread in the incident signal, or possibly slightly rounded edges of the two concentric cylinders introducing a spread in *L*. However, as the finite element model agrees fully with the data, then this discrepancy may not be attributed merely to beam spread, or any other experimental geometric factors. Instead the problem is with equation *8.2.6,* which predicts resonant frequencies higher than that observed in the transmittance due to a Takakura type shift in resonant frequency, arising simply from end affects [*Y. Takakura,* (2001)]. In order to explain the nature of each resonance and to further the discussion of the discrepancy between the predictions of equation *8.2.6* and the observed transmittance, we need to be able to characterise each resonance by considering the field profiles obtained from the FEM code.

The time-averaged magnitude (i) and (iv) of the electric field together with the *E* and *H*-vector magnitudes ((ii) and (iii) respectively) are displayed in *Figure* 8.5.3, evaluated at the resonant transmission frequencies of (a) 35.2, and (b) 36.1 GHz, corresponding to modes B and C of *Figure* 8.5.1 The *E* and *H*-vectors are calculated at a phase corresponding to maximum enhancement, and plotted over the surface of the coaxial core of radius *a*. Radiation is incident with its wave vector in the *z*-direction at $\theta = 0^{\circ}$, and the incident electric vector is polarised parallel to the *x*-axis. Mode B is characterised by two nodes in its electric field around the circumference of the annulus (*i.e.* a whole wavelength), and a single node along its length. Hence this mode is a $P = 1$ $N = 1$ mode. Similarly, mode C is shown to also possess a single wavelength about the circumference and two nodes along its length. Thus mode C is a $P = 1$, $N = 2$ mode. Each mode supported at normal incidence within the experimental frequency range was characterised in this way. With the exception of mode A, which will be discussed in due course, all were found to be standing wave states about both the circumference and the length of the annulus (with $P = 1$ and consecutive values of N). Further, the magnitude of the *E* and *H*-vectors evaluated over the surface of the inner cylindrical core for modes B and C clearly show $E_z = 0$ and $H_z \neq 0$. Hence these quantised standing wave states are not derived from reflections of the TEM mode at each end of the cavity, but rather the TE_{11} waveguide mode (*subscripts in wave-guide notation denote the periodicity in the radial, and transverse directions respectively*) . The cut-off wavelength (λ_c) for the TE_{11} mode in this geometry is simply the average circumference $\lambda_c = \pi(a+b)$, which corresponds exactly to the resonant frequency of the $P = 1$, $N = 1$ mode. This simple approximation is valid even as *a* tends to zero, and the coaxial pair approximates to a cylindrical wave guide. The expression for λ_c reduces to $2\pi b/2$ whereas the exact expression for the cut-off wavelength of the dominant TE_{11} mode in a cylindrical wave guide (derived from the first derivative of the Bessel function of the first kind [*Chapter 3, section 5.1*]) yields $\lambda_c = 2\pi b/1.841$.

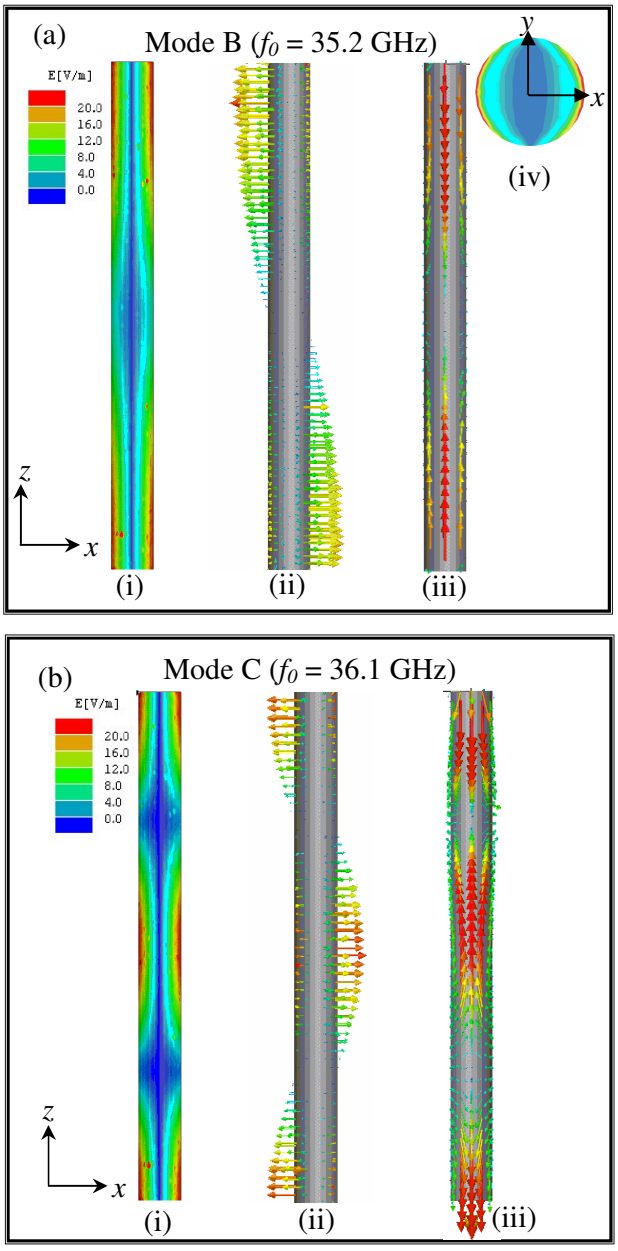

Figure 8.5.3. The time averaged magnitude (i) of the electric field together with the *E* and *H*-vector magnitudes ((ii) and (iii) respectively), evaluated at the peak transmission frequencies of (a) mode B (35.2 GHz), and (b) mode C (36.1 GHz). The *E* and *H*-vectors are calculated at a phase corresponding to maximum enhancement, and plotted over the surface of the inner core of radius *a*. Plane wave radiation is incident from above with its wave vector in the *z*-direction, and incident electric vector lying parallel to the *x*-axis.

Let us now return to the more interesting field profiles of Mode A (*Figure 8.5.4*). Once again, the time averaged magnitude of the *E*-field is shown (i), calculated over the inner coaxial core. Also shown is the magnitude of the electric vector evaluated at two values of phase separated temporally by 180º ((ii) and (iii)), with radiation incident at θ = 0º, polarised parallel to the *x*-axis.

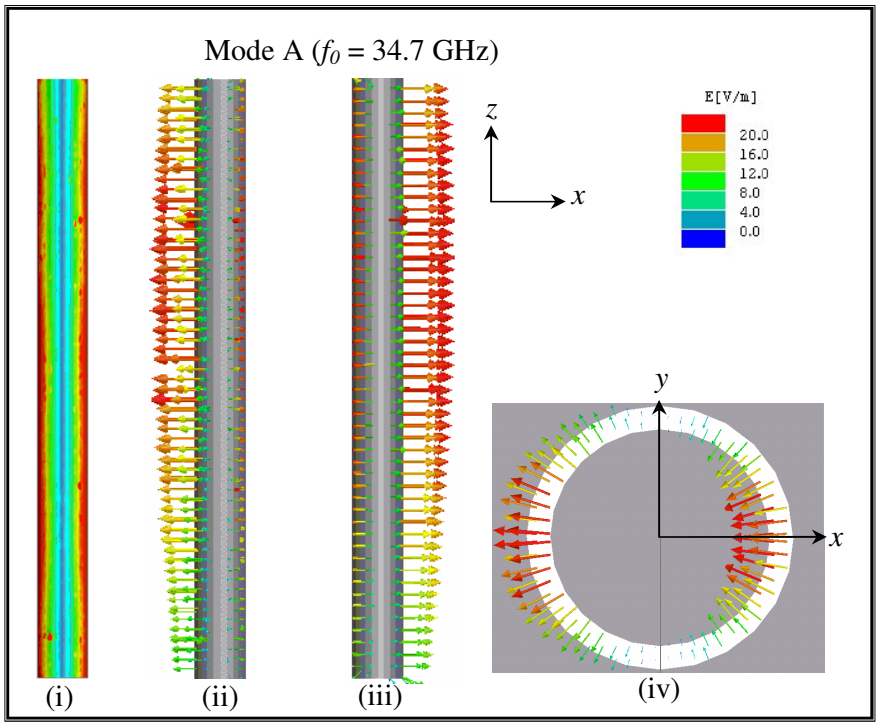

Figure 8.5.4. The time averaged magnitude of the *E*-field (i) calculated over the inner coaxial core. Also shown is the magnitude of the electric vector ((ii) and (iii)) evaluated at values of phase separated by 180º. Radiation is normally incident, polarised parallel to the *x*-axis. (iv) the electric vector magnitude calculated over the *xy*-plane at *z* = 0 (the illuminated face of the sample).

It is clear from the time averaged *E*-field magnitude that mode A forms a standing wave state about the circumference of the annulus, and exhibits no variation of *E*-field strength in the *z*-direction. This suggests that the mode is a circumferential standing wave state of the TE_{11} mode that propagates in the *z*-direction. However, the evaluation of the electric vector magnitude over the surface of the inner core clearly shows no variation along its length, and therefore is 'DC' in nature, with $\lambda_\phi = \pi(a+b)/2$ and $\lambda_z \approx \infty$, hence $k_z \approx 0$. The peak transmission wavelength of this mode corresponds exactly to the cut-off frequency of the TE_{11} mode (*Figure* 8.5.5): the resonance being dependent only upon the mean circumference of the annulus and independent of *L*, and therefore characterised as a $P = 1$ $N = 0$ mode. This unique field distribution is also more susceptible to absorption, and hence is the primary reason for the difference in intensity between this and other $P = 1$ modes. To verify this, modelling the two coaxial cylinders (*Figure* 8.5.5 *inset*) as perfect conductors instead of aluminium is undertaken, and shows that the intensity of mode 1 rises to match that of the other $P = 1$ modes.

For all $P = 1$, and higher odd-numbered modes, coupling by incident plane wave radiation is possible at normal incidence since the electric vector on either side of the inner core must oscillate in phase. Further, modes corresponding to even values of circumferential quantum number (*P*) may only be coupled to at $\theta \neq 0^\circ$, due to the horizontal phase variance of the incident plane wave introduced across the sample surface. It is important to note here that, due to the circular symmetry of the coaxial system, the polarisation of the incident plane wave is irrelevant in terms of modes excited at normal incidence, since TE (electric vector normal to the plane of incidence) and TM (electric vector parallel to the plane of incidence) polarisations are equivalent. However, at higher values of θ, TE-polarised incident radiation possesses no horizontal phase variation in the incident electric vector. Therefore, TE-polarised incident radiation will not excite modes with even values of circumferential quantum number in this plane of incidence.

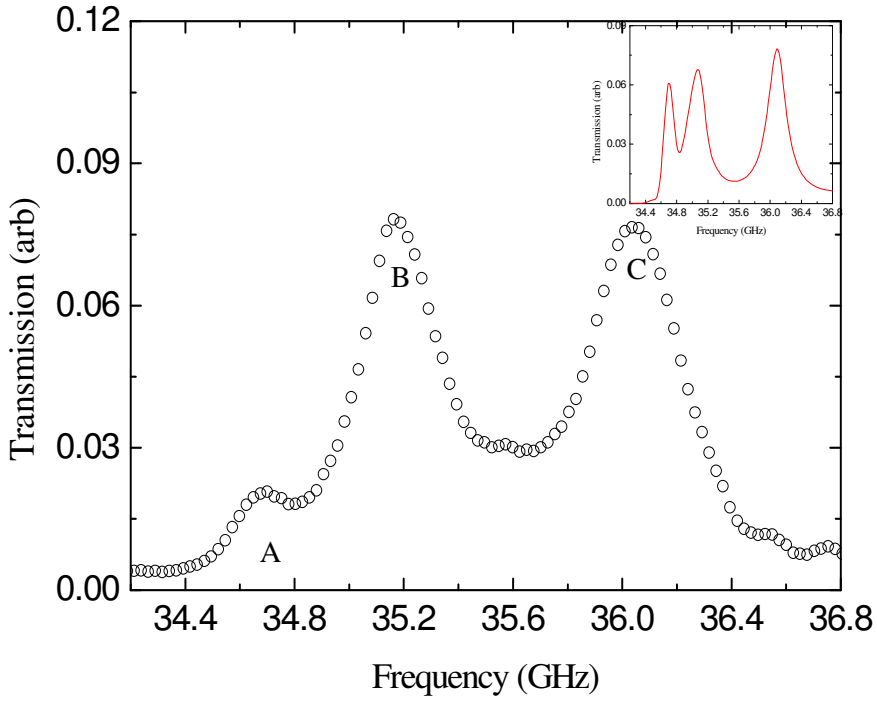

Figure 8.5.5 Frequency dependent transmission data obtained at θ = 0º, ψ = 0º, over a reduced frequency range showing modes 1, 2 and 3. *Inset*: Theoretical transmission spectrum obtained using the FEM, using identical geometric parameters, but with the aluminium substrate and inner core replaced with a perfectly conducting material.

Figure 8.5.6 shows transmission via the annulus as a function of frequency for four consecutive values of θ in 20º increments. Each transmission spectrum is taken at a transmission angle of ψ = 60º, for reasons which will become apparent later in this section. Modes B, C, D, and E are shown to reduce in intensity as the angle of incidence is increased. This is as expected, since these modes are all P = 1 modes which become more difficult to excite as the horizontal phase variation increases. Modes a* and b* however are clearly not visible in the transmission spectrum at normal incidence. Indeed, the coupling efficiency for these two modes is shown to increase with increasing θ. It is therefore apparent that these two modes, one of which is lower in frequency than the cut-off frequency for the TE_{11} mode, possess electromagnetic symmetry that is not compatible with a driving incident plane wave at normal incidence.

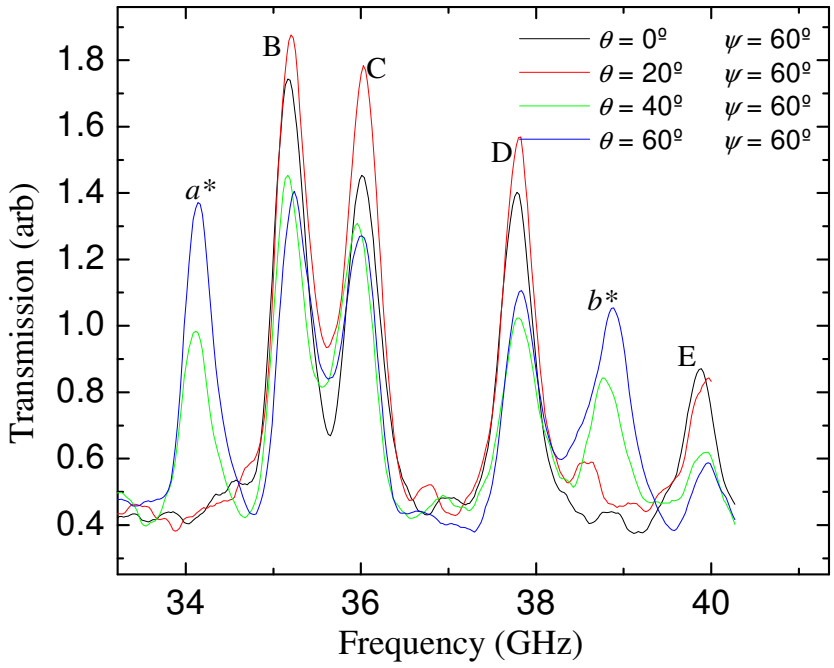

Figure 8.5.6. The frequency dependent transmission spectra obtained for four consecutive values of θ in the range $0 < \theta < 60^{\circ}$, in increments of 20º. Each transmission spectrum is taken at a transmission angle $\psi = 60^{\circ}$, due to the angular distribution of the transmittance being dependent on the circumferential quantum number.

The predicted field profiles at the resonant frequency of mode *a** (34.1 GHz) are plotted over the cylindrical inner core in *Figure* 8.5.7. In each case, radiation is incident in the *xz*-plane, at an angle of 60º from normal to the illuminated face of the sample and TM-polarised (*i.e.* the electric vector also lying in the *xz*-plane). The time averaged electric field magnitude (*Figure* 8.5.7 (i)) shows mode *a** to be a standing wave state in *z*, with a mode number $N = 7$. Note here the distortion in the *E*-field magnitude of the mode, which is more pronounced at the illuminated end of the structure, is due to the relatively large angle of incidence. Further, recall that this mode exists below the cut-off frequency of the dominant TE_{11} mode.

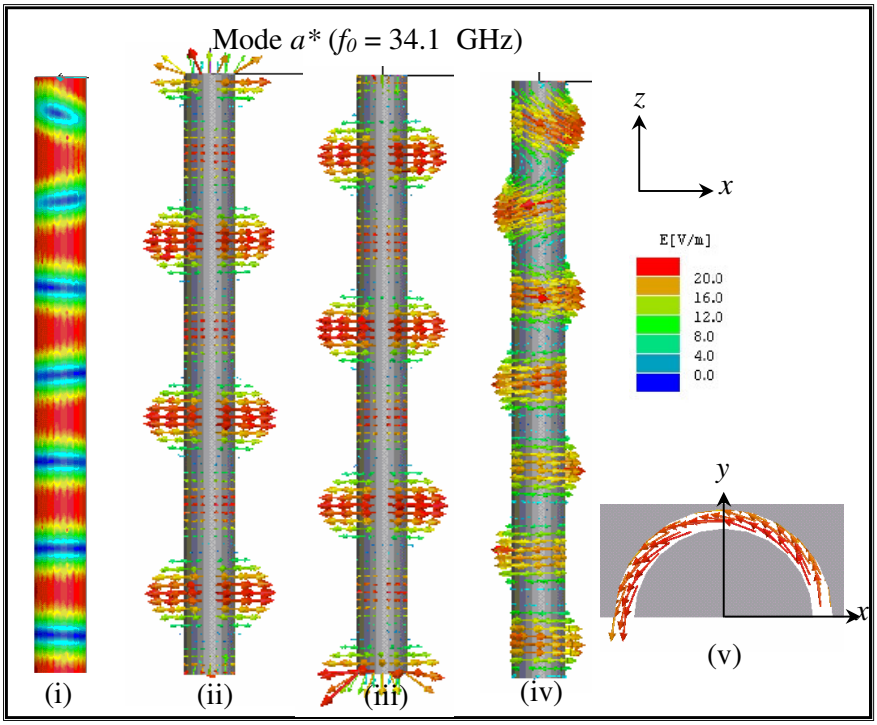

Figure 8.5.7. The field profiles calculated using the finite element code at a fixed frequency of 34.1 GHz, corresponding to the resonant frequency of mode a^* and plotted over the cylindrical inner core, with θ = 60º, ψ = 60º. (i): The time averaged electric field magnitude. (ii) and (iii): *E*-vector magnitude evaluated at a phase separated by 180º. (iv): The *H*-vector magnitude at a phase corresponding to maximum enhancement. (v) the *H*-vector magnitude calculated over a plane parallel to the *xy*-plane at z = -15 mm.

Calculation of both the *E*-vector magnitude (*Figure* 8.5.7 (ii) and (iii) plotted at values of phase separated by 180º) and *H*-vector magnitude (*Figure* 8.5.7 (iv) at a phase corresponding to maximum enhancement) shows the fundamental nature of the mode. Due to the azimuthal symmetry of the coaxial structure, there is no field variation in ϕ. The electric vector within the cavity is shown to be radial, oscillating with time entirely in the *xy*-plane. The magnetic vector is orthogonal to the *E*-vector, containing only H_x and H_y components. Hence we observe $E_z = H_z = 0$, and therefore mode A is a TEM mode quantised by the parameters $P = 0$, $N = 7$. As such, this mode possesses a

propagation constant β and wave impedance Z equal to the wave number k_0 and wave impedance Z_0 of a plane wave propagating in an identical dielectric media. The cut off wave number $k_c = \sqrt{k_0^2 - \beta}$ is zero, and $\lambda_\phi = \infty$, so the resonant frequency is dependent upon the cylindrical length of the annulus, and independent of the radii of the two coaxial cylinders.

Other $P = 0$ modes existing within the studied experimental frequency range ($N > 7$) were characterised using a similar analysis. The square of the resonant frequency pertaining to each mode is shown in *Figure* 8.5.8, as a function of N^2, and once again excellent agreement is obtained between the experimentally determined frequencies of the modes and the calculations from the FEM model, although as before, equation 8.2.6 predicts resonant frequencies which are too high.

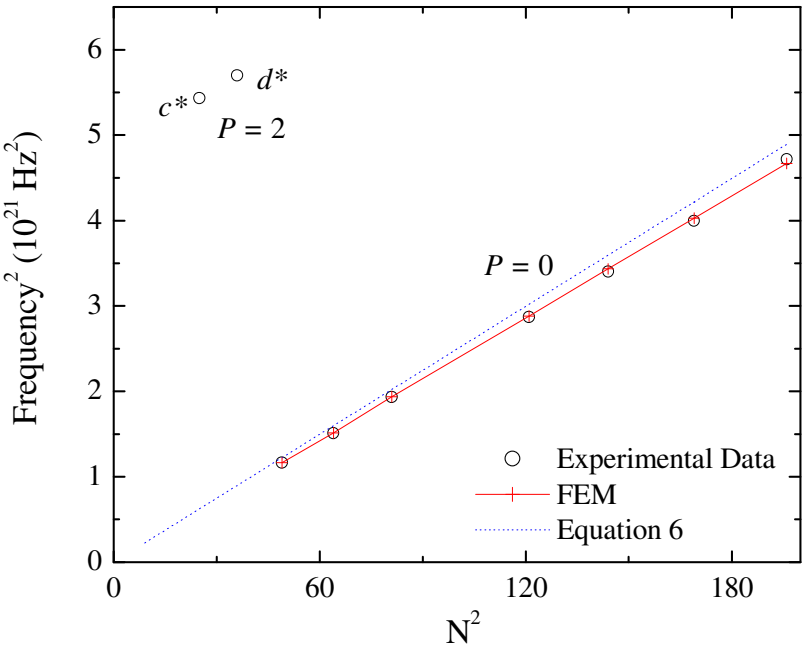

Figure 8.5.8. Resonant frequency squared as a function of N^2 for the experimental transmission data obtained at $\theta = 60°$ $\psi = 60°$, compared to the theoretical electromagnetic response of the sample calculated using the finite element code. $P = 1$ modes are omitted for clarity. Also shown are the predictions of equation *6*. Modelling has shown modes *c** and *d** to be $P = 2$ modes, with the remainder possessing a circumferential quantum number of zero.

There also exist another two modes in the experimental data (denoted modes *c** and *d** respectively) at the high frequency end of the range which appear unlike the others in both their coupling strength (peak intensity for modes *c** and *d** are an order of magnitude less than that of mode B) and field profiles. *Figure* 8.5.9 shows the time averaged magnitude of the *E*-field calculated over the surface of the inner coaxial cylinder at the resonant frequencies of modes (i) *c** and (ii) *d** respectively when $\theta = 60°$. Also shown in parts (iii) and (iv) is the instantaneous E-vector magnitude for the resonant frequency of mode *d** at a phase corresponding to maximum enhancement evaluated over the surface of the inner coaxial cylinder. This modelling demonstrates that modes *c** and *d** are derived from the TE_{11} waveguide mode as the electric vector is entirely transverse to the z direction and $H_z \neq 0$), quantised by a circumferential

quantum number $P = 2$. However the coupling of incident plane wave radiation to the $P = 2$ mode is inefficient, resulting in a lower transmittance at the resonant wavelength of the mode. This is due to the oscillating nature of the mode about the circumference of the annulus, as the electric vector magnitude within the resonant cavity may not easily be matched to the incident electric vector, even for high values of θ (*Figure* 8.5.9 (iv)).

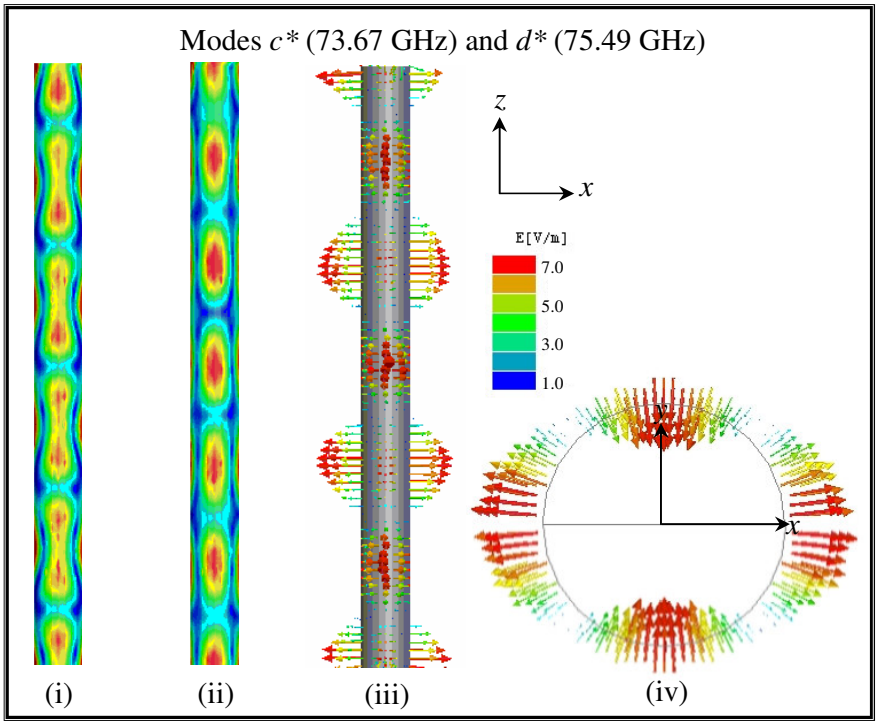

Figure 8.5.9. The time averaged magnitude of the *E*-field calculated over the surface of the inner coaxial cylinder at the resonant frequencies of (i) 73.67 GHz, and (ii) 75.49 GHz, corresponding to the resonant frequency of modes *c** and *d** respectively. Plane wave radiation is incident at an angle of $\theta = 60^{\circ}$ and polarised with the incident electric vector in the *xz*-plane. Also shown is the instantaneous E-vector magnitude (iii) and (iv) at a frequency corresponding to mode *d**, at phase corresponding to maximum enhancement and evaluated over the surface of the inner coaxial cylinder.

It is important to note here that despite the experimental frequency range being relatively large ($30<f_0<75$ GHz), only the TEM and TE_{11} resonances contribute to the

mediated transmission of the structure. As previously noted, the coaxial waveguide supports TEM, TE and TM modes as well as hybrid modes, although no higher order TE, or TM modes are visible. To explain why the TM and higher order TE resonances are excluded, the eigen-modes of a coaxial waveguide with radii a = 1.25 and b = 1.50 mm and of infinite length were calculated using the FEM model. This is a reasonable comparison to the terminated coaxial line studied experimentally, since at cut-off, each mode is invariant in the z-direction and therefore independent of length. Further, modelling the system as infinite in the z-direction reduces the number of solutions dramatically, since $N = 0$. Also, solving the structure as an eigen-mode solution rather than a driven solution [*Chapter 4 section 3.5*] removes the added complexity of coupling incident radiation to the mode. *Figure* 8.5.10 (a) and (b) show the time averaged magnitude of the E and H-fields pertaining to the fundamental resonance of the TM_{01} and TM_{11} waveguide mode respectively, calculated over a plane parallel to the surface of the sample. Also shown are the E and H-vector magnitudes, obtained at a phase corresponding to maximum enhancement (and separated by 90º as expected for a standing wave state). The TM_{10} waveguide mode is absent since it is not supported by a coaxial structure (the azimuthal periodicity of the magnetic field imposes a periodicity transverse to the direction of propagation, excluding the TM_{10} mode).

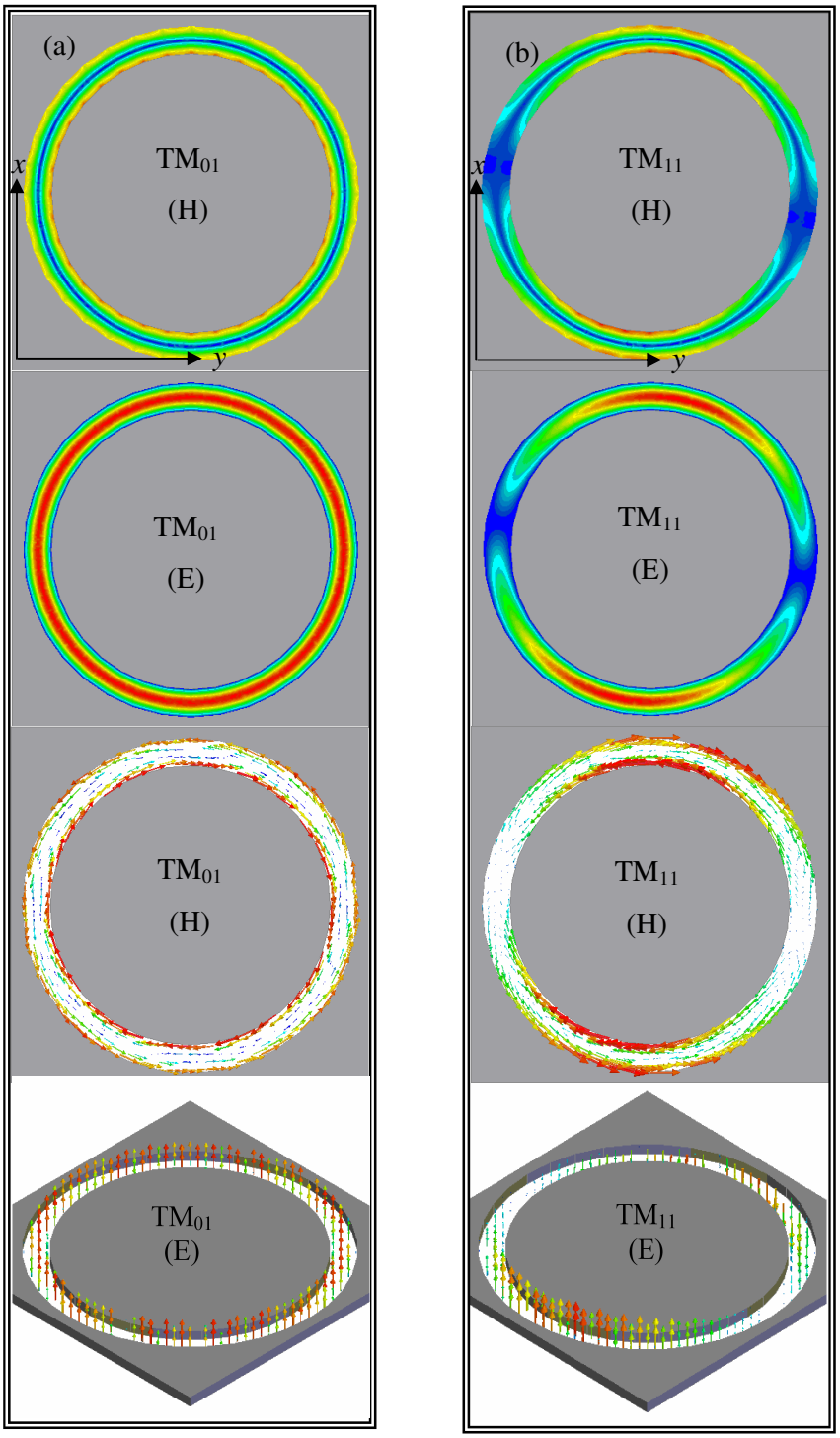

Figure 8.5.10 The eigen-modes of an infinite coaxial waveguide, calculated using the FEM. (a) The TM_{01} mode, showing the electric vector uniform in ϕ, and oscillating with phase entirely in the z-direction. (b) The TM_{11} mode, with the magnetic field forming closed loops in the xy-plane and electric vector reversing in direction as the circumference is traversed.

It is clear that the profiles in *Figure* 8.5.10 (a) possess no azimuthal field variation, and a single maximum in the radial direction, whilst the resonance presented in (b) displays periodicity in both directions. This coupled with the orientation of the *E* and *H*-vectors, identify the two resonances as standing wave states of the TM_{01} and TM_{11} mode respectively. The interesting point to note here is that the frequencies of these two resonances correspond to the cut-off frequency of the respective modes due to the infinite dimension in the *z*-direction, predicted by the FEM to be 600.09 GHz for the TM_{01} mode, and 600.27 GHz for the TM_{11} mode. The reason that the TM modes are separated in frequency from the TE_{11} mode by such a large increase lies in the orientation of the respective *E* or *H*-vector. For the TE_{11} mode, the *E*-vector is entirely transverse to the *z*-direction with the azimuthal periodicity forming two nodes, and the transverse periodicity arising from the change in sign from the inner to the outer coaxial cylinder. Therefore the cut-off frequency for this mode is dependent upon the circumference of the structure and independent of the gap *w*. The same is true for the TE_{21}, TE_{31}, TE_{41} and so on. However, as we see from *Figure* 8.5.10, the orientation of the *H*-vector for TM modes must change sign across the gap. Hence for a TM_{mn} mode, the cut-off frequency is predominantly defined by the separation between the two coaxial cylinders since $n/2$ wavelengths must fit across the gap. For $w = 0.25$ mm as in this case, the cut-off frequency for the lowest TM mode (excluding the TEM mode) is in excess of 599.6 GHz. By a similar argument, the TE_{mn} modes with $n>1$ are also gap dependent.

Figure 8.5.11 shows the ψ-dependent transmission spectra with $\theta = 60^{\circ}$ obtained at the resonant frequency of the $P = 1$, $N = 1$ mode (35.2 GHz), and the $P = 0$ $N = 7$ mode (34.1 GHz). After similar analysis with other modes (not shown), it becomes clear that the $P = 0$ modes possess a very different angular distribution of the transmitted signal than that observed for the $P = 1$ modes. In the case of the $P = 1$ mode, the transmitted signal exits largely normal to the surface plane of the sample, with an angular divergence of $\pm 38.9^{\circ}$, whereas the $P = 0$ mode exhibits two distinct lobes, with the peak intensity of the transmitted signal occurring at $\psi = \pm 60^{\circ}$. The asymmetry of these two lobes in the transmittance arises due to the orientation of the incident wave vector as shown in *Figure* 8.5.11 (b).

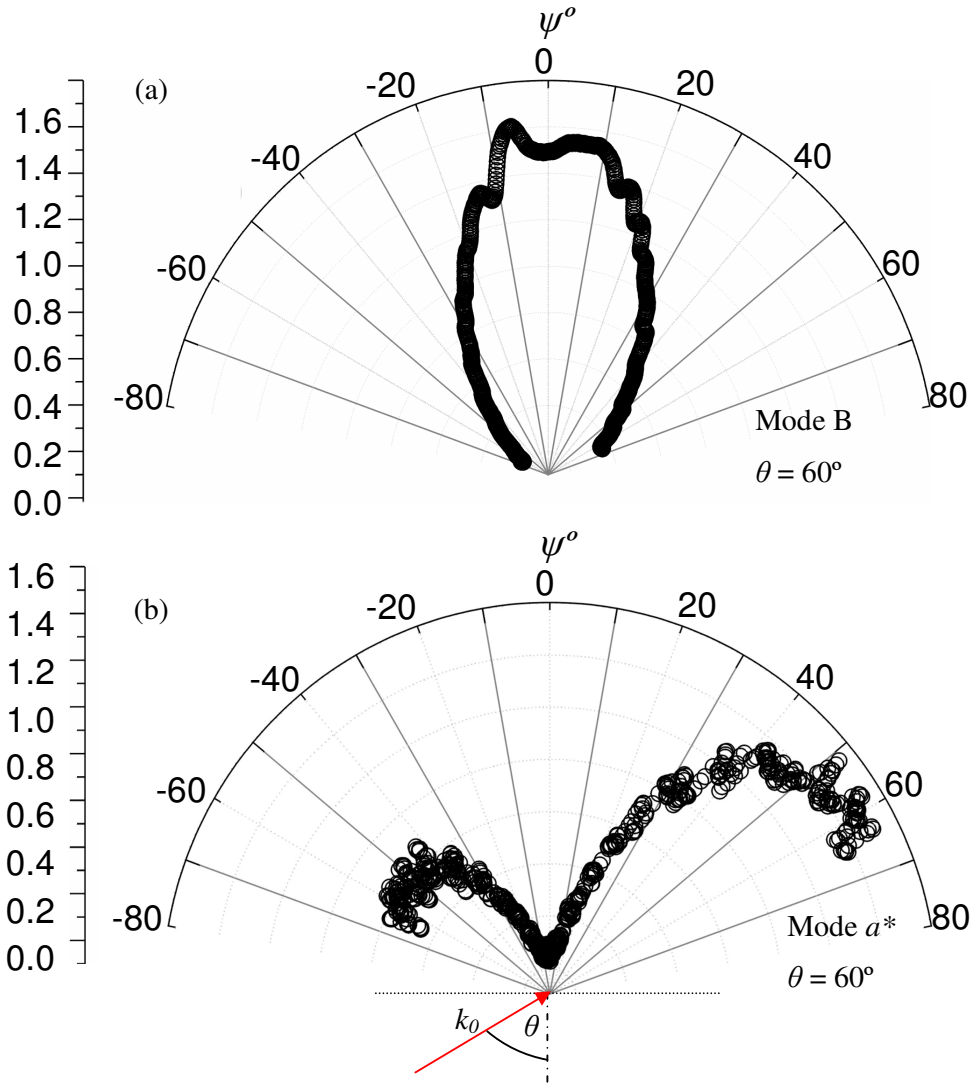

Figure 8.5.11. ψ-dependent transmission spectra obtained at the resonant frequency of (a) 35.2 GHz, corresponding to the $P = 1$ $N = 1$ mode, and (b) 34.1 GHz, corresponding to the $P = 0$ $N = 7$ mode. In each case, plane wave radiation is incident at $\theta = 60°$.

Further analysis of the experimental results have shown that the position in ψ of the peak intensity for both $P = 0$ and $P = 1$ modes is independent of incident angle. Once again, it is useful to evaluate the radiation pattern obtained using the FEM model for

both the quantised TE_{11}, and TEM mode, in order to understand the angular distribution characteristics of the transmitted signal.

Figure 8.5.12 shows the instantaneous *E*-field magnitude for θ = 0º at a frequency corresponding to the resonant frequency of the *P*=1, *N*=1 mode, plotted in the transmitted half-space, over the *xz*-plane passing through the centre of the annulus in the direction of polarisation. In addition the electric field lines are shown, at a lower resolution for clarity. The instantaneous magnetic vector orientation is also shown (although not representative of field magnitude), calculated over the same plane at an identical point in phase (circles denote out of the plane, crosses denote into the plane). It appears that the transmitted fields of this quantised TE_{11} mode (possessing one wavelength around the circumference of annulus) resemble the radiation pattern of an oscillating dipole, since at each point the electric vector is in the plane of the cross-section, with the electric field lines forming closed loops (a characteristic of an induced electric field). However, for a true dipole oscillation the electric field magnitude must be greatest in the direction perpendicular to the dipole moment, with no radiation propagating in the plane containing the dipole axis. This is clearly not the situation here. For this coaxial structure to act as an oscillating electric dipole orientated in the *x*-direction, the two regions of maximum field enhancement (the "hot spots" shown in red, at the exit aperture of the annulus) are required to oscillate exactly out of phase (*i.e.* always of equal magnitude and opposite sign). Whilst the first criterion is met, for the TE mode the latter is not. Instead, the electronic field configuration (as shown by *Figure* 8.5.11 *inset*) forms a pair of electric dipoles, on either side of the annulus. Thus the radiation pattern observed for this mode, and all other P = 1 modes, is that of the superposition of two oscillating dipoles, which is further complicated by the fact that the source is two dimensional, with the regions of high field situated on the corners of the two coaxial cylinders on the exit face of the sample being maximum in amplitude on the *x*-axis, but gradually reducing to zero as we follow the cylinders around in ϕ to the *y*-axis.

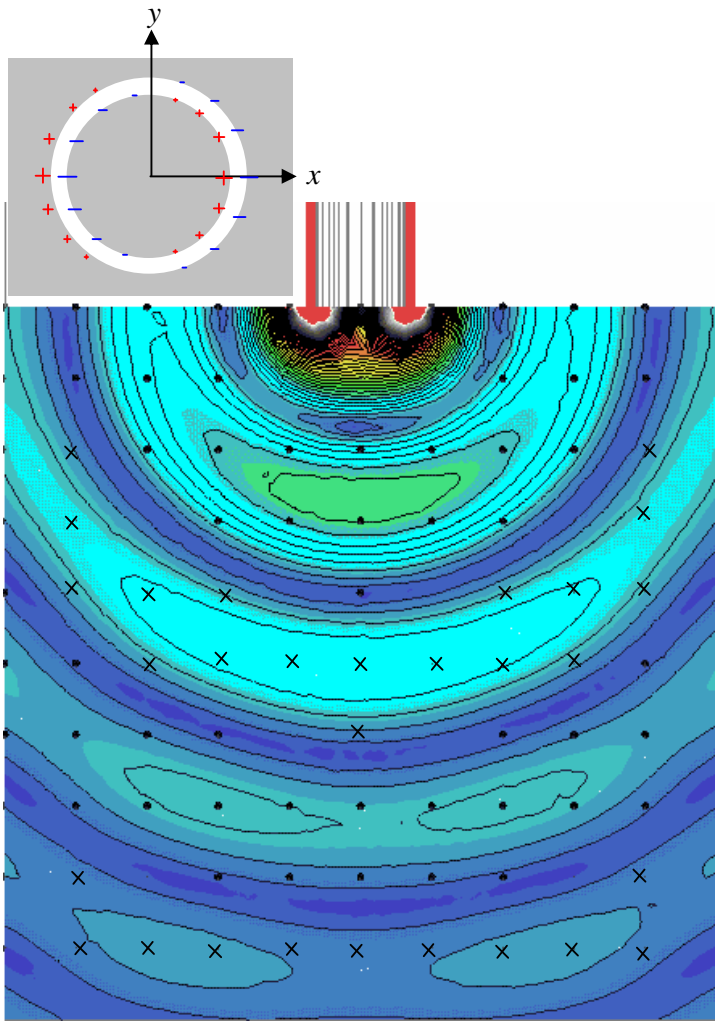

Figure 8.5.12. The instantaneous *E*-field magnitude for θ = 0º at a frequency corresponding to the resonant frequency of the *P*=1 *N*=1 mode. Fields are obtained using the FEM and plotted in the transmitted half-space, over the *xz*-plane passing through the centre of the annulus in the direction of polarisation. In addition the *E*-field contour lines are shown, together with the instantaneous magnetic vector orientation (circles denote out of the plane, crosses denote into the plane). *Inset:* The electronic charge configuration at the exit surface of the annulus arrangement at a particular point in phase.

The radiation pattern for the quantised TEM mode is slightly less complicated. *Figure* 8.5.13 shows the instantaneous *E*-field magnitude at a frequency corresponding to the *P* = 0, *N* = 7 mode.

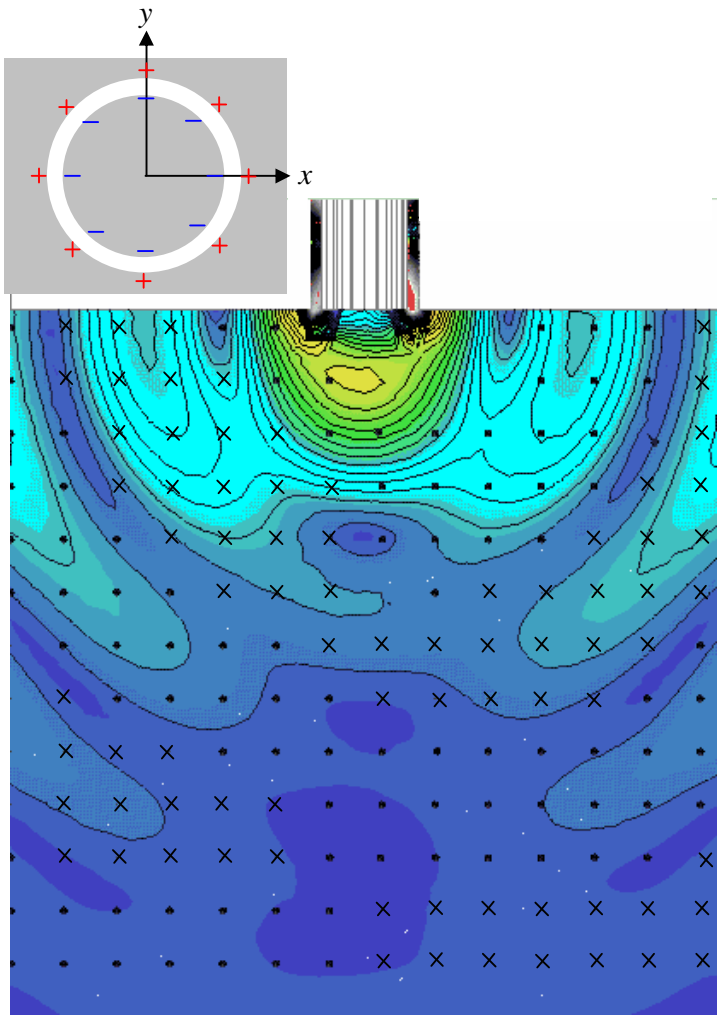

Figure 8.5.13. The instantaneous *E*-field magnitude for θ = 60º at a frequency corresponding to the resonant frequency of the *P*=0 *N*=7 mode. Fields are plotted in the transmitted half-space, over the *xz*-plane passing through the centre of the annulus in the direction of polarisation. In addition the electric field lines are shown, together with the instantaneous magnetic vector orientation (circles denote out of the plane, crosses denote into the plane). *Inset:* The electronic charge configuration at the exit surface of the annulus arrangement at a particular point in phase.

Radiation is incident at an angle $\theta = 60º$, due to the horizontal phase variation required to excite the $P = 0$ modes. The electromagnetic fields on resonance are once again evaluated in the transmitted half-space, over the *xz*-plane passing through the centre of the annulus and parallel to the plane of polarisation. The radiation pattern again resembles that of an oscillating dipole, with the electric field lines forming closed loops in the plane of the cross-section. However, the magnetic field lines now form loops in the *xy*-plane, and energy propagation in the far field region does not occur along the *z*-axis. This result would suggest that the observed radiation pattern is that of an oscillating electric dipole emitter with its dipole moment orientated along the *z*-axis, or a magnetic dipole, which would require a current loop lying in the *xy*-plane centred upon the *z*-axis. As previously discussed however, due to the azimuthal symmetry of the coaxial structure there is no field variation in ϕ for the TEM mode, excluding the possibility that the radiation pattern is formed by a magnetic dipole emitter. As previously shown, the electric vector within the cavity is radial, with the magnetic vector orthogonal to the electric vector and lying in the *xy*-plane at any point between the two conducting cylinders. Hence charge forms on the inner conductive surface of the outer coaxial cylinder that is uniformly distributed in ϕ, alternating in sign in the *z*-direction, separated by the nodes of the quantised standing wave state. A similar charge distribution forms on the inner coaxial cylinder of opposite sign to that on the outer cylinder, as shown by *Figure* 8.5.13 *inset*. Thus the line current on the inner cylinder flows in the *z*-direction, whilst a current of equal magnitude flows in the opposite direction on the outer cylinder. Due to the spatial separation between the two coaxial cylinders, there remains a residual *E*-field.

8.6 Summary

In this chapter, a thorough angle dependent investigation into the enhanced transmission of radiation through a single sub-wavelength annular aperture has been presented. To the best of the author's knowledge this is the first experimental study of enhanced transmission through such a structure to be conducted in the microwave regime, and excellent agreement between empirical data and FEM theory has been obtained. In addition, the FEM modelling of the system has provided remarkable and original insight

into the characteristics observed in the transmission spectra. It has been shown that transmission through the coaxial structure is mediated by Fabry-Perot like resonances arising from the partial reflection of the TE_{11} and TEM waveguide modes at the open ends of the structure, which are quantised into standing wave states by the geometry of the system. Three values of circumferential quantum number are recorded over the selected frequency range. The TEM mode is shown to require a horizontal phase variation in the incident electric vector for coupling to occur, and thus may only be excited when $\theta \neq 0^{o}$. The angular distribution of the transmittance is found to be dependent upon the mediating waveguide mode. For the TE_{11} mode, the transmission exits largely normal to the surface plane of the sample, with a radiation pattern formed by the superposition of two oscillating dipole emitters aligned with the surface plane. For the TEM mode however, the residual line current flowing on both the inner surface of the outer coaxial cylinder, and outer surface of the inner, results in the system acting as an antenna, the radiation pattern of which is that of a dipole emitter with its dipole moment aligned with the cylindrical length of the cylinder, producing two distinct lobes in the angular distribution of the transmitted signal.

Chapter 9
Conclusions

9.1 Summary of Thesis

In this thesis it has been shown that the electromagnetic response of metallic structures at microwave frequencies may be dramatically altered, and in some cases manipulated, through the excitation of modes that exist on the surface of the structure. In the case of flat, textured surfaces, this results in extraordinarily efficient absorption at selective frequencies, and in the case of sub-wavelength apertures results in remarkable enhancement of the transmitted signal through structures that until recently were believed to possess poor transmissive properties. These results have many applications, and with appropriate consideration given to the frequency dependence of the metal surface, the structures presented in this thesis could be scaled to work in any frequency regime.

In *Chapter 5* a thorough reflectivity study of a dual pitch non-diffracting metal bi-grating in the microwave regime has been presented. The dual periodicity and four fold symmetry of the bi-grating results in a structure which supports a remarkably non-dispersive SPP mode that is truly independent of polarisation and direction of the incident beam. This mode is shown to be an extremely efficient absorber of incident radiation at frequencies which may be tuned by the physical parameters of the grating, clearly demonstrating the potential of selectively absorbing designer-surfaces. Further, since the skin depth of the metal is in the order of microns at microwave frequencies, this structure could be pressed into thin metal sheet, resulting a thin and lightweight shielding material which is less than one quarter of the resonant wavelength thick.

In *Chapter 6* an angle dependent reflectivity study of a dual period zero-ordered hexagonal tri-grating has been presented as an extension to the bi-grating work presented in *Chapter 5*. Although it is difficult to improve upon the remarkable degree

of azimuth angle independence displayed by modes supported by the bi-grating structure through the introduction of a higher degree of rotational symmetry, the hexagonal structure gives rise to an increase in the modes supported. At least five of these modes are shown to be remarkably non-dispersive as a function of both θ and ϕ. The work on high impedance absorbing surfaces presented in this thesis has formed the basis of an ongoing study by this author. Already, surfaces (which may not be detailed here due to security clearance issues) that display equally impressive incident angle and polarisation independence, and are 100% efficient, have been constructed and investigated. This next generation of EM-shielding material is as flexible and lightweight as paper, and less than $1/300^{th}$ of the resonant wavelength thick.

In the second section of this thesis, attention focuses on a topic that is generating great interest amongst the research community at the present time. *Chapter 7* presents a thorough experimental investigation into the enhanced microwave transmission through a novel sub-wavelength countersunk aperture surrounded by concentric grooves. To the best of the authors knowledge, this is the first such experimental study conducted using an effectively zero-depth hole, and the first single circular aperture study to be conducted in the microwave regime. In addition, the FEM modelling of the geometry has provided original insight into the transmission enhancement mechanism. A 17-fold enhancement of transmission is illustrated, together with a remarkable angular confinement of the transmitted signal. The transmission enhancement mechanism is shown to be primarily associated with a pseudo-standing wave formed by near field diffraction on the illuminated side of the sample. Its presence results in a strong redistribution of energy density such that regions of high density are located in the vicinity of the countersunk aperture. However, while it is often wrongly assumed that structured metal substrates at microwave frequencies cannot support SPPs, it is illustrated in this chapter that the contribution to the enhanced transmission from SPP-coupling is significant, answering a long running debate which has been conducted through current literature as to the extent of SPP involvement in the enhancement process. The angular confinement of the transmitted signal is shown to be a result of identical patterning on the exit side, supporting a standing wave which radiates from the surface as a set of coherent sources. It is the two dimensional pattern of secondary sources that results in a complex multiple source interference pattern, giving rise to

strong angular confinement of the transmitted beam, and maintaining independence to the angle of incidence. This work is important to the scientific community in general, since the enhanced transmission phenomenon has a wide variety of applications in the field of optical technology, such as high density magneto-optic data storage, and miniaturised photonic circuits. The ability to dramatically enhance the transmission of information via an aperture which is much less than the wavelength of the resonant transmission is therefore of great interest. A structure which may potentially enhance transmission through an aperture with a diameter less than $1/50^{th}$ of the peak transmitted wavelength is presented in *Chapter 8*. Here is recorded resonant transmission of microwaves through a single small annular slit in a metal plate. At normal incidence a family of modes with azimuthal quantum number 1 are found, with frequencies dictated by the plate thickness and the mean radius of the annulus. For non-normal incidence a second family of modes is found corresponding to zero azimuthal quantum number. These modes, essentially like those of an infinite slit have frequencies dictated by the plate thickness and, were it not for the finite conductance of the plate would allow annular transmission at negligible radius. This shows that the enhanced hole transmission recorded by Ebbesen and co-workers may now be substantially strengthened by putting a central metal post in each hole and ensuring the pitch of the grating and the metal film thickness are in accord.

9.2 Future Work

The Thin Film Photonics research group has amassed over 20 years of scientific experience in the area of diffractive optics. Without such a knowledge base, many of the results presented here would have been difficult to achieve. The microwave studies presented in this thesis were carried out as part of the microwave group, which is a smaller subsection of the main Thin Films group, but which produces a large volume of work for publication in some of the worlds leading journals. The possibility of undertaking experiments at much longer wavelengths has allowed the microwave group to consider an enormous range of studies that are impractical or simply much harder to investigate in the visible regime. Hence the list of potentially interesting future work is very large indeed, and just a small selection of ideas are listed here.

For example, consider the fundamental Fabry-Perot-like resonance supported in the standard narrow slit structures discussed previously in *Chapter 8*,. It has already been shown by the microwave group that since a standing wave is established along the length of the cavity, the electric field is maximum at the entrance and exit faces, and zero at its mid-length, while the magnetic field shows a maximum at the slit mid-length. Increasing the width of a central portion of the slit, to form a "notch" where the magnetic field is high, results in an extraordinary reduction in the frequency of resonance (*Figure 9.1*). At the same time, the resonant frequency of the second harmonic is increased (not shown). This effect is associated with the expansion of the field at the boundary between the narrow and wide sections, where the slit is exhibiting a capacitive effect on the mode in the narrow sections, and an inductive effect in the wide section. Bottle-shaped grooves are expected to demonstrate similar effects in absorption, where the boundary condition at the bottom of the groove will be similar to that at the mid-length of the slit. A simple structure to illustrate these effects is an array of metal pipes, into each of which a single slit is cut along its length, where a narrowing of the slits should result in a decrease of the resonant frequency.

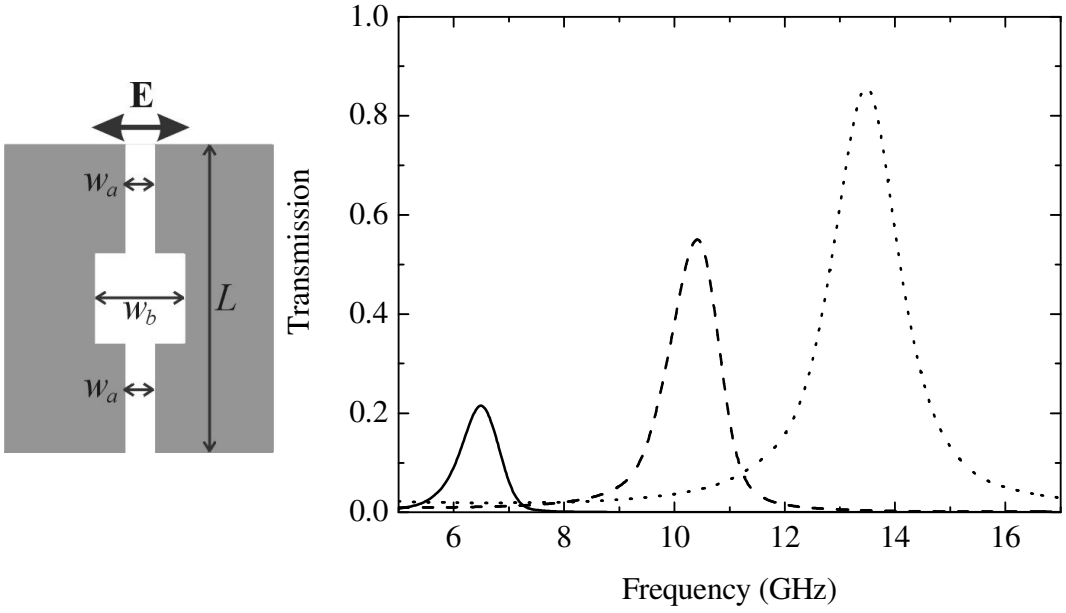

Figure 9.1 Left: Cross-section schematic of a sub-wavelength slit with notch. Right: HFSS predicted response of an array (pitch = 10 mm) of notched slits with L = 10 mm, w_b = 0.7mm and w_a = 0.7 mm (dotted), 0.3 mm (dashed) and 0.1 mm (solid).

Once thorough understanding of this phenomenon is achieved, a full experimental study could be undertaken and verified using the finite element method modelling software. The following questions may then be answered:

- What are the limits to the frequency reduction and sample thickness
- What about higher harmonics? Are multiple notches required to maximise the effect.
- Indeed, can the resonant frequency of the third harmonic be decreased so that it occurs at a lower frequency than that of the second harmonic?
- Instead of widening a section of the cavity, can a similar effect be observed by filling the same section with a material with permeability greater than unity?

It is worth noting that the top surfaces of these cavity arrays appear to act as "magnetic walls" (high-impedance surfaces) on resonance [*D. Seivenpiper* (1999)b], since the electric field strength is now significant on their upper face. Interestingly, preliminary results using photo-etched aluminised mylar sheets as flexible 'magnetic conduction' boundaries for use in other wave-guiding geometries, or high impedance surfaces which act as electromagnetic shields, has provided promising results, and warrant further development, as do structures composed of magnetic layers, or composite metals.

The microwave group have recently demonstrated yet another remarkable result that deserves further investigation. It has been shown [*Suckling et al.*(2004)] that finite conductivity has a pronounced effect on the resonant frequency for small slit widths. Continuation of this work is required, with an aim to discover to what extent the resonant frequency can be lowered, and how its line-width is affected. For example, is it really possible to couple to an extremely low frequency mode? In addition, a number of different metallic materials should be considered to study the effect of different conductivities. The possibility of combining this geometry with the frequency reduction techniques discussed above will be assessed.

Other structures that support coupled-SPP's also warrant investigation. These include an array of metal cylinders laid on a metal substrate, and separated at their closest approach by a sub-wavelength distance. For the reasons discussed above, varying their separation will change the resonant frequency. On resonance, intense fields will occur at the point

where the bottom of the cylinder meets the substrate. Does this realise the possibility of absorption via losses in the metal? Another structure worth consideration in the form of an array is the annulus. While a cylindrical hole in a metallic substrate will not support coupled-SP modes, this co-axial-like structure clearly will (*Figure 9.2* [*Badia et al.*(2003)]).

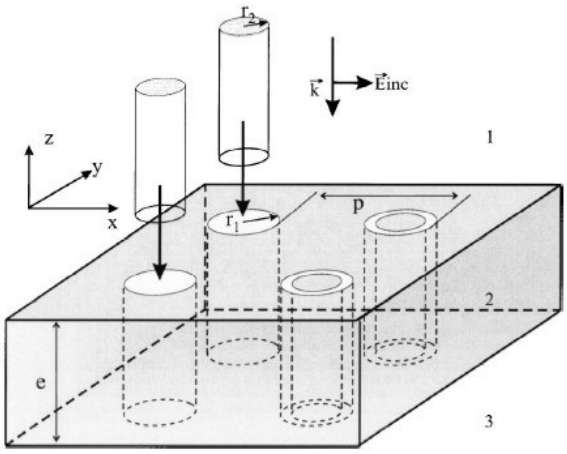

Figure 9.2. An array of dielectric filled annuli in a metal substrate.

Modes are not only quantised by the substrate thickness, but also by the circumference of the annulus. It will be extremely interesting to taper the radii of the structure to instead form a conical structure, whereby at some critical distance along the taper, the momentum matching condition can no longer be satisfied. Hence, the modes will become evanescent, permitting the significant absorption of energy into the metal. This structure could be built for experimental study by placing metal half-spheres into an array of metal "bowls" of slightly larger diameter.

Pendry et al. (2004) has recently shown how a structured metal surface supports a new type of pseudo surface plasmon, just below the waveguide cut-off frequency. This is also an area which could be studied. Further, the sub-wavelength transmitting slits as described in *Chapter 8* of this thesis, in combination with liquid crystals acting as a dielectric filler opens a new line of possible investigation. The refractive index of the dielectric material in such a system will have an effect on the resonant frequency. Liquid crystals are materials that may display not only birefringent properties, but also a substantial change in effective refractive index in response to an applied voltage, and as

such it is possible to construct liquid crystal filled microwave devices that enable a high degree of control over the transmission and absorption properties of the device.

In summary, there exists an extremely large volume of research stemming from a wide range of physical principles that remains to be investigated at microwave frequencies, only a fraction of which has been commented upon in this section.

9.3 List of Publications

Low angular-dispersion microwave absorption of a dual-pitch non-diffracting metal bi-grating

Matthew J. Lockyear, Alastair P. Hibbins, J. Roy Sambles, and Christopher R. Lawrence

Applied Physics Letters, **83**, 806, (2003)

Surface-topography-induced enhanced transmission and directivity of microwave radiation through a subwavelength circular metal aperture

Matthew J. Lockyear, Alastair P. Hibbins, J. Roy Sambles, and Christopher R. Lawrence

Applied Physics Letters, **84**, 2040, (2004)

Finite Conductance Governs the Resonance Transmission of Thin Metal Slits at Microwave Frequencies

James R. Suckling, Aastair P. Hibbins, Matthew J. Lockyear, Trevor W. Preist, J. Roy Sambles, and Christopher R. Lawrence

Physical Review Letters, 2004, **92**, 147401

Enhanced microwave transmission through a single subwavelength aperture surrounded by concentric grooves

Matthew J. Lockyear, Alastair P. Hibbins, J. Roy Sambles, and Christopher R. Lawrence

J. Opt. A: Pure Appl. Opt. **7**, 152, (2005) (Special issue article for Nanostructured Optical Meta-materials).

Microwave transmission through a single sub-wavelength annular aperture in a metal plate.

Matthew J. Lockyear, Alastair P. Hibbins, J. Roy Sambles, and Christopher R. Lawrence

Submitted for publication to PRL.

Low angular-dispersion microwave absorption of a metal dual-pitch non-diffracting hexagonal grating.
Matthew J. Lockyear, Alastair P. Hibbins, J. Roy Sambles, and Christopher R. Lawrence
Accepted for publication to Applied Physics Letters.

Microwave reflectivity of a dual-pitch non-diffracting metal bi-grating
Progress in Electromagnetics Research Symposium (PIERS) Conference Proceedings Jult 1st-5th, 2002, Cambridge, Massachusetts, USA (*oral presentation*).

Surface-topography induced enhanced transmission and directivity of microwave radiation through a sub-wavelength circular metal aperture.
EuroConference, Nano-Optics; Surface Plasmon Photonics, Grenada, Spain, September 2003 (*poster presentation*).

Chapter 9
Conclusions

9.1 Summary of Thesis

In this thesis it has been shown that the electromagnetic response of metallic structures at microwave frequencies may be dramatically altered, and in some cases manipulated, through the excitation of modes that exist on the surface of the structure. In the case of flat, textured surfaces, this results in extraordinarily efficient absorption at selective frequencies, and in the case of sub-wavelength apertures results in remarkable enhancement of the transmitted signal through structures that until recently were believed to possess poor transmissive properties. These results have many applications, and with appropriate consideration given to the frequency dependence of the metal surface, the structures presented in this thesis could be scaled to work in any frequency regime.

In *Chapter 5* a thorough reflectivity study of a dual pitch non-diffracting metal bi-grating in the microwave regime has been presented. The dual periodicity and four fold symmetry of the bi-grating results in a structure which supports a remarkably non-dispersive SPP mode that is truly independent of polarisation and direction of the incident beam. This mode is shown to be an extremely efficient absorber of incident radiation at frequencies which may be tuned by the physical parameters of the grating, clearly demonstrating the potential of selectively absorbing designer-surfaces. Further, since the skin depth of the metal is in the order of microns at microwave frequencies, this structure could be pressed into thin metal sheet, resulting a thin and lightweight shielding material which is less than one quarter of the resonant wavelength thick.

In *Chapter 6* an angle dependent reflectivity study of a dual period zero-ordered hexagonal tri-grating has been presented as an extension to the bi-grating work presented in *Chapter 5*. Although it is difficult to improve upon the remarkable degree

of azimuth angle independence displayed by modes supported by the bi-grating structure through the introduction of a higher degree of rotational symmetry, the hexagonal structure gives rise to an increase in the modes supported. At least five of these modes are shown to be remarkably non-dispersive as a function of both θ and ϕ. The work on high impedance absorbing surfaces presented in this thesis has formed the basis of an ongoing study by this author. Already, surfaces (which may not be detailed here due to security clearance issues) that display equally impressive incident angle and polarisation independence, and are 100% efficient, have been constructed and investigated. This next generation of EM-shielding material is as flexible and lightweight as paper, and less than $1/300^{th}$ of the resonant wavelength thick.

In the second section of this thesis, attention focuses on a topic that is generating great interest amongst the research community at the present time. *Chapter 7* presents a thorough experimental investigation into the enhanced microwave transmission through a novel sub-wavelength countersunk aperture surrounded by concentric grooves. To the best of the authors knowledge, this is the first such experimental study conducted using an effectively zero-depth hole, and the first single circular aperture study to be conducted in the microwave regime. In addition, the FEM modelling of the geometry has provided original insight into the transmission enhancement mechanism. A 17-fold enhancement of transmission is illustrated, together with a remarkable angular confinement of the transmitted signal. The transmission enhancement mechanism is shown to be primarily associated with a pseudo-standing wave formed by near field diffraction on the illuminated side of the sample. Its presence results in a strong redistribution of energy density such that regions of high density are located in the vicinity of the countersunk aperture. However, while it is often wrongly assumed that structured metal substrates at microwave frequencies cannot support SPPs, it is illustrated in this chapter that the contribution to the enhanced transmission from SPP-coupling is significant, answering a long running debate which has been conducted through current literature as to the extent of SPP involvement in the enhancement process. The angular confinement of the transmitted signal is shown to be a result of identical patterning on the exit side, supporting a standing wave which radiates from the surface as a set of coherent sources. It is the two dimensional pattern of secondary sources that results in a complex multiple source interference pattern, giving rise to

strong angular confinement of the transmitted beam, and maintaining independence to the angle of incidence. This work is important to the scientific community in general, since the enhanced transmission phenomenon has a wide variety of applications in the field of optical technology, such as high density magneto-optic data storage, and miniaturised photonic circuits. The ability to dramatically enhance the transmission of information via an aperture which is much less than the wavelength of the resonant transmission is therefore of great interest. A structure which may potentially enhance transmission through an aperture with a diameter less than $1/50^{th}$ of the peak transmitted wavelength is presented in *Chapter 8*. Here is recorded resonant transmission of microwaves through a single small annular slit in a metal plate. At normal incidence a family of modes with azimuthal quantum number 1 are found, with frequencies dictated by the plate thickness and the mean radius of the annulus. For non-normal incidence a second family of modes is found corresponding to zero azimuthal quantum number. These modes, essentially like those of an infinite slit have frequencies dictated by the plate thickness and, were it not for the finite conductance of the plate would allow annular transmission at negligible radius. This shows that the enhanced hole transmission recorded by Ebbesen and co-workers may now be substantially strengthened by putting a central metal post in each hole and ensuring the pitch of the grating and the metal film thickness are in accord.

9.2 Future Work

The Thin Film Photonics research group has amassed over 20 years of scientific experience in the area of diffractive optics. Without such a knowledge base, many of the results presented here would have been difficult to achieve. The microwave studies presented in this thesis were carried out as part of the microwave group, which is a smaller subsection of the main Thin Films group, but which produces a large volume of work for publication in some of the worlds leading journals. The possibility of undertaking experiments at much longer wavelengths has allowed the microwave group to consider an enormous range of studies that are impractical or simply much harder to investigate in the visible regime. Hence the list of potentially interesting future work is very large indeed, and just a small selection of ideas are listed here.

For example, consider the fundamental Fabry-Perot-like resonance supported in the standard narrow slit structures discussed previously in *Chapter 8*,. It has already been shown by the microwave group that since a standing wave is established along the length of the cavity, the electric field is maximum at the entrance and exit faces, and zero at its mid-length, while the magnetic field shows a maximum at the slit mid-length. Increasing the width of a central portion of the slit, to form a "notch" where the magnetic field is high, results in an extraordinary reduction in the frequency of resonance (*Figure 9.1*). At the same time, the resonant frequency of the second harmonic is increased (not shown). This effect is associated with the expansion of the field at the boundary between the narrow and wide sections, where the slit is exhibiting a capacitive effect on the mode in the narrow sections, and an inductive effect in the wide section. Bottle-shaped grooves are expected to demonstrate similar effects in absorption, where the boundary condition at the bottom of the groove will be similar to that at the mid-length of the slit. A simple structure to illustrate these effects is an array of metal pipes, into each of which a single slit is cut along its length, where a narrowing of the slits should result in a decrease of the resonant frequency.

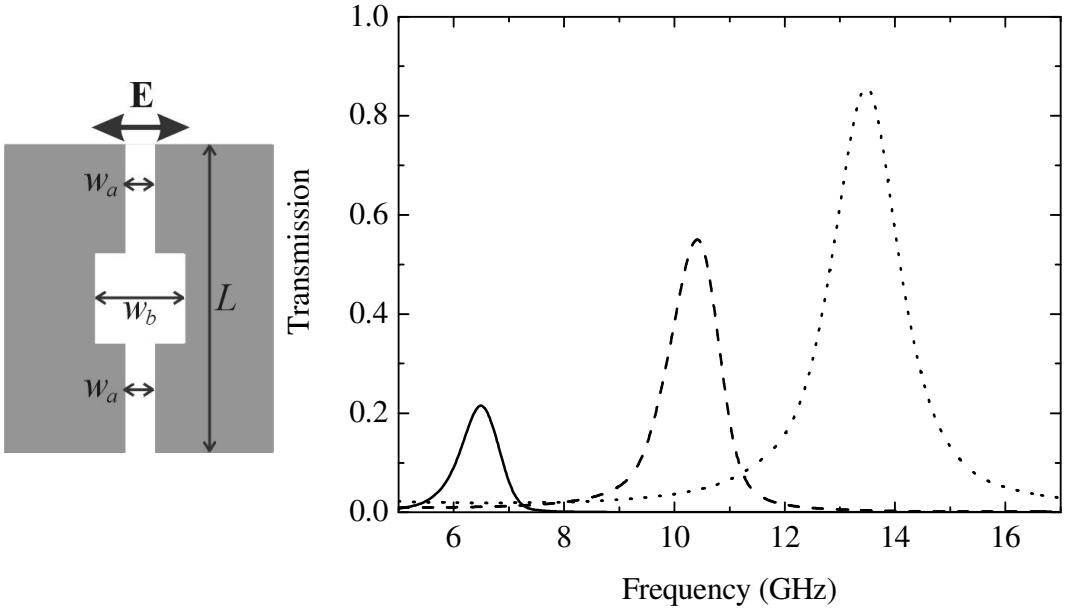

Figure 9.1 Left: Cross-section schematic of a sub-wavelength slit with notch. Right: HFSS predicted response of an array (pitch = 10 mm) of notched slits with L = 10 mm, w_b = 0.7mm and w_a = 0.7 mm (dotted), 0.3 mm (dashed) and 0.1 mm (solid).

Once thorough understanding of this phenomenon is achieved, a full experimental study could be undertaken and verified using the finite element method modelling software. The following questions may then be answered:

- What are the limits to the frequency reduction and sample thickness
- What about higher harmonics? Are multiple notches required to maximise the effect.
- Indeed, can the resonant frequency of the third harmonic be decreased so that it occurs at a lower frequency than that of the second harmonic?
- Instead of widening a section of the cavity, can a similar effect be observed by filling the same section with a material with permeability greater than unity?

It is worth noting that the top surfaces of these cavity arrays appear to act as "magnetic walls" (high-impedance surfaces) on resonance [*D. Seivenpiper* (1999)b], since the electric field strength is now significant on their upper face. Interestingly, preliminary results using photo-etched aluminised mylar sheets as flexible 'magnetic conduction' boundaries for use in other wave-guiding geometries, or high impedance surfaces which act as electromagnetic shields, has provided promising results, and warrant further development, as do structures composed of magnetic layers, or composite metals.

The microwave group have recently demonstrated yet another remarkable result that deserves further investigation. It has been shown [*Suckling et al.*(2004)] that finite conductivity has a pronounced effect on the resonant frequency for small slit widths. Continuation of this work is required, with an aim to discover to what extent the resonant frequency can be lowered, and how its line-width is affected. For example, is it really possible to couple to an extremely low frequency mode? In addition, a number of different metallic materials should be considered to study the effect of different conductivities. The possibility of combining this geometry with the frequency reduction techniques discussed above will be assessed.

Other structures that support coupled-SPP's also warrant investigation. These include an array of metal cylinders laid on a metal substrate, and separated at their closest approach by a sub-wavelength distance. For the reasons discussed above, varying their separation will change the resonant frequency. On resonance, intense fields will occur at the point

where the bottom of the cylinder meets the substrate. Does this realise the possibility of absorption via losses in the metal? Another structure worth consideration in the form of an array is the annulus. While a cylindrical hole in a metallic substrate will not support coupled-SP modes, this co-axial-like structure clearly will (*Figure 9.2* [*Badia et al.*(2003)]).

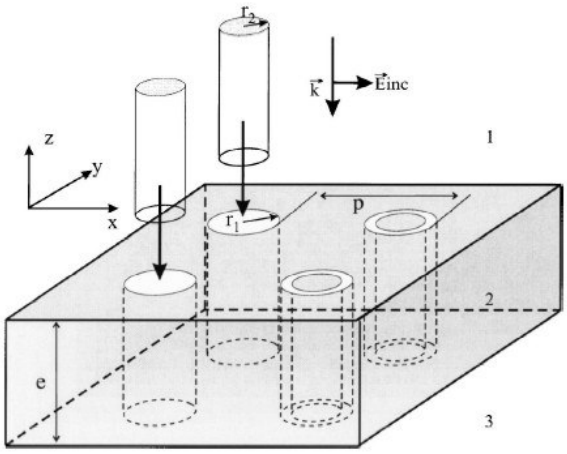

Figure 9.2. An array of dielectric filled annuli in a metal substrate.

Modes are not only quantised by the substrate thickness, but also by the circumference of the annulus. It will be extremely interesting to taper the radii of the structure to instead form a conical structure, whereby at some critical distance along the taper, the momentum matching condition can no longer be satisfied. Hence, the modes will become evanescent, permitting the significant absorption of energy into the metal. This structure could be built for experimental study by placing metal half-spheres into an array of metal "bowls" of slightly larger diameter.

Pendry et al. (2004) has recently shown how a structured metal surface supports a new type of pseudo surface plasmon, just below the waveguide cut-off frequency. This is also an area which could be studied. Further, the sub-wavelength transmitting slits as described in *Chapter 8* of this thesis, in combination with liquid crystals acting as a dielectric filler opens a new line of possible investigation. The refractive index of the dielectric material in such a system will have an effect on the resonant frequency. Liquid crystals are materials that may display not only birefringent properties, but also a substantial change in effective refractive index in response to an applied voltage, and as

such it is possible to construct liquid crystal filled microwave devices that enable a high degree of control over the transmission and absorption properties of the device.

In summary, there exists an extremely large volume of research stemming from a wide range of physical principles that remains to be investigated at microwave frequencies, only a fraction of which has been commented upon in this section.

9.3 List of Publications

Low angular-dispersion microwave absorption of a dual-pitch non-diffracting metal bi-grating

Matthew J. Lockyear, Alastair P. Hibbins, J. Roy Sambles, and Christopher R. Lawrence

Appllied Physics Letters, **83**, 806, (2003)

Surface-topography-induced enhanced transmission and directivity of microwave radiation through a subwavelength circular metal aperture

Matthew J. Lockyear, Alastair P. Hibbins, J. Roy Sambles, and Christopher R. Lawrence

Appllied Physics Letters, **84**, 2040, (2004)

Finite Conductance Governs the Resonance Transmission of Thin Metal Slits at Microwave Frequencies

James R. Suckling, Aastair P. Hibbins, Matthew J. Lockyear, Trevor W. Preist, J. Roy Sambles, and Christopher R. Lawrence

Physical Review Letters, 2004, **92**, 147401

Enhanced microwave transmission through a single subwavelength aperture surrounded by concentric grooves

Matthew J. Lockyear, Alastair P. Hibbins, J. Roy Sambles, and Christopher R. Lawrence

Accepted for publication; Journal of Optics A: Pure and Applied Optics, as a special issue article for Nanostructured Optical Meta-materials on the 28th October 2004. Expected online publication: January 2005 (Print: February 2005)

Microwave transmission through a single sub-wavelength annular aperture in a metal plate.

Matthew J. Lockyear, Alastair P. Hibbins, J. Roy Sambles, and Christopher R. Lawrence

Submitted for publication to Nature.

Low angular-dispersion microwave absorption of a metal dual-pitch non-diffracting hexagonal grating.
Matthew J. Lockyear, Alastair P. Hibbins, J. Roy Sambles, and Christopher R. Lawrence
Submitted for publication to Applied Physics Letters.

Microwave reflectivity of a dual-pitch non-diffracting metal bi-grating
Progress in Electromagnetics Research Symposium (PIERS) Conference Proceedings Jult 1st-5th, 2002, Cambridge, Massachusetts, USA (*oral presentation*).

Surface-topography induced enhanced transmission and directivity of microwave radiation through a sub-wavelength circular metal aperture.
EuroConference, Nano-Optics; Surface Plasmon Photonics, Grenada, Spain, September 2003 (*poster presentation*).

REFERENCES

Andrewartha, J. R., Fox J.R., Wilson I.J.	1979	*Opt.Acta.* **26**, 197
Astilean, S., Lalanne, P., Palamaru, M.	2000	*Opt. Commun.* **175**, 265
Baida, F. I. and Van Labeke, D.	2003	*Phys Rev. B.* **67**, 155314
Barnes, W. L., Murray, W. A., Dintinger, J., Devaux, E., Ebbesen T. W.,	2004	*Phys Rev Lett* **92**, 107401
Barnes, W. L., Preist, T. W., Kitson, S. C. and Sambles, J. R.	1996	*Phys. Rev. B.* **54**, 6227
Beaglehole, D.	1969	*Phys. Rev. Lett.* **22**, 708
Bethe, H.	1944	*Phys Rev.* **66**, 163
Bryan-Brown, G. P. and Sambles, J. R.	1990	*J. Mod, Opt.*, **37,** 1227
Cao, Q., Lalanne, P.	2002	*Phys Rev. Lett.* 88*,* 5
Chen, Y. J., Koteles, E. S. and Seymour, R. J.	1983	*Solid State Comm.* **46**, 95
Collin, R. E.	1991	*Field Theory of Guided Waves*, 2nd Ed, IEEE, New York
Depine, R. A., Lester, M.	2001	*J. Mod. Opt.* **48** 1405
Elston, S. J., Bryan-Brown G. P. and Sambles, J. R.	1991	*Phys. Rev. B.* **44**, 6393
Fano, U.	1941	*J. Opt. Soc. Am.* **31**, 213
Ferrell, R. A.	1958	*Phys. Rev.* **111**, 1214.
García-Vidal, F. J., Lezec, H. J., Ebbesen T. W., Martín-Moreno, L.,	2003	*Phys. Rev. Lett.* **90**, 213901
Garcia-Vidal, F.J., Pendry, J.B.	1996	*Phys.Rev.Lett.* **77**, 1163
Garcia-Vidal, F.J., Sanchez-Dehesa, J., Dechlette, A., Bustarret, E., Lopez-Rios, T., Fournier, T., Pannetier, B.	1999	*J. Lightwave Technol.* **17**, 2191
Ghaemi, H. F., Thio, T., Grupp, D.E., Ebbesen, T. W., Lezec, H. J.	1998	*Phys. Rev. B.* **58**, 6779

Grupp, D. E., Lezec, H. J., Ebbesen, T. W., Pellerin, K. M., Thio, T.	2000	*Appl. Phys. Lett* **77**, 1569
HFSS	N/A	*Ansoft Corporation*, Pittsburgh CA, U.S.A
Hibbins, A.P., Sambles, J.R., Lawrence, C.R.	2002	*App. Phys. Lett.* **80,** 13
Hibbins, A.P., Sambles, J.R., Lawrence, C.R., Robinson, D.M.	2001	*Appl. Phys. Lett.* **79**, 2844
Hooper, I.R., Sambles, J.R.	2002	*Phys. Rev. B.* 65, 165432
Inagaki, T., Goudonnet, J.P., Arakawa, E.T	1986	*J. Opt. Soc. Am.* **7** 992
Ingersoll, L. R.	1920	*Astophys. J.* **51**, 129
Kitson, S. C., Barnes, W. L. and Sambles, J. R.	1995	*Phys. Rev. B.* **52**, 11441
Kretschmann E. and Raether H.	1968	*Z. Natur*. 23a, 2135
Laks, Mills, Maradudin	1981	*Phys. Rev. B.* **23**, 4965
Lalanne, P., Hugonin, J,. Astilean, S., Palamaru, M., Moller, K.	2000	*J. Opt. A, Pure Appl. Opt.* **2**, 48
Lezec, H. J., Degiron, A., Devaux, E., Linke, R. A., Martin-Moreno, L., Garcia-Vidal, F. J., Ebbesen, T. W.	2002	Science 297, 820
Lopez-Rioz, T., Mendoza, D., Garcia-Vidal, F., Sanchez-Dehesa, J., Pannetier B.	1998	*Phys. Rev. Lett.* **81**, 665
Martin-Moreno, L., Garcia-Vidal, F. J., Lezec, H. J., Degiron, A., Ebbesen, T. W.	2003	*Phys. Rev. Lett.* **90**, 16, 167401
Martin-Moreno, L., Garcia-Vidal, F. J., Lezec, H. J., Pellerin, K. M., Thio, T., Pendry, J. B., Ebbesen, T. W.	2001	*Phys. Rev. Lett.* **86**, 1114
McDonald, N. A.	1972	*IEEE Trans Microwave Theory Tech,* **20**, 10
Meecham, W. C. and Peters, C. W.	1957	*J. Appl. Phys.* **28**, 216

Nash, D. J. and Sambles, J. R.	1995	*J. Mod. Opt.* **42**, 1639
Otto, A.	1968	*Z. Phys.* **216**, 398
Pendry, J. B., Martín-Moreno L., Garcia-Vídal, F. J.	2004	*Science,* **305**, 847
Pockrand, I.	1976	*J. Phys. D* **9**, 2423
Popov, E. Neviere, M. Enoch, S. Reinisch, R.	2000	*Phys. Rev. B.* **62**, 16 100
Popov, E., Tsonev, L., Maystre, D.	1994	*Appl. Opt.* **33**, 5214
Porto, J., Garcia-Vidal, F., Pendry, J.B	1999	*Phys. Rev. Lett.* **83**, 2845
Raether, H.	1988	*Surface Plasmons on Smooth and Rough Surfaces and on Gratings*, (Berlin: Springer).
Rayleigh, Lord	1907	*Phil. Mag.* **14**, 213
Ritchie, R. H.	1957	*Phys. Rev.* **106**, 874
Ritchie, R. H., Arakawa, E. T., Cowan, J. J. and Hamm, R. N.	1968	*Phys. Rev. Lett.* **21**, 1530
Sambles, J. R.	1998	*Nature* **391**, 641
Schelkunoff , S. A.	1943	*Electromagnetic Waves*, Van Nostrand, New York
Schroter U., Heitmann D.,	1998	*Phys. Rev. B.* **58**, 15 419
Sievenpiper, D., Zhang, L., Jimenez Broas, R. F., Alexopolous, N. G., Yablonovitch, E.	1999	*IEEE Trans Microwave Theory Tech,* **47**, 2059
Sievenpiper, D.	1999b	*'High-impedence Electromagnetic Surfaces'* Ph.D dissertation, Dept. Elect.Eng., University of California, Los Angeles, CA, U.S.A
Sobnack, M. B., Tan, W. C., Wanstall, N. P., Preist T. W., and Sambles, J. R.	1998	*Phys. Rev. Lett.* **80**, 5667
Sommerfeld, A.	1909	*Ann. Physik* **28**, 665

Steinmann, W.	1960	*Phys. Rev. Lett.* **5,** 470
Stratton, J. A.	1941	*Electromagnetic Theory,* McGraw-Hill
Strong, J.	1935	*Phys. Rev.* **48**, 480
Suckling, J. R., Hibbins, A. P., Lockyear, M. J., Preist, T. W., Sambles, J. R., Lawrence C. R.	2004	*Phys. Rev. Lett.* **92**, 147401
Takakura, Y.	2001	*Phys. Rev. Lett.* **86**, 5601
Tan, W. –C., Preist, T. W., Sambles, J. R.	2000	*Phys.Rev.B,* **61**, 13177
Tan, W. –C., Preist, T. W., Sambles, J. R. and Wanstall, N. P.	1999	*Phys. Rev. B* **59**, 12661
Teng, Y.-Y., and Stern, E. A.	1967	*Phys. Rev. Lett.* **19**, 511
Thio, T., Pellerin, K. M., Linke. R. A., Lezec H. J., Ebbesen, T. W.	2001	*Opt. Lett.* **26**, 1972
Treacy, M. M. J.	2002	*Phys Rev. B.* **66**, 195105
Vigoureux J.,	2001	*Opt. Commun.* **198**, 257
Watts, R. A. and Sambles, J. R.	1997	*Opt. Commun.* **140**, 179
Weber, M. G., and Mills, D. L.	1985	*Phys. Rev. B* **31,** 2510
Went, H. E., Hibbins, A. P., Sambles, J. R., Lawrence, C. R., and Crick, A. P.	2000	*Appl. Phys. Lett.* **77**, 2789
Wirgin, A., Lopes-Rios, T.	1984	*Opt.Commun.* **48**, 416
Wood, R. W.	1902	*Phil. Mag.* **4**, 396
Wood, R. W.	1912	*Phil. Mag.* **23**, 310
Wood, R. W.	1935	*Phys. Rev.* **48**, 928
Yablonovitch, E., Gmitter, T., Harbison, J. P., Bhat, R.	1987	*Appl. Phys. Lett.* **51**, 222
Yablonovitch. E	1993	*J. Opt. Soc. Am. B.* **10**, 283
Yang F., Sambles, J. R.	2002	*Phys. Rev. Lett.* **89**, 063901

Zenneck, J.	1909	*Ann. Phys.* **28**, 665
Zhijun Sun, Yun Suk Jung, and Hong Koo Kim	2003	*Appl. Phys. Lett.* **83**, 3021